The University of Sheffield

Investigation of Magnetic Gearing Effect in Fractional Slot and Vernier Permanent Magnet Synchronous Machines

Yue Liu

A thesis submitted for the degree of Doctor of Philosophy

Department of Electronic and Electrical Engineering

The University of Sheffield

Mappin Street, Sheffield, S1 3JD, UK

April 2019

ABSTRACT

This thesis investigates the torque production mechanism of rotor permanent magnet synchronous machines (PMSMs), with emphasis on the contribution of magnetic gearing effect. Fractional slot concentrated winding (FSCW) and Vernier permanent magnet synchronous machines (VPMSMs) will be used as examples for investigation. Then, the torque production mechanism of all existing rotor-PM machine types will be unified and new slot/pole number combinations are proposed.

For both FSCW PMSMs and VPMSMs, the torque production mechanisms are analysed from the perspective of the air-gap field harmonics modulation and the magnetic gearing effect, accounting for slotting effect. It is found that for both machine types, the average torque is produced by both the principle of conventional PMSM torque production and the magnetic gearing effect. A finite element analysis (FEA)-based equivalent current sheet model (ECSM) and a harmonic restoration method are firstly applied to a 12-slot/8-pole FSCW PMSM and a 12-slot/22-pole VPMSM, respectively, to quantify the respective contributions of the conventional principle and the magnetic gearing effect. Hence, the magnetic gearing effect in both machine types are revealed and the expressions of gear ratios are derived. The influence of gear ratio on different performance metrics are analysed and it shows that it can act as an index for a quick overall performance comparison in each machine type.

The influence of slot opening on the torque production of all existing N_s-slot/$2p_r$-pole rotor-PM machine types are analysed from the perspectives of both energy conversion and magnetic gearing effect. It shows that for large torque production, all rotor-PM machines with $2p_r<N_s$ should have small slot openings to enlarge the torque produced via the conventional principle, since the contributions from the magnetic gearing effect are weak. For those with $2p_r>N_s$, there exists an optimal slot opening for the best trade-off between the conventional principle and magnetic gearing effect. The higher the PM pole number is, the larger the optimal slot opening will be. VPMSM can be regarded as a kind of conventional rotor-PM machine of special slot/pole number combinations, whose slot opening plays a critical role in the torque production. For FSCW PMSMs, a machine with $2p_r>N_s$ can also be seen as a Vernier counterpart of one with $2p_r<N_s$. In this way, the torque production mechanisms of all kinds of rotor-PM machines are unified.

Finally, a series of high power factor VPMSMs with coil-pitch of two slot pitches are developed, expanding the selections of slot/pole number combinations of rotor-PM machines.

All theoretical analyses have been validated experimentally.

ACKNOWLEDGEMENTS

Foremost, I would like to express my sincere gratitude to my supervisor, Prof. Zi-Qiang Zhu, for his continuous guidance and support on my research and life throughout my PhD years.

I would also like to thank Dr. S. S. Xue, Dr. L. R. Huang, Dr. Y. X. Li, Mr Jie Ma, Mr H. Y. Li, Mr Lu Wang, Mr Y. F. Zhang and all my fellows from The Electrical Machine and Drives Group of the University of Sheffield for their inspirations in research and companionship in life. Particularly, I would like to thank Mr Laurence Obodo, Mr Karl Rotchell and all the staff from the workshop for their help in prototyping.

I would also like to thank the China Scholarship Council and Protean Electric Ltd for their sponsorship for such a valuable academic and industrial experience.

Last but not the least, special thanks go to my family: my parents, my sister and my wife for their unconditional love.

CONTENTS

NOMENCLATURES

Symbol	Meaning	Unit
B_g	Air gap flux density	T
B_{gr}, B_{gt}	Radial/tangential components of air gap flux density	T
B_{grk}, B_{gtk}	Amplitudes of the kth radial/tangential air gap flux density harmonics	T
B_m	Maximum value of stator/rotor flux density	T
B_{PM1}	Amplitude of the fundamental component of PM air gap flux density	T
B_{PMh}	Amplitude of slot harmonic component of PM air gap flux density	T
B_r, B_s	Air gap flux density components produced by rotor PMs/stator windings	T
B_{ri}, B_{si}	Amplitudes of the ith PM/armature reaction air gap flux density harmonics	T
B_δ	Amplitude of the PM air gap flux density	T
C_T	"Goodness" factor	
e	Instantaneous phase back EMF	V
E_1	Fundamental harmonic of phase back EMF	V
E_{n}	Amplitude of the nth back EMF harmonic	V
f_p	Radial magnetic force density	N/mm^2
f_{rv}	Frequency of induced eddy current in the rotor	Hz
F_s, F_r	Armature reaction/PM MMFs	A
F_{si}, F_{ri}	Amplitudes of the ith armature reaction/PM MMF harmonics	A
F_{wA}	Phase winding function considering slot opening	
$\mathrm{G_r}$	Gear ratio	
h_f	Height of flux modulation pole	mm
h_{so}	Height of slot opening	mm
I_a, I_b, I_c	Amplitudes of phase A/B/C currents	A
I_{ch}	Characteristic current	A
I_d	D-axis current	A
I_m	Amplitude of the phase current	A

I_q	Q-axis current	A
I_{rl}	Index of rotor loss	
k_{d1}	Distribution factor of the fundamental harmonic	
k_e	Coefficient of voltage boost	
k_e	Excess loss coefficient	
k_f	Lamination factor	
k_h	Hysteresis coefficient	
k_{p1}	Pitch factor of the fundamental harmonic	
k_{so}	Slot opening coefficient	
k_w	Winding factor of the fundamental harmonic	
k_{wf}	Flux weakening coefficient	
k_{wv}	Winding factor of the vth harmonic	
l_a	Air gap length	mm
L_d	D-axis inductance	mH
l_{ef}	Stack length	mm
L_m	Mutual inductance	mH
l_{pm}	PM height	mm
L_q	Q-axis inductance	mH
N_a	Winding function	
N_c	Least common multiple of $2p_r$ and N_s	
N_f	Number of flux modulation poles	
N_p	Number of turns per phase	
n_r	Mechanical speed of rotation	rpm
n_{rh}, n_{rl}	Mechanical speed of rotation of machine with higher/lower PM number	rpm
N_s	Number of stator slots	
N_{sm}	Number of sub-motors	
N_{tpc}	Number of turns per coil	
p	Instantaneous power	W

P	Air gap permeance function	H/mm^2
P_0	Amplitude of the DC component of the air gap permeance function	H/mm^2
p_h, p_l	PM pole pair numbers of the high/low speed rotor in a magnetic gear	
P_j	Amplitude of the jth harmonic of permeance function	H/mm^2
p_r, p_s	Pole pair numbers of PM/armature reaction magnetic fields	
p_{rh}, p_{rl}	Pole pair numbers of machine with higher/lower PM pole number	
q	Number of slots per pole per phase	
r_g	Air gap radius	mm
r_i	Stator inner radius	mm
r_o	Stator outer radius	mm
r_y	Stator yoke radius	mm
s_o	Slot opening angle	deg.
t	Time	s
T_0	Average torque	Nm
T_{6n}	Amplitude of the $6n$th torque harmonic	Nm
T_{cogpp}	Amplitude of cogging torque	Nm
T_{em}	Instantaneous electromagnetic torque	Nm
T_h	Torque of high speed rotor	Nm
T_k	Instantaneous torque produced by the kth air-gap flux density harmonic	Nm
T_M	Torque produced by magnetic gearing effect	Nm
T_{pp}	Peak-to-peak torque	Nm
T_U	Torque produced by the principle of conventional PMSM	Nm
U_1	Fundamental harmonic of terminal voltage	V
W_f	Co-energy in air gap	W
w_f	Width of flux modulation pole	mm
w_t	Width of stator tooth	mm
X_q	Q-axis inductive reactance	Ω
α	Ratio of stator tooth arc to stator tooth pitch	

α_i	PM pole arc ratio	
θ	Circumferential position	rad
θ_c	Power factor angle for conventional PMSM	rad
θ_r, θ_s	Phases of PM/armature reaction air gap flux density harmonics	rad
θ_{rk}, θ_{tk}	Phases of the *k*th radial/tangential air-gap magnetic flux density harmonics	rad
θ_{ver}	Power factor angle of a Vernier machine	rad
λ	Winding pole pitch	
μ_0	Permeance of free air space	H/mm
ξ	Wavelength	m
ρ	Ratio of the torque produced by the magnetic gearing effect to the total torque	
σ	Conductivity of rotor core	S/m
σ_0	Leakage coefficient	
τ	Coil pitch	
τ_1	Pole arc of PM fundamental harmonic	mm
φ	Power factor angle	rad
ϕ	Phase of back EMF	rad
Φ_1	Maximum flux per PM pole	Wb
φ_A	Flux linkage per turn	Wb
ψ_1	Fundamental harmonic of phase flux linkage	Wb
ψ_d	D-axis flux linkage	Wb
ψ_{PM}	Fundamental flux linkage produced by PMs	Wb
ω	Electrical frequency	rad/s
Ω_r	Rotor mechanical speed of rotation	rad/s
ω_r, ω_s	Electrical frequencies of the PM/armature reaction magnetic field	rad/s

Abbreviation

BLAC	Brushless alternating current
BLDC	Brushless direct current
CW	Concentrated winding
DL	Double layer
DW	Distributed winding
ECSM	Equivalent current sheet
EMF	Electromotive force
FEA	Finite element analysis
FMP	Flux modulation pole
FS	Fractional slot
GCM	Greatest common divisor
ISDW	Integral slot distributed winding
IPM	Interior permanent magnet
IS	Integral slot
LCM	Least common multiple
MG	Magnetic gear
MMF	Magnetomotive force
PMSM	Permeant magnet synchronous machine
SL	Single layer
SPM	Surface permanent magnet
VPMSM	Vernier permeant magnet synchronous machine

CHAPTER 1

General Introduction

1.1 General PM Machine Topologies

Electrical machines are devices which use the magnetic field as a medium for energy conversion between electrical and mechanical power. Generally, there are three ways to produce a magnetic field excitation which is essential for the electromechanical energy conversion. One is to inject current into the windings, such as DC electrical machines [HUG13] and conventional synchronous machines with rotor field windings [HUG13]. These machines need specially designed winding structures (such as brush and slip) and continuous power supply. The magnetic field can also be generated by electromagnetic induction. A typical example is that in an induction machine, the rotor magnetic field is induced by the magnetic field produced by the stator windings. The third way is to use a permanent magnet to provide a magnetic field. A permanent magnet can provide a magnetic field once it is magnetised, without external power supply or specially designed winding structures, which in turn reduces the cost of manufacture and assembly, increases its reliability and efficiency, and decreases the loss.

The development of permanent magnet synchronous machines (PMSMs) depends highly on the development of PM materials. During the 90's, with the development of the PM materials and the power electronic components, PM machines started to gain popularity in both academia and industry. The general machine topologies are shown in Fig. 1.1. It shows that a PM machine is composed of the stator, windings, the rotor and PMs. According to different conditions of classification, the PMSMs have different types as shown in Table 1.1. From the direction of the magnetic flux, PM machines can be categorized into radial flux and axial flux types, as shown in Fig. 1.1 (a) and (b), respectively. PM machines can also be categorized into rotor-PM and stator-PM machines based on the position of the PMs, as shown in Fig. 1.1 (a) and (c), respectively. In terms of the PM rotor position, PM machines can be grouped into internal rotor and external rotor types, as shown in Fig. 1.1 (a) and (d), respectively. From the perspective of the driving current, PM machines can be categorized into brushless direct current (BLDC) and alternating current (BLAC) machines. From the number of slot per pole per phase (q), PM machines can be categorized into integral slot (IS) machines and fractional slot (FS) machines,

as shown in Fig. 1.1 (a) and (d), respectively. Nowadays, the research and development of PM machines has come to a new stage. Many new PM machine structures with high torque, high power and high function are proposed. Consequently, new theories, new analyses and calculation methods, new control methods and new manufacturing technologies are required.

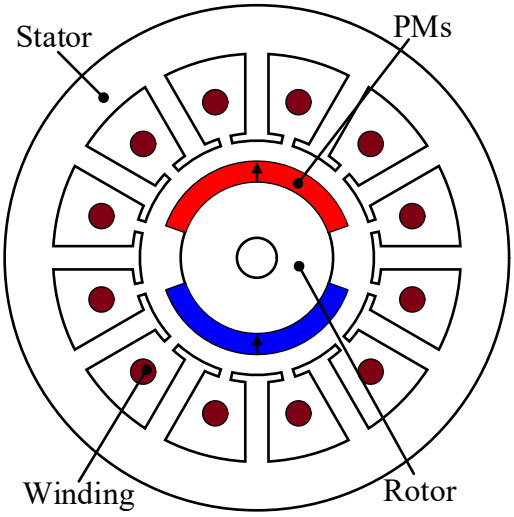

(a) IS-internal-rotor-PM machine

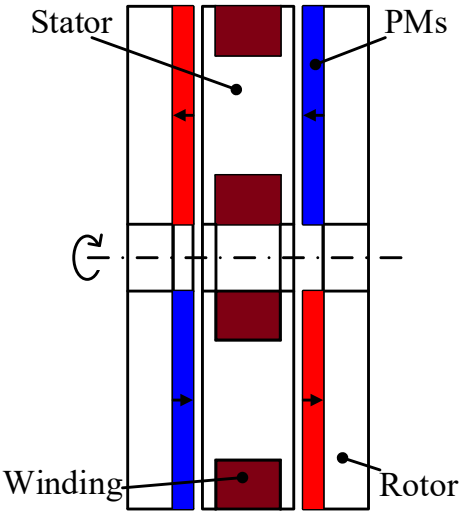

(b) Axial flux PMSM

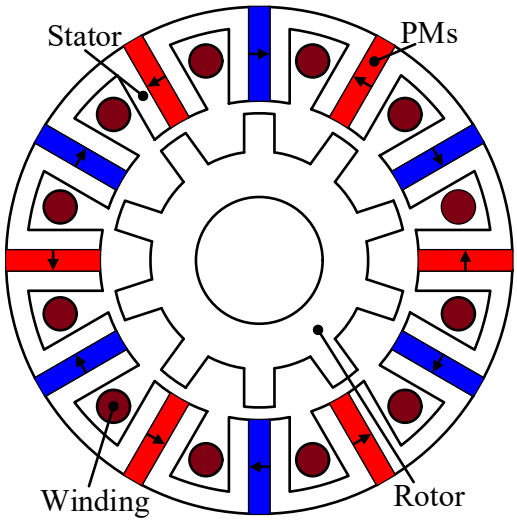

(c) Stator-PM machine

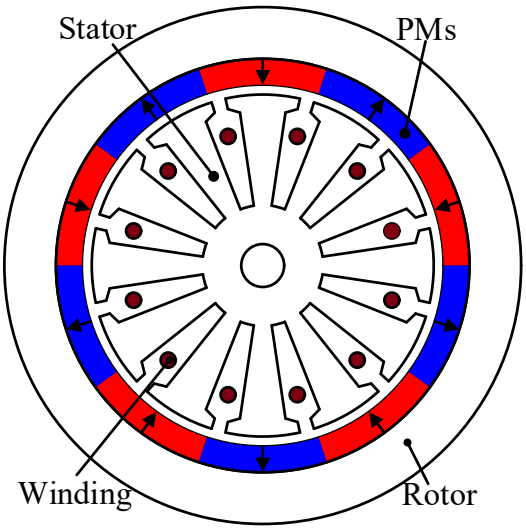

(d) FS-external-rotor-PM machine

Fig. 1.1. General machine topologies.

Table 1.1. Different PMSM types.

PMSM	Flux direction	Radial flux PMSM
		Axial flux PMSM
	PM position	Rotor-PM machine
		Stator-PM machine
	Rotor PM position	Internal rotor PMSM
		External rotor PMSM
	Driving current	BLAC PMSM
		BLDC PMSM
	q	IS PMSM
		FS PMSM
	…	…

This thesis investigates the torque production mechanism of fractional slot concentrated winding PMSMs and Vernier PMSMs from both energy conversion and rotating field theory, and a series of rotor-PM machines with new slot/pole number combinations will be proposed and analysed.

1.1.1 Stator Topologies

The stator core of a PM machine is similar to that of an induction machine [HUG13], which is usually made of silicon steel laminations to reduce the iron loss. Fig. 1.1 shows that the stator has slots in which the windings are accommodated. The stator windings can be either distributed windings (DW) or concentrated tooth-coil windings (CW), as shown in Fig. 1.2. (b) and (c). For DWs, the coil pitch is greater than two slot pitches and for CWs, the coil is wound around each stator tooth. Consequently, the PM machines with DWs have longer end windings than those with CWs. Before the introduction of Vernier PM machines, DW type is usually used for PM machines with q>1. CW type is commonly used for PM machines with q<1. Compared with CWs, the armature reaction magnetic field produced by DWs has low content of higher order harmonics, which helps for loss, torque ripple and noise reduction, as shown in Fig. 1.5. Moreover, the machines with DWs have a potential to generate the reluctance torque. Apart from the stator with AC field windings, the stator can also be equipped with PMs or DC field windings, which are named as stator-PM machines and variable flux machines but are beyond the scope of this thesis.

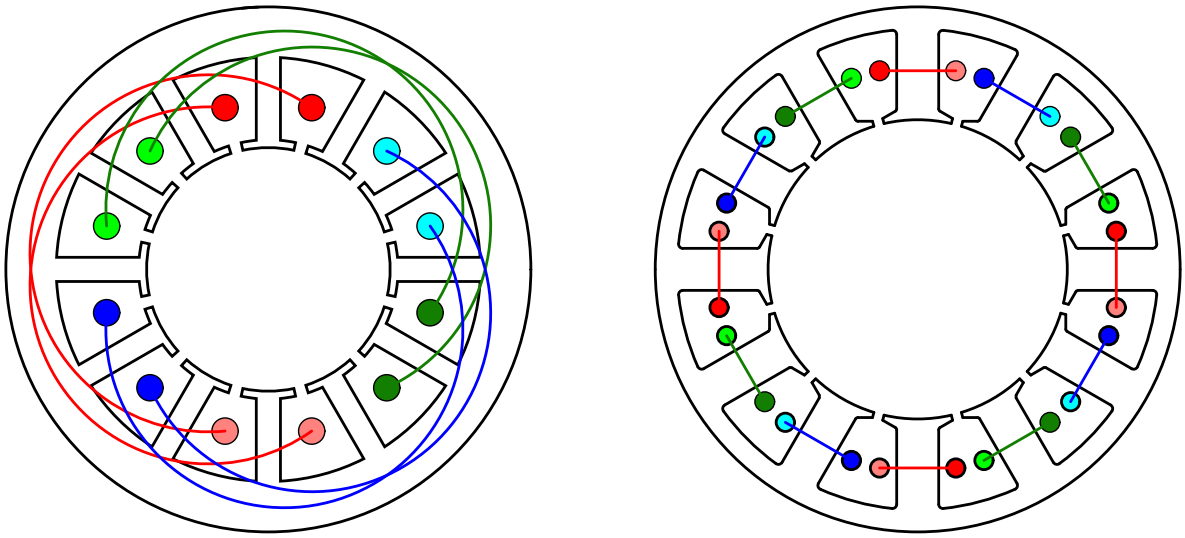

(a) Distributed windings (b) Concentrated windings

Fig. 1.2. General winding types.

1.1.2 Rotor Topologies

The major difference between the PM machine and other machine types lies in the rotor structure, which will be introduced in this section. PM machines with different rotor structures have different performance, control strategies and applications. Recently, PM machines with external rotor topologies have been gaining popularities in specific applications such as in-wheel driving [IFE12]. The advantage of external rotor topology is that it has a larger space utilisation ratio and hence a larger torque density. Moreover, it has a larger moment of inertia, which helps to improve the output power and efficiency under pulsating loadings. Despite the rotor position, the torque production and analysis method of machines with internal rotors and external rotors are the same. In this chapter, only the PM machines with internal rotors will be discussed.

(a) Surface PM rotors

In this kind of rotor, the PMs are mounted on the rotor surface. The magnetisation direction of PMs can be radial or parallel. For high speed applications, the PMs are usually protected by sleeves made from non-magnetic materials. Surface PM (SPM) rotors can be categorized into surface-mounted PM rotors and surface-inset PM rotors, as shown in Fig. 1.3 (a) and (b), respectively. A surface-mounted rotor is regarded as a non-salient rotor as the relative permeance of rare earth PMs is close to that of the air. The structure is simple and easy to manufacture. Moreover, magnet shaping technique can be more easily applied to surface mounted PMs to optimise the air gap flux density distribution so that

the performance can be improved.

For a surface-inset PM rotor, there is magnetic material such as silicon steel between two PM poles, consequently, it is regarded as a salient rotor. Reluctance torque can be generated from the rotor saliency, and hence, the torque and power density can be improved. Compared with surface-mounted PM rotors, surface-inset PM rotors have more leakage flux but it is easier to fix the PMs.

(b) Interior PM rotors

For interior PM (IPM) rotors, the PMs are embedded in the rotor core. Similar with surface-inset PM rotors, IPM rotors are also salient rotors, which can improve the torque and power capabilities by introducing the reluctance torque and improve the flux weakening capability.

IPM rotors can be categorized into three types by the directions of PM magnetisation: I-type, spoke type and hybrid type. An I-type rotor is shown in Fig. 1.3 (c), which shows that the PMs are inserted into the rotor core along axial direction. There are thin iron bridges between adjacent PM poles to maintain the mechanical strength. Compared with a spoke type rotor, it has small leakage coefficient. The pole arc is easy to design and adjust, and the rotor lamination has higher mechanical strength. A spoke rotor is shown in Fig. 1.3 (d). Compared with an I-type rotor, the flux lines from one pole can be provided by two adjacent PMs, so that the torque and power can be enhanced. The advantage of spoke type over I-type rotors becomes obvious when the PM pole number increases and the I-type rotor cannot provide sufficient flux lines per pole. The V-type rotor, being one variation of the I-type rotor, can also take advantage of flux focusing effect and improve the torque and power, Fig. 1.3 (e). The hybrid type rotor combines the merits of I-type and spoke type rotors. As shown in Fig. 1.3 (f), the rotor can provide more space for the I- and spoke type PMs, the leakage coefficient is reduced. However, the rotor structure is more complex, and hence the difficulty in manufacturing increases, while the mechanical strength of the rotor decreases.

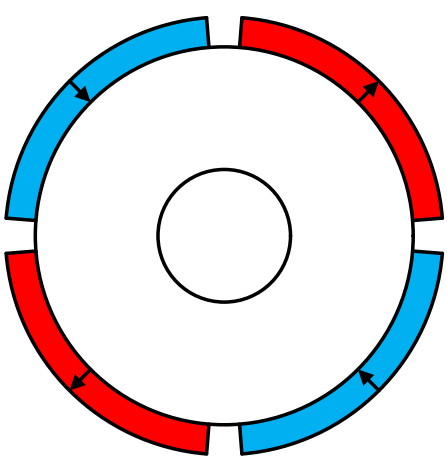

(a) Surface-mounted PM rotor

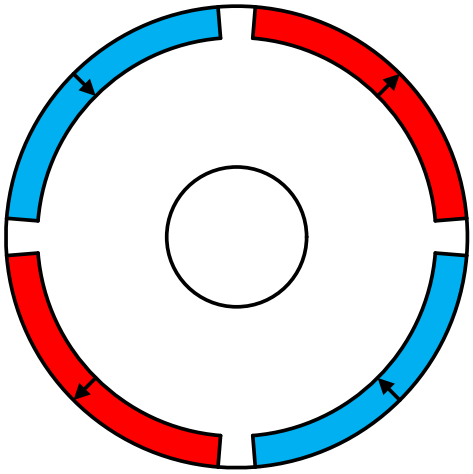

(b) Surface-inset PM rotor

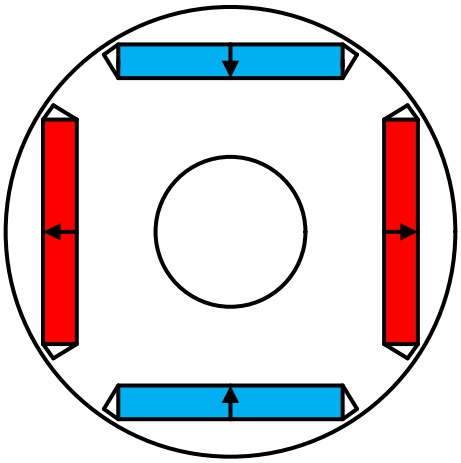

(c) I-type

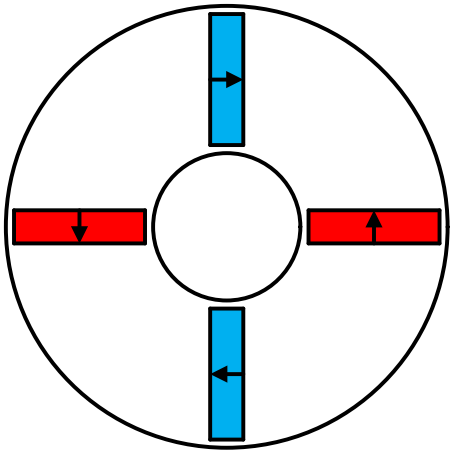

(d) Spoke type

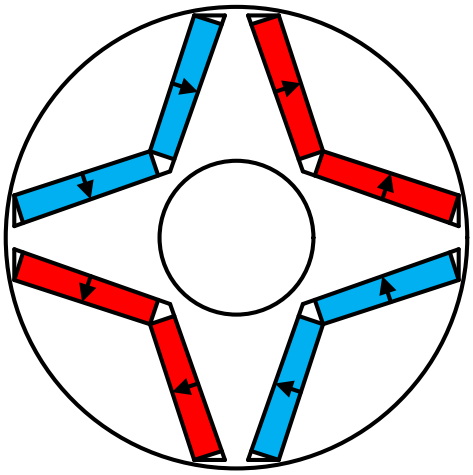

(e) V-type

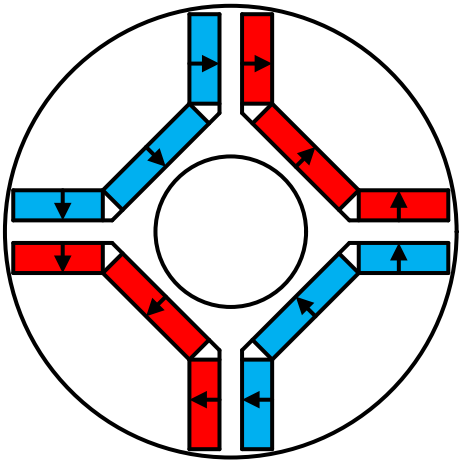

(f) Hybrid type

Fig. 1.3. Rotor topologies.

1.2 Fractional Slot Concentrated Winding PM Machines

1.2.1 Alternate Topologies

Fractional slot concentrated winding (FSCW) PMSMs have been gaining popularities in academia and industry in the past few decades [ELR10]. This kind of machine employs concentrated tooth-coil windings. The q is a fraction lower than 1. Table 1.2 compares the concentrated tooth coil winding and distributed winding. It shows that compared with distributed windings, PM machines with concentrated tooth coil windings have larger slot filling factor and shorter end windings. The torque is produced by the interaction of the PM and a higher order armature reaction magnetomotive force (MMF) harmonics instead of the fundamental armature reaction MMF harmonic. As a result, FSCW PMSMs have advantages of compact size, high torque density, high efficiency, and fault tolerance [ELR10] [ISH05a].

As for the winding configuration, concentrated windings can be either double layer (DL) or single layer (SL) windings. For DL windings, each tooth is wound by a coil. For SL windings, alternate tooth is wound by a coil. Compared with FSCW PMSMs with DL windings, the slot/pole combinations for SL windings are limited. The electromagnetic performance of various performance metrics such as the back electromotive force (EMF), cogging torque and inductances of machines equipped with DL and SL windings are compared in [ISH06] [BIA06]. They show that although FSCW PMSMs with DL and SL windings share the same torque production principle, they perform differently due to the different winding factors. Fig. 1.5 (a) and (b) show the winding diagrams, MMF waveforms and spectra of 12-slot/10-pole FSCW PMSM with SL and DL windings, respectively. They show that FSCW PMSMs with SL windings have more armature reaction MMF harmonic content than those with DL windings. Apart from conventional stator structure, there are also other structures such as unequal tooth [ISH05a] and modular tooth [ZHU11a] designs.

Table 1.2. Comparison between DW and CW [ELR10]

	DW	CW
Typical slot filling factor	35~45%	50%~65%
End winding	Long overlapping	Short non-overlapping
Torque producing stator space harmonic content	fundamental	In most cases a higher order harmonic (except q=0.5)

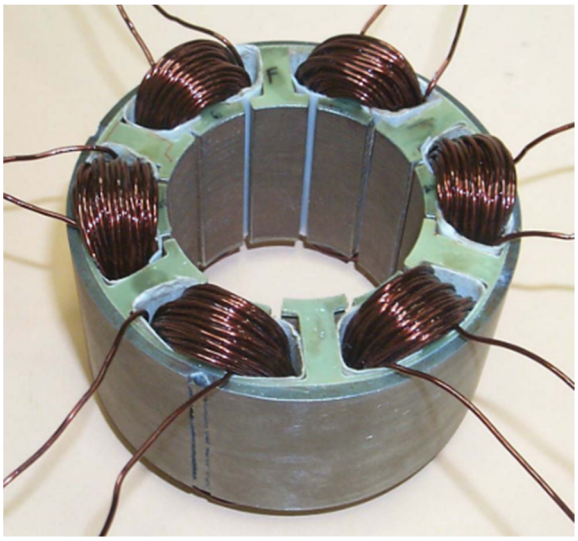

(a) Single layer windings

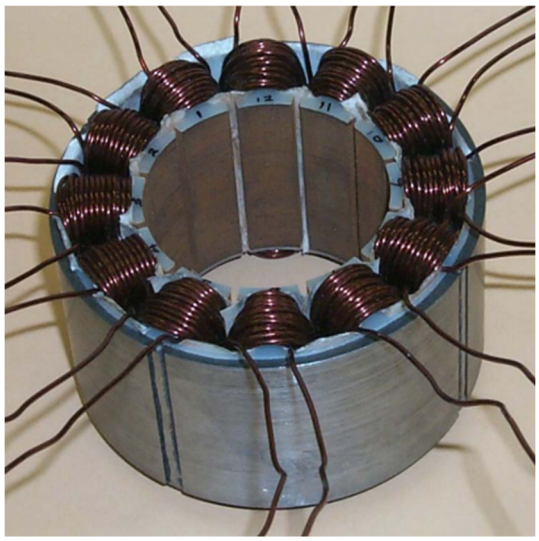

(b) Double layer windings

Fig. 1.4 Pictures of SL and DL windings. [ISH05a]

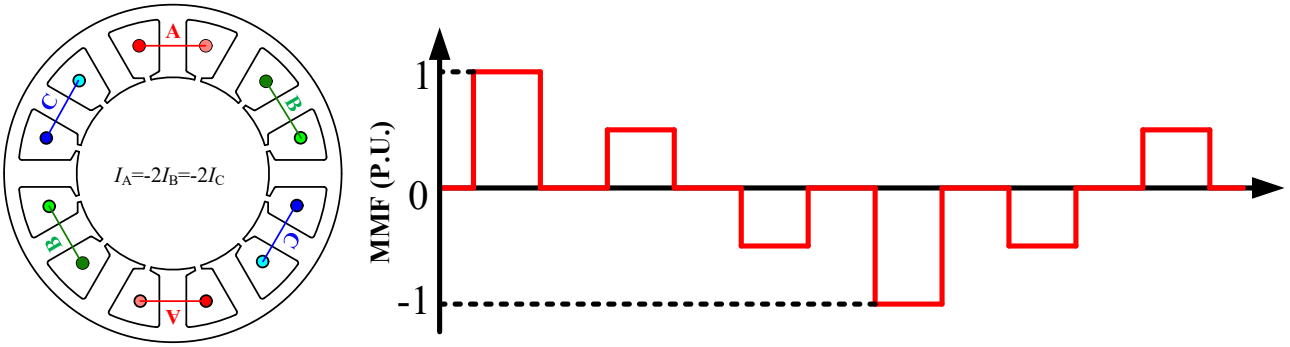

(a) MMF waveform of a 10-pole FSCW PMSM with single layer windings

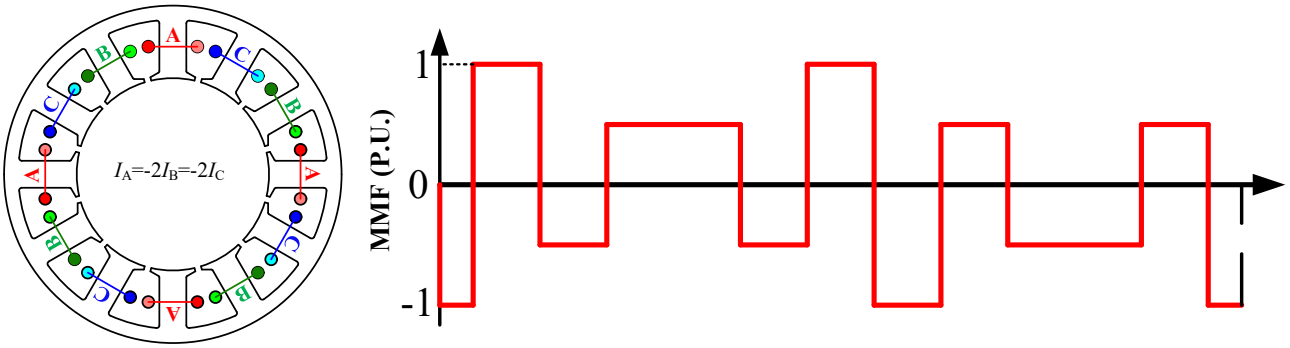

(b) MMF waveform of a 10-pole FSCW PMSM with double layer windings

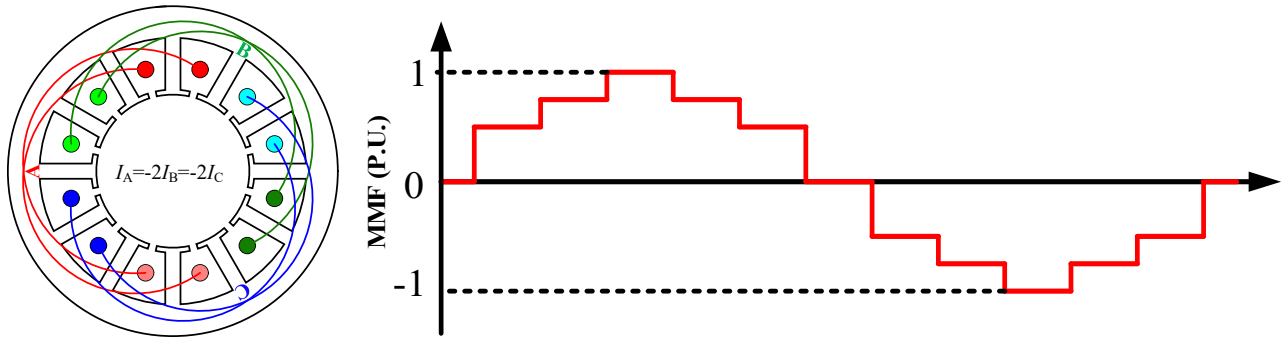

(c) MMF waveform of a 2-pole integral slot distributed winding (ISDW) PMSM

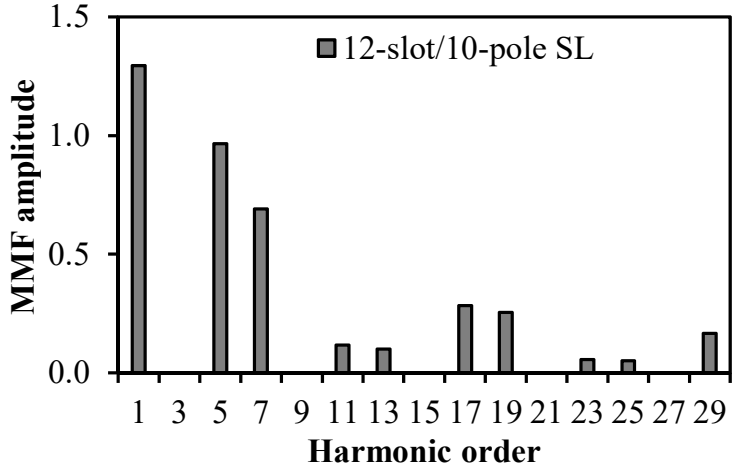

(d) Spectrum of a 10-pole FSCW PMSM with single layer windings [BIA06]

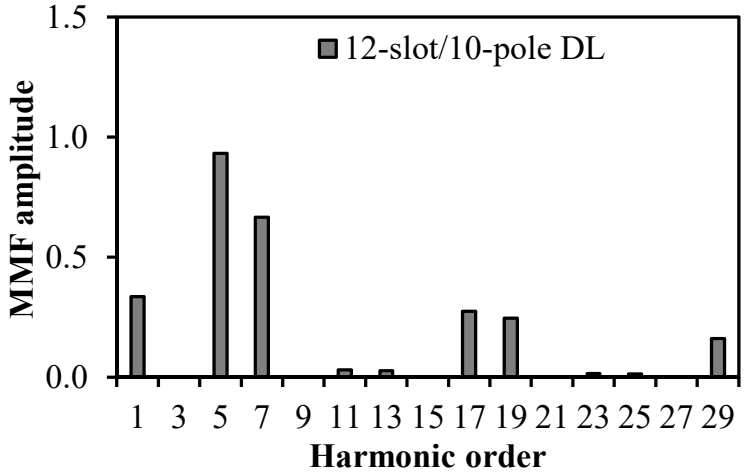

(e) Spectrum of a 10-pole FSCW PMSM with double layer windings [BIA06]

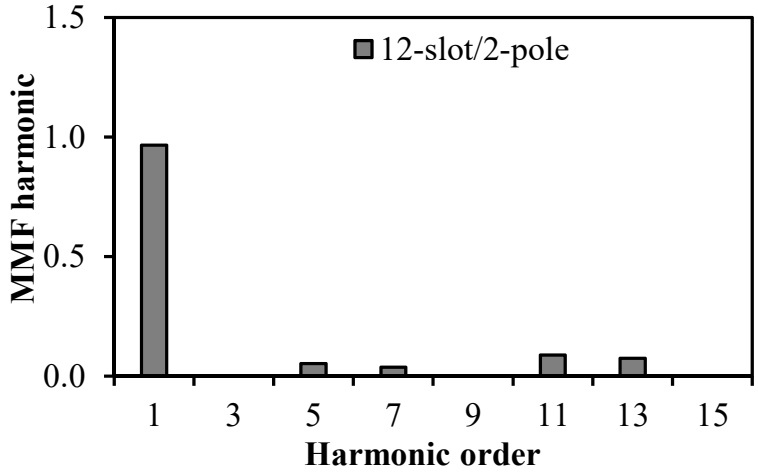

(f) Spectrum of a 2-pole ISDW PMSM

Fig. 1.5 Armature reaction MMF waveforms and spectra.

The rotors of FSCW PMSMs can adopt either surface or interior PM types. However, the reluctance torque of FSCW PMSMs with interior PMs is low and even negligible. Hence, this section will mainly focus on the performance metrics of FSCW PMSM with surface mounted PM rotors and the investigation of FSCW PMSM in this thesis will be focused on the SPM types. To reduce and PM usage and increase the PM utilisation ratio, consequent pole rotors are also adopted in FSCW PMSMs, as shown in Fig. 1.6. In consequent pole rotors, the PMs with the same polarity are separated by magnetic material. It has been proven in [CHU12] [CHU15] that a FSCW PMSM with a consequent pole rotor has good flux weakening capability and can be a cost-effective solution for FSCW PMSMs.

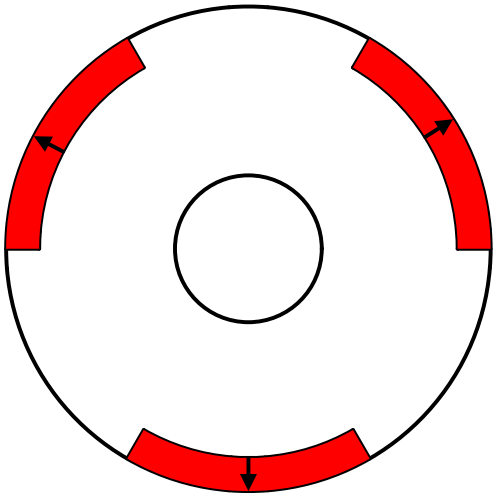

Fig. 1.6. Consequent pole rotor.

1.2.2 Slot/Pole Number Combinations and Winding Factors

To increase the PM utilisation ratio under concentrated tooth coil windings, the coil pitch is expected to be as close to the PM pole pitch as possible [ZHU11a]. Consequently, the slot and PM pole numbers in FSCW PMSMs are usually selected close to each other. Take 3-phase FSCW PMSMs as examples, although there are many feasible slot/pole number combinations, the most popular slot/pole number combinations are limited to those with *qs* ranging from to 1/4~1/2 since their fundamental winding factors are larger than 0.866 [TAN10]. The feasible slot/pole number combinations for FSCW PMSMs are shown in Table 1.3, together with their fundamental winding factors. It shows that the feasible slot/pole number combinations can be categorized into q=1/4 or 1/2, N_s=2p_r±1 or N_s=2p_r±2 [ZHU11a].

Table 1.3. Slot/pole combinations and winding factors for FSCW PMSMs with DW [LIB04]

		N_s						
		3	6	9	12	15	18	21
$2p_r$	2	0.866						
	4	0.866	0.866					
	6			0.866				
	8		0.866	0.945	0.866			
	10			0.945	0.933	0.866		
	12			0.866			0.866	
	14				0.933	0.951	0.902	0.866
	16				0.866	0.951	0.945	0.890
	18							
	20					0.866	0.945	0.953
	22						0.902	0.953
	24						0.866	
	26							0.890
	28							0.866

In FSCW PMSMs, the fundamental winding factor is one of the most important metrics because the torque is proportional to it [MAG03]. The winding configuration method and calculation method of winding factor have been presented in the literature. [CRO02] provides a systematic method to determine the balanced concentrated winding configurations according to different slot/pole number combinations. In [MAG03] [BIA06] [LIB04], EMF phasor (or star of slots) is used to determine the winding configurations and calculate the winding factors of FSCW PMSMs. Compared with conventional ISDW machines whose winding factors can be calculated by equations, in most literatures, the winding factors of FSCW PMSMs of different slot/pole number combinations are

provided by tables [CRO2] [MAG3] [LIB04] [JUS07] [ELR08]. Table 1.3 shows some feasible slot/pole number combinations and their corresponding winding factors for FSCW PMSMs with double layer windings. In [LIB04], it is found out that the slot/pole number combination has a great influence on the winding factor. The machines with the same q will have the same winding factor. The machines with N_s=2p_r±1 (or 2) have the same winding factor. Among all the feasible slot/pole combinations, those with q=1/4 and q=1/2 have the smallest winding factor of 0.866, which marks the boundary of feasible slot/pole number combinations. The winding factor increases when q approaches to 1/3.

1.2.3 Cogging Torque and Torque Ripple

In slotted FSCW PMSMs, cogging torque is produced by the interaction between the PM MMF and the air gap permeance at no-load condition. Cogging torque can make contribution to the torque ripple, causing speed ripples and vibration. For a PM machine, the frequency of cogging torque in a mechanical period equals to the least common multiple (LCM) of the slot and PM pole numbers [JUS07]. The larger the frequency is, the lower amplitude it will be. Consequently, it is predictable that FSCW PMSMs have small cogging torque because they have close numbers of slot and poles which leads to a higher LCM. It can therefore be deduced that the cogging torque is lower in the machines with same q but larger slot/pole numbers. In [ELR08] [MAG03] [SAL04] [LIB04], the LCM is used as a cogging torque indicator for FSCW PMSMs. Apart from the LCM, in [ZHU00], "goodness" of slot/pole combination, which is defined as

$$C_T = \frac{2p_r N_s}{N_c} \tag{1.1}$$

and is used as an index for evaluating the cogging torque amplitude, where N_c is the least common multiple of 2p_r and N_s. It has been analytically proven in [ZHU09a] that for a given slot number, the smaller the "goodness" is, the smaller the cogging torque will be. It is revealed in [JUS07] that the machines with q=0.5 have the worst cogging torque among all feasible slot/pole number combinations. In [ZHU14], the influence of slot/pole combination on the cogging torque of FSCW PMSMs with static and rotating eccentricities is investigated. It shows that the influence of eccentricity has the largest influence on FSCW PMSMs with N_s=2p_r±1, followed by N_s=2p_r±2 and q=1/2. Apart from the influence of slot/pole combination, the influence of slot opening, i.e., open slot, closed slot, and hybrid slot, along with the influence of manufacturing tolerance on the cogging torque of FSCW PMSMs have been covered in [AZA12]. Several cogging torque reduction techniques, such as stator/rotor

skewing, auxiliary slots, pole arc/pole pitch ratio optimisation and slot opening optimisation, have also been summarised and theoretically justified in [BIA02].

Apart from cogging torque, the torque ripple introduced by the interaction between the back EMF harmonics and the current is another factor which contributes to the torque ripple. The instantaneous electromagnetic torque will contain an average component T_0 and $6n^{th}$ harmonics, which can be expressed as [ISL05]

$$T_{em}(t) = T_0 + \sum_{n=1}^{\infty} T_{6n} \cos(n6\omega t) \tag{1.2}$$

where ω is the electrical frequency, t is the time and n is an integer. It shows that in a FSCW PMSM, the most influential torque harmonic is the 6th harmonic, followed by 12th, 18th, etc. It is also revealed in [ATA03] that the 6th torque harmonic is produced by the 5th and 7th back EMF harmonic. In FSCW PMSMs (except those with q=0.25 or 0.5), the winding factors of all, except the fundamental, PM harmonics are reduced, yielding a reduction in the torque ripple produced by the back EMF harmonics [BIA06] [SAL04]. [LIB04] and [WAN05] finds out that the FSCW PMSMs present much lower torque ripple than the conventional ISDW PMSMs as a consequence of lower harmonic winding factors and cogging torque. The influence of slot/pole number combination on the torque ripple is also investigated, and it is stated in [JUS07] that the FSCW PMSMs with q=1/2 seem to have the worst torque ripple among FSCW PMSMs. In [CRO02], the authors find out that when q decreases from 1/2 to 1/4 (q≠1/3), the back-EMF of FSCW PMSMs becomes more sinusoidal, and therefore, the torque ripple produced by back-EMF harmonics decreases. Some favourable slot/pole number combinations for larger torque and smaller torque ripple are 12-slot/14-pole, 12-slot/10-pole [CRO02] [JUS07] and 24-slot/22-pole [WAN05]. In [BIA06] and [ISK06], 12-slot/10-pole FSCW PMSMs with both SL and DL windings are compared, it is found that FSCW PMSMs with SL windings have larger torque ripple than those with DL windings under BLAC mode as a consequence of increased harmonic contents. [ISH05a] shows that FSCW PMSMs with N_s=2p_r±2, SL winding and unequal tooth can have larger torque and smaller torque ripple than other candidates. Apart from the torque ripple introduced by back EMF harmonic, the local saturation also has influence on the on-load cogging torque and torque ripple [WU15a]. Similar with cogging torque reduction techniques, the techniques for torque ripple minimisation include stator or rotor skewing [ISL09], magnet shaping [SHA12] [HSI05] [WAN14a], magnet shifting [DOS07], etc.

1.2.4 Winding Inductance

Winding inductance is a very important parameter for FSCW PMSMs. Different from conventional ISDW PMSMs which have nearly sinusoidal armature reaction MMF waveforms (shown in Fig. 1.5), the armature reaction MMFs of FSCW PMSMs have more harmonic content. Hence, the components and calculation of phase inductance for FSCW PMSMs are also different [LIU15]. It is revealed in [ZHU95] [ELR05] that the FSCW PMSMs have large stator leakage inductance, which makes up most of the winding inductance and makes the winding inductance of FSCW PMSMs larger than that of IDSW PMSMs. It has also been proven in [ELR05] that FSCW PMSMs with surface mounted PMs can achieve good flux weakening performance. The reason for this can be found by considering the characteristic current, defined as

$$I_{ch} = \frac{\psi_{PM}}{L_d} \tag{1.3}$$

where ψ_{PM} is the flux linkage provided by the PMs and L_d is the d-axis inductance, which is close to the q-axis inductance L_q in electrical machines with surface-mounted PMs. Since the phase inductance of surface-mounted electrical machines increases when CWs are introduced, the machine's characteristic current is reduced sufficiently to match its rated current. In [PON13], the influence of slot/pole number combination on the leakage inductance of double layer FSCW PMSMs is investigated, it is found out that for the machines with q<0.5, the leakage inductance is considerably higher than the magnetizing inductance and has surprisingly large impact on the machine performance. Based on this, several suggestions on proper selection of slot/pole number combinations are provided. In [NI14], the "inductance capability" is used as an index for inductance comparison between different slot/pole number combinations.

Another advantage of the FSCW PMSM is its fault tolerant capability. The magnetic coupling between phases should be as weak as possible so that the healthy phases can work properly when the other phases are under faulty condition. The magnetic coupling characteristics between phases can be reflected by the mutual inductance between phases. As a consequence of concentrated tooth coil winding, FSCW PMSMs are proved to have low mutual inductance except those with q=1/2 or q=1/4, and the closer q to 1/3, the lower the mutual inductance will be [LIU15]. In [PON14], mutual inductance coefficient is provided for different slot/pole combinations for a quick mutual inductance comparison. It was shown in [BIA06] that the employment of SL windings provides higher self-inductance and lower mutual inductance, which leads to a better fault tolerant and flux-weakening

capability. A small mutual inductance can even provide an opportunity to build modular segmented stators with physically separated phase coil sections [LIB04]. Rules for design a zero mutual inductance FSCW PMSM have also been provided in [BIA06].

1.2.5 Rotor Losses

For FSCW PMSMs, there are a large amount of harmonics in the air gap due to the winding distribution and slotting effect. Hence, the rotor losses, including the PM eddy current loss and the rotor iron loss, cannot be neglected because the asynchronous harmonics can induce a large amount of eddy current in the PMs and the rotor iron lamination. This results in Joule loss, particularly in NdFeB magnets due to their relatively high electric conductivity. The eddy current can heat up the magnets, cause irreversible PM demagnetisation and reduce the efficiency. Eddy-current losses in the rotor are caused by two kinds of harmonics: slotting permeance harmonics and armature reaction harmonics [PYR12]. The losses caused by slotting harmonics depend mainly on the structure of the teeth, which is generally less important when the slot opening is not large [ASL14]. In [ATA00], an analytical method is proposed to predict the PM eddy current loss induced by armature reaction MMF harmonics in FSCW PMSMs. It shows that PM segment in the circumferential direction is an effective way to mitigate eddy current loss when the PM pole number is larger than the order of fundamental armature reaction harmonic. In [ISH05b], the analytical model is employed on double layer and single layer FSCW PMSMs, with BLAC and BLDC driving modes respectively. It finds out that the FSCW PMSM with BLDC has significantly higher eddy current loss than that with BLAC, and the FSCW PMSM with single layer winding has almost twice PM eddy current loss as much as that with double layer winding. The influence of slot/pole number combination on the rotor losses have also been analysed in various papers [NAK06] [BIA09]. In [BIA09], a map of rotor loss index is proposed and used for fast rotor loss comparison among different slot/pole number combinations. It reveals that the FSCW PMSM with q=0.5 tends to have the smaller rotor losses as a result of no sub-harmonics. For the machines with $2p_r>N_s$, the rotor iron losses increase with the increase of PM pole number.

1.2.6 Noise and Vibration

The abundant stator MMF harmonics bring about other parasitic effects such as noise and vibration. The following terms must be satisfied for an electrical machine to deform and vibrate [GIE06]:

$$\begin{cases} \text{radial force harmonic order=mode of vibration} \\ \text{radial force harmonic frequency} \approx \text{modal frequency} \end{cases} \tag{1.4}$$

The mode of vibration and modal frequency depend on the mechanical structure. The radial magnetic force density f_p over 360 mechanical degrees in the air gap is calculated by:

$$f_p = \frac{B_{gr}^2 - B_{gt}^2}{2\mu_0} \tag{1.5}$$

where B_{gr} and B_{gt} are the flux density components in radial and tangential directions, respectively. μ_0 is the permeance of the air. As there are abundant stator MMF harmonics with small difference between the orders, FSCW PMSMs usually have lower orders of radial force with lower frequencies, which makes it more susceptible to low frequency resonant vibrations [WAN06]. Hence, the lowest radial force harmonic order is crucial for the noise and vibration analysis of FSCW PMSMs and has been analysed on different slot/pole number combinations in various literatures [VAL14a] [VAL14b] [DAJ13] [ZHU09b] [ZHU10a]. It is found out that FSCW PMSMs with q=0.5 show distinct difference with other FSCW PMSMs [VAL14b], with their lowest radial force harmonic order equalling p_r [DAJ13] [ZHU09b]. For N_s=2p_r±2 with double layer windings, the lowest radial force harmonic order is 2. For N_s=2p_r±2 with single layer windings, if N_s/GCD(N_s, 2p_r) is even, the lowest radial force harmonic order is 2; if N_s/ GCD(N_s, 2p_r) is odd, the lowest radial force harmonic order is 1. For N_s=2p_r±1, the lowest radial force harmonic order is 1. Generally, the machines with N_s=2p_r-2 tend to induce higher noise and vibration than and N_s=2p_r+2 [ZHU09b].

1.3 Vernier PM Machines

1.3.1 Torque Production Mechanisms

Low-speed PM machines have increasingly gained attention in direct-drive applications such as wind energy generation, vehicle traction propulsion, and domestic appliances [JIA11]. One of the most promising candidates for low-speed direct drive applications is the Vernier PMSM (VPMSM). VPMSMs are known to exhibit the following relationship:

$$p_r = N_f \pm p_s \tag{1.6}$$

where N_f is the number of flux modulation poles (FMPs) in the stator and p_s is the armature reaction magnetic field pole pairs.

It is shown that the VPMSM has higher torque density than the conventional PM machines [FU10]

[YAN13] and the magnetically-geared machines with more than one air gap [LI11]. The concept of Vernier machine was firstly proposed by [LEE63], in which a Vernier machine with a salient pole rotor was introduced. Vernier machines with PM rotors become a research hotspot in the past 10 years. Being a relatively new PM machine topology, the torque production mechanism of VPMSMs has been analysed from different perspectives. In 2011, [QU11] presents a way to evolve a VPMSM from a magnetic gear. Fig. 1.7 (a) shows a magnetic gear with a high speed rotor, low speed rotor and FMPs between them. Assuming the pole pair number of the high speed rotor to be p_h, the pole pair number of the low speed rotor to be p_l and the number of FMPs to be N_f. In a magnetic gear, p_l, p_h and N_f satisfy

$$p_l = N_f \pm p_h \tag{1.7}$$

The gear ratio G_r is defined as the ratio between the numbers of the pole-pairs of the two rotors:

$$G_r = \frac{p_h}{p_l} \tag{1.8}$$

Assuming the mechanical speed of rotation and the torque of the high speed rotor to be n_{rh} and T_h, the mechanical speed of the rotation and torque of the low speed rotor are shown in Table 1.4. It can be seen that the torque of the low speed rotor is amplified by $1/G_r$ times whereas the speed is reduced to $n_{rh}G_r$ as a result of the energy conservation. This is called magnetic gearing effect. It should be noted that although a combination of $p_h=N_f+p_l$ is feasible, it is not favourable due to inferior torque performance [ATA04].

Table 1.4 Attributes of a magnetic gear

	Pole pair number	Speed of rotation	Torque
High speed rotor	p_h	n_{rh}	T_h
Low speed rotor	p_l	$n \cdot G_r$	T_h/G_r

The rotary magnetic field from the high speed rotor can be replaced by a stator with windings, as shown in Fig. 1.7 (b). When symmetrical poly-phase current is injected, it can produce a rotary magnetic field with the same pole number. Since both the stator and the FMPs are stationary, the air gap between them becomes unnecessary and the FMPs can be attached to the stator, shown in Fig. 1.7 (c). After that, the stator can become a whole stator with FMPs, as shown in Fig. 1.7 (d). It should be noted Fig. 1.7 (d) is a VPMSM with concentrated windings and FMPs. For those with the FMP number

equals stator tooth number, the FMPs can be replaced by the stator tooth directly. Hence, when compare Fig. 1.7 (a) and (d), it is easy to correspond the magnetic field harmonics in VPMSMs to a magnetic gear: in a VPMSM, the armature reaction magnetic field with a pole pair number of p_s plays the role of the high speed rotor. The PM magnetic field with a pole pair number of p_r plays the role of the low speed rotor and the stator teeth play the role of the FMPs. In this way, the VPMSMs can produce a large torque at a low speed by magnetic gearing effect.

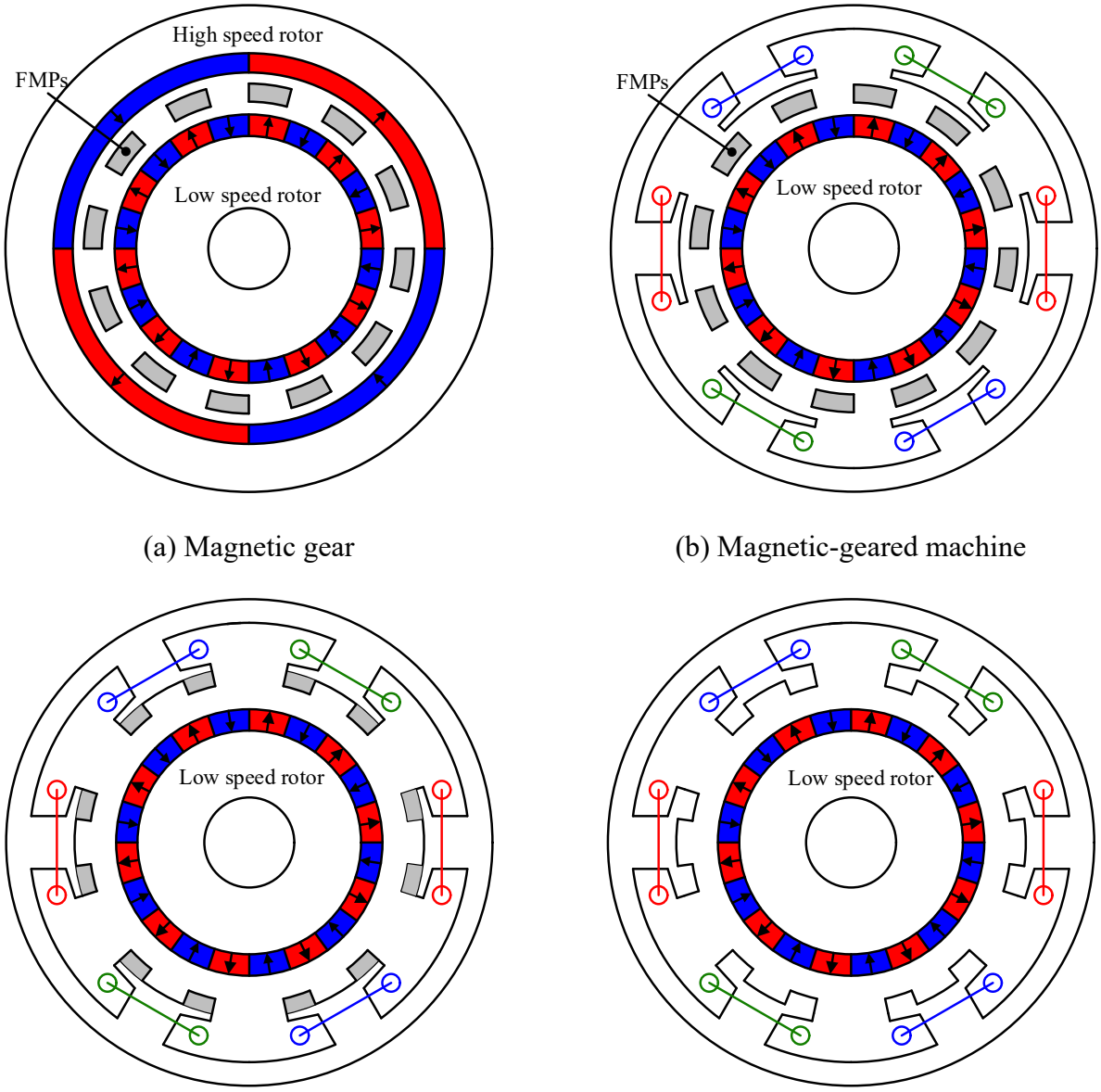

(a) Magnetic gear

(b) Magnetic-geared machine

(c) FMPs attached on the stator

(d) VPMSM

Fig. 1.7. Evolution of VPMSM from a magnetic gear. [QU11]

Despite the fact that it is relatively straightforward to explain the torque production of VPMSMs from

the evolution of a magnetic gear, most people use the air gap flux modulation to predict the airgap magnetic field and explain the torque production of VPMSMs. In [TOB00], the modulation effect of the stator slotting on the air gap PM harmonics is considered by a permeance function, and the torque of a VPMSM is derived as:

$$T_0 = 3\frac{\lambda l_{ef}}{\pi} p_r k_w N_p I_m (B_{PM1} \mp \frac{B_{PMh}}{p_r / p_s}) \tag{1.9}$$

where λ is the winding pole pitch, l_{ef} is the stack length, k_w is the winding factor of the fundamental harmonic, N_p is the total number of turns per phase, I_m is the effective value of the current, B_{PM1} and B_{PMh} correspond to the fundamental and slot harmonic components. It shows that the interaction between the fundamental harmonic and the air gap permeance provides an additional component to the torque of VPMSMs, this phenomenon is called "harmonic coupling" and believed to be the reason for high torque of VPMSMs. In [TOB00], the slot/pole number combinations with

$$p_r = N_f - p_s \tag{1.10}$$

have been proven to have inherent higher torque density. This is consistent with the conclusion drawn from a magnetic gear [ATA04]. Most research activities regarding the torque production are based on this point of view. In [KIM14], the permeance function coefficient as a function of slot geometries are derived, the influence of q and geometrical parameters on the back EMF and torque capability of VPMSMs are presented. [LI16] develops the flux interaction theory and extends the average torque equation to instantaneous torque equation for the first time, it shows that low torque ripple is an inherent characteristic of VPMSMs.

As VPMSMs have relatively more complex stator structure, analytical method is also derived to predict the air gap flux density, back-EMF and torque. The governing Laplacian/quasi-Poissonian field equations in the air gap regions of the VPMSMs is analytically solved in [LI11]. A series slot model on scalar magnetic potential is proposed and solved to calculate the magnetic field distribution [JIA11]. In [ONE16], the on-load air gap flux density distribution accounting for slotting effect of a VPMSM is developed based on sub-domain model, from which the instantaneous torque, power factor, and losses can be predicted.

1.3.2 Alternate VPMSM Topologies

From the perspective of winding configuration, there are mainly two kinds of VPMSMs: VPMSMs

with distributed windings and VPMSMs with concentrated windings. Fig. 1.8 (a) and (b) show a 6-slot/12-FMP/20-pole FSCW VPMSM and a 12-slot/20-pole FSDW VPMSM, respectively. The number of p_r, N_f and p_s for both topologies are shown in Table 1.5.

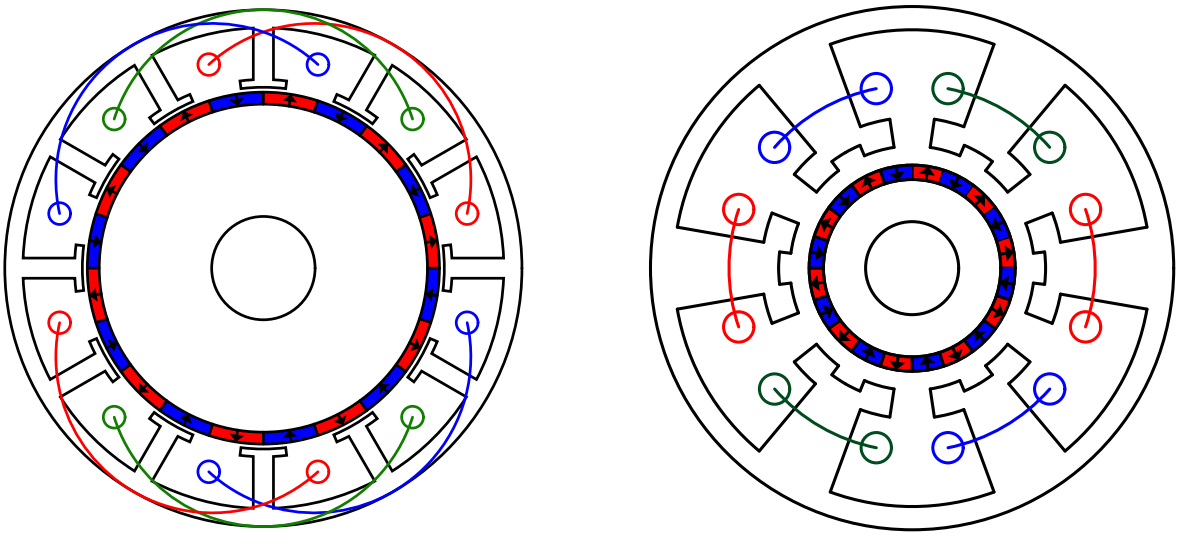

(a) 12-slot/20-pole DW

(b) 6-slot/12-FMP/20-pole CW [ONE16]

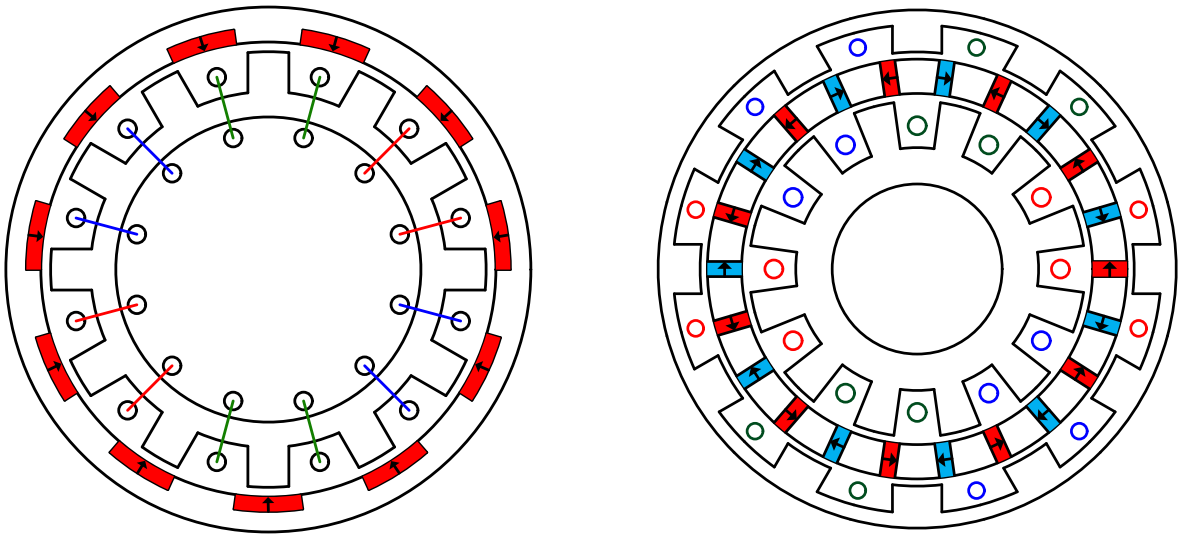

(c) Toroidal winding stator, consequent pole rotor [LI15]

(d) Double stator, spoke type rotor [LI14a]

Fig. 1.8. VPMSM topologies.

It shows that for VPMSM with concentrated windings, FMPs are needed for stator armature reaction MMF modulation, whereas for VPMSMs with distributed windings, the stator teeth play the role of FMPs. For VPMSMs with concentrated windings, the number of FMPs varies in different papers [LI12] according to different slot/pole number combinations. In [LI18a], the influence of FMP number on the

torque performance of VPMSMs of different sizes are investigated, it shows that optimal FMP number is dependent on the machine size and air gap length. The influence of slot/pole number combination on the performance of VPMSMs with distributed windings can be found in [WU15b], in which the pole ratio is proposed as a function of the modulation effect. Comparison between VPMSMs with concentrated windings and distributed windings has also been carried out in [XU15]. In general, VPMSMs with distributed windings have much larger torque than those with concentrated windings under the same electric loading as a result of larger modulation ratio [XU15]. However, VPMSMs with concentrated windings have reduced copper usage and therefore lower copper loss. [LI15] proposed a VPMSM with toroidal windings, as shown in Fig. 1.8 (c). When it is compared with a regular 12-slot/22-pole VPMSM with overlapping windings, the proposed machine can exhibit ~20% higher torque under the same machine size (outer diameter: 40mm; stack length: 50mm; air-gap length: 1mm, PM thickness: 4.5mm) and electrical loading. VPMSMs with concentrated windings can be excellent choices in special applications with requirement on reliability and fault tolerance [LIU12a].

For the rotor topologies, the surface mounted PM rotors are commonly adopted for VPMSMs. Similar with FSCW PMSMs, VPMSM has negligible reluctance torque as a result of high PM pole number. Apart from the conventional rotor structures, a consequent pole rotor is reported for VPMSMs with concentrated windings and distributed windings in [CHU11] and [LI15], respectively. In [LI15], it is reported that the VPMSM with consequent pole has 20% larger torque and 60% larger PM utilisation rate than VPMSM with surface mounted PMs.

Table 1.5. Modulation effect in different VPMSMs.

	6-slot/12-FMP/20-pole	12-slot/20-pole DW
Winding type	Distributed winding	Concentrated winding
p_r	10	
FMP	12	12
N_s	6	12
p_s	2	2

Apart from the aforementioned references, more research activities focus on the innovation of machine topologies mainly to improve the torque density. The method can be classified as:

Employing flux enhancing structure. From the stator side, [ZOU17] shows that with specially designed stator FMPs, the rotor PMs can be more effectively used and VPMSMs with concentrated windings could achieve ~20% higher torque density with the same magnet usage. The output torque can be further developed by inserting PMs between the FMPs on the stator [JAN14]. From the rotor side, the design aims to take advantage of the flux focusing effect, and hence, spoke type rotors [LI15], V-shape rotor [LIU17] and Halbach array [JAN14] have been employed.

Increasing the space utilisation ratio. With a large number of rotor PM poles, the rotor yoke can be designed thinner. Consequently, external rotor VPMSM is also a favorable choice to improve the torque density and has been employed in many applications [GER15] [YAN13] [JAN14] [LI15] [LI10] [LI12].

In order to increase the space utilisation, double stator and double rotor structures are also employed by some researchers. In [LIU12b], a double stator VPMSMs with an outer FSCW PMSM and inner VPMSM with concentrated windings is proposed and compared with some design variations. The conclusion shows that all the machines are able to output high torque at low speed operation. The torque ripple and cogging torque of the machines are significantly small due to the multipole structure design. In 2014, a double stator VPMSM is proposed in [LI14a], shown in Fig. 1.8 (d). It has been proven that the proposed VPMSM topology can greatly reduce the magnet flux leakage, and all magnets contribute to the torque production at the same time. This improvement is benefited from the special structure, i.e., the inner stator tooth has half teeth pitch displacement relative to the outer stator tooth.

A double rotor VPMSM is proposed in [NIU10]. The main merits of this machine are compact structure, improved torque density, reduced stator end winding length, and reduced copper loss.

1.3.3 Power Factor

It has been mentioned in various literatures that Vernier machines suffer from lower power factors compared with the traditional PMSMs. Low power factor means power converters of larger sizes are required for the same output power, which increases the cost and hinders the application of VPMSMs. In [SPO03], it is reported the power factor of a hybrid Vernier machine can be lower than 0.4. Fig. 1.9 gives a phasor diagram of a PMSM under I_d=0 control. When a PMSM is under I_d=0 control and the resistance of the stator windings is ignored, the phasors of q-axis current I_q and the back EMF E_1 are in the same direction, the voltage phasor produced by I_q and the inductive reactance X_q has a 90-

electrical-degree shift from E_1, and U_1 is the resultant phasor of terminal voltage. In this case, the power factor can be expressed as:

$$\cos\varphi = \frac{1}{\sqrt{1+\left(\frac{I_q X_q}{E_0}\right)^2}} = \frac{1}{\sqrt{1+\left(\frac{I_q L_q}{\psi_{PM}}\right)^2}} \tag{1.11}$$

$$X_q = \omega L_q = \frac{2\pi}{60} n_r p_r L_q \tag{1.12}$$

where n_r is the mechanical speed of rotation in rpm and ψ_{PM} is the fundamental harmonic of flux linkage produced by the PMs.

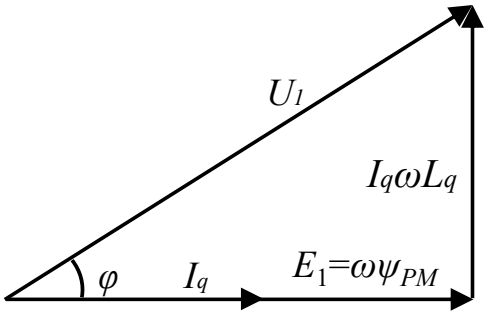

Fig. 1.9. Phasor diagram.

The low power factor of VPMSMs can be mainly explained from two perspectives:

The first is the high leakage flux and low fundamental flux linkage which come together high PM pole number. [LI14a] shows that for a typical VPMSM, there are only half magnets contributing to the torque production whereas other half producing leakage flux. Moreover, as VPMSMs are featured large slot opening and large number of PM poles which reduce the amplitude of the PM fundamental harmonic in the air gap. As a result, VPMSMs have smaller ψ_{PM} than the conventional PMSMs. However, compared with the conventional PMSMs with either CW or DW, VPMSMs have similar winding inductance as a result of same winding configuration. These two factors in turn reduce the power factor of VPMSMs according to (1.12).

The second perspective can be described as low power factor of the VPMSM is mainly caused by the increased number of rotor PM poles which leads to a much greater inductive reactance [KIM14]. When a VPMSM is compared with a conventional PMSM with the same winding configuration, the q-axis inductances L_q of both machines are similar since they share the same winding configuration. However,

it can be seen in (1.13) that the increase in X_q is proportional to the increase of PM pole number p_r. Although the back EMF is also proportional to the frequency, ψ_{PM} is reduced due to large leakage flux and the increase in X_q is larger than the increase in E_1. This consequently causes a larger φ and smaller power factor for VPMSMs.

It is reported that the power factor of VPMSM is related with the slot/pole number combination. In [KIM14], the influence of q on the power factor of VPMSMs is presented, it shows that the relationship in terms of power factor between VPMSM and conventional PMSMs with the same slot number can be expressed by:

$$\cos\theta_{Ver} = \frac{1}{\sqrt{1+(\frac{6q-1}{k_e})^2 \tan^2\theta_c}} \tag{1.13}$$

where k_e is the coefficient of voltage boost between VPMSM and conventional PMSM, θ_c is the power factor angle for the conventional PMSM. It shows that the power factor will decrease when q increases. The influence of pole ratio on the power factor has also been investigated in [WU15b]. It is found out that the power factor of VPMSMs can be as high as 0.9 for those with q=1/2 or pole ratio=2. However, the power factor rapidly decreases with the increase of q or pole ratio [KIM14] [WU15b]. Therefore, it is suggested to select a VPMSM with a smaller q or lower pole ratio for high power factor. However, it should be noted that there is always a tradeoff between power factor and torque improvement in VPMSMs.

Apart from proper selection of slot/pole number combinations, other approaches have also been taken to improve the power factors of VPMSMs. In [KAT12], Halbach PM rotor is employed without rotor iron, it is reported that the power factor can be improved with ~50% reduction in the torque. In [LI14a], a dual-stator structure VPMSM is proposed, as shown in Fig. 1.8 (d), it reports that with a shift between the internal and external stators and shared spoke type rotor, the double stator structure can take full use of the leakage flux in both the internal and external air gaps and improve the power factor to 0.9. Similar idea is applied to an axial flux VPMSM and the power factor of 0.89 is reported [ZHA14].

1.4 Alternate Torque Production Mechanisms

1.4.1 Torque Production Mechanism from the Perspective of Energy Conversion

In this section, the general torque production mechanism of PMSMs will be derived from energy conversion point of view. At no load condition, the air gap flux density waveform of a PM can be approximated by a rectangular waveform shown in Fig. 1.10, in which B_δ is the amplitude of the flux density, α_i is the pole arc ratio.

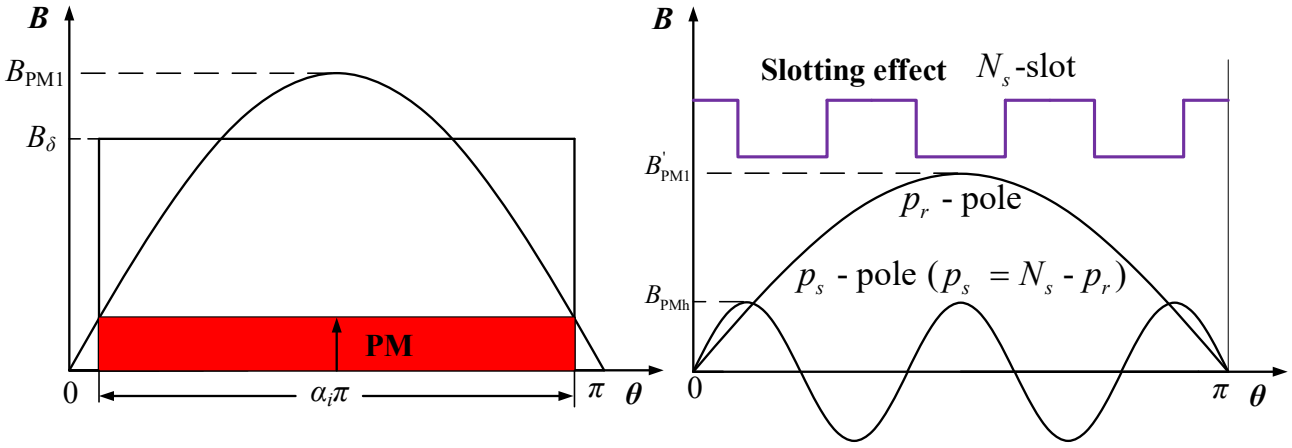

Fig. 1.10. No-load air gap PM flux density.

The amplitude of the fundamental harmonic under 180 electrical degrees can be calculated by:

$$B_{PM1} = \frac{4}{\pi} B_\delta \sin\frac{\alpha_i \pi}{2} \tag{1.14}$$

For a N_s-slot/2p_r-pole PMSM, if the slotting effect is considered, the p_r-pole PM fundamental air-gap flux density harmonic can be modulated into harmonics of different orders, among which the most dominant harmonics are p_rth and p_sth harmonics, satisfying p_s=|N_s-p_r| [TOB00]. It has been proven in [TOB00] that both the p_rth and p_sth harmonics have the same electrical frequency. As shown in Fig. 1.10, the p_rth and p_sth harmonics have amplitudes of B'_{PM1} and B_{PMh}. If N_s-p_r >0, the p_sth harmonic can have a positive contribution to the phase flux linkage and back-EMF [TOB00]. Only the machines satisfying N_s-p_r >0 will be considered in this thesis.

When the d-axis is aligned with the axis of one coil, as shown in Fig. 1.11, the flux linkage in one turn can be calculated by:

$$\begin{aligned}\Phi_1 &= \frac{2k_{p1}l_{ef}}{\pi\sigma_0}(B'_{\mathrm{PM1}}\tau_1 + B_{\mathrm{PMh}}\tau_h) \\ &= \frac{2k_{p1}l_{ef}}{\pi\sigma_0}(B'_{\mathrm{PM1}}\frac{\pi r_g}{p_r} + B_{\mathrm{PMh}}\frac{\pi r_g}{p_s}) \\ &= \frac{2k_{p1}l_{ef}r_g}{\sigma_0}(\frac{B'_{\mathrm{PM1}}}{p_r} + \frac{B_{\mathrm{PMh}}}{p_s})\end{aligned} \tag{1.15}$$

where k_{p1} is the pitch factor of the fundamental harmonic, τ_1 and τ_h are the pole arc lengths of the p_rth and p_sth harmonics, r_g is the radius of the air gap and σ_0 is the leakage coefficient, representing the leakage flux between the PM poles and the leakage flux in the end parts.

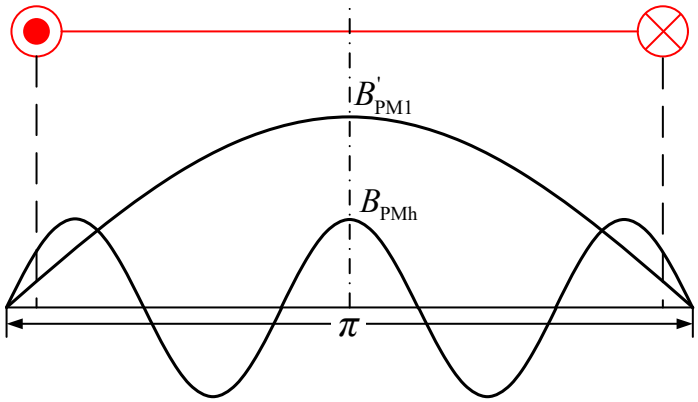

Fig. 1.11. Flux linkage of one turn.

Hence, the fundamental harmonic of the phase flux linkage can be derived by:

$$\psi_1 = N_p k_{d1}\Phi_1 = \frac{2k_w N_p l_{ef} r_g}{\sigma_0}(\frac{B'_{\mathrm{PM1}}}{p_r} + \frac{B_{\mathrm{PMh}}}{p_s}) \tag{1.16}$$

where k_{d1} is the distribution factor of the fundamental harmonic.

If the rotor rotates at a constant speed n_r, the phase flux linkage contributed by the p_rth and p_sth harmonics will vary at the same frequency and the back EMF will be induced as:

$$E_1 = \omega\psi_1 \tag{1.17}$$

and

$$\omega = 2\pi f = 2\pi\frac{n_r p_r}{60} \tag{1.18}$$

where f is the electrical frequency of the fundamental harmonic. Substituting (1.16) and (1.18) to (1.17):

$$E_1 = \frac{\pi N_p r_g l_{ef} n_r k_w}{15\sigma_0}\left(B'_{\mathrm{PM1}} + \frac{B_{\mathrm{PMh}}}{p_s / p_r}\right) \tag{1.19}$$

Hence, it can be seen that if the slotting effect is considered, both the conventional principle and the modulation effect can contribute to the back-EMF, as shown in (1.20).

$$E_1 \begin{cases} \dfrac{\pi N_p r_g l_{ef} n_r k_w}{15\sigma_0} B'_{\mathrm{PM1}} & \text{conventional principle} \\ \dfrac{\pi N_p r_g l_{ef} n_r k_w}{15\sigma_0} \dfrac{B_{\mathrm{PMh}}}{p_s / p_r} & \text{modulation effect} \end{cases} \tag{1.20}$$

However, as shown in Fig. 1.10, the flux density waveform in the air gap is not sinusoidal, there are higher order harmonics such as 3rd, 5th and 7th harmonics which rotate at the same mechanical speed of rotation with the fundamental harmonic. If the higher order PM MMF harmonics are considered, there will be also higher order harmonics in the phase back EMF waveform with the same order. For an m-phase electrical machine, the instantaneous phase back EMF in the jth phase can be expressed as [ATA03]:

$$e(t) = \sum_n E_n \sin\left(n\left(p_r \Omega_r t - \frac{2\pi j}{m} - \phi\right)\right) \tag{1.21}$$

where E_n is the amplitude of the nth back EMF harmonic, ϕ is the initial phase and Ω_r stands for the mechanical speed of rotation in rad/s.

For the m-phase electrical machine, the m-phase symmetrical instantaneous phase current can be injected for constant power production, the current in the jth phase can be expressed as:

$$i(t) = I_m \sin\left(p_r \Omega_r t - \frac{2\pi j}{m}\right) \tag{1.22}$$

where I_m is the amplitude of the current.

Hence, the instantaneous power generated in the machine can be expressed as [ATA03]:

$$p(t) = \sum_{j=1}^{m} \sum_n \left\{ I_m E_n \sin\left[n\left(p_r \Omega_r t - \frac{2\pi j}{m} - \phi\right)\right] \sin\left(p_r \Omega_r t - \frac{2\pi j}{m}\right)\right\} \tag{1.23}$$

According to the energy conversion theory, the electrical power can be converted into mechanical power in an electrical machine, the instantaneous torque can be calculated by [ATA03]

$$T_{em}(t)=\frac{p(t)}{\Omega_r}=\frac{m}{2}\frac{I_m E_1}{\Omega_r}\cos(\phi)+\frac{I_m}{2\Omega_r}\times$$
$$(\sum_{j=1}^{m}\sum_{n}E_n\left\{\cos\left[(n-1)p_r\Omega_r t-(n-1)\frac{2\pi j}{m}-n\phi\right]-\cos\left[(n+1)p_r\Omega_r t-(n+1)\frac{2\pi j}{m}-n\phi\right]\right\}) \quad (1.24)$$

In a three-phase PMSM, the instantaneous torque can be expressed as

$$T_{em}(t)=\frac{p(t)}{\Omega_r}=\frac{3}{2}\frac{I_m E_1}{\Omega_r}\cos(\phi)-\frac{3E_5 I_m}{2\Omega_r}\cos(6p_r\Omega_r t-5\phi)+\frac{3E_7 I_m}{2\Omega_r}\cos(6p_r\Omega_r t-7\phi)... \quad (1.25)$$

From (1.25), it can be seen that steady torque can only be generated when the back EMF harmonic has the same order and frequency with the current harmonic. Here, a three phase electrical machine is used as an example. Fig. 1.12 (a) shows the waveforms of 3-phase symmetrical back EMF and current fundamental harmonics. It shows that if the product of back EMF and current in each phase is summed up, they generate a steady constant power which can be converted into steady torque in the electrical machine. It is also noteworthy that the amplitude of the generated power depends on the phase difference between the back-EMF and current in the same phase. The maximum torque can be generated when the back EMF and current fundamental harmonics are in phase. When there is a 90 electrical degree phase shift between the back EMF and current fundamental harmonics, the electromagnetic torque will be 0.

If the back EMF harmonic has a different order and frequency with the current harmonic, torque ripple instead of steady torque will be generated as shown in (1.25). Fig. 1.12 (b) shows the waveforms of 3-phase symmetrical 5th back EMF harmonics and current fundamental harmonics. The generated power shows a 6th harmonic with no DC component which will lead to a 6th harmonic in the torque waveform.

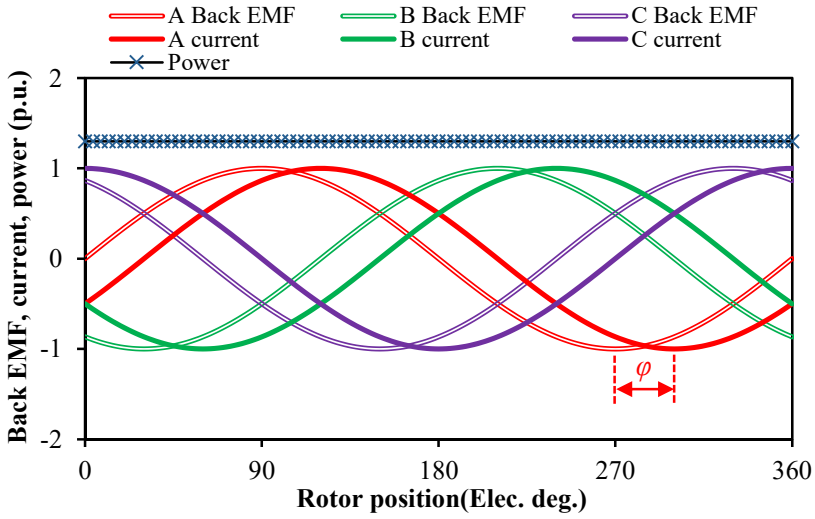

(a) Steady power

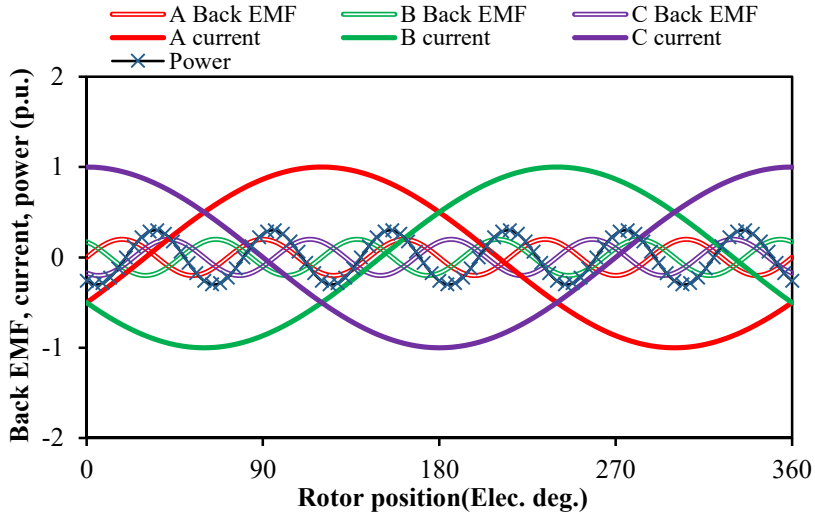

(b) Power ripple

Fig. 1.12. Power generation in electrical machines.

The back EMF waveforms are different due to different slot/pole number combinations and PM magnetisations, they can be generally categorized as more sinusoidal and more trapezoidal waveforms. To maximize the torque and minimize the torque ripple, their preferred driving current waveforms are also sinusoidal and rectangular, respectively, which are referred to as BLAC [JAH96] and BLDC [HEN94], as shown in Fig. 1.13.

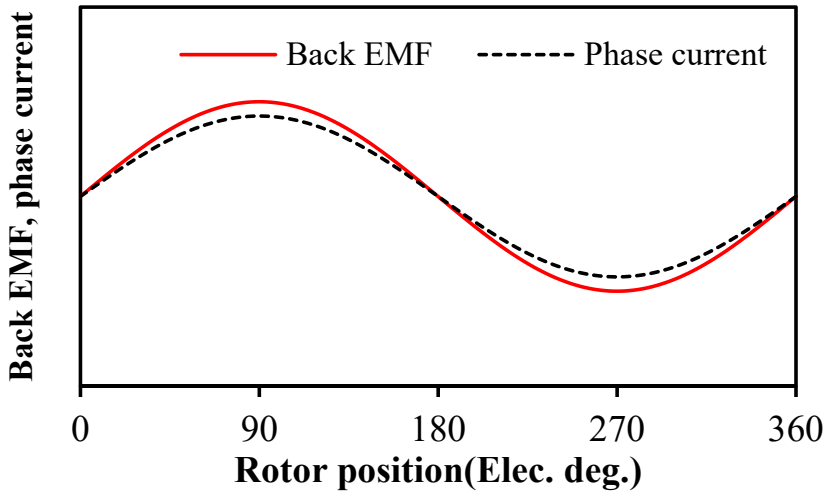

(a) BLAC

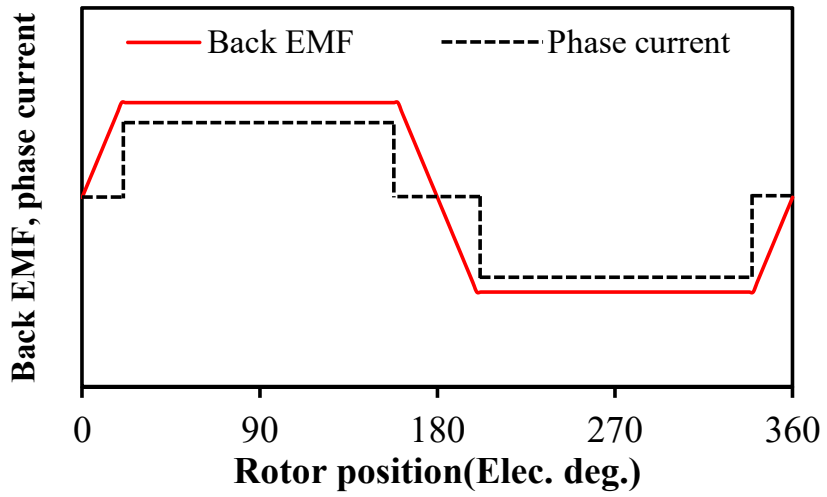

(b) BLDC

Fig. 1.13. Different driving modes.

1.4.2 Torque Production Mechanism from the Perspective of Rotating Field

When a PMSM carries symmetrical phase current, a rotating armature reaction magnetic field can be generated in the air gap, the MMF waveform of the armature reaction magnetic field can be expressed as:

$$F_s(\theta,t)=\sum_{k}^{\infty}F_{sk}\cos(\omega_s-k\theta)+\sum_{i}^{\infty}F_{si}\cos(-\omega_s-i\theta) \tag{1.26}$$

where ω_s is its electrical rotating velocity, i and k are the positive integers depending on the distribution of stator windings, F_{sk} and F_{si} are the amplitudes of the kth and the ith order harmonics. It shows that the armature reaction MMF field have harmonics rotating at opposite directions. Hence, in addition to the PM magnetic field, there are multiple magnetic field rotating in the air gap at the same time. To analyse the interaction between the armature reaction and PM harmonics, the p_sth and p_rth harmonics are selected from armature reaction and PM harmonics for analysis. The p_sth and p_rth flux density harmonics can be expressed as

$$\begin{cases} B_s = B_{sps}\cos(\omega_s t + p_s\theta + \theta_s) \\ B_r = B_{rpr}\cos(\omega_r t + p_r\theta + \theta_r) \end{cases} \tag{1.27}$$

where B_{sps} and θ_s are the amplitude and phase of the p_sth armature reaction air gap flux density harmonic, B_{rpr}, ω_r and θ_r are the amplitude, electrical frequency and phase of the p_rth PM air gap flux density harmonic.

The resultant flux density waveform can be expressed as:

$$B_g(\theta,t) = B_s + B_r = B_{sps}\cos(\omega_s t + p_s\theta + \theta_s) + B_{rpr}\cos(\omega_r t + p_r\theta + \theta_r) \tag{1.28}$$

The co-energy in the air gap can be calculated by

$$\begin{aligned} W_f &= \frac{1}{2\mu_0}\int_0^{2\pi} B^2 l_{ef} r_g l_a d\theta \\ &= \begin{cases} \dfrac{l_{ef} r_g l_a \pi}{2\mu_0}(B_{sps}^2 + B_{rpr}^2 + 2B_{sps}B_{rpr}\cos((\omega_s - \omega_r)t + (\theta_s - \theta_r))) & p_s = p_r \\ \dfrac{l_{ef} r_g l_a \pi}{2\mu_0}(B_{sps}^2 + B_{rpr}^2) & p_s \neq p_r \end{cases} \end{aligned} \tag{1.29}$$

where l_a is the length of the air gap.

The torque can be derived by [MEN93]:

$$T_{em} = p_r \frac{dW_t}{d\theta_r}$$

$$= \begin{cases} \dfrac{l_{ef} r_g l_a \pi p_r}{\mu_0} (B_{sps} B_{rpr} \sin(\theta_s - \theta_r)) & p_s = p_r, \omega_s = \omega_r \\ \dfrac{l_{ef} r_g l_a \pi p_r}{\mu_0} (B_{sps} B_{rpr} \sin((\omega_s - \omega_r)t + (\theta_s - \theta_r))) & p_s = p_r, \omega_s \neq \omega_r \\ 0 & p_s \neq p_r \end{cases} \tag{1.30}$$

Based on (1.30), there are three conditions for torque production between two magnetic field harmonics, which are summarized as follows:

(a) They have the same pole pairs and speed, and then produce steady torque. This can be achieved in two circumstances:

(a-1) Two MMF harmonics have the same pole-pair number and electrical frequency, there is no flux modulation poles (FMPs) between them. Hence, the air gap permeance function only contains the DC component P_0 as shown in (1.32). The resultant air gap flux density harmonics have the same order and frequency with the MMFs, as shown in Table 1.6. They can interact with each other directly in the air gap and produce steady torque as shown in Fig. 1.14 (a).

(a-2) Two MMF harmonics have different pole-pairs and mechanical speed of rotations. However, there are FMPs between them. The stator and rotor MMF harmonic can be expressed as:

$$\begin{cases} F_s = F_{sps} \cos(\omega_s t + p_s \theta + \theta_s) \\ F_r = F_{rpr} \cos(\omega_r t + p_r \theta + \theta_r) \end{cases} \tag{1.31}$$

where F_{sps} and F_{rpr} are the amplitudes of the p_sth armature reaction and p_rth PM MMF harmonics, respectively.

The air gap pearmeance function considering the N_f - pole FMPs can be approximated as:

$$P(\theta) = P_0 + P_1 \cos(N_f \theta) \tag{1.32}$$

where P_1 is the fundamental harmonic of the permeance function. For either the stator or PM MMF, the air gap flux density can be calculated by

$$B_s = F_s P = F_{sps} P_0 \cos(\omega_s t + p_s \theta + \theta_s) + \frac{1}{2} F_{sps} P_1 \cos(\omega_s t + (p_s \pm N_s)\theta + \theta_s)$$
$$= B_{sps} \cos(\omega_s t + p_s \theta + \theta_s) + B_{s(p_s \pm N_s)} \cos(\omega_s t + (p_s \pm N_s)\theta + \theta_s) \quad (1.33)$$

The orders and frequencies of the air gap flux density harmonics under this circumstances are shown in Table 1.6. It shows that resultant flux density does not only contain the DC related component, but also modulated components with p_s(or p_r)$\pm N_f$ orders. Moreover, the modulated flux density harmonics and the original MMF harmonics share the same frequency - the stationary FMPs do not change the frequency of the modulated harmonics.

Table 1.6 Conditions for steady torque production.

Before modulation			After modulation		
MMF	Frequency	Permeance	Flux density	Frequency	Condition
p_s	ω_s	P_0	p_s	ω_s	ω_s=ω_r
p_r	ω_r		p_r	ω_r	p_s=p_r
p_s	ω_s	P_1	$p_s \pm N_f$	ω_s	ω_s=ω_r
p_r	ω_r		$p_r \pm N_f$	ω_r	p_r=$p_s \pm N_f$

Under this circumstance, if the two rotating MMFs share the same frequency and their pole numbers satisfy

$$p_s = N_f \pm p_r \quad (1.34)$$

Steady torque can still be produced since their resultant flux density harmonics still share the same order and frequency after introducing the FMPs. This phenomenon is termed as air gap field modulation and/or magnetic gearing effect, i.e. field modulation effect from the view point of air gap field and magnetic gearing effect from the view point of torque production. Fig. 1.14. (b) shows a schematic of magnetic gearing effect. The FMPs can modulate the magnetic fields and make them have the same pole-pair number and speed of rotation in the corresponding air gap to produce steady torque.

(b) They have the same pole pairs but different speed, and then produce torque ripple;

(c) The pole pairs of the two harmonics are different, and they will produce no torque.

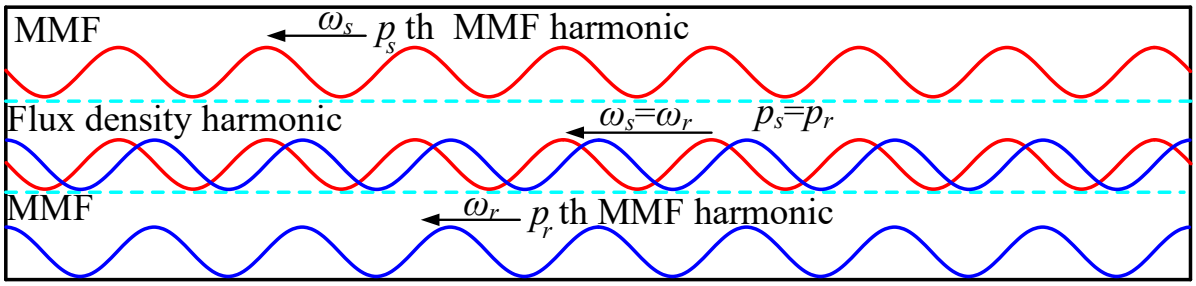

(a) Principle of conventional PM machine torque production (a-1).

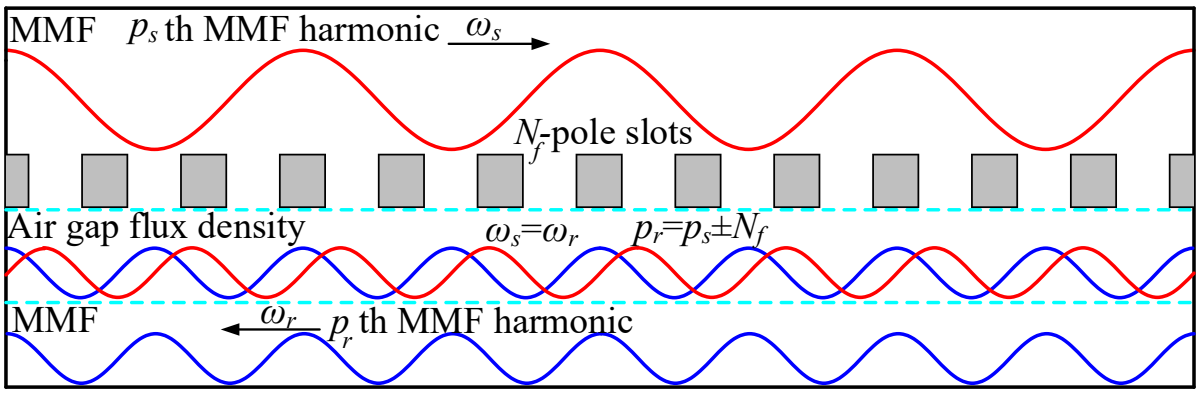

(b) Principle of magnetic gearing effect (a-2).

Fig. 1.14. Illustration of torque production mechanisms.

1.5 Scope of Research and Contributions of Thesis

The aim of this thesis is to investigate the torque production mechanism of PMSMs with PMs on the rotor. The emphasis will firstly be put on FSCW PMSMs and VPMSMs. The torque production of rotor-PM machines will be unified from both energy conversion and rotating field theory. Based on the unified theory, a series of rotor-PM machines with new slot/pole number combinations will be proposed.

Chapter 1: The general PM machine topologies are reviewed. The investigations on FSCW PMSMs and VPMSMs have also been reviewed for further investigation. The general torque production mechanisms from both energy conversion and rotating field points of view are reviewed for further investigation.

Chapter 2: The torque production mechanism of FSCW PMSMs is investigated from airgap field modulation and magnetic gearing effect. It is found that the torque production in FSCW PMSMs is based on both conventional PMSM principle and magnetic gearing effects. The respective

contributions of the conventional PMSM and the magnetic gearing effect to the total torque are quantified. The results show that the contribution of the magnetic gearing effect is not ignorable, and the larger the slot opening, the higher the magnetic gearing effect.

Chapter 3: The gear ratio in FSCW PMSMs is introduced. It is found that the gear ratio is an inherent parameter of the FSCW PMSMs regardless of the phase number. The relationship between gear ratio and various machine performance of FSCW machines with different phases and slot/pole number combinations is investigated. Therefore, it can contribute to a proper slot/pole number selection in any multi-phase FSCW PMSMs by acting as a unified index for a quick overall performance comparison.

Chapter 4: The torque production mechanism of VPMSMs is investigated from airgap field modulation and magnetic gearing effect. The respective contributions of the conventional PMSM and the magnetic gearing effect to the total torque are quantified. The influence of slot opening on the magnetic gearing effect in VPMSMs is also investigated, revealing that the magnetic gearing effect makes the main contribution to the total torque in VPMSMs.

Chapter 5: The gear ratio in VPMSMs is introduced and employed to investigate its relationship with various electromagnetic performance metrics of surface-mounted PM Vernier machines. It is found that the gear ratio is not only a representation of the gearing effect, but also an index for performance comparison and selection of the appropriate slot/pole number combination at the machine design stage.

Chapter 6: The torque production mechanism of rotor-PM machines, including ISDW PMSMs, FSCW PMSMs and FSDW VPMSMs are firstly unified from two viewpoints: the energy conversion and magnetic gearing effect. The influence of slot opening on the torque production mechanism of different machine types are also analysed from both viewpoints. Design guidelines for taking advantage of slot opening for the designs of different machine types are provided.

Chapter 7: An 18-slot/26-pole VPMSM with coil-pitch of two slot pitches is proposed from two counterparts. Compared with its counterparts, the proposed design reduces the armature reaction space harmonic content and phase inductance without affecting the fundamental harmonic, and hence increases the power factor with better torque and flux weakening capability. A series of VPMSMs with high power factor are derived from the same design principle.

Chapter 8: The general conclusions are drawn based on the previous chapters. Potential futures work will be proposed.

Major contribution of this thesis:

(1) The torque production mechanism of FSCW PMSMs is firstly explained from magnetic gearing effect. The contribution of magnetic gearing effect to the total torque is quantified for both FSCW PMSM and VPMSM. The gear ratio is proposed and can be used as performance indicators for both machine types.

(2) The torque production mechanisms of rotor-PM machines including ISDW, FSCW and FSDW VPMSMs are firstly unified from two viewpoints: the energy conversion and magnetic gearing effect. The role which the slot opening plays in the torque production of different machine types and slot/pole number combinations is revealed. Design guidelines for taking advantage of slot opening for the designs of different machine types are provided.

(3) A series of VPMSMs with high power factors are derived from the unified theory, which expands the feasible slot/pole number combinations of rotor-PM machines.

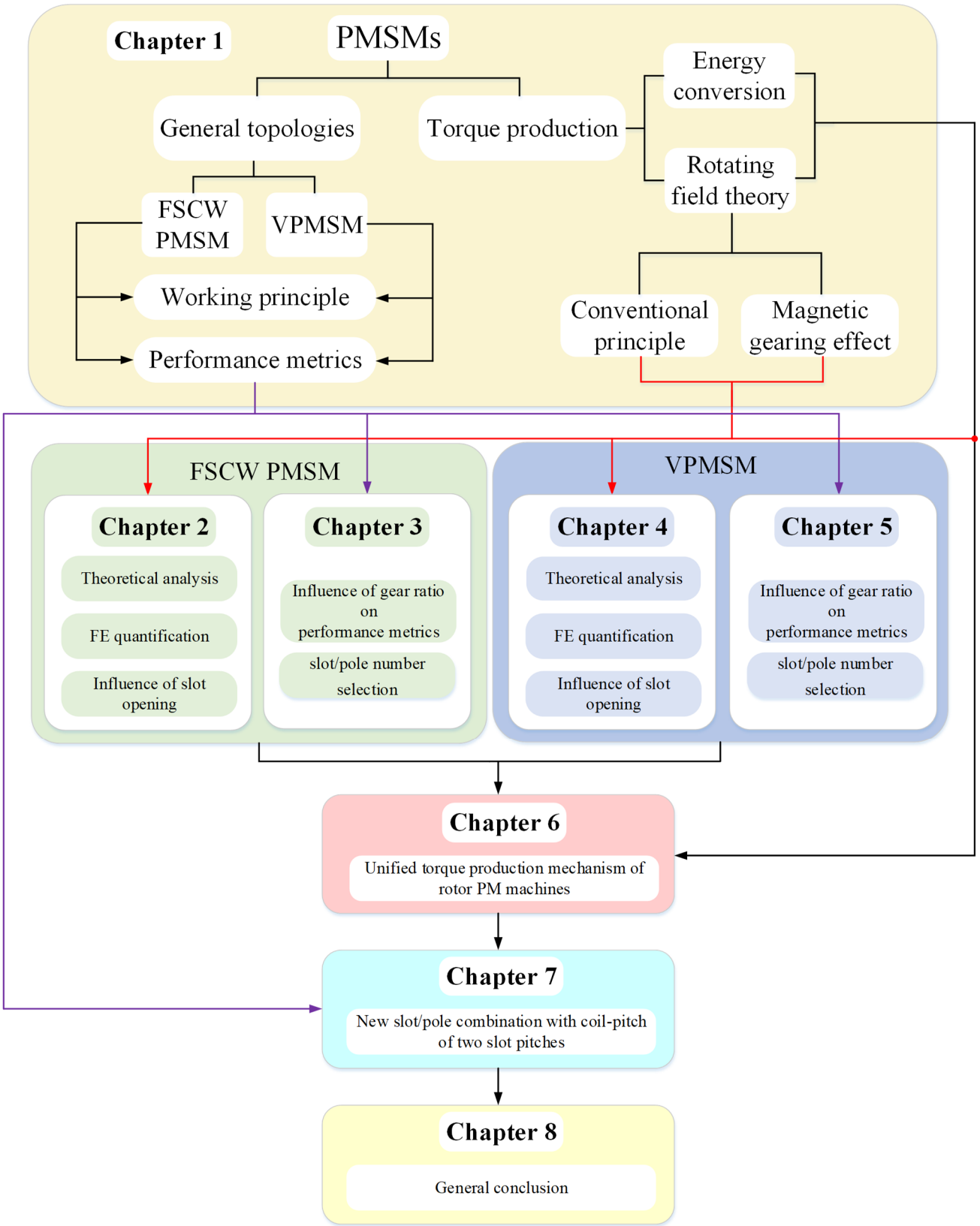

Fig. 1.15. Research scope and chapter arrangements.

CHAPTER 2

Analysis of Air-gap Field Modulation and Magnetic Gearing Effect in Fractional Slot Concentrated Winding Permanent Magnet Synchronous Machines

In this chapter, the torque production of fractional slot concentrated winding (FSCW) permanent magnet synchronous machines (PMSM) are analysed from the perspective of the air-gap field harmonics modulation accounting for slotting effect. It is found that the average torque of FSCW PMSM is produced by both the principle of conventional PMSM torque production and the magnetic gearing effect. A finite element analysis (FEA)-based equivalent current sheet model (ECSM) and harmonic restoration method is firstly used in FSCW PM machines with different slot-pole number combinations to quantify the respective contribution of the conventional PMSM torque and the magnetic gearing effect to the average torque. The influence of slot opening on the magnetic gearing effect, cogging torque and torque ripple is analysed. The results show that the magnetic gearing effect makes a non-ignorable contribution to the average torque when a large slot opening stator is used. The expression of the gear ratio in FSCW PMSMs is derived. The influence of gear ratio on the contribution of the magnetic gearing effect to the total torque is investigated by FEA. The FEA predicted torques are validated by experiments on the prototypes.

2.1 Introduction

Fractional slot concentrated winding (FSCW) permanent magnet synchronous machines (PMSMs) have been gaining popularities in academics and industries in the past few decades [ELF10]. They have advantages of compact size, high efficiency, high torque density, low cogging torque and fault tolerance [ELF10] [ISH05a]. Overviews of the research on FSCW PM machines can be found in [ELF10] and [ZHU11a].

Different from integral slot distributed winding machines which generally have more sinusoidal armature reaction flux density distributions, the FSCW machines have usually non-sinusoidal armature reaction flux density distributions in the air-gap, which means there are abundant armature field harmonics in the air-gap magnetic field. When open or semi-closed slots are used together with

fractional-slot windings, for a more accurate calculation, slotting effect should be taken into consideration. The influence of stator slotting on the air-gap flux density waveform may be accounted for by using relative permeance model [ZHU93] [KIM98], complex permeance model [ZAR06] or subdomain model [ZHU10b].

In the past years, the research of slot harmonics and modulation effect are mainly focused on parasitic effects such as cogging torque [ZHU09a] [ZAR08], torque ripple [ZAR10], unbalanced magnetic force [DAJ13] [ZHU10a], noise and vibration [VAL14a] [FAK15]. The influence of slotting modulation on the PM and rotor iron losses have also been investigated in [FAN12]-[FOR12].

Recently, the modulation effect in electrical machines has drawn researchers' attention [CHE17] mainly because the average torque can be produced by two magnetic field with different pole numbers after modulation. This phenomenon is termed as airgap field modulation and/or magnetic gearing effect, which has been proven to be the working principle of magnetic gear [ATA04] and magnetic geared machines [QU11] such as Vernier [LI16], flux-modulated [CRI15] and switched flux (SF) [WU15c] [SHI16] machines. Although the slot harmonics and modulation effect has been researched extensively in FSCW PMSMs, the contribution of the modulation effect/magnetic gearing effect to the average torque has not been researched in FSCW PMSMs yet. The torque in FSCW PMSMs was believed to be produced by classical torque production principle of PM machines only.

The aim of this chapter is to reveal the contribution of modulation effect to the average torque, i.e., the magnetic gearing effect in FSCW PMSMs. It contributes a non-ignorable part to the total torque especially when FSCW PMSMs have large slot openings. Since average electromagnetic torque is the most critical performance for PMSMs, this chapter will analyse the torque production mechanism in depth. The contribution of magnetic gearing effect to the average electromagnetic torque can be quantified using the finite element analysis (FEA)-based equivalent current sheet model (ECSM) and a harmonic restoration method. The results reveal that the FSCW PMSM is a combination of a PM machine and a magnetic gear in terms of average torque production.

This chapter is organized as follows. In Section 2.2, the general torque production mechanism of FSCW PM machines is investigated based on the air-gap flux harmonics modulation accounting for slotting effect. It is found that the average electromagnetic torque is produced via two principles: the conventional PMSM and the magnetic gearing effect. In Section 2.3, a FEA-based ECSM is employed for a 12-slot/8-pole FSCM PMSM to quantify the respective contribution of conventional PMSM and magnetic gearing effect to the average electromagnetic torque. In section 2.4, the influence of slot

opening on the magnetic gearing effect, cogging torque and torque ripple is analysed. In section 2.5, based on the former analysis, the expression of gear ratio is given in this chapter. The influence of gear ratio on the contribution of the magnetic gearing effect to the average torque is investigated by FEA in alternate FSCW PMSMs. Finally, prototypes are manufactured to validate the FEA results.

2.2 Modulated Magnetic Field and Torque Production Analysis in FSCW PMSMs

In this section, the general PM and armature reaction air-gap magnetic fields of FSCW surface-mounted PM machines are derived. Their interaction and torque production mechanism will be given. To obtain an analytical model for the air-gap flux density, the discussion in this section is based on the following assumptions:

1) The permeance of the steel lamination is infinite and saturation is not considered. The aim of this section is focused on the modulating effect of the stator slots, viz., the modulated harmonic orders and speed of rotation but not on the actual amplitudes of the field harmonics. The tangential component of the air-gap magnetic field is, therefore, also neglected for simplicity.
2) The relative permeability of permanent magnets is equal to that of the air. The relative permeability of PM is close to 1 and hence can be approximated.
3) The leakage flux and end effect are ignored for simplicity.

2.2.1 PM Air-Gap Flux Density

For a FSCW machine with surface mounted PMs, the magnetic motive force (MMF) generated by the PMs is shown in Fig. 2.1, and its Fourier series expansion $F_r(\theta,t)$ is given by (2.1).

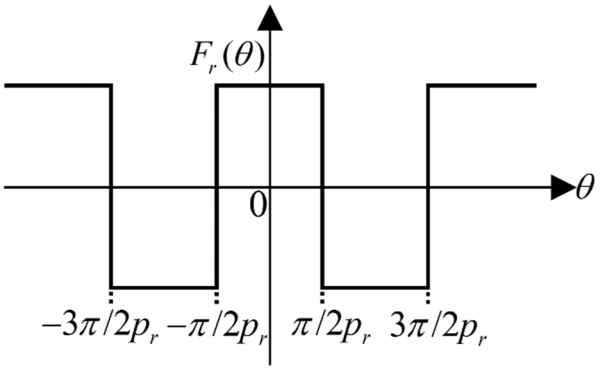

Fig. 2.1 MMF distribution generated by the PMs in FSCW machines.

$$F_r(\theta,t)=\sum_{i=1,3,5...}^{\infty} F_{ri}\cos ip_r(\Omega_r t-\theta) \tag{2.1}$$

where p_r is the number of the PM pole pairs, which is defined to be the fundamental harmonic of the FSCW PMSM in this chapter, Ω_r is its mechanical speed of rotation, i is a positive odd integer, F_{ri} is the amplitude of the ith order harmonic and θ is the air-gap circumferential position. The zero position of θ is aligned with the axis of Phase A of the machine.

The air-gap permeance and the influence of slotting may be accounted for by introducing a permeance function shown in Fig. 2.2, in which θ_t is half-arc of a stator tooth.

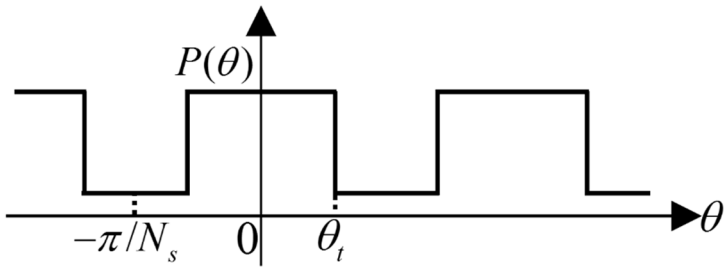

Fig. 2.2 Air-gap permeance function accounting for slotting effect.

And its Fourier series can be obtained as:

$$P(\theta)=\sum_{j=0,1,2...}^{\infty} P_j\cos(jN_s\theta) \tag{2.2}$$

where N_s is the number of the stator tooth, j is either 0 or a positive integer, P_j is the amplitude of jth order harmonic.

Thus, the modulated PM air-gap flux density in the radial direction can be expressed as:

$$\begin{aligned} B_r &= F_r P \\ &= \frac{1}{2}\sum_{j=0,1,2...}^{\infty}\sum_{i=1,3,5...}^{\infty} F_{ri}P_j\cos[ip_r\Omega_r t-(ip_r+jN_s)\theta] \\ &+\frac{1}{2}\sum_{j=0,1,2...}^{\infty}\sum_{i=1,3,5...}^{\infty} F_{ri}P_j\cos[ip_r\Omega_r t-(ip_r-jN_s)\theta] \end{aligned} \tag{2.3}$$

From (2.3), the attributes of the modulated PM air-gap harmonics are given in Table 2.1. After the modulation of stator slots, apart from the original harmonics of order ip_r with the mechanical speed of rotation of Ω_r, there also exist modulated harmonics with the order of $|ip_r \pm jN_s|$ rotating at the speed of

$ip_r\Omega_r$/ ($ip_r \pm jN_s$). The positive and negative speeds of rotations correspond to the harmonics rotating in the same or reverse direction with the p_rth harmonic in the air gap. The rotating direction of the rotor is also the same with the p_rth air-gap harmonic.

Table 2.1 Attributes of Modulated PM Field Harmonics

Harmonic order	Mechanical speed of rotation
$\lvert ip_r \pm jN_s \rvert$	$\frac{ip_r\Omega_r}{ip_r \pm jN_s}$

2.2.2 Armature Reaction Air-Gap Flux Density

For a FSCW PM machine, the armature reaction MMF can be expressed as:

$$F_s(\theta,t) = \sum_{k}^{\infty} F_{sk} \cos(\omega_s - k\theta) + \sum_{m}^{\infty} F_{sm} \cos(-\omega_s - m\theta) \tag{2.4}$$

where ω_s is its electrical rotating velocity, $\omega_s = p_r\Omega_r$, m and k are positive integers depending on the distribution of stator windings, F_k and F_m are the amplitudes of the kth and the mth order harmonics.

Similarly, the modulated armature reaction air-gap flux density in the radial direction can be deduced by multiplying $F_s(\theta,t)$ and $P(\theta)$ from (2.4) and (2.2), the attributes of the modulated armature reaction air-gap field flux harmonics are given in Table 2.2. It can be seen that apart from the original kth (or mth) armature reaction magnetic field harmonic with the mechanical speed of rotation of $p_r\Omega_r/k$ (or -$p_r\Omega_r/m$), there also exist modulated harmonics with the order of $|k(m) \pm jN_s|$ rotating at the mechanical speed of $p_r\Omega_r/(k \pm jN_s)$ (or -$p_r\Omega_r/(m \pm jN_s)$).

Table 2.2 Attributes of Modulated Armature Reaction Field Harmonics

Harmonic order	Mechanical speed of rotation	Harmonic order	Mechanical speed of rotation
$\lvert k \pm jN_s \rvert$	$\frac{p_r\Omega_r}{k \pm jN_s}$	$\lvert m \pm jN_s \rvert$	$\frac{-p_r\Omega_r}{m \pm jN_s}$

2.2.3 Interaction of Air-Gap Magnetic Field Harmonics

Based on the classical electromagnetic theory, there are three conditions for torque production between two magnetic field harmonics, which are summarized as follows:

(a) They have the same pole pairs and speed, and then produce steady torque. In this case, there are two possible cases which are listed as follows:

(a-1) Two MMF harmonics have the same pole-pair number and the speed, they can interact with each other directly in the air-gap and produce steady torque as shown in Fig. 2.3 (a). This was believed to be the principle of the conventional PMSMs such as FSCW PMSMs.

(a-2) Two MMF harmonics have different pole-pairs and mechanical speed of rotations. However, there are flux modulation poles (FMPs) between them, and steady torque can still be produced if they have the same frequency and their pole-pair numbers satisfying:

$$p_h = N_f \pm p_l \tag{2.5}$$

where p_l is the pole-pair number of the low-speed MMF harmonic and p_h is the pole-pair number of the high-speed MMF harmonic. N_f is the pole number of FMPs. This phenomenon is termed as air-gap field modulation and/or magnetic gearing effect, i.e. field modulation effect from the viewpoint of air-gap field and magnetic gearing effect from the viewpoint of torque production. Fig. 2.3 (b) shows a schematic of magnetic gearing effect. The FMPs can modulate the magnetic fields and make them have the same pole-pair number and speed of rotation in the corresponding air-gap to produce steady torque. The gear ratio, which is the ratio of speeds of rotation between two MMF harmonics, is given by:

$$G_r = \frac{p_h}{p_l} \tag{2.6}$$

Table 2.3 shows the attributes of magnetic gearing effect. Since p_l is larger than p_h as shown in Fig. 2.3 (b), it can be seen that the low speed field can have an increased torque at a reduced speed. The torque production principle of magnetic gearing effect has drawn researchers' attention because of this reason and has been proven to be the working principle of high torque density magnetic gears [ATA04]. Moreover, the magnetic gearing effect in the torque production have also been investigated widely in Vernier, flux-modulated and switched flux (SF) machines [QU11]-[DU16].

(b) They have the same pole pairs but different speed, and then produce torque ripples [LI16];

(c) The pole pairs of the two harmonics are different, and they will produce no torque [LI16].

Table 2.3 Attributes of Magnetic Gearing Effect

	Pole pair number	Speed of rotation	Torque
High speed field	p_h	n_{rh}	T_h
Low speed field	p_l	$n_{rh}\cdot G_r$	T_h/G_r

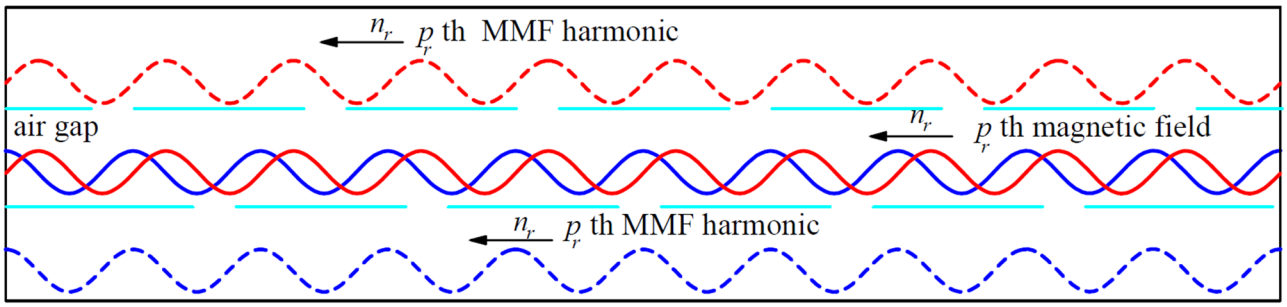

(a) Principle of conventional PM machine torque production (a-1).

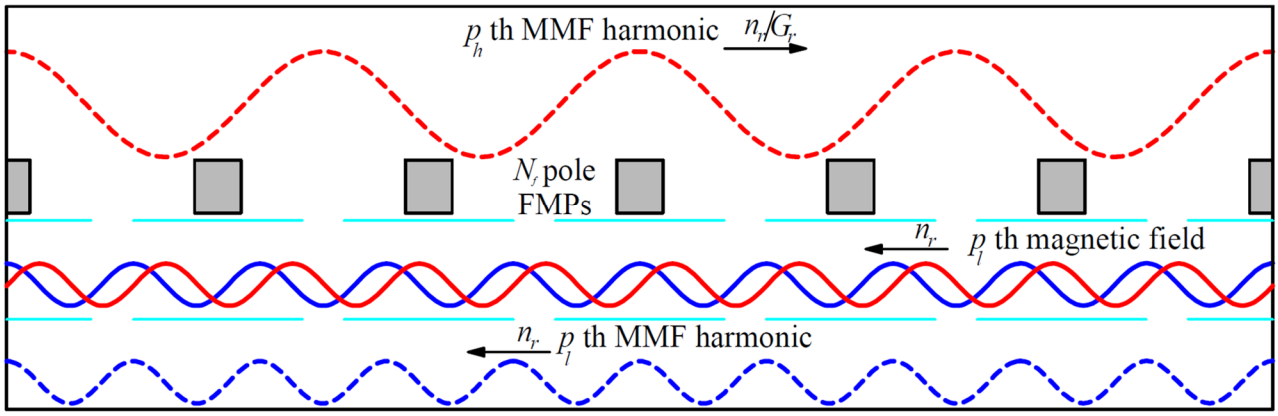

(b) Principle of magnetic gearing effect (a-2).

Fig. 2.3 Illustration of torque production mechanisms.

2.2.4 Torque Production Mechanisms in FSCW PMSMs

According to the analysis above, in a FSCW PM machine, the following equations must be satisfied to produce steady torque:

$$\begin{cases} \left|ip_r \pm nN_s\right| = \left|k \pm jN_s\right| \\ \dfrac{ip_r\Omega_r}{ip_r \pm nN_s} = \dfrac{p_r\Omega_r}{k \pm jN_s} \text{ or } \dfrac{-p_r\Omega_r}{m \pm jN_s} \end{cases} \tag{2.7}$$

where n is either 0 or a positive integer.

This means

$$\begin{cases} p_r = k \quad \text{Principle of conventional PM machines} & \text{(2.8-a)} \\ p_r = \left|k \pm jN_s\right| \quad \text{Magnetic gearing effect} & \text{(2.8-b)} \end{cases} \tag{2.8}$$

From (2.8), it is clear that the steady torque of FSCW PMSM can be generated from two main mechanisms:

(2.8-a) p_r=k: the fundamental PM MMF harmonic and the unmodulated armature reaction MMF harmonic share the same order and speed of rotation, they can interact with each other and produce useful torque. In this way, the torque is produced by the principle of the conventional PMSM.

(2.8-b) $p_r \neq k$: the $p_r th$ PM MMF harmonic and the kth armature reaction MMF harmonic do not share the same order or speed of rotation, however, they have the same frequency ($p_r\Omega_r$) as shown in Table 2.1 and 2.2. Hence, they can still interact with each other and produce steady torque under the modulation of air-gap permeance of order jN_s as long as they satisfy (2.8-b).

It is noteworthy that in FSCW PMSMs with p_r pole pairs of rotor PMs, due to the winding distribution, there exists armature reaction harmonic of order N_s-p_r and it has the same frequency with the $p_r th$ PM MMF harmonic, which satisfies (2.8-b). In this way, the torque in FSCW PMSMs can be produced by the magnetic gearing effect. The PM and armature reaction MMF harmonics play the role of the two magnetic fields, and the N_s-pole stator tooth and slots play the role of FMPs. However, the magnetic gearing effect in FSCW PMSMs was ignored in the previous papers.

It should be noted that for FSCW PMSMs injected with sine wave current, only the $p_r th$ PM field harmonic is the working harmonic in the air-gap [CHE17] [CIE06]. Hence, the magnetic gearing effect in FSCW PMSMs can be further described as: the armature reaction harmonic is modulated to the fundamental order by the stator slots, it can interact with the fundamental PM harmonic in the air-gap and produce steady torque.

Hence, it can be seen that the torque output of FSCW PMSM is not only produced by the principle of

conventional PMSM but also by the magnetic gearing effect. The contribution of magnetic gearing effect to torque is highlighted and will be firstly quantified in this chapter.

2.2.5 Finite Element Validation

In this section, a 12-slot/8-pole surface-mounted PM synchronous machine with open slots is used to validate the former theoretical analysis. The main design parameters of the machine are listed in Table 2.5. A 1/4 model of the 12-slot/8-pole machine is shown in Fig. 2.4.

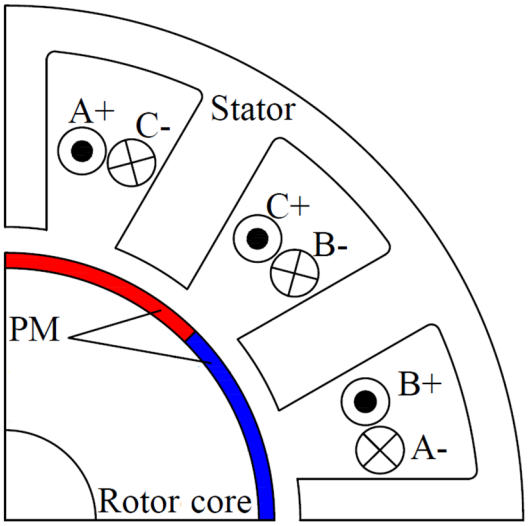

Fig. 2.4 ¼ model of a 12-slot/8-pole FSCW PMSM.

To validate (2.8), the torque produced by each air-gap magnetic flux density harmonic need to be identified. The air-gap magnetic flux density radial component B_{gr} and tangential component B_{gt} can be expanded by Fourier series:

$$\begin{cases} B_{gr}(t,\theta) = \sum_{k} B_{grk} \cos(k\theta - \theta_{rk}) \\ B_{gt}(t,\theta) = \sum_{k} B_{gtk} \cos(k\theta - \theta_{tk}) \end{cases} \tag{2.9}$$

where B_{grk} and B_{gtk} are the kth Fourier coefficients of B_{gr} and B_{gt}, θ_{rk} and θ_{tk} are their respective phases.

The electromagnetic torque produced by the kth radial and tangential airgap field flux harmonics can be derived by [SPA14]:

$$T_k(t) = \frac{\pi r_g^{\,2} l_{ef}}{\mu_0} B_{grk} B_{gtk} \cos(\theta_{rk} - \theta_{tk}) \tag{2.10}$$

where r_g is the air-gap radius, μ_0 is the vacuum permeability, l_{ef} is the effective axial length. It is noteworthy that (2.10) is a general equation that can be used for either cogging torque or on-load torque.

The contribution of each air-gap harmonic to the torque can be obtained by combining FEA results and (2.10) as follows: at a certain time in an electrical period, the FE predicted B_{gr} and B_{gt} are expanded to the Fourier series. Hence, the value of B_{grk}, B_{gtk}, θ_{rk} and θ_{tk} can be obtained. After this, the contribution of individual air-gap field harmonics to torque production at any time instant within the period can be quantified by (2.10) [SPA14]. After repeating the above procedures over an electrical period, the average torque produced by the kth field harmonic within the full electric period can be obtained.

The cogging torque and on-load torque (the machine is fed with sinusoidal currents with the maximum phase current I_{max}=5A and operating under I_d=0 control) are calculated in FEA and the results are provided in Fig. 2.5 (a). For the cogging toque, the contribution of each air-gap magnetic flux density harmonic is calculated using (2.10) at the maximum value point which is 36 electrical degrees. The result is shown in Fig. 2.5 (b). It can be seen that the 20th harmonic makes the most contribution to the cogging torque whereas the 28th harmonic has a negative effect on it. For the on-load torque in this 12-slot/8-pole machine, the torque ripple is mainly determined by the cogging torque as shown in Fig. 2.5 (a). Hence, the 4th, 20th and 28th harmonics are used to investigate the variations of air-gap space harmonics with respect to the rotor position. The amplitudes, the cosine values of the phase difference of their radial and tangential components over an electrical period are shown in Fig. 2.5 (c) - (e). The instant contribution of each air-gap magnetic flux density harmonic to the instant torque are calculated by (2.10) at each time instant and shown in Fig. 2.5 (f). The average on-load torque produced by each air-gap harmonic within an electrical period is also calculated and the result is given in Fig. 2.5 (g). It shows that only the 4th air-gap magnetic flux density harmonic contributes to the total torque. For other harmonics such as 20th and 28th air-gap magnetic flux density harmonics, the average value of $\cos(\theta_{rk} - \theta_{tk})$ in (2.9) is 0 in an electrical period as shown in Fig. 2.5 (e). Since the 4th harmonic is the fundamental harmonic in this machine, this means no useful torque will be produced by other harmonics except the fundamental harmonic, which validates the conclusion drawn from (2.8) that only p_rth PM air-gap flux density harmonic is the working harmonic. However, it is still unclear how much contribution the magnetic gearing effect makes to the average torque, i.e., to decompose the torque according to different torque production mechanisms shown in (2.8), which will be revealed in the next section.

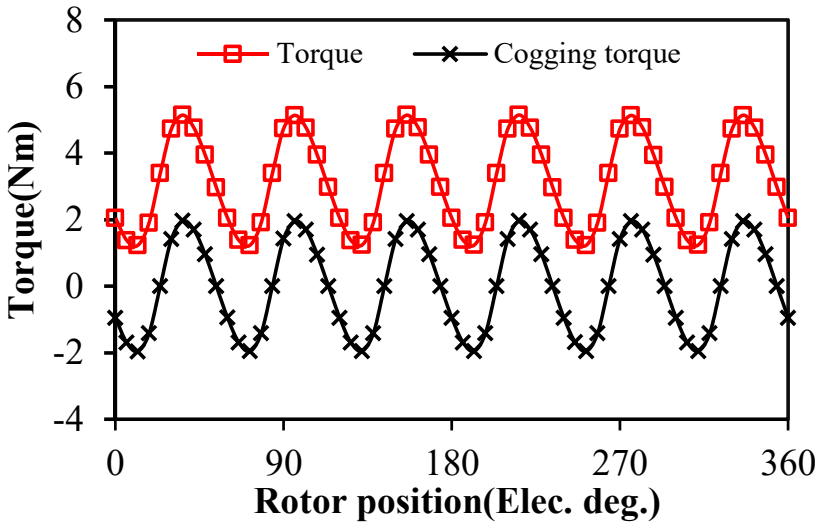

(a) Waveforms of torque and cogging torque.

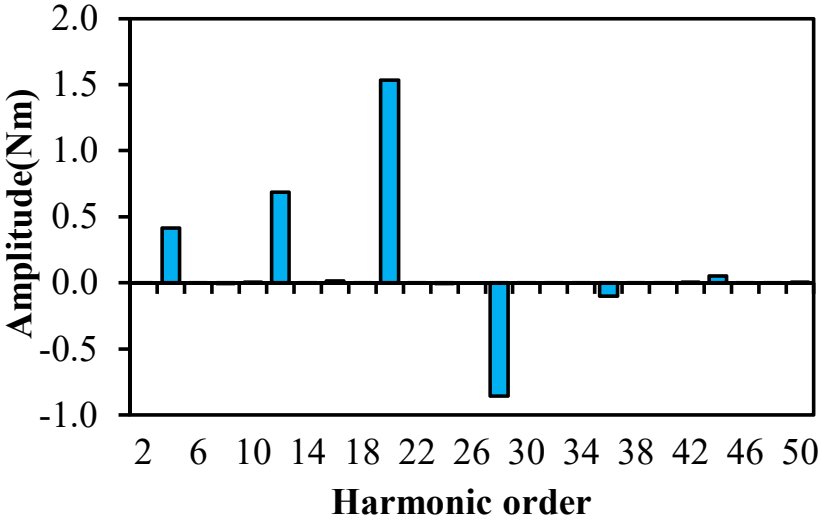

(b) Torque contribution of air-gap magnetic flux harmonics to the cogging torque.

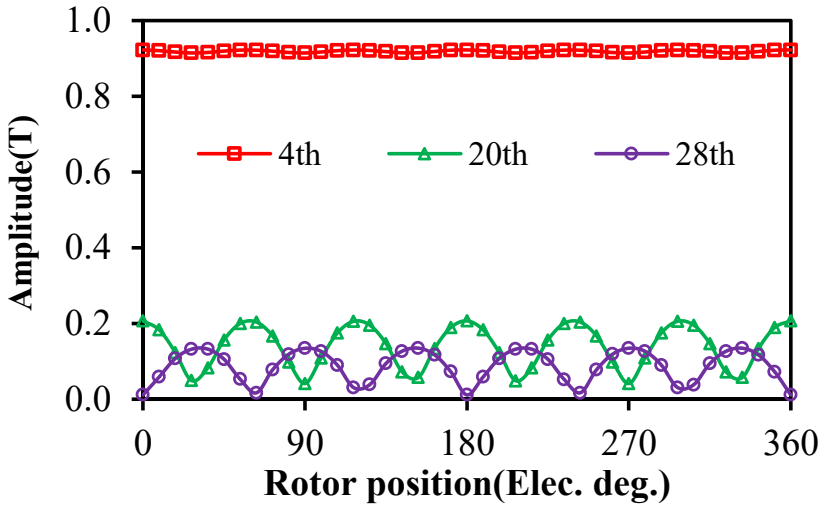

(c) Amplitude of radial component of air-gap magnetic flux density harmonics vs rotor position.

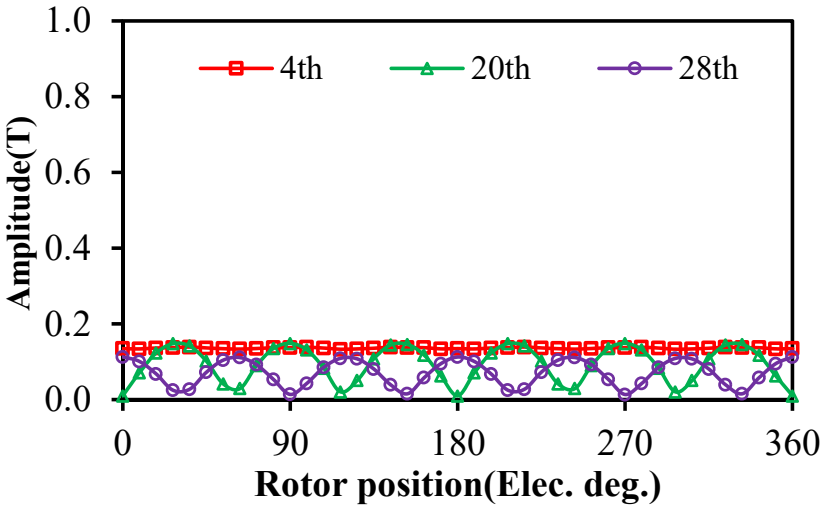

(d) Amplitude of tangential component of air-gap magnetic flux density harmonics vs rotor position.

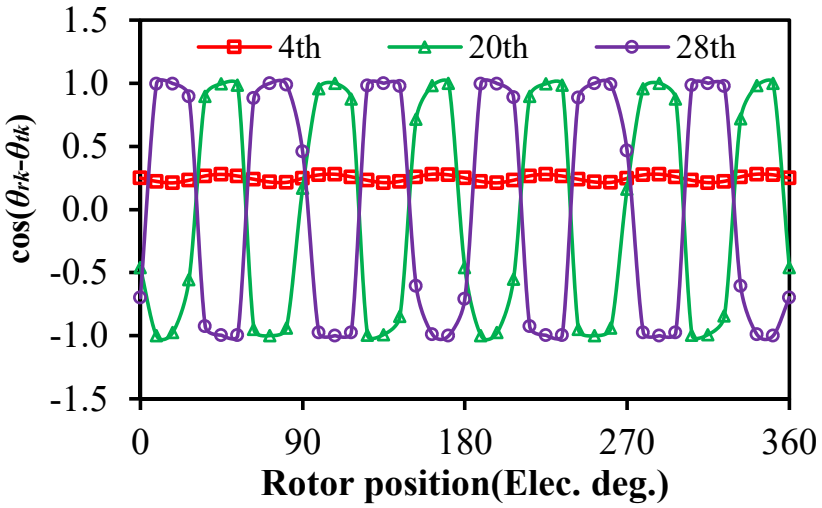

(e) Variation of cos(θ_{rk} -θ_{tk}).

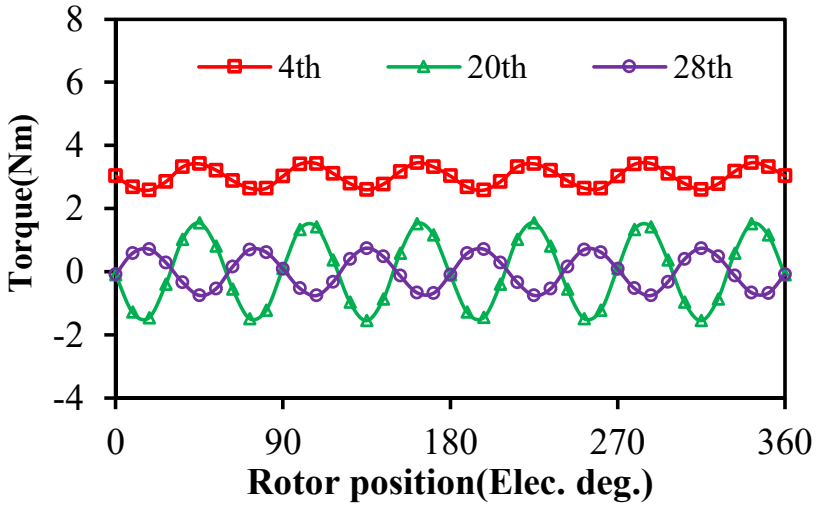

(f) Instant torque contribution of individual air-gap flux density harmonic.

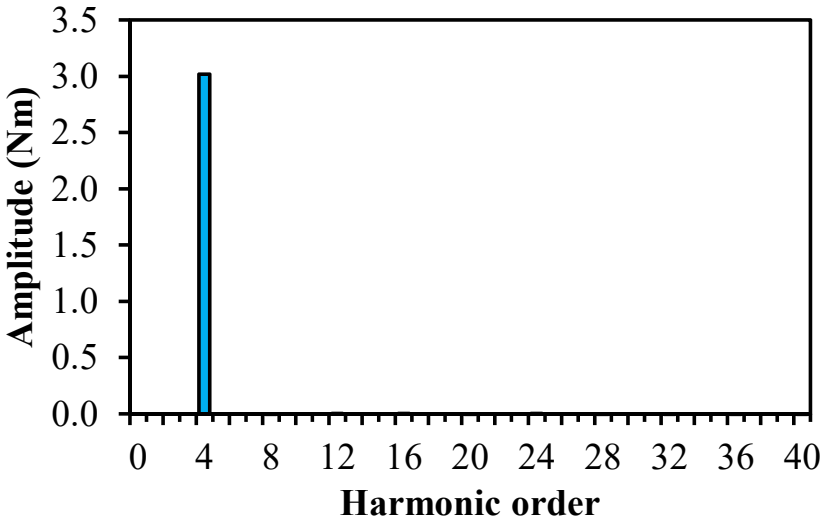

(g) Torque contribution of each MMF harmonic.

Fig. 2.5 FEA-predicted torque performance.

2.3 Magnetic Gearing Effect in a 12-Slot/8-Pole FSCW PMSM

2.3.1 Introduction of FEA-Based ECSM

In this subsection, an FEA-based equivalent current sheet (ECSM), which is the application of equivalent current sheet [ISH05b] [RAS00] in FEA, is used to study the harmonic behaviour under the modulation of stator slots, Fig. 2.6. The ECSM is a method in which the winding currents are approximated by an equivalent current sheet of infinitesimal thickness distributed over the stator slot openings. This method is used to be applied to analytical derivation of air-gap flux density harmonics [ISH05b] [RAS00]. The FEA-base ECSM is to build an ECSM in the FEA software. Similar as the conventional ECSM in analytical method, in the FEA-based ECSM, the coils are wound in the same manner with the 12-slot/8-pole PM machine shown in Fig. 2.4. The thickness of the equivalent current sheet is designed very small compared to the air-gap length (<5%).

The armature reaction flux lines of the model in Fig. 2.4 and its FEA-based ECSM in Fig. 2.6 are given in Fig. 2.7. It can be seen that the 12-slot/8-pole model and its FEA-based ECSM have the same main flux, the only difference between them is that the 12-slot/8-pole model has slot opening leakage flux whereas its FEA-based ECSM does not due to different position of coils. This means that the FEA-based ECSM is an approximation method because it changes the position of the coils. Since the leakage flux does not contribute to the steady torque production, the FEA-based ECSM can be seen as an FE

assisted analytical method for air-gap magnetic field and torque production calculation.

In general, the differences between the conventional current sheet model and the FEA-based ECSM are summarized and provided in Table 2.4. It shows that the advantages of FEA-based ECSM over analytical ECSM is that: 1) the field modulation effect in both radial and tangential directions can be more accurately calculated by FEA than analytical method; 2) non-linear steel materials can be used in FE simulation, which means that the non-linear characteristics of the materials can be taken into consideration.

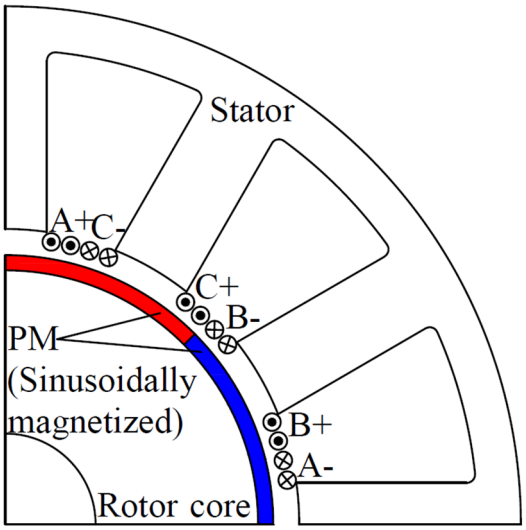

Fig. 2.6 ECSM of the 12-slot/8-pole machine.

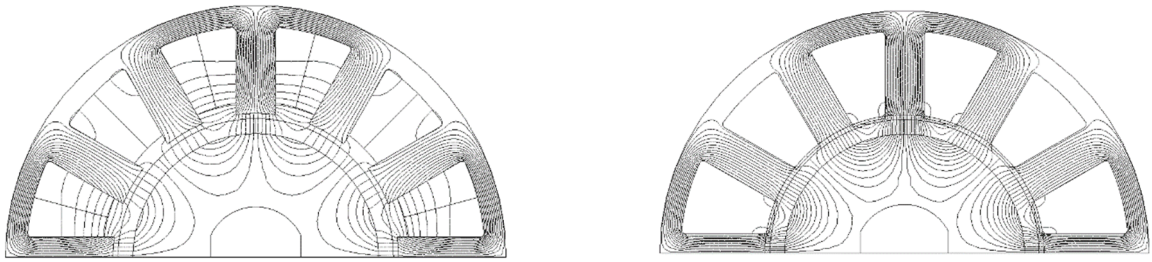

(a) Original model. (b) FEA-based ECSM.

Fig. 2.7 Armature reaction flux lines (I_a=5A, I_b=I_c=-2.5A).

Table 2.4 Analytical and FEA-based ECSMs

	Calculation method	Thickness of current sheet	Material
Analytical ECSM	Analytical method	Infinitesimal	linear
FEM-based ESCM	FEA	<5% of air-gap length	Non-linear

2.3.2 Quantification of Torque Contribution in a 12-Slot/8-Pole PMSM

As has been analysed and validated in Section 2.2, the magnetic gearing effect only exists if the armature reaction harmonic of certain order is modulated to the fundamental order by the stator slots. Hence, it is important to have the information of each armature reaction harmonic before and after stator slotting modulation. However, all the armature reaction harmonics are from the same current excitation and cannot be separated once the current is injected. In this section, a harmonic restoration method is used to analyse the behaviour of each armature reaction harmonic individually.

From FEA-based ECSM, a model without rotor PMs and stator slots is firstly built to gain the information of the armature reaction harmonics before being modulated by stator slots, Fig. 2.8. The spectra and phases of the armature reaction air-gap magnetic flux density before modulation are calculated by FEA and shown in Fig. 2.9. According to Fig. 2.9, the amplitudes of the 4th, 8th and 20th harmonics are larger than the other harmonics. Moreover, since they satisfy (2.8), they are considered as priorities.

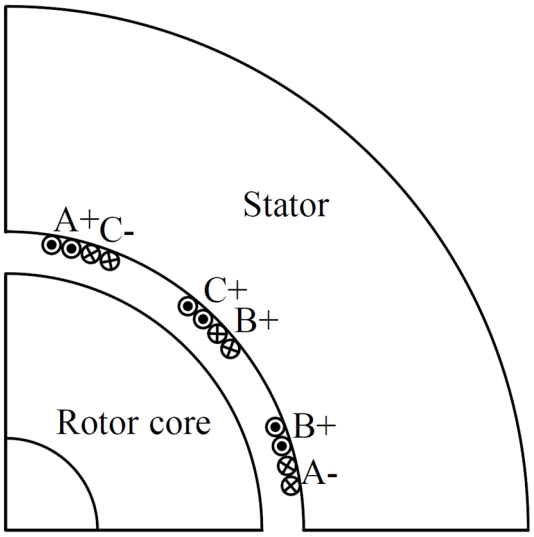

(a) A model without PMs and stator slots.

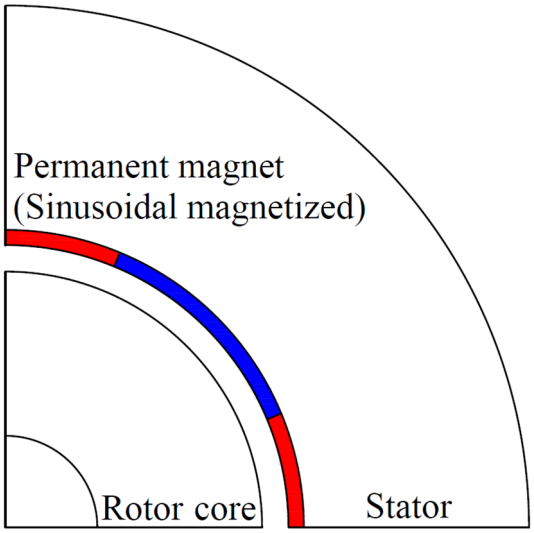

(b) 4th armature reaction magnetic field.

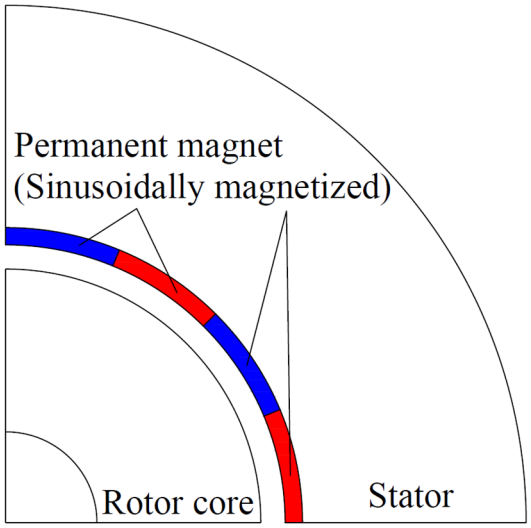

(c) 8th armature reaction magnetic field.

Fig. 2.8 Restoration of magnetic fields before modulation.

To analyse the behaviour of the armature reaction magnetic flux density harmonic individually, they need to be restored individually. For the 4th harmonic as an example, it can be restored by the following way: an 8-pole outer rotor which consists of sinusoidally magnetised permanent magnets are built, which are shown in Fig. 2.8 (b). In Altair Flux 12.1, sinusoidally magnetised PMs can be achieved by the following ways: 1) Define spatial quantities X1, Y1 and THETA1 with expressions of CLCS(XY1, 1), CLCS(XY1, 2) and ATAN2(Y1, X1), respectively. 2) Define a spatial quantity BR_SPATIAL expressed as -B_R*Cos(PP*THETA1+THETA0)*Vec3(Cos(THETA1),Sin(THETA1),0), where PP is the number of pole pairs of the magnetic field to be restored, B_R and THETA0 are the remanence and phase of the magnetic field to be restored. 3) Create a spatial linear magnet material named PM_OUT with the BR_SPATIAL to be its remanent flux density, select yes under “Taking the movement of mechanical sets into account”. 4) Assign the spatial linear magnet PM_OUT to the outer PM rotor. The thickness of the PMs is the same with that of the equivalent current sheet in Fig. 2.6. The remanence and the initial angle of the permanent magnets are adjusted so that the amplitude and phase of the 4th harmonic produced by outer PMs are the same with those by the armature reaction field before modulation (shown in Fig. 2.9). Similarly, a 16-pole outer rotor consists of sinusoidally magnetised permanent magnets are also built to simulate the 8th armature reaction field before being modulated by stator slotting, Fig. 2.8 (c).

After restoring the information of the armature reaction harmonics before modulation, their behaviour

under modulation effects can be seen in the following way: the interactions between the 4th PM MMF harmonic and the 4th and 8th armature reaction MMF harmonics under the modulation effect are shown in Fig. 2.10. An 8-pole inner rotor, which is identical to the rotor in Fig. 2.6, is used to interact with the outer PMs. According to Table 2.1 and Table 2.2, in Fig. 2.10 (a), both of the inner and outer PMs are rotating in the same direction at the mechanical speed n_r, whereas in Fig. 2.10 (b), the 16-pole outer PMs rotate at half mechanical speed of the 8-pole inner rotor, in the opposite direction. Considering the slotting effect, the torque produced by each air-gap field harmonic is calculated by (2.10) over an electrical period and the results are shown in Fig. 2.11.

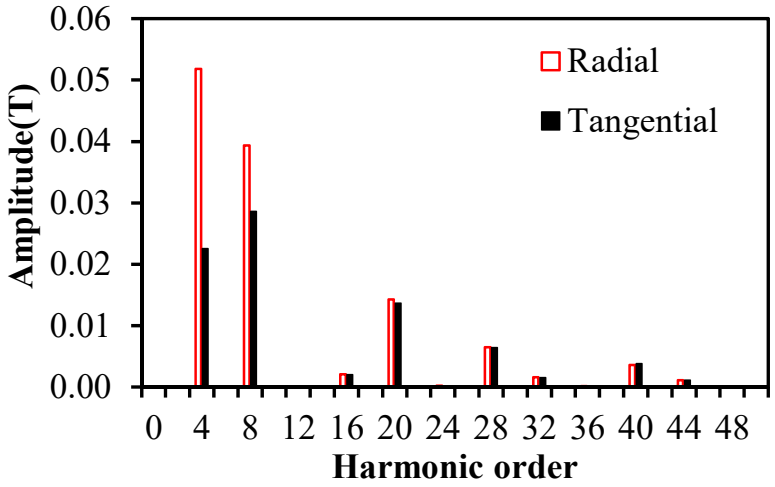

(a) Spectra.

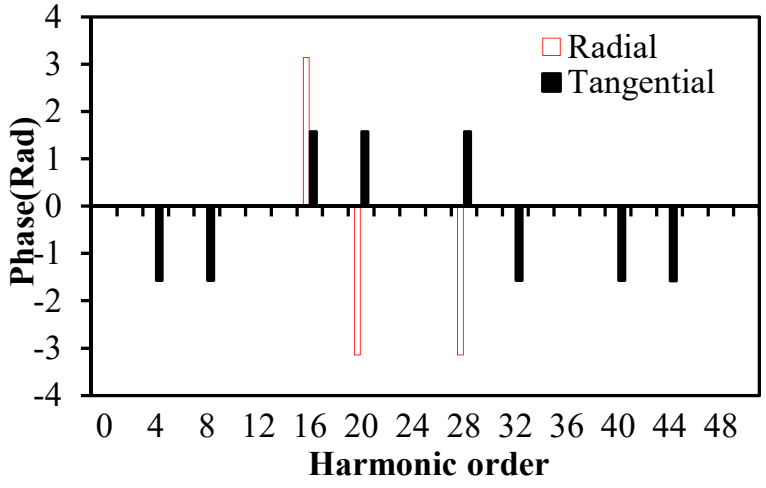

(b) Phases.

Fig. 2.9 FE predicted armature reaction air-gap magnetic flux density harmonics before modulation.

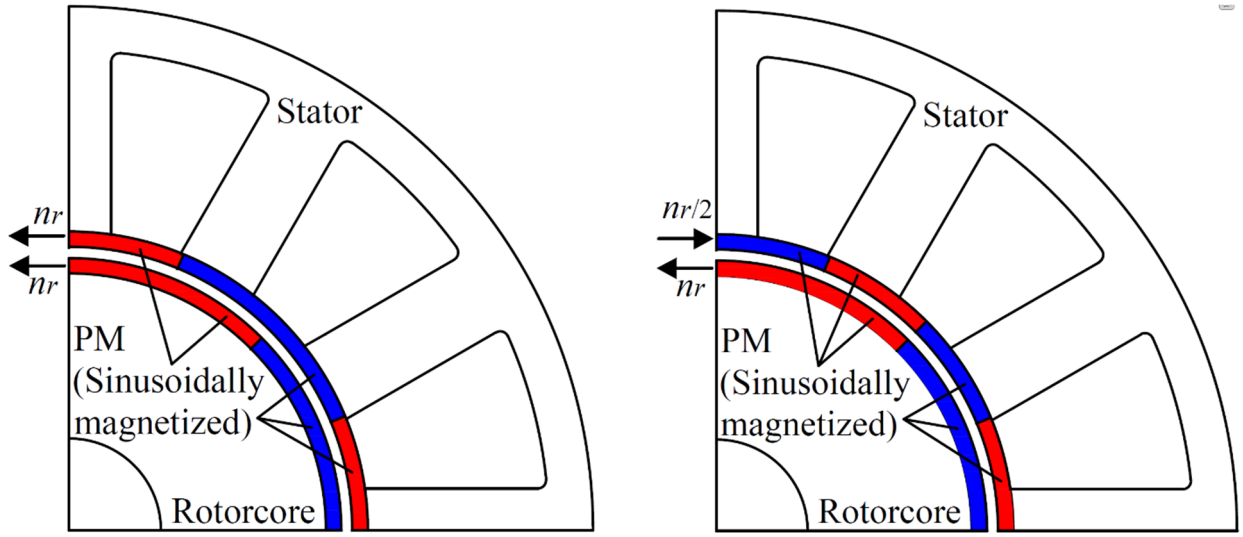

(a) 4th PM and 4th armature reaction MMF. (b) 4th PM and 8th armature reaction MMF.

Fig. 2.10 Interaction of the MMF harmonics.

In Fig. 2.11, the torque produced by the interaction of magnetic fields Fig. 2.10 (a) is shown by legend "PMSM". Since the armature reaction and PM magnetic fields share the same order in this case, the torque component is produced by the principle of the conventional electrical machine. The torque produced by the interaction of magnetic fields in Fig. 2.10 (b) is illustrated by legend "MG". Since the 8th armature reaction and the 4th PM MMF harmonics do not share the same order, the torque component in this case is produced by the principle of the magnetic gearing effect, viz, the 8th armature reaction and 4th PM MMF harmonics can produce steady torque with the modulation effect of 12th air-gap permeance. In fact, Fig. 2.10 (b) is a magnetic gear with 8-pole inner rotor, 16-pole outer rotor and 12-pole iron pieces. For the FEA-based ECSM shown in Fig. 2.6, the average on-load torque produced by each air-gap harmonic within an electrical period is also calculated and the result shown by legend "Total".

The accumulated result of the torque produced by the principle of conventional PMSM and magnetic gearing effect is given and compared with the total torque in Fig. 2.11. It can be seen that the accumulated result makes up >99% of the average torque, in which the magnetic gearing effect contributes 9.37% and the conventional PM machine principle contributes 89.63%. Hence, the correctness of the harmonic restoration method in this subsection is validated when the saturation level is not high. From this perspective, the FSCW PMSM can be regarded as a combination of conventional PMSM and a magnetic gear.

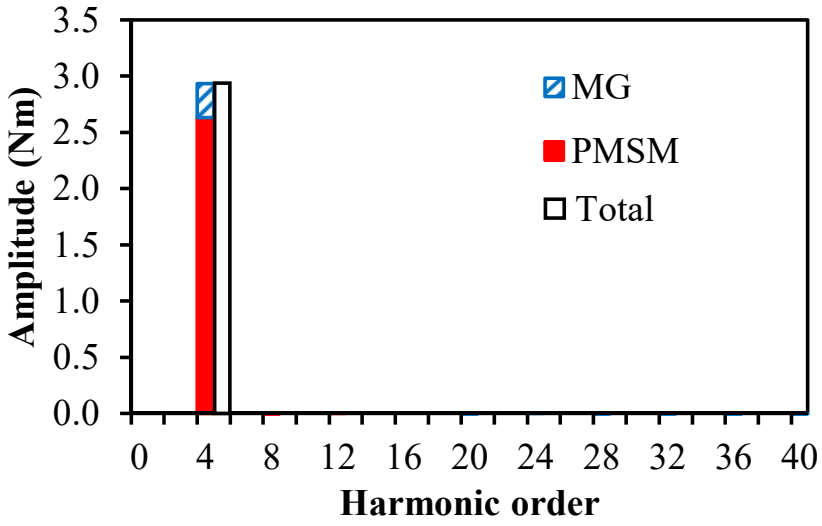

Fig. 2.11 Quantification of torque production.

2.4 Influence of Slot Opening on Magnetic Gearing Effect

Since the slotting effect is the main cause of gearing effect in FSCW PMSMs, the influence of stator slot opening on the field harmonics and the contribution of gearing effect to the average torque are investigated in this section. The amplitudes of the 4th armature reaction and the PM radial air-gap magnetic flux density harmonics and average torque with respect to different slot opening angles for the 12-slot/8-pole machine are provided in Fig. 2.12 and Fig. 2.13.

By adopting the FEA-based ECSM and the harmonic restoration method, the modulated 4th armature reaction air-gap magnetic flux density harmonic which is originated from the 8th armature reaction MMF and the unmodulated 4th armature reaction air-gap magnetic flux density harmonic which is originated from the 4th armature reaction MMF can be separated, as shown in Fig. 2.12 (a). It shows that the modulated 4th armature reaction air-gap magnetic flux density harmonic increases with the increase of slot opening.

In Fig. 2.12 (b), since the DC component of equivalent air-gap permeance increases with the decrease of slot opening, the amplitudes of fundamental harmonics increase with the decrease of slot opening. However, with the decrease of the slot opening, the tooth-tip leakage flux increases, and therefore, the amplitude of 4th armature reaction air-gap magnetic flux density harmonic as well as the average torque decreases when the slot opening is very small. The tangential PM and armature reaction air-gap flux density harmonics follow the same trend with the radial components.

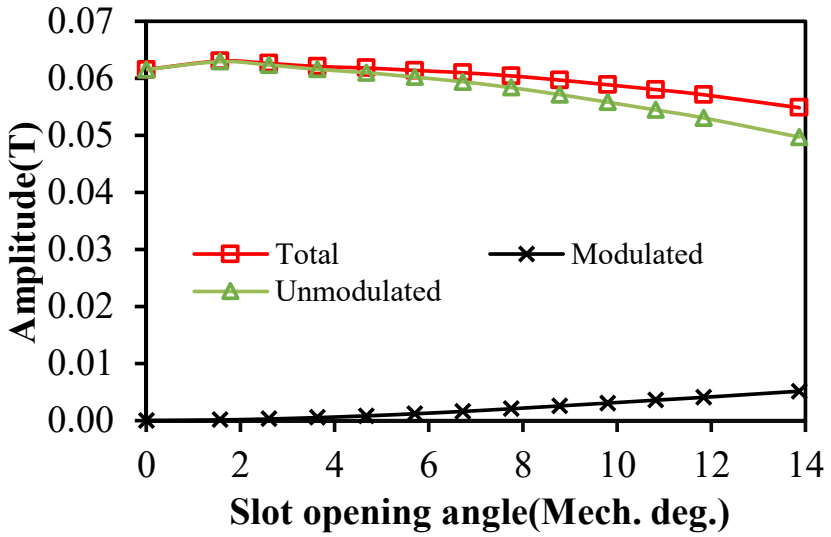

(a) Armature reaction harmonics.

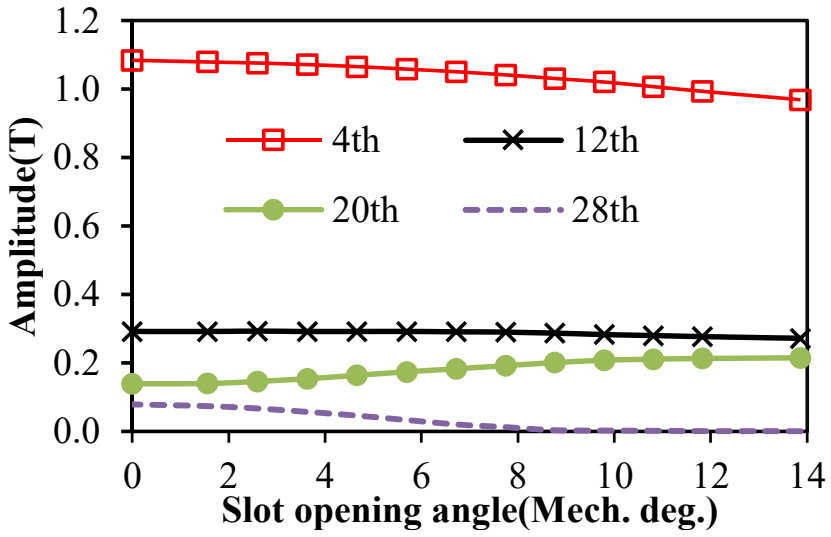

(b) PM harmonics.

Fig. 2.12 Influence of slot opening on the field harmonics.

The torque produced by the interaction of the modulated 4th armature reaction harmonic and PM harmonic is based on the principle of magnetic gearing effect, whereas the torque produced by the unmodulated 4th armature reaction harmonic and PM harmonic is based on the principle of conventional PMSM. Therefore, their respective contribution to the average electromagnetic torque can also be quantified, which is shown in Fig. 2.13 (a). It can be seen that with the increase of slot opening, the amplitude of modulated 4th armature reaction field harmonic increases (shown in Fig. 2.12 (a)), therefore, the contribution of magnetic gearing effect to the total torque increases.

To evaluate the contribution of the magnetic gearing effect to the average torque in an electrical machine, the ratio of the torque produced by the magnetic gearing effect to the total torque is employed:

$$\rho = \frac{T_M}{T_0} \tag{2.11}$$

where T_M is the torque produced by the magnetic gearing effect, T_0 is the average torque. The ratio ρ with respect to the slot opening angle for the 12-slot/8-pole machine is also illustrated in Fig. 2.13 (a). It shows that the magnetic gearing effect becomes stronger with the increase of the slot opening.

Since slotting effect also brings about parasitic effects, Fig. 2.13 (b) shows the influence of the slot opening on the cogging torque and torque ripple. For the 12-slot/8-pole machine investigated in this chapter, the cogging torque is the main ripple source for the torque ripple. According to Fig. 2.5, the 20th open-circuit air-gap flux density harmonic makes the most contribution to the cogging torque whereas the 28th harmonic has a negative contribution on it. From Fig. 2.12 (b), it can be seen that with the increase of the slot opening, the amplitude of 20th harmonic increases whereas the amplitude of 28th decreases. This explains why the cogging torque increases with the increase of slot opening.

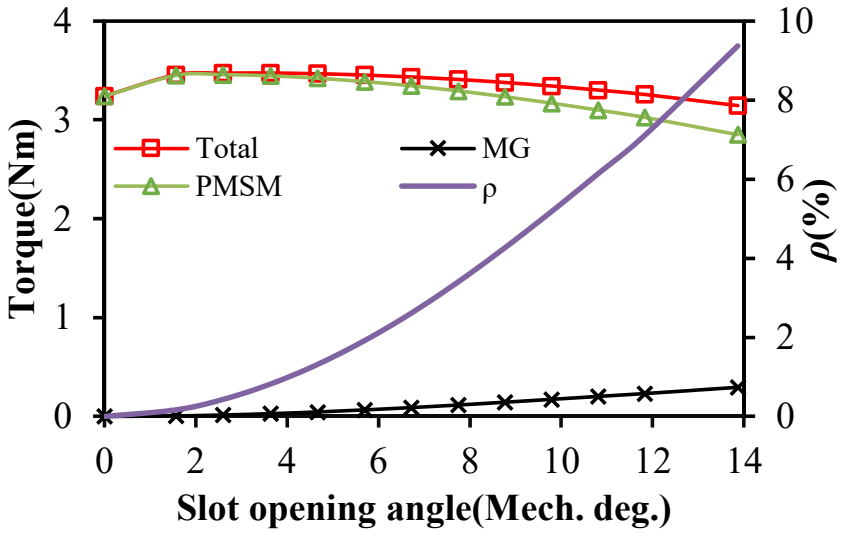

(a) Average torque and torque contribution.

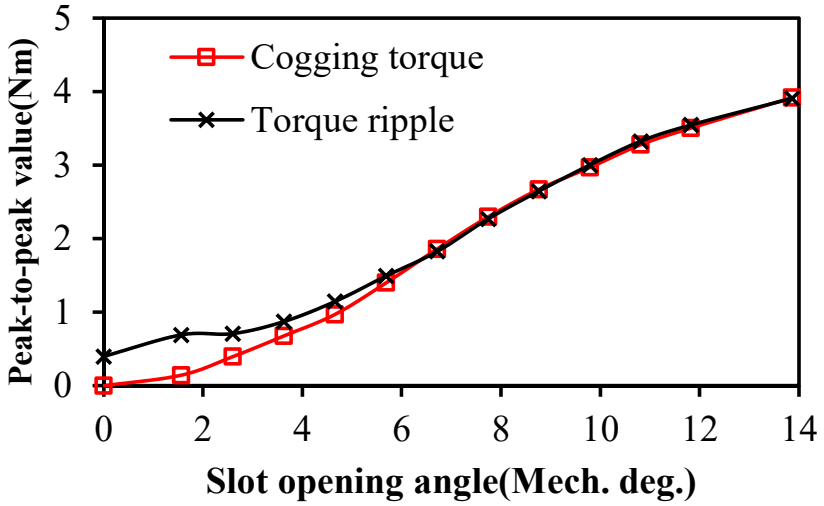

(b) Cogging torque and torque ripple.

Fig. 2.13 Influence of slot opening on torque performance.

2.5 Gear Ratio in FSCW PMSMs

In the 12-slot/8-pole PM machine, the 8th armature reaction MMF harmonic can produce steady torque with the 4th PM MMF harmonic under the modulation effect of stator slotting. The gear ratio, which is the ratio of speed between the high speed magnetic field and low speed magnetic field [ATA04], is

$$G_r = \frac{-8}{4} = -2 \tag{2.12}$$

For FSCW PM machines with p_r pole pairs of rotor PMs, due to the winding distribution, the armature reaction harmonic of order N_s-p_r has a comparable amplitude with the fundamental p_rth armature reaction harmonic. With the speed of rotation of $-\omega_s/(N_s-p_r)$, the (N_s-p_r)th harmonic can form a magnetic gear with the fundamental open-circuit harmonic and stator tooth, making a contribution to the average torque.

Based on the analysis above, the gear ratio of the (N_s-p_r)th harmonic and the fundamental harmonic in FSCW PM machines can be defined as the ratio of their speed of rotation:

$$G_r = \frac{p_r - N_s}{p_r} \tag{2.13}$$

2.6 Experimental Validation

The magnetic gearing effect and its contribution to the average torque in the foregoing sections cannot be measured directly on the prototypes because only the resultant torque waveform can be measured in the experiment. However, the influence of slot opening on torque can be validated by experiments. Hence, three 12-slot/8-pole machine prototypes with closed slot stator, semi-closed slot stator and open slot stator topologies are built, Fig. 2.14 (a)-(d). The dimensional parameters of the three prototypes are given in Table 2.5.

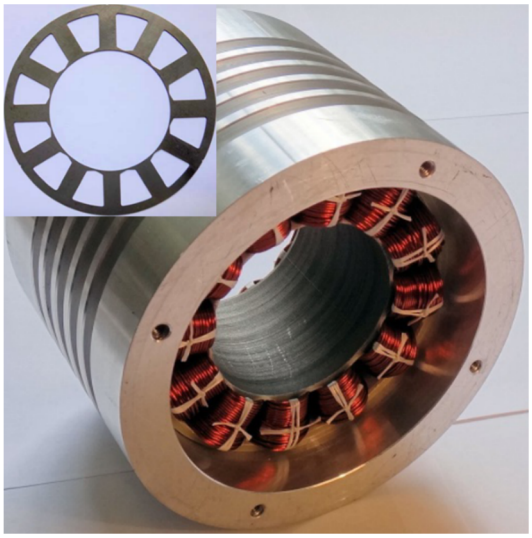

(a) Closed-slot stator.

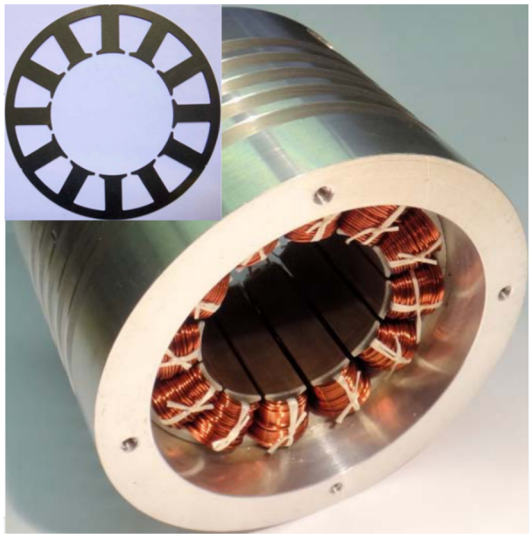

(b) Semi-closed slot stator.

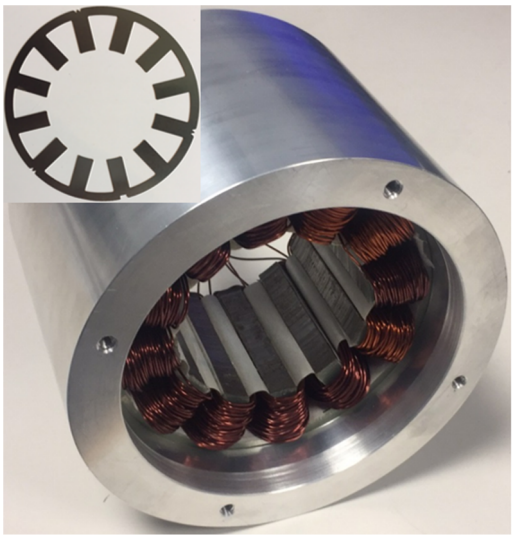

(c) Open-slot stator.

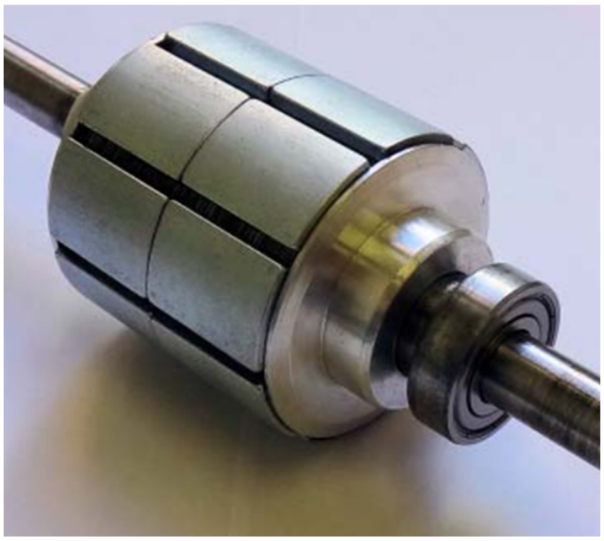

(d) Rotor.

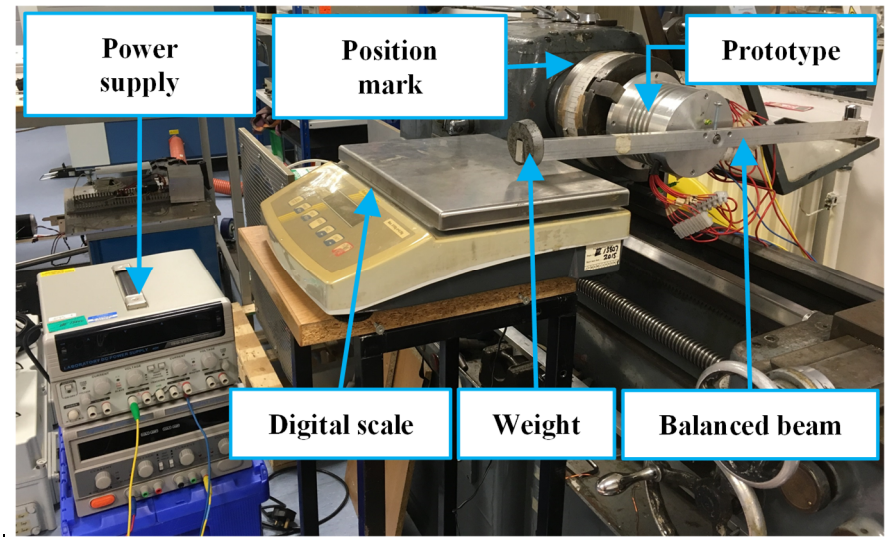

(e) Test rig.

Fig. 2.14 Photos of prototypes and the test rig.

The experiments are implemented on the experimental setup shown in Fig. 2.14 (e). For the 12-slot/8-pole FSCW PMSMs with different slot openings, the experiments are done by applying DC current to phase A in series connection to the parallel phase B and phase C, i.e. $-2I_b=-2I_c=I_a=5$A. The static torques within 0-180 electric degrees of the prototype machines can subsequently be measured by rotating the stator housings in 180 electric degrees with fixed step [ZHU09c].

Table 2.5 Dimensional Parameters of Prototypes

Parameters	Closed	Semi-closed	Open
Slot/pole number		12/8	
Stator outer/inner diameter		100mm/57mm	
Rotor outer diameter		55mm	
Turns per phase		184	
PM thickness/ pole arc		3mm/155° Elec.	
Axial length		50mm	
Slot opening angle	0° Mech.	4° Mech.	14° Mech.

Fig. 2.15 compares the FEA and test results of the back-EMF waveforms and spectra. Fig. 2.16 compares the FEA and test results of the cogging torque and spectra. The measured static torque waveforms are compared with the FEA results in Fig. 2.17. Although 2-D FEA results are slightly higher than those of measurements due to end effect, friction, etc., good agreements are obtained. It also shows that the peak-to-peak value of cogging torque increases with the increase of slot opening, which validates the correctness of the analysis.

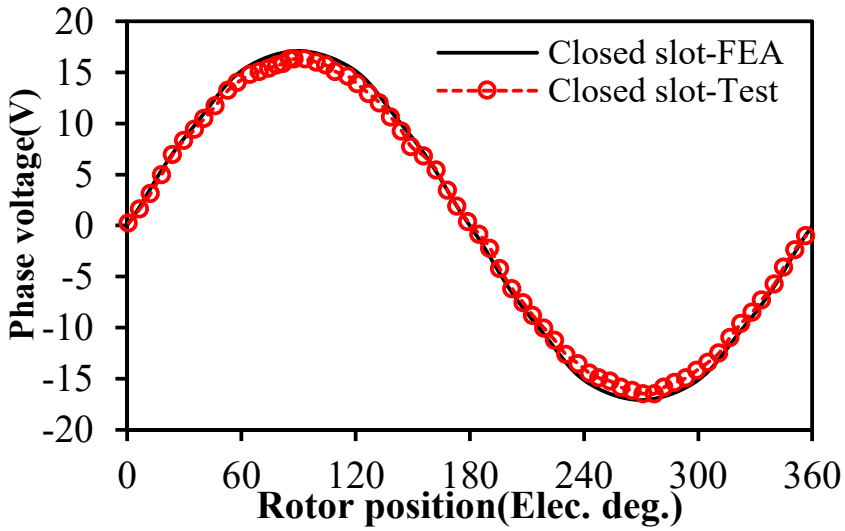

(a) Closed-slot stator.

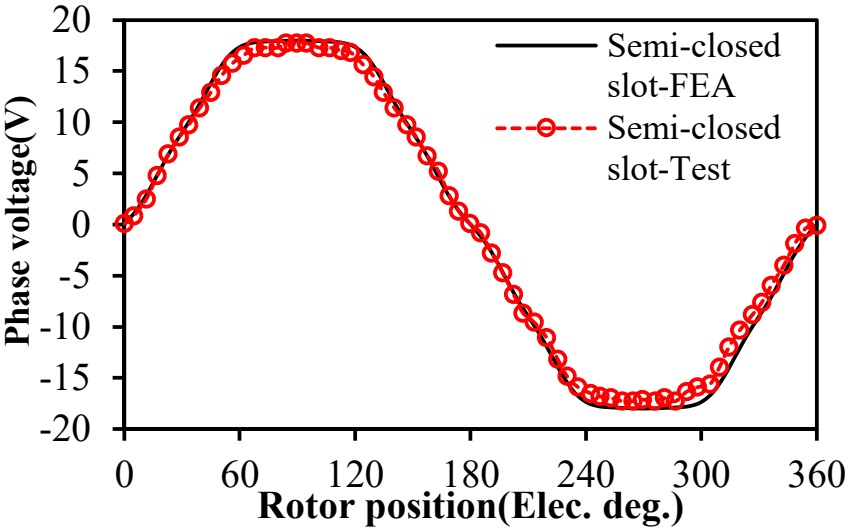

(b) Semi-closed slot stator.

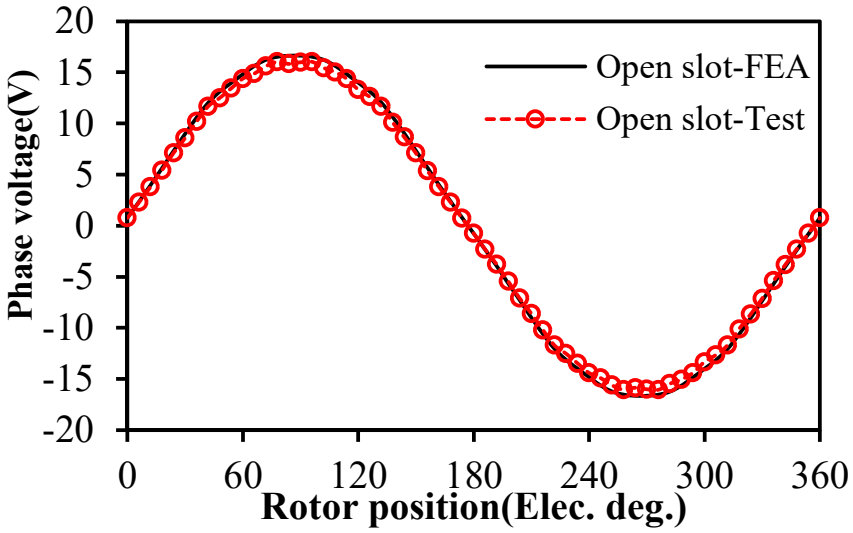

(c) Open-slot stator.

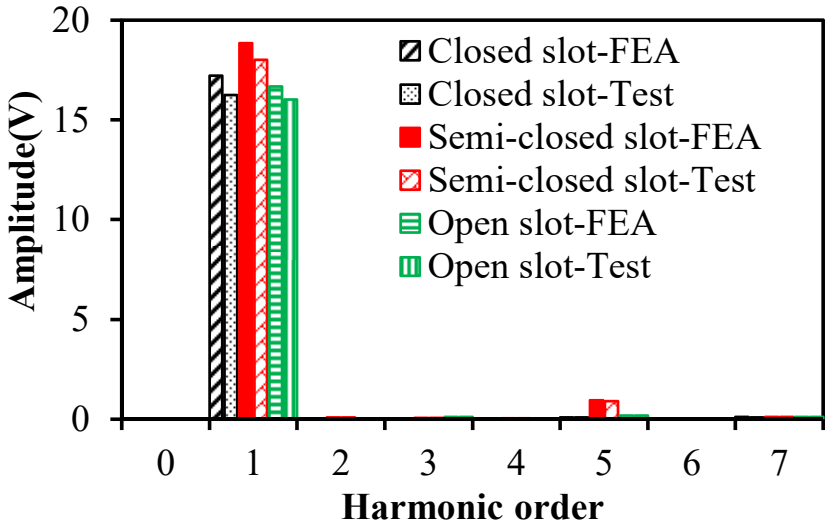

(d) Spectra.

Fig. 2.15 Comparison of measured and predicted back EMF waveforms and spectra.

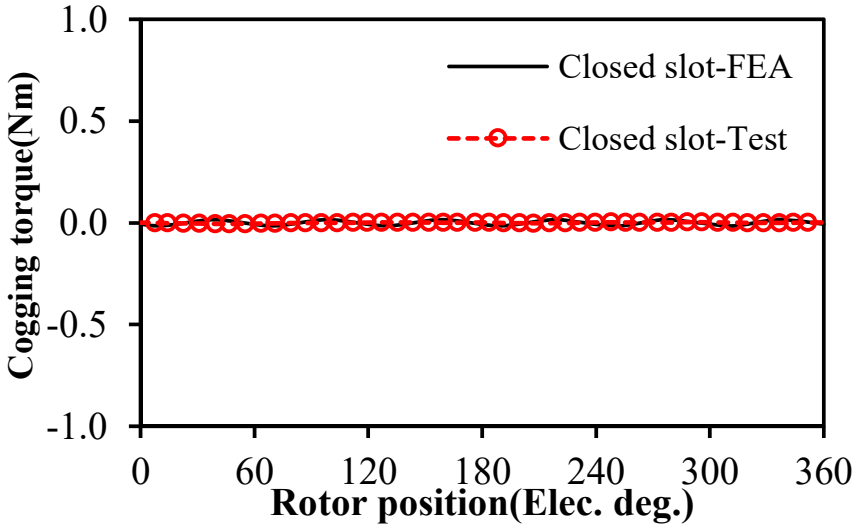

(a) Closed-slot stator.

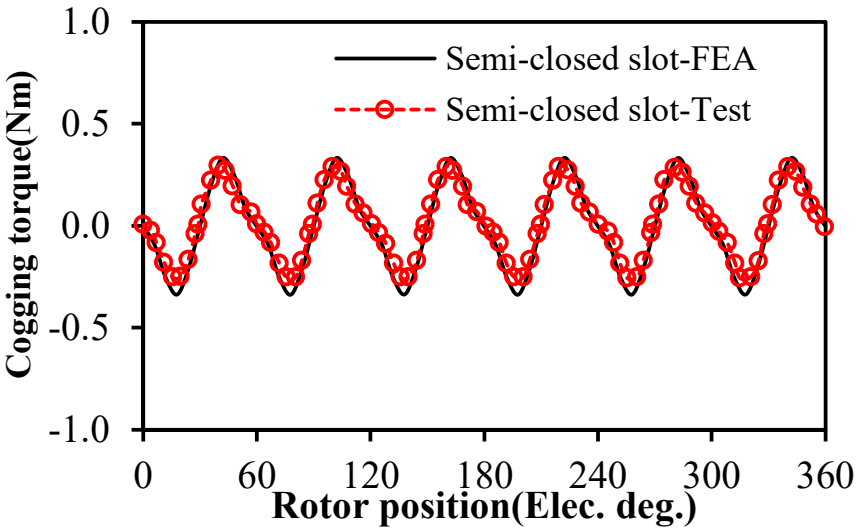

(b) Semi-closed slot stator.

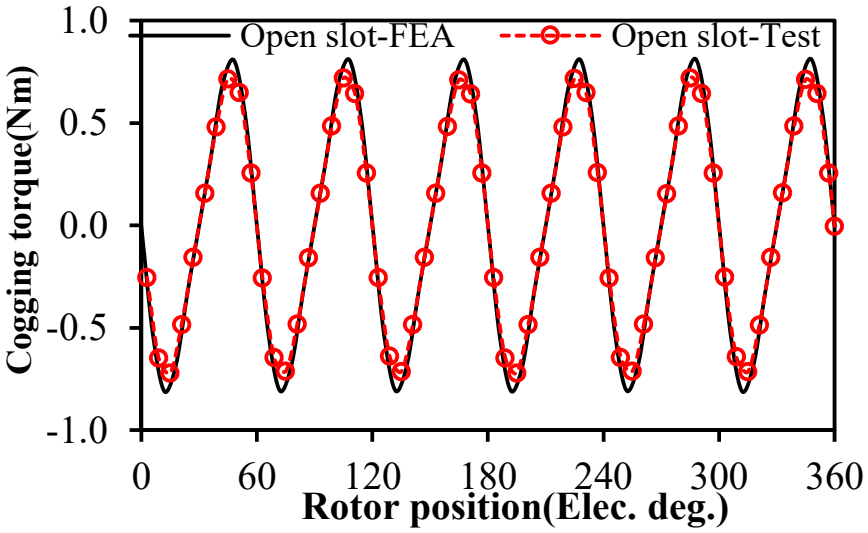

(c) Open-slot stator.

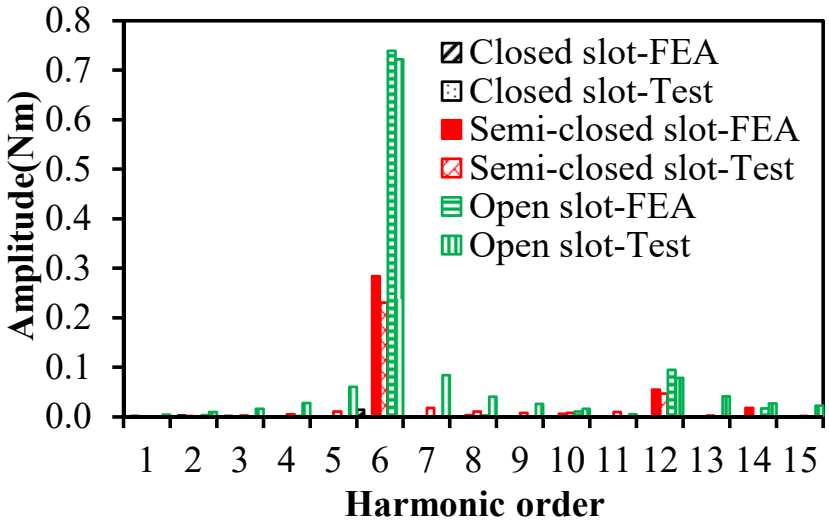

(d) Spectra.

Fig. 2.16 Comparison of measured and predicted cogging torque waveforms and spectra.

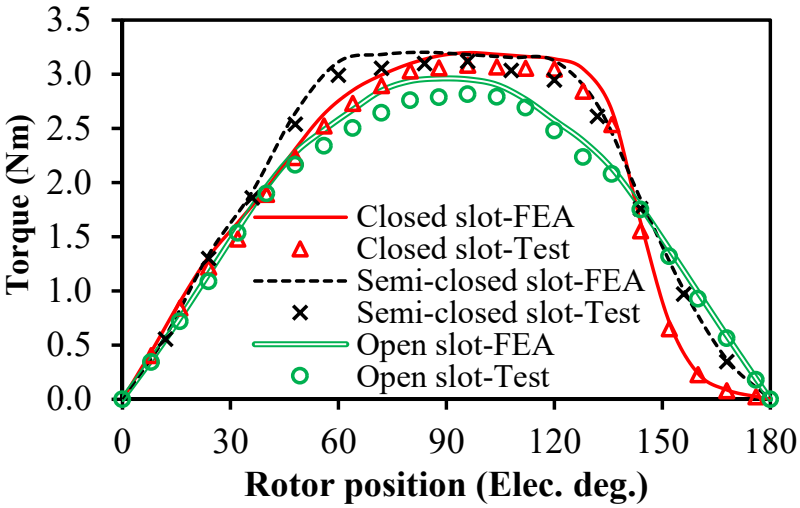

Fig. 2.17 Comparison of measured and predicted torque waveforms. (I_a=5A, I_b=I_c=-2.5A)

2.7 Summary

In this chapter, the torque production mechanism of FSCW PMSMs is investigated from a new perspective, i.e. airgap field modulation and magnetic gearing effect. It is found that the torque production in FSCW PMSMs is based on both conventional PMSM principle and magnetic gearing effects. The respective contributions of the conventional PMSM and the magnetic gearing effect to the total torque are quantified by introducing a FEA-based ECSM and harmonic restoration method. The expression of the gear ratio in FSCW PMSMs is derived. The results show that the contribution of the magnetic gearing effect is non-ignorable, and the larger the slot opening, the higher the magnetic gearing effect. The influence of the slot opening on cogging torque and torque ripple is also investigated by FEA and validated by experiments.

CHAPTER 3

Influence of Gear Ratio on the Performance of Fractional Slot Concentrated Winding Permanent Magnet Machines

Fractional slot concentrated winding (FSCW) permanent magnet synchronous machines (PMSMs) have been a research hotspot over the past few decades. In Chapter 2, the magnetic gearing effect in FSCW PMSMs is revealed along with its gear ratio which is a function of slot/pole number combination. At the design stage of FSCW PMSMs, one of the key issues is the selection of the slot/pole number combination. This chapter shows that the gear ratio can contribute to a proper slot/pole number selection in any multi-phase FSCW PMSMs by acting as a unified index for a quick overall performance comparison. Firstly, the magnetic gearing effect in FSCW PMSMs is explained and the gear ratio is further discussed. The advantages of adopting gear ratio as the overall performance index over other indices are revealed. The influence of the gear ratio on the winding factor, torque output, cogging torque, inductance and rotor losses of 3- and 6-phase FSCW PMSMs are analysed and validated by experiments, thus proving the analyses.

3.1 Introduction

Permanent magnet synchronous machines (PMSMs) with fractional slot concentrated windings (FSCW) have been gaining popularity with academics and industries in the past few years due to their compact size, high torque and power density [LEV08] [ELF10].

At the initial design stage of FSCW PMSMs, one of the key issues is to make a rapid performance comparison to select the most promising slot/pole combinations since it significantly affects the machine's performance [FOR13]. In [MAG03], [CRO02] and [LIB04], the winding factors for FSCW PMSMs with several slot/pole combinations, as well as the influence of slot/pole combination on cogging torque, are clearly given. In [PON14] and [NI14], it is found that the slot/pole combination has an impact on the mutual and air-gap leakage inductances, which are related to the fault tolerant [BAR11] and flux weakening performance [REF05], respectively. In [BIA09] and [FOR12], the influence of the number of slots per pole per phase (q) and number of phases on the rotor losses are investigated. The unbalanced magnetic force in FSCW PMSMs is investigated and some suggestions are made on the choice of the slot/pole number [JUS07] [ZHU13]. The influence of the slot/pole

combination on the radial force and vibration mode was shown in [VAL14b]. The influence of q on the irreversible demagnetisation risk was shown in [PET17].

Although the performance indicators for different slot/pole number combinations have been provided in some of the previous papers, they focus more on how precisely the indicators can predict the relevant performance metrics. It is inconvenient to make a rapid overall performance comparison among FSCW PMSMs because different performance metrics use different indicators. Therefore, when slot/pole number changes, a unified performance index for all the performance metrics is desirable for sake of rapid comparison. To achieve this, slot per pole per phase (q) is adopted. The adoption of q makes the discontinuous slot/pole number be a continuous function. If the relationship between q and various machine performance metrics was established, people would be able to make a rapid comparison for slot/pole number selection by just comparing q. However, only [BIA09] shows the relationship between q and the iron loss index even though it contributes to a rapid comparison. Moreover, one problem for adopting q is that it is also a function of the number of phases: q changes when the number of phase changes. Since multi-phase FSCW PMSMs have also been a hotspot in industry and academia, using q as the index for comparison could bring about inconvenience when different phase numbers are considered. Up to now, there is no paper providing an index which does not change with phase number and can be used for a quick overall performance comparison.

In Chapter 2, the magnetic gearing effect /modulation effect in FSCW PMSMs was revealed. The parameter used to represent the gearing effect in FSCW PMSMs is defined as the gear ratio, which is a function of the slot and pole numbers. In this chapter, the influence of gear ratio on different machine performance metrics will be investigated for machines with different slot/pole number combinations and particularly different phases. It shows that gear ratio can contribute to a proper slot/pole number selection in any multi-phase FSCW PMSMs by acting as a unified index for a quick overall performance comparison.

This chapter is organized as follows: The magnetic gearing effect in FSCW PMSMs is explained and gear ratio is further discussed in section II. It is found that the gear ratio is not only a representation of the gearing effect but also an inherent parameter of the FSCW PMSMs regardless of the phase number. Hence, it is more convenient than other performance indicators in that it can be a unified index for all the performance metrics and it does not change with the phase number. Then, the influence of the gear ratio on the winding factor, back EMF, torque output, cogging torque, inductances and rotor losses of 3- and 6-phase FSCW PMSMs are demonstrated. In section IV, prototypes are built and tested, thus

proving the claims.

3.2 Magnetic Gearing Effect and Gear Ratio in FSCW PMSMs

In this section, the magnetic gearing effect in FSCW PMSMs is briefly explained based on Chapter 2 and the gear ratio is further discussed.

3.2.1 Magnetic Gearing Effect in FSCW PMSMs

For a N_s-slot/2p_r-pole FSCW PMSM, where N_s is the slot number and p_r is the pole pair number, due to the winding distribution, the p_rth and $|p_r\text{-}N_s|$th armature reaction MMF harmonics always exist in pairs. If $p_r > |p_r\text{-}N_s|$, the $|p_r\text{-}N_s|$th harmonic is called the sub-harmonic; $p_r < |p_r\text{-}N_s|$, the $|p_r\text{-}N_s|$th harmonic is called the super-harmonic. In FSCW PMSMs, the $|p_r\text{-}N_s|$th harmonic has a comparable amplitude with the fundamental armature reaction harmonic and larger than any other armature reaction harmonics. From Chapter 2, useful torque can be generated under the following circumstances.

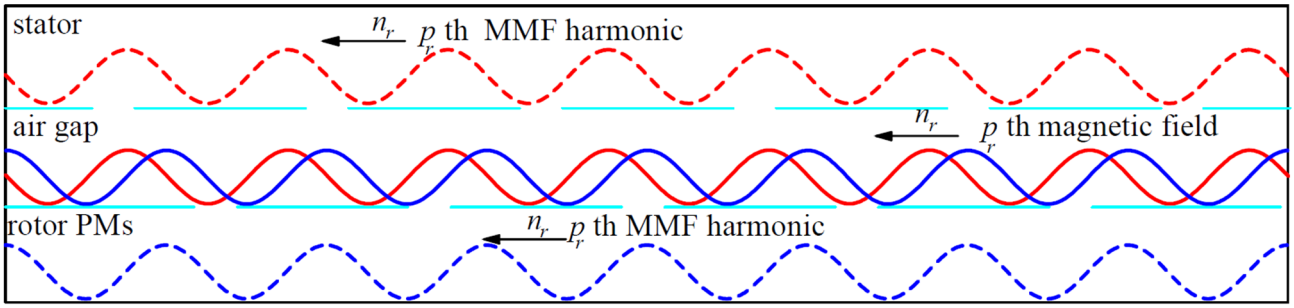

(a) Principle of conventional PM machine torque production.

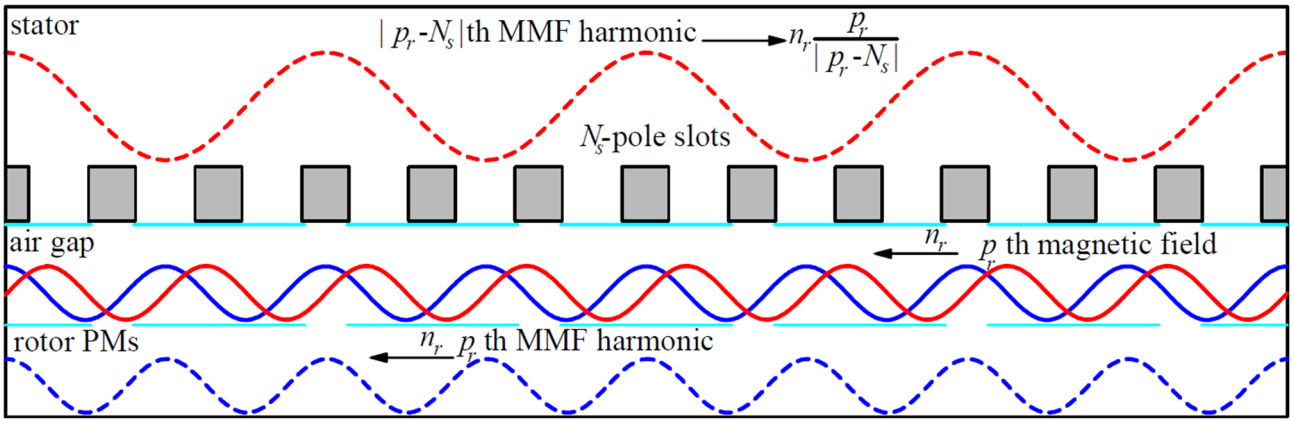

(b) Principle of magnetic gearing effect.

Fig. 3.1 Illustration of torque production mechanisms in FSCW PMSMs.

(a) the p_rth PM fundamental and original p_rth armature reaction MMF harmonic share the same order and speed of rotation n_r, they can interact with each other and produce useful torque. Here "original" means that the harmonic is not modulated by the stator slots. In this case, the torque is produced by the principle of the conventional PMSM as shown in Fig. 3.1 (a).

(b) the $|p_r\text{-}N_s|$th armature reaction harmonic has different order and speed of rotation with the p_rth PM fundamental harmonic. However, it can be modulated by the N_s-pole stator teeth, which results in the space field harmonic with the order of p_r and the speed of n_r. The modulated harmonic can interact with the p_rth PM harmonic to produce a steady torque as shown in Fig. 3.1 (b). This phenomenon is called magnetic gearing effect and it has been proven in Chapter 2 that the contribution of the magnetic gearing effect to the total torque is non-ignorable, and the larger the slot opening, the higher the magnetic gearing effect.

3.2.2 Gear Ratio in FSCW PMSMs

In a magnetic gear, the change of speed between high and low speed rotors is called the gear ratio [ATA04]. For FSCW PMSMs, the magnetic gearing effect exists between the p_rth PM and $|p_r\text{-}N_s|$th armature reaction MMF harmonics. From Fig. 3.1 (b) and Chapter 2, the gear ratio in FSCW PMSMs can be defined as the ratio of their speeds:

$$G_r = -\frac{|p_r - N_s|}{p_r} = \frac{p_r - N_s}{p_r} \tag{3.1}$$

The denominator of G_r is the order of the fundamental harmonic and the nominator is the order of the harmonic which makes the main contribution to the torque via magnetic gearing effect. As mentioned above, these two harmonics are critical harmonics in FSCW PMSMs since they always exist in pairs, have larger amplitude than any other harmonics and are highly involved in the torque production, flux weakening operation and losses generation. Their behaviour has decisive influence on the related machine performance, and therefore, G_r, as a function of their orders can not only reflect the magnetic gearing effect in FSCW PMSM but also be used as an index for the performance comparison between FSCW PMSMs with different slot/pole number combinations. The variation of the performance can be shown directly with respect to G_r. It is noteworthy that G_rs in FSCW PMSMs always have negative values because the p_rth and $|p_r\text{-}N_s|$th MMF harmonics always rotate in opposite direction.

3.3 Alternate Slot/Pole Number Combinations and Global Optimisation

Several FSCW PMSM models with different slot/pole combinations were built to investigate the influence of gear ratio on the machine performance. For sake of simplicity, of all the feasible slot/pole combinations and phase numbers, only 12- and 24-slot machines with 3- and 6- phase designs are considered. The conclusion drawn from 3- and 6-phase machines can also be applied to other multi-phase machines, which is proven in Appendix A. For the 12- and 24-slot machines, the feasible pole numbers and the corresponding gear ratios for both 3- and 6-phase machines are given in Table 3.1. Although there are many feasible slot/pole combinations, the present investigation is limited to those have G_r ranging from -0.5 to -2. Designs with G_r falling out of this range are proven to have inferior performance such as low torque and power density, and therefore were eliminated from consideration.

To make a fair comparison, all the machine candidates are globally optimised. The optimisation is carried out based on Maxwell software using genetic algorithm to achieve the maximum torque under the following constrains: (1) Fixed stator outer radius r_o=50mm; (2) Fixed air-gap length l_a=1mm; (3) Fixed stack length l_{ef}=50mm; (4) Fixed shaft radius=10mm; (5) Fixed copper loss at 75W considering the end winding. It should be noted that copper loss is the main loss and source of heating for the machine of this size at low speed. 75W is selected within a reasonable copper loss range for the machine of this size. Therefore, all the machine candidates are optimised under the same thermal loading; (6) Fixed slot packing factor; (7) Fixed overall PM volume, the PM used in the simulation has remanence of 1.2T with the relative permeability of 1.05. The related dimensional parameters are illustrated in Fig. 3.2. During the optimisation, the stator yoke radius r_y, stator tooth width w_t, stator inner radius r_i, slot opening angle s_o and the PM height l_{pm} are variables. The optimised machine parameters are provided in Table 3.2, in which N_{tpc} stands for number of turns per coil. The q-axis currents at 75W copper loss for all the machine candidates are also listed in Table 3.2.

Table 3.1 Gear Ratios in FSCW PM Electrical Machines

(a) 12-slot

$2p_r$	8	10	14	16
3-phase	-2.00	-1.40	-0.71	-0.50
6-phase	-	-1.40	-0.71	-

(b) 24-slot

$2p_r$	16	20	22	26	28	32
3-phase	-2.00	-1.40	-1.18	-0.85	-0.71	-0.50
6-phase	-	-1.40	-1.18	-0.85	-0.71	-

Table 3.2. Optimised Dimensional Parameters.

Phase no.	N_s	$2p_r$	r_y (mm)	w_t (mm)	s_o (Mech. deg.)	r_i (mm)	l_{pm} (mm)	I_q (A)	N_{tpc}
3	12	8	46.3	7.2	4.8	28.6	3	7.78	46
		10	46.6	6.6	3.7	29.5	2.9	7.95	
		14	47.3	5.4	10.4	31.0	2.7	8.21	
		16	47.7	4.6	12.7	33.1	2.5	8.08	
6	12	10	46.7	6.6	3.8	29.6	2.9	7.95	46
		14	47.5	5.4	10.5	31.1	2.7	8.21	
3	24	16	47.8	4.0	3.1	32.3	2.6	8.00	23
		20	48.0	3.8	3.4	33.4	2.5	7.95	
		22	48.1	3.5	3.8	33.8	2.5	8.02	
		26	48.4	3.1	3.6	34.3	2.4	8.27	
		28	48.5	2.9	3.3	34.7	2.4	8.29	
		32	48.8	2.4	3.4	35.4	2.4	8.44	
6	24	20	48.1	3.8	3.3	33.4	2.5	7.95	23
		22	48.2	3.5	3.7	33.8	2.5	8.02	
		26	48.5	3.1	3.5	34.3	2.4	8.27	
		28	48.6	2.9	3.2	34.7	2.4	8.29	

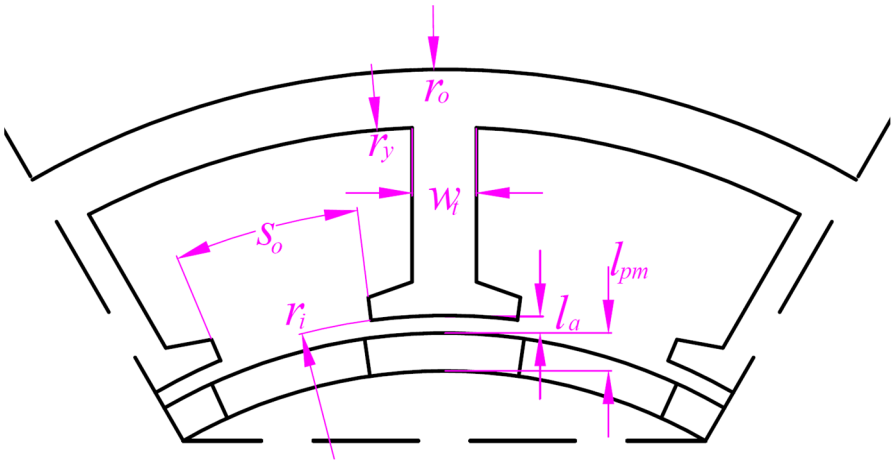

Fig. 3.2 Dimensional parameters.

3.4 Influence of Gear Ratio on Single and Multi-3-Phase Machine Performance

In this section, the gear ratio is compared with other machine performance indicators. The relationship between the gear ratio and winding factor, back EMF, output torque, cogging torque, inductance and rotor losses will be analysed in 3- and 6-phase FSCW PMSMs with double-layer windings. After the clarification of the relationships, the gear ratio can be used for performance comparison at the machine design stage.

3.4.1 Comparison of Gear Ratio and Slot Number per Pole per Phase

There are various aspects of machine performance needed to be considered at the design stage. Regarding the relationship between the slot/pole combination and different motor performance metrics, a number of researches have been reviewed in the introduction. However, different performance metrics use different indicators which increases the calculation and makes a rapid overall performance comparison and proper slot/pole number selection impossible. To have a more generalized and direct insight into the relationship between the slot/pole combination and the machine performance, slot per pole per phase (q) is usually used. Compared with slot/pole combination which is discontinuous, q has a continuous value. By using q, a direct and continuous relationship between machine performance and slot/pole combination can be established. Comparison can be made by just comparing q.

In this chapter, the gear ratio, which is also a function of slot/pole combination is used instead of q to carry out the machine performance comparison. Compared with q, G_r can also establish a direct and continuous relationship between various machine performance metrics and slot/pole combination,

apart from this, the major advantage of using G_r is that it shows directly the harmonic behaviour in the FSCW PMSMs regardless of the phase number. It can eliminate the influence of the phase number and provide a unified reference value for performance comparison for machines with any phase number. For example, for winding factor comparison which is shown in Fig. 3.3 (a) and (b), if G_r is used as the index, for both 3- and 6- phase machines, the reference value is -1: the closer gear ratio to -1, the higher winding factor it will be. However, if q is used, the reference value varies with the phase number, which is 1/6 for the 6-phase and 1/3 for the 3-phase machine. Table 3.3 provides a comparison of reference values when q and G_r are used as the performance index respectively, where m is the phase number. It shows that if q is used as the index, different reference values should be calculated and used for performance comparison for different phase numbers. In comparison, G_r is more convenient for performance comparisons not only because it reduces redundant performance indicator calculations but also provides fixed reference of -1 when the phase number changes. Moreover, a reference value should be easy to compare with. It is easier to compare a fraction with -1 than with $1/m$. More importantly, G_r is not only the index for winding factor comparison, it also applies to other performance metrics such as back EMF, torque, cogging torque and inductance as will be seen in the sections below. Its advantage over q also applies to the aforementioned performance metrics: for all the performance comparisons and all phase numbers, the reference value is unified as -1 instead of a varying $1/m$.

Table 3.3 Comparison of Reference Value between q and Gr

Index	q	G_r
Reference value	$1/m$	-1

3.4.2 Influence of Gear Ratio on Winding Factor

In FSCW PMSMs, the fundamental winding factor is one of the important metrics that directly influences the machine's torque density. It is therefore important to check the fundamental winding factor k_w at the machine design stage. The fundamental winding factors of FSCW PMSMs can be calculated using the back EMF phasors [LIB04].

The winding factors for the 3 and 6-phase machines with different G_rs are provided in Fig. 3.3. Since the machines with 3-slot/2-pole(G_r=-2) and 4-pole(G_r=-0.5) sub-motors have the lowest fundamental winding factor of 0.866 among double-layer FSCW PM machines [CRO02], the fundamental winding factor is above 0.866 when G_r is between -0.5 and -2 for a double-layer FSCW PM machine. For both

3- and 6-phase machines, the winding factor approaches to 1 when G_r approaches -1, and the winding factor decreases monotonically when G_r is either less than or greater than -1. This can be explained from (3.1), since G_r approaches to -1 means that the pole number is closer to the slot number, which then leads to a higher winding factor in FSCW PMSMs. The machines with the same G_r, same phase number but different slot number have the same winding factor. For the machines with the same G_r but different phase number, the ones with higher number of phases have higher winding factors.

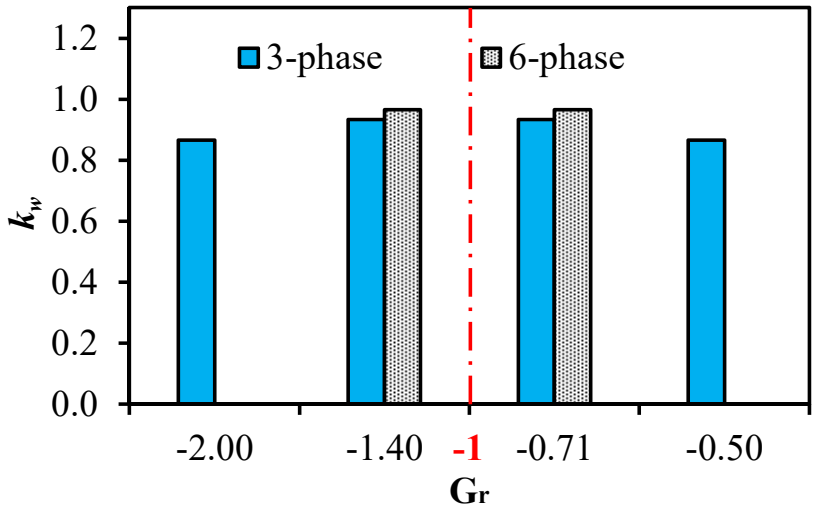

(a) 12-slot.

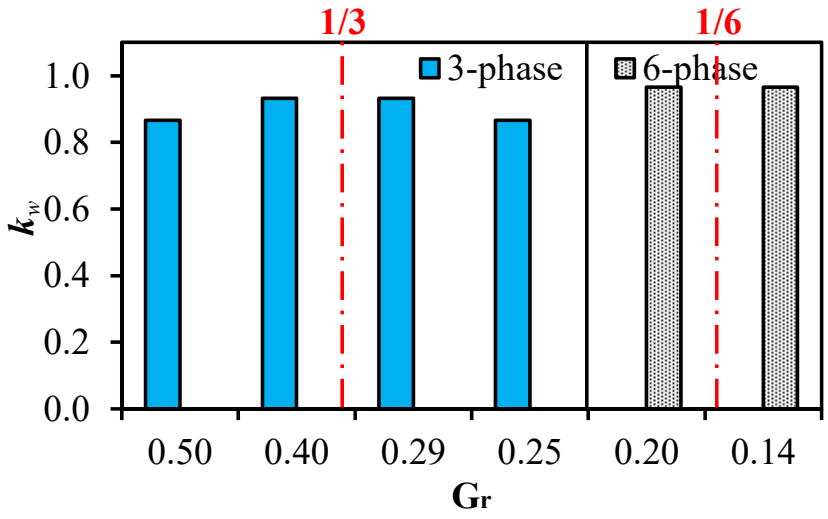

(b) Comparison between G_r and q as reference.

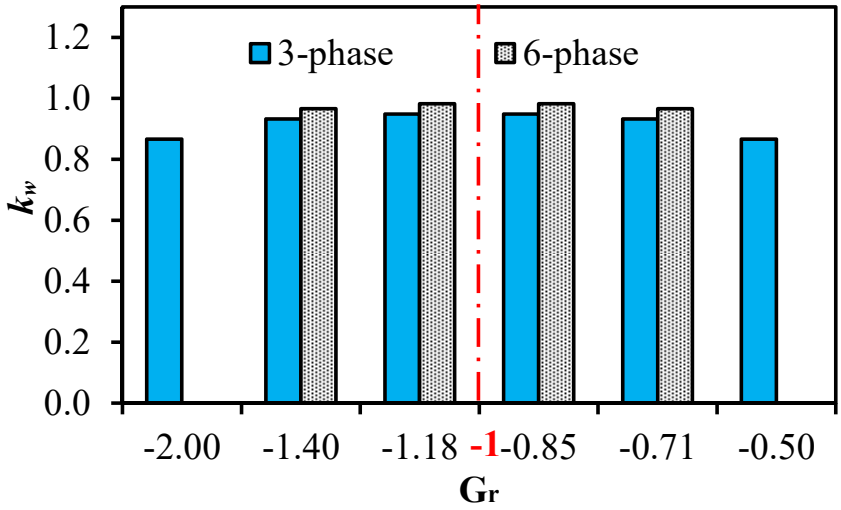

(c) 24-slot.

Fig. 3.3 Winding factors for different machines.

3.4.3 Influence of Gear Ratio on Back-EMF

For FSCWs with surface mounted PMs, the back EMF is an important torque indicator since it contributes to the electromagnetic torque from the energy conversion. From Chapter 1, the fundamental component of the back EMF can be expressed as

$$\begin{aligned} E_1 &= \frac{\pi N_p r_g l_{ef} n_r k_w}{15\sigma_0}\left(B'_{\mathrm{PM1}} + \frac{B_{\mathrm{PMh}}}{p_s / p_r}\right) \\ &= \frac{\pi N_p r_g l_{ef} n_r k_w}{15\sigma_0}\left(B'_{\mathrm{PM1}} + \frac{B_{\mathrm{PMh}}}{|G_r|}\right) \end{aligned} \tag{3.2}$$

For a fair comparison, the fundamental back EMF/turn of the machine candidate under 100rpm is calculated by FEA and shown in Fig. 3.4. It can be seen that the fundamental back EMF/turn increases when G_r approaches to -1, which is the same with the variation of winding factor. Hence, within a certain phase number, a larger back EMF/turn is more likely to be obtained when the gear ratio approaches -1. It can also be seen that the 12-slot machine with G_r equals -0.71 has only slightly larger back EMF/turn than that with G_r equals -0.5. This is because that although the 12-slot machine with G_r equals -0.71 has a larger winding factor, it has smaller back-EMF contributed by modulation effect as a result of larger $|G_r|$, shown in (3.2). Hence, although this trend is still applicable, it should be used for a general comparison to exclude the machine candidates with potentially smaller back EMF and to select a range of promising machine candidates of different slot/pole number combinations at the initial

design stage. Fig. 3.4 also shows that under the same G_r and slot number, the 6-phase machine has a larger back EMF/turn than the 3-phase machine's. This is because the 6-phase machine candidate has larger winding factor as shown in Fig. 3.3. This indicates that for the machines with the same slot number and G_r but different phase number, the ones with higher number of phases will have higher torque under the same electrical loading as will be shown in the next sub-section.

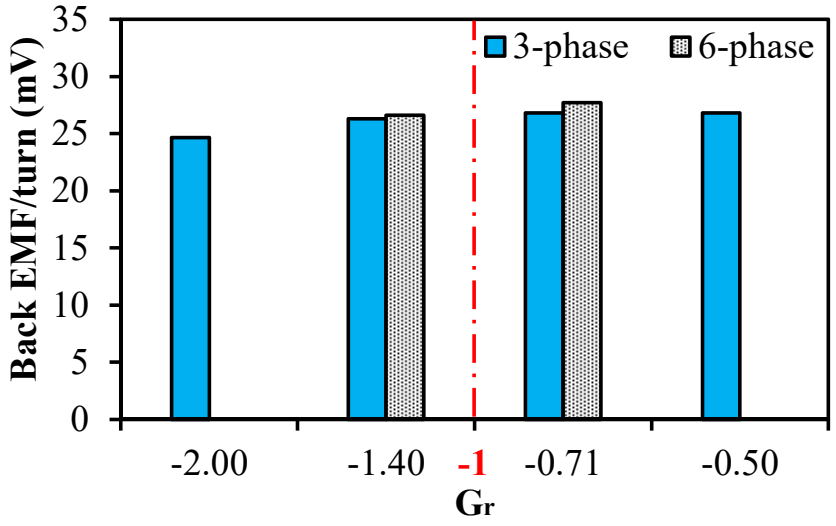

(a) 12-slot.

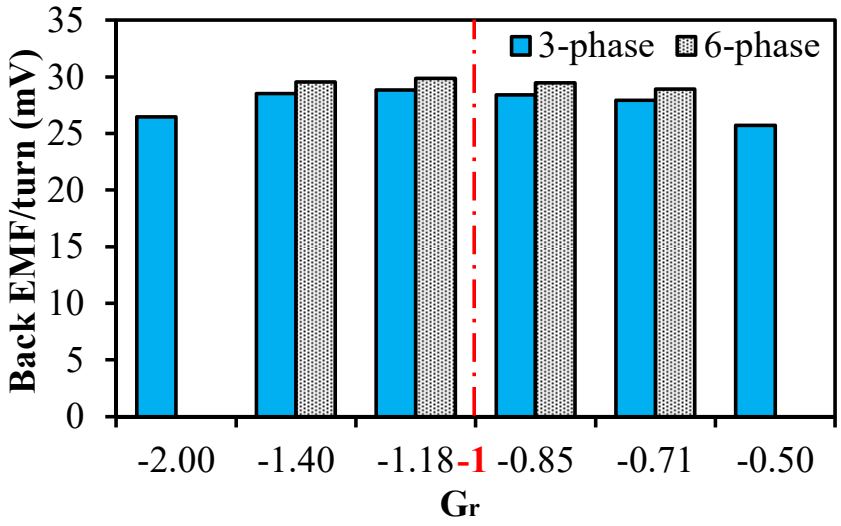

(b) 24-slot.

Fig. 3.4. Fundamental back EMFs for different machines.

3.4.4 Influence of Gear Ratio on Torque Output

The average electromagnetic torque of a FSCW surface mounted PM machine fed with sinusoidal

currents under I_d=0 control is given by

$$T_0 = \frac{15m}{\pi n_r} E_1 I_q \tag{3.3}$$

where n_r is the mechanical speed of the rotor, m is the number of phases and I_q is the amplitude of the phase current.

The output torque of the machine candidates under 75W copper loss are calculated by FEA and shown in Fig. 3.5. It can be seen that the torque variation trend with the gear ratio is almost the same with the back EMF. This is because the amplitude of the fundamental back EMF is proportional to the electromagnetic torque once the current is fixed, as shown in (3.3). Hence, within a certain phase number, a larger torque output can be obtained when the gear ratio approaches -1. As Fig. 3.5 (a) shows that the 12-slot machine with G_r equals -0.71 has similar torque with that having G_r equals -0.5, it also needs to be mentioned that this rule should be used for a general comparison to exclude the machine candidates with potentially smaller torque and to select a range of promising machine candidates of different slot/pole number combinations for more detailed comparison. Fig. 3.5 also shows that for the machines with the same slot number and G_r but different phase number, the ones with higher number of phases will have higher torque, which is consistent with the analysis in the last sub-section.

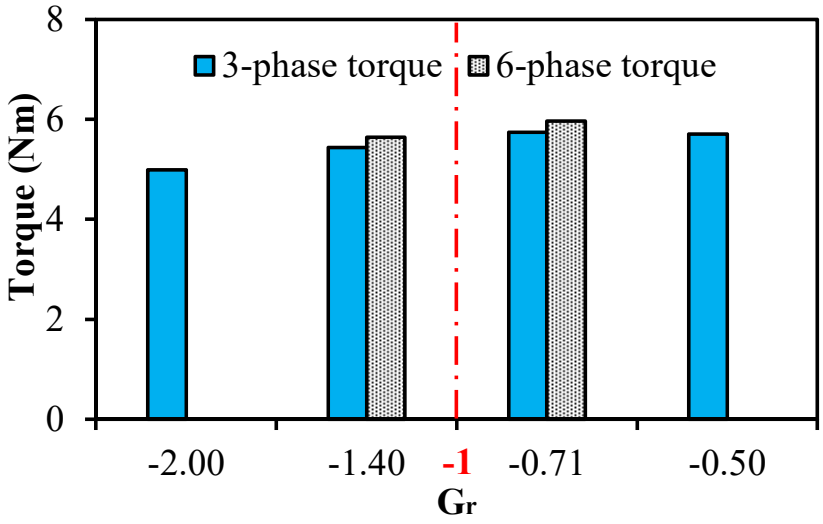

(a) 12-slot.

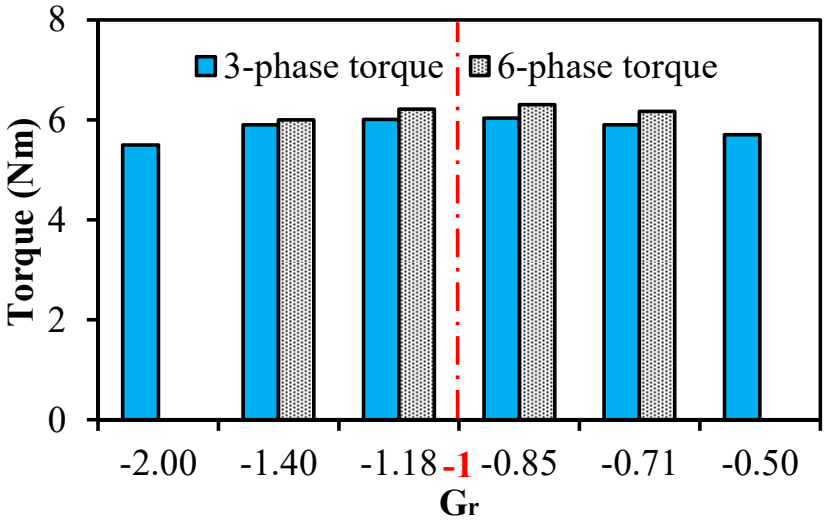

(b) 24-slot.

Fig. 3.5. Torque for different machines.

3.4.5 Influence of Gear Ratio on Cogging Torque

In the slotted FSCW PMSMs, cogging torque is produced by the interaction between the PM MMF and the air-gap permeance. Cogging torque can cause speed ripples and induces vibration at low load and speed. There has been intensive research on the reduction of cogging torque. Although there are many methods to reduce the cogging torque, such as rotor skewing, employing auxiliary slots, magnet shaping, etc., they require a more complicated structure, thus making them more difficult to manufacture and assemble. Therefore, it is important to select a proper slot/pole combination with inherent low cogging torque at the design stage. In [ZHU00], "goodness" of slot/pole combination, which is defined as

$$C_T = \frac{2p_r N_s}{N_c} \tag{3.4}$$

is used as an index in evaluating the cogging torque amplitude, where N_c is the least common multiple of the $2p_r$ and N_s. It has been analytically proven in [ZHU09a] that for a given slot number, the smaller the "goodness" is, the smaller the cogging torque will be. It should also be noted that C_T can also be used to show the vibration mode of the machine.

The relationship between C_T and G_r for different machines are provided in Fig. 3.6. It can be seen that for the FSCW PMSMs in this chapter, C_T has a decreasing trend when Gr approaches -1. It should be noted that this trend is only applicable to the FSCW PMSMs with sub-motors whose G_rs are within -

2~-0.5 and slot/pole number combinations satisfy $N_s=2p_r\pm1$(or 2). For other slot/pole number combinations, G_r can still be used for C_T comparison among machines with the same slot but different pole numbers if it is represented as a fraction. As shown in Fig. 3.6, for gear ratios less than -1, C_T increases as the denominator decreases; while, for gear ratios greater than -1, C_T increases as the numerator decreases. For any given slot number, the machines with G_r equal to -2 or -0.5 have greater cogging torque than the others. For the machines with the same G_r but different slot number, a higher number of slot means a higher C_T, lower cogging torque and larger vibration mode.

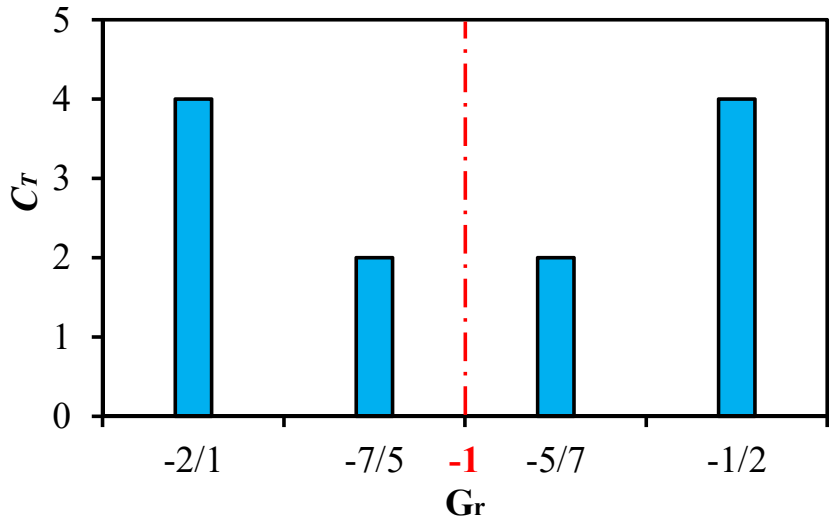

(a) 12-slot.

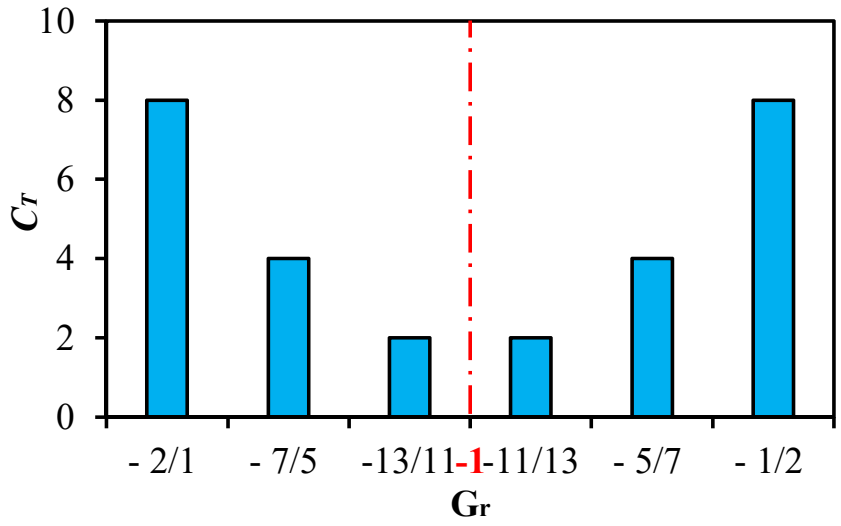

(b) 24-slot.

Fig. 3.6. "Goodness" for different machines.

3.4.6 Influence of Gear Ratio on Inductance

It has been proven that FSCW machines with surface mounted PMs can achieve good flux weakening performance. The reason for this can be found by considering the characteristic current [12], defined as

$$I_{ch} = \frac{\psi_{PM}}{L_d} \tag{3.5}$$

where ψ_{PM} is the flux linkage provided by the PMs and L_d is the d-axis inductance, which is almost equal to the q-axis inductance in electrical machines with surface-mounted PMs.

Since the phase inductance of surface-mounted electrical machines increases when concentrated fractional-slot stator windings are introduced, thus reducing the machine's characteristic current sufficiently to match its rated current. The FSCW machines with surface-mounted PMs have a better flux-weakening performance than the integral slot distributed winding surface-mounted PMSMs.

The d-axis inductances of the different machines are calculated by FEA. The relationships between G_r and L_d for the 12- and 24-slot machines of different phases are provided in Fig. 3.7. It shows that for both 3- and 6-phase machines, L_d becomes larger when G_r approaches -1, and L_d decreases monotonically when G_r is either less than or greater than -1. The reason is that there are two types of armature reaction flux in one phase of FSCW PMSMs [LIU15]. Type 1 flux links $2N$ turns of windings, whereas Type 2 flux links N turns of windings as shown in Fig. 3.7 (c). For FSCW PMSMs, when the PM pole number approaches the slot number, the proportion of Type 1 flux increases while Type 2 flux decreases, which indicates that L_d will increase. For the machines with the same G_r but different phase number, the ones with higher number of phases have smaller L_d. This is because with the increase of the number, the number of turns per phase decreases.

Another important application for FSCW PMSMs is as fault tolerant machines. The magnetic coupling between the phases should be as weak as possible so that the healthy phases can work properly when the other phases are under faulty condition. This addresses the importance of the mutual inductance between phases, which acts as an index for evaluating the magnetic coupling between phases. A small mutual inductance can even provide an opportunity to build modular segmented stators with physically separate phase coil sections [LIB04].

The absolute values of mutual inductance $|L_m|$ of the different machines are calculated by FEA. The

relationships between G_r and $|L_m|$ for the 12-slot and 24-slot machines are given in Fig. 3.7. It can be seen that $|L_m|$ decreases when G_r approaches to -1, and $|L_m|$ increases monotonically when G_r is either less than or greater than -1. The reason for this is that for FSCW PMSMs, when the PM pole number approaches the slot number, the armature reaction flux becomes more concentrated in one phase whereas the flux linking two phases reduces, thus indicating a decrease in $|L_m|$.

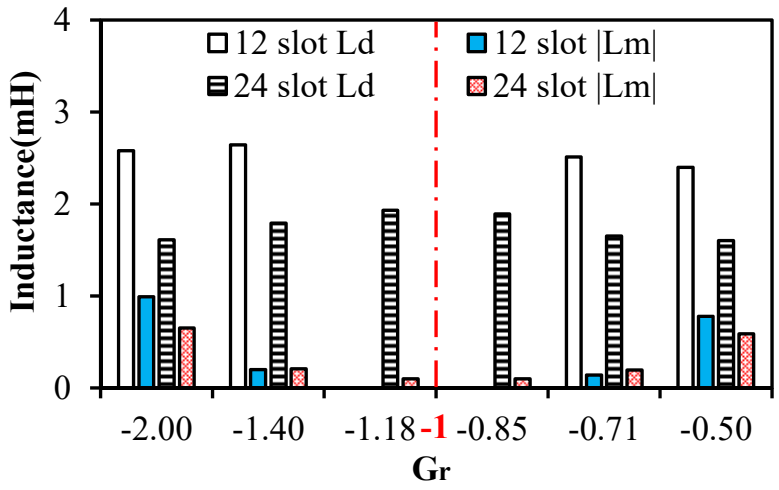

(a) 3-phase.

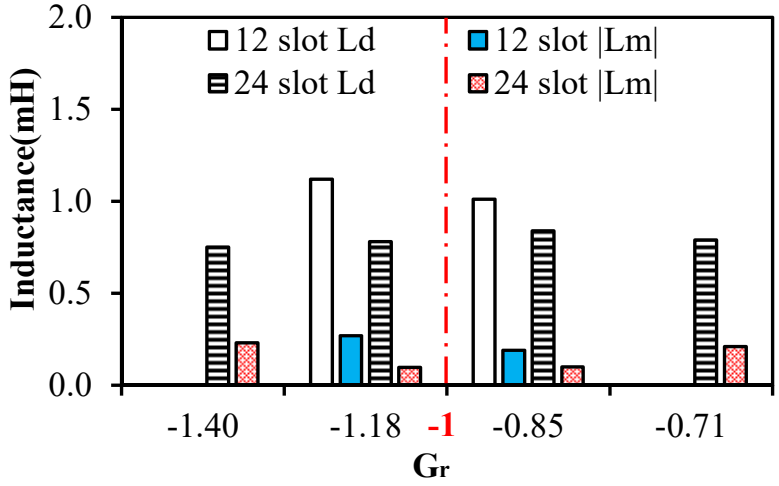

(b) 6-phase.

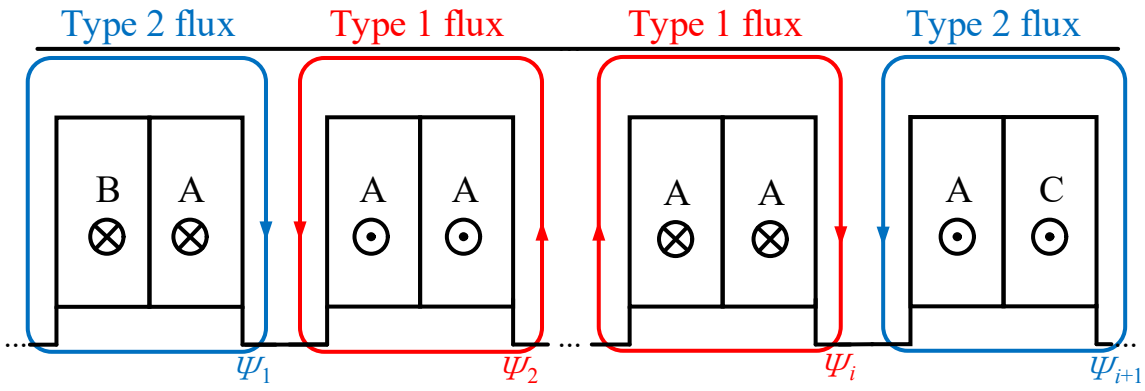

(c) Illustration of Type 1 and 2 flux [LIU15].

Fig. 3.7. D-axis and mutual inductances for different machines.

3.4.7 Influence of Gear Ratio on PM Losses

For FSCW PMSMs, there are a large amount of harmonics in the air gap due to the winding distribution and slotting effect. In surface mounted PMSMs, the PMs are exposed to the air-gap harmonics directly. Hence, the PM eddy current losses cannot be neglected because the asynchronous harmonics can induce a large amount of eddy current in the PMs. This results in joule loss in the magnets, particularly in NdFeB magnets due to their relatively high electric conductivity. The PM losses can heat up the magnets and cause irreversible demagnetisation of the PMs.

Eddy-current losses in the rotor surface PMs are caused by two kinds of harmonics: slotting permeance harmonics and armature reaction harmonics. The losses caused by slotting harmonics depend mainly on the structure of the teeth, which is generally less important when the slot opening is not large. In this chapter, the PM losses is mainly caused by armature reaction harmonics.

As stated in Section II, for an N_s-slot/2p_r-pole FSCW PMSM, apart from the fundamental p_rth harmonic, the major armature reaction harmonic which contributes to the torque production via magnetic gearing effect is the $|p_r$-$N_s|$th harmonic. It has a comparable amplitude with the fundamental armature reaction harmonic and is larger than any other armature reaction harmonics. Therefore, it can make a great contribution to the rotor PM losses. For a FSCW PMSM with a certain number of slots, electrical loading and phases, with the increase of G_r, the order of the $|p_r$-$N_s|$th harmonic decreases whereas its amplitude increases, as shown in Fig. 3.8 (a). When the machine is rotating at the speed of $n_r$rpm, the frequency of the current induced by the $|p_r$-$N_s|$th harmonic at the rotor side will be

$$f = n_r N_s \tag{3.6}$$

Generally, an index of the rotor losses can be used to evaluate the PM losses in FSCW PMSMs of different slot/pole combinations at the design stage [BIA09]:

$$I_{rl} = \sum_{v} \frac{\xi^4}{\sqrt[4]{(\xi^4 + \pi^4)^3}} \left(\frac{k_{wv}}{k_w} \right)^2 \frac{v}{p_r} k_{gap} \tag{3.7}$$

where ξ is the specific wavelength, k_{wv} is the winding factor of the harmonic of order v and k_{gap} is the air-gap coefficient.

The indices of PM losses in the 3- and 6 phase, 12- and 24-slot machines rotating at 100rpm under 75W copper loss are calculated and given in Fig. 3.8. FEM is also used to calculate PM losses in the different machines for validation. The result shows that for both phase numbers, the PM eddy current loss caused by armature reaction harmonics increases with the increase of G_r for a given slot number. This is because under the same slot number, the frequency of the induced current for all feasible pole numbers is the same when the speed of rotation is fixed as shown in (3.6). Thus, the eddy current only depends on the amplitude of the $|p_r\text{-}N_s|$th harmonic which increases with the increase of G_r as shown in Fig. 3.8 (a).

3.4.8 Influence of Gear Ratio on Rotor Core Losses

In FSCW PMSMs, the rotor iron losses may also make a significant contribution to the total losses. It is particularly important when the rotor thermal condition is considered. The rotor iron losses in one element can be calculated by the Bertotti losses equation, which is given by

$$P(t) = k_f \left\{ k_h B_m^2 f + \sigma \frac{d^2}{12} \int_T \left(\frac{\mathrm{d}B}{\mathrm{d}t}(t) \right)^2 \frac{1}{T} + k_e \int_T \left(\frac{\mathrm{d}B}{\mathrm{d}t}(t) \right)^{1.5} \frac{1}{T} \right\} \tag{3.8}$$

where d is the depth of the steel lamination, k_f is the lamination factor, B is the value of flux density on the rotor core, B_m is its maximum value, σ is the conductivity of the rotor core, f is the fundamental frequency of the variation of B in the element, T is the electrical period, k_h and k_e are the hysteresis and excess loss coefficients respectively. The three parts at the right side of the equation represent hysteresis losses, classical eddy current losses and excess losses respectively.

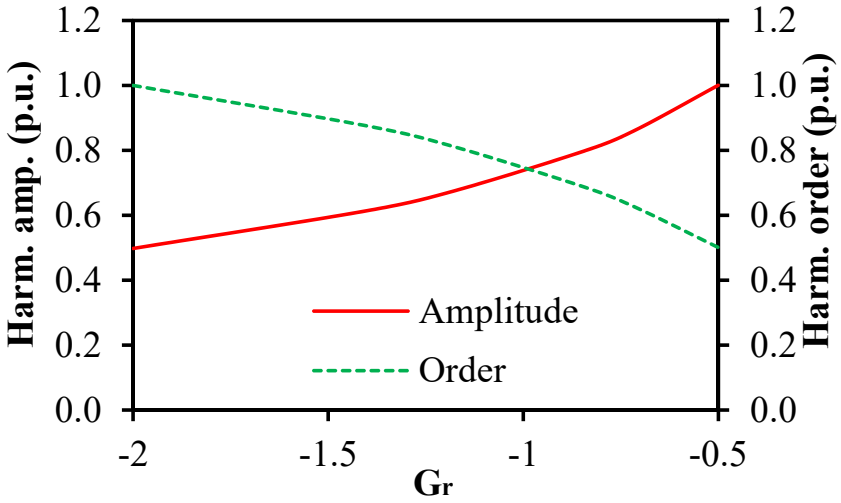

(a) Variation of the major harmonic.

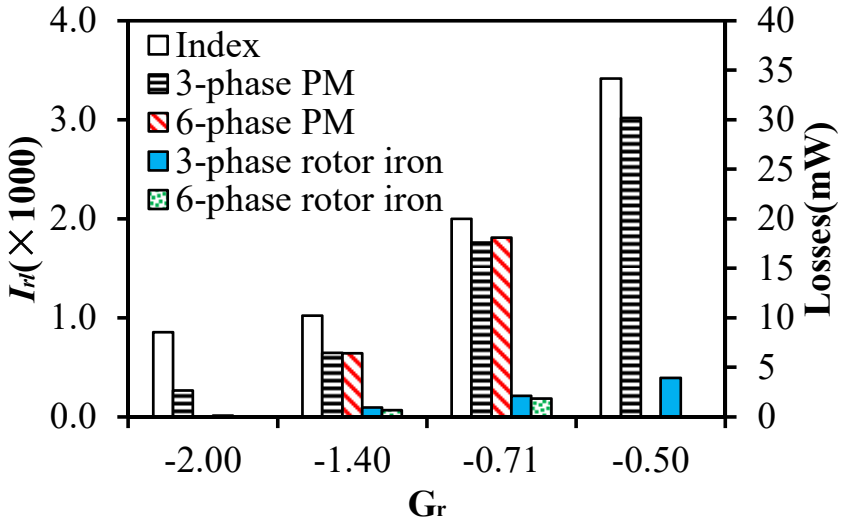

(b) 12-slot.

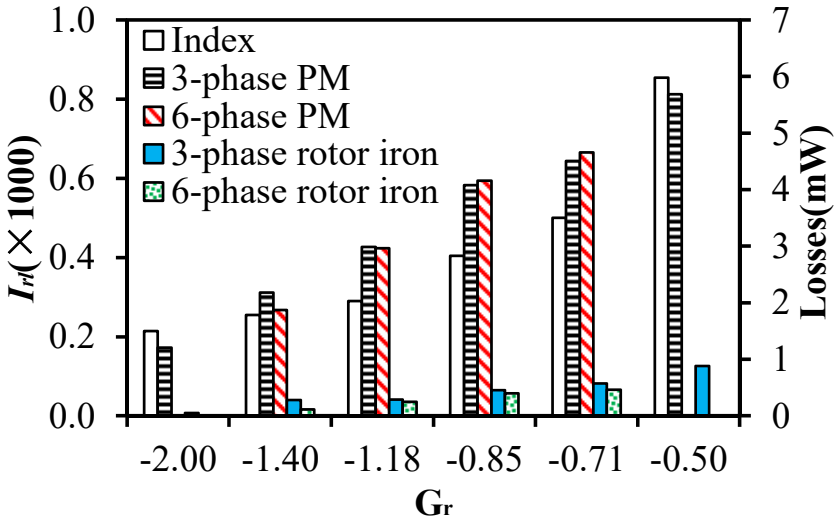

(c) 24-slot.

Fig. 3.8. PM losses index, PM and rotor iron losses (75W copper loss, 100rpm).

The rotor iron losses in different machines of different phases were calculated by FEM under the same copper loss of 75W, as shown in Fig. 3.8. It can be seen that the rotor iron loss increases with the increase of G_r for both 3- and 6-phase machines under fixed slot numbers. This can be explained by the same reason with the PM loss. Since the $|p_r\text{-}N_s|$th armature reaction harmonic still plays an important role in the rotor iron loss. Under the same slot number, the frequency of flux density variation on the rotor core for all feasible pole numbers is the same when the speed of rotation is fixed as shown in (3.6). Thus, the rotor iron loss will highly depend on the amplitude of the $|p_r\text{-}N_s|$th harmonic which increases with the increase of G_r.

3.5 Experimental Validation

In this section, 12-slot/8-pole and 12-slot/10-pole FSCW PMSMs are built and their performances are tested to validate the analysis in the above sections, Fig. 3.9. The main dimensional parameters of the prototypes are given in Table 3.4, except that the pole arc of the 8-pole PM is optimised as 155 electrical degrees. For the machine performance analysed above, the correctness of the winding factor and "goodness" can be validated by [LIB04] and [ZHU00]. The correctness of the influence of G_r on the rotor losses has also been validated by the index I_{rl} proposed in [BIA09] and the FEA validation. Hence, only the back EMF, torque output and inductance, which were only calculated by FEA, need to be validated by experiments.

Table 3.4. Dimensional Parameters

Parameters	Values
Stator outer diameter	100mm
Stator inner diameter	57mm
Rotor outer diameter	55mm
Turns per phase	184
PM thickness	3mm
PM pole arc	180°
Axial length	50mm

First, the back EMF waveforms of the prototypes are measured. Fig. 3.11 (a)-(c) show the back EMF waveforms of the 3-phase 12-slot/8-pole, 3-phase 12-slot/10-pole and dual 3-phase 12-slot/10-pole machine prototypes. Fig. 3.11 (d) shows the comparison of their spectra. It can be seen that good agreements between FEA and test results are obtained. The FEA results are slightly higher than those of measurements mainly due to end effect.

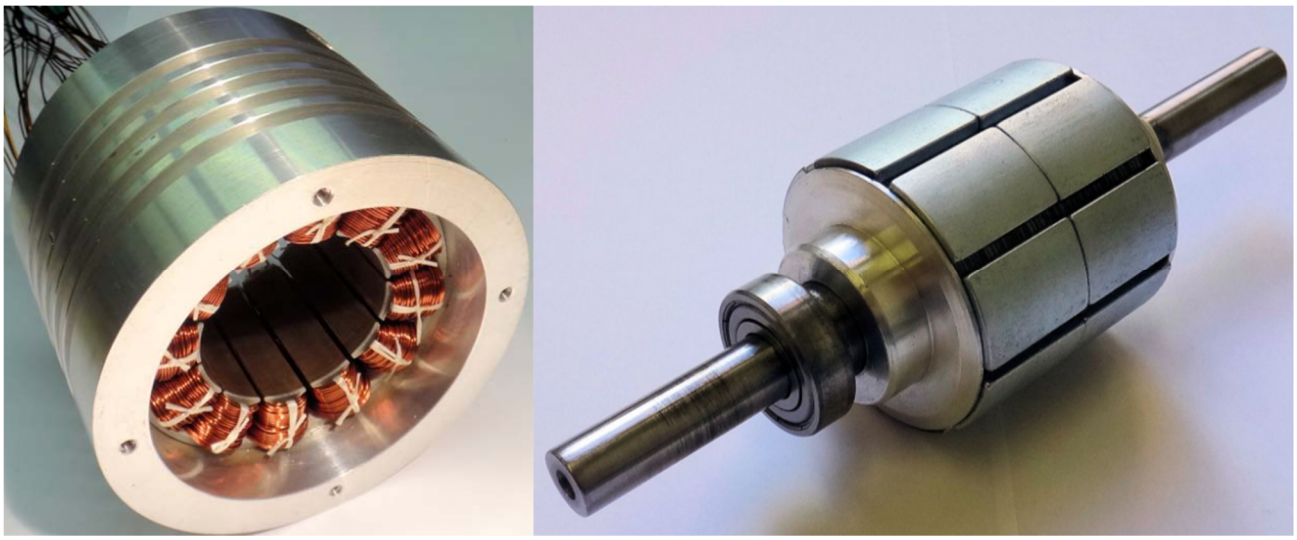

(a) 12-slot/8-pole.

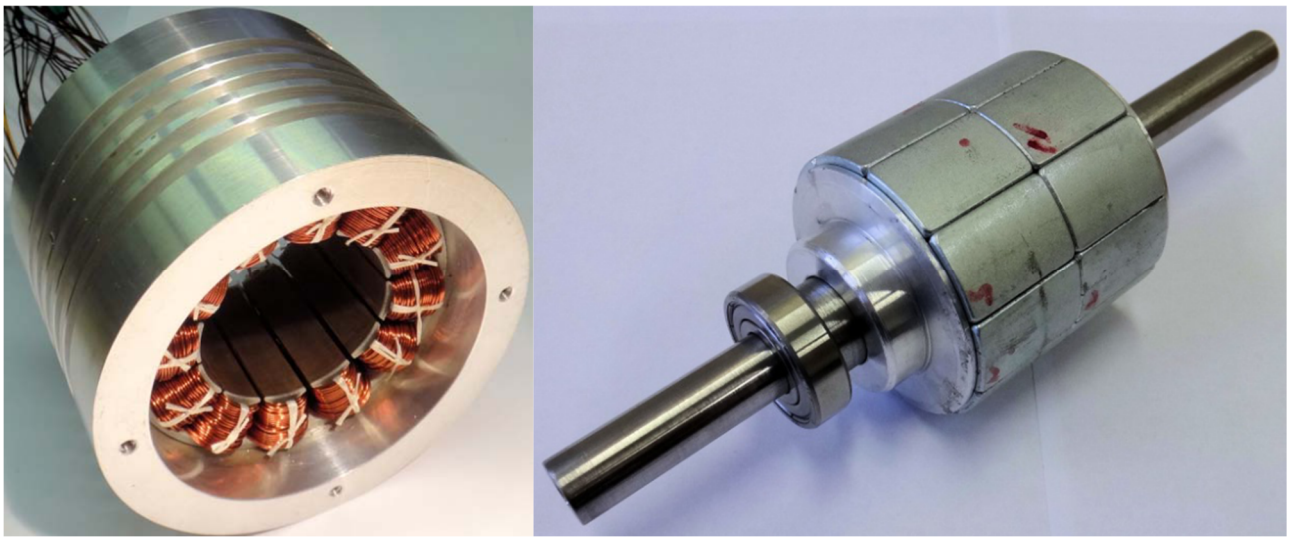

(b) 10-pole-12slot.

Fig. 3.9. Photos of prototypes.

Then, static torques of the prototypes are measured. The test rig is shown in Fig. 3.10. For the 3-phase 12-slot/8-pole and 12-slot/10-pole machines, the experiments are done by applying DC current to phase A in series connection to the parallel phase B and phase C, i.e. $-2I_b=-2I_c=I_a=5$A. For the 6-phase 12-slot/10-pole machine, the experiment is done by applying one DC current to phase A in series connection to the parallel phase B and phase C, i.e. $-2I_b=-2I_c=I_a=5$A and another DC current to phase D in series connection to phase F, i.e. $-I_f=I_d=4.33$A, $I_e=0$A. The static torques within 0-180 electric degrees of the prototype machines can subsequently be measured by rotating the stator housings in 180 electric degrees with fixed steps [ZHU09c]. The measured results are given and compared with the 2-D FEA results in Fig. 3.11. Although the FEA predicted torques are slightly higher than the measured results, good agreements are obtained. The experimental results show that the output torque of the 12-slot/8-pole machine is smaller than that of the 12-slot/10-pole machine. The 6-phase 12-slot/10-pole machine has larger output torque than the 3-phase one. Hence, the analyses in the above section have been proven by the experiment.

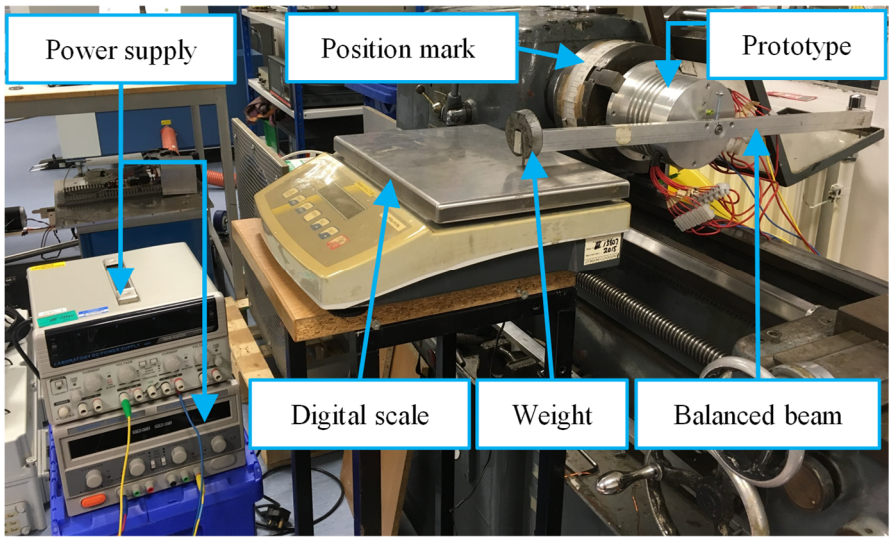

Fig. 3.10. Photo of the test rig.

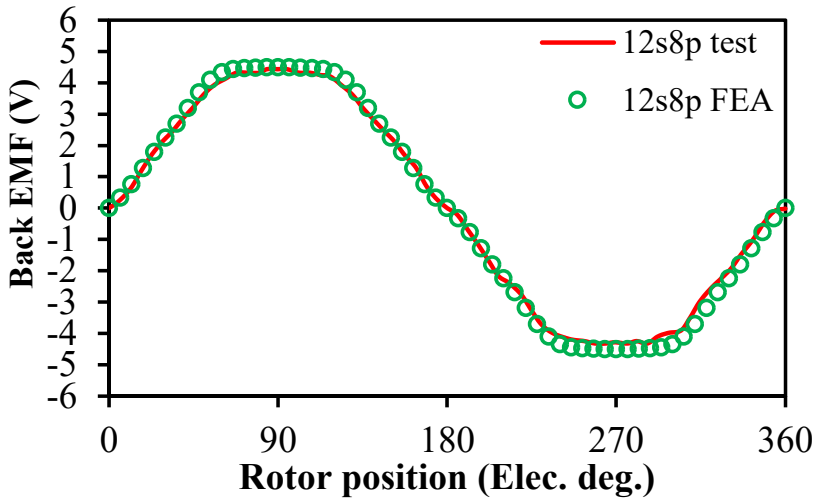

(a) Back EMF of 12-slot/8-pole machine @100rpm.

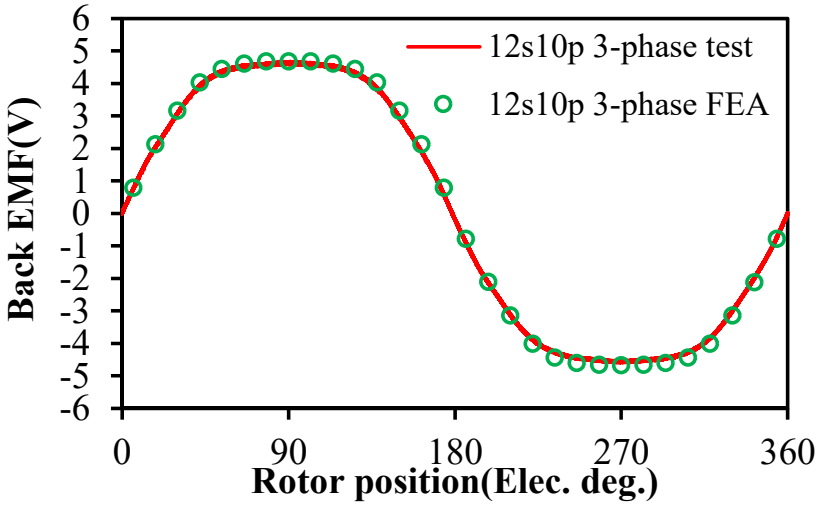

(b) Back EMF of 3-phase 12-slot/10-pole machine @100rpm.

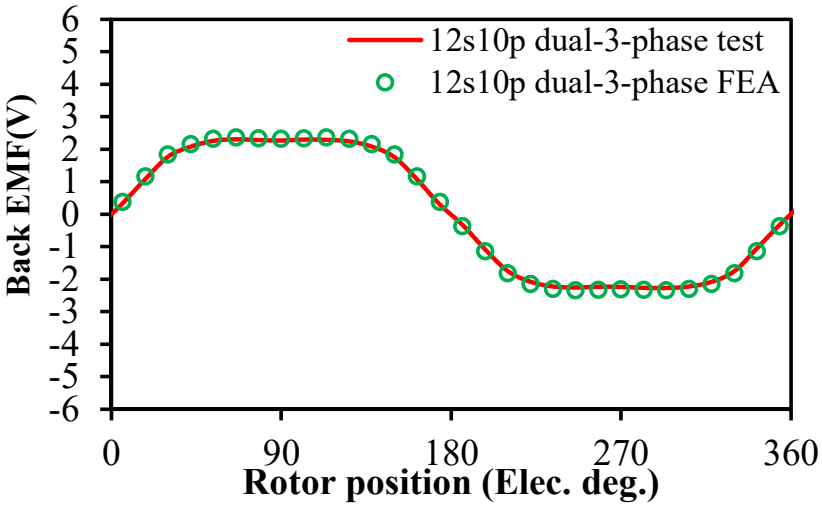

(c) Back EMF of dual 3-phase 12-slot/10-pole machine @100rpm.

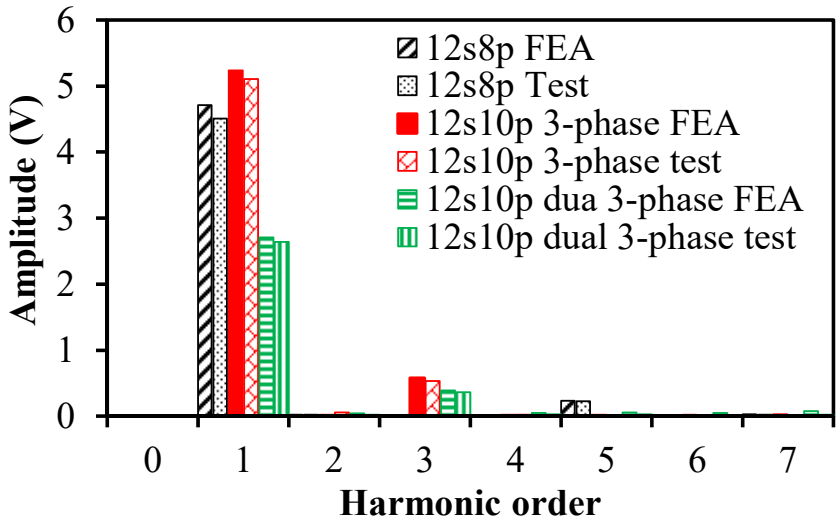

(d) Back EMF spectra.

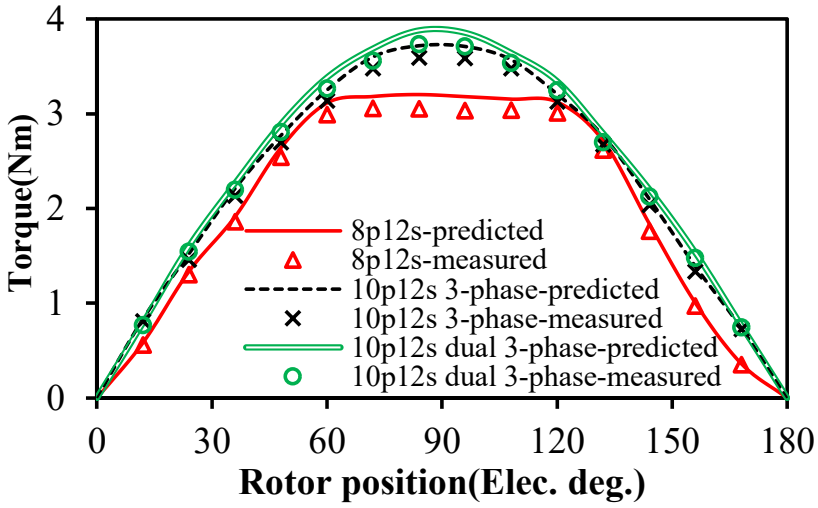

(e) Static torque waveforms (I=5A).

Fig. 3.11. Comparison of FEA and test results.

The d-axis and mutual inductances of the two 3-phase prototypes are tested by a LCR meter in the following way [LIU15]:

Step 1: During the experiment, the winding inductance of A-phase is tested by the LCR meter, when the inductance of A-phase achieves its minimum value L_{Ad}, the d-axis coincides with the axis of A-phase.

Step 2: Lock the rotor position, test the B-phase inductance L'_{Bd} and the line inductance between A-phase and B-phase L_{ABd}.

Step 3: The d-axis and mutual inductance L_d and L_m can be calculated by (3.9) and (3.10), respectively.

$$L_d = \frac{L_{ABd} + L_{Ad} - L'_{Bd}}{2} \tag{3.9}$$

$$L_m = \frac{L_{ABd} - L_{Ad} - L'_{Bd}}{2} \tag{3.10}$$

The d-axis and mutual inductances of the 6-phase prototype are tested by a LCR meter in the following way:

Step 1: During the experiment, the winding inductance of A-phase is tested by the LCR meter, when the inductance of A-phase achieves its minimum value L_{Ad}, the d-axis coincides with the axis of A-phase.

Step 2: Lock the rotor position, test the D-phase inductance $L^{`}_{Dd}$

Step 3: Connect phase A and D in series, test the line inductance between A-phase and D-phase L_{ADd}.

Step 4: The mutual and d-axis inductance L_d and L_m can be calculated by (3.11) and (3.12), respectively.

$$L_m = \frac{\left|L_{ADd} - L_{Ad} - L'_{Dd}\right|}{2} \tag{3.11}$$

$$L_d = L_{Ad} + \sqrt{3}L_m \tag{3.12}$$

The experimental measured and FEA results are given in Table 3.5. It can be seen that the FEA results match well with the experimental results. The measured results also show that L_d of the 12-slot/8-pole machine is smaller than that of the 12-slot/10-pole machine, whereas $|L_m|$ of the 12-slot/8-pole machine is larger than that of the 12-slot/10-pole machine, the 6-phase 12-slot/10-pole machine has smaller L_d and $|L_m|$ than the 3-phase one, which validates the analyses in the above section.

Table 3.5. Inductance of the Prototypes

Slot/pole combination		8p12s	10p12s	
			3-phase	6-phase
L_d(mH)	FEA	3.61	4.36	2.24
	Measured	3.81	4.33	2.33
$\|L_m\|$(mH)	FEA	1.17	0.41	0.38
	Measured	1.16	0.40	0.35

3.6 Summary

In this chapter, the magnetic gearing effect and the gear ratio in FSCW PMSMs are introduced and employed to investigate its relationship with the various machine performance of FSCW machines with different phases and slot/pole number combinations. It is found that the gear ratio is not only a representation of the gearing effect, but, once the slot and pole numbers are fixed, also an inherent parameter of the FSCW PMSMs regardless of the phase number. Hence, it can provide a unified reference for FSCW PMSMs of different phase numbers to evaluate the performance and select the proper correct slot/pole combination at the machine design stage. For a given slot number, the following conclusions can be drawn for FSCW PMSMs of all phases: under the same slot number, (a) when the gear ratio approaches -1, the winding factor and d-axis inductance increase whereas the mutual inductance and vibration mode decrease monotonically; (b) the FSCW PM machine will have larger torque output and smaller cogging torque with the gear ratio close to -1; and (c) the rotor losses, including the PM eddy current losses and the rotor iron losses, increase with the increase of the gear ratio. In this way, gear ratio can contribute to a proper slot/pole number selection in any multi-phase FSCW PMSMs by acting as a unified index for a quick overall performance comparison. This chapter can also provide a good in-depth understanding of FSCW machines.

CHAPTER 4

Analysis of Magnetic Gearing Effect in Vernier Permanent Magnet Synchronous Machines

As a promising candidate for direct drive application, Vernier permanent magnet synchronous machines (VPMSMs) feature high torque density due to magnetic gearing effect. This chapter reveals the nature of magnetic gearing effect in VPMSMs in depth. Firstly, the general torque production mechanism of Vernier permanent magnet synchronous machines with surface mounted PMs are analysed. It reveals that the VPMSM with surface mounted PMs is a mono-harmonic torque production machine. Then, an FEA-based equivalent current sheet model (ECSM) and harmonic restoration method is applied to a 12-slot/22-pole VPMSM to study the behaviour of each air-gap harmonic under the modulation effect and to quantify the contribution of magnetic gearing effect to the torque for the first time. The influence of slot opening on the magnetic gearing effect and torque production in VPMSMs is also quantified. Based on the analysis, the expressions of gear ratios for different topologies are provided. Finally, a prototype is manufactured and tested to validate the FEA results.

4.1 Introduction

Low-speed permanent magnet (PM) machines have increasingly gained attention in direct-drive applications such as wind energy generation, vehicle traction propulsion, and domestic appliances [JIA11]. One of the most promising candidates is the Vernier PM synchronous machine (VPMSM), known as:

$$p_r = N_f - p_s \tag{4.1}$$

where p_r is the number of PM pole-pairs in the rotor, N_f is the number of flux modulation poles (FMPs) in the stator and p_s is the armature winding pole pairs in the stator.

It is shown that the VPMSM has higher torque density than the conventional PM machines [FU10] [YAN13] and the magnetically-geared machines [LI11]. The high torque density of a VPMSM is due to magnetic gearing effect [TOB00] [QU11]. In [JIA11], [LI11] and [ONE16], the air-gap field distribution in VPMSMs is calculated by analytical method. In [TOB00] and [KIM14], some design

principles for maximizing the torque output are provided, while in [LI16], it is verified that torque smoothness is the inherent characteristic of VPM machines. Apart from the aforementioned references, more research activities focus on the machine topology such as structure optimisation [GER15] [ZOU17], employing flux enhancing structure [JAN14] [LI15] [CHU11] [LI14a], double stator [LI14a] [LI14b], double rotor [NIU10] and stator wound [JIA15] etc. Apart from radial flux VPMSM, a linear VPMSM is also proposed [ZHA16a]

Although there are extensive research activities on VPMSMs, the torque production mechanism in terms of magnetic gearing effect is not fully explained. The aim of this chapter is to reveal the role of magnetic gearing effect plays in the torque production of VPMSMs. It is well known that the torque production of the VPMSM is based on magnetic gearing/modulation effect [TOB00] [QU11]. However, the contribution of the torque produced by gearing effect in VPMSMs has not be quantified before. In this chapter, an FEA-based equivalent current sheet model (ECSM) will be used together with a harmonic restoration method to analyse a VPMSM, by which the contribution of magnetic gearing effect in the torque production can be quantified. Moreover, FEA-based ECSM will also be used to investigate the influence of the slot opening on the air-gap magnetic field modulation and torque production, through which the guidelines of taking advantage of magnetic gearing effect in VPMSMs design can be derived.

This chapter is organized as follows: In section 4.2, the torque production mechanism of VPMSMs is analysed. The order of the working harmonic is identified and validated by FEA on a 12-slot/22-pole VPMSM. In section 4.3, the FEA-based equivalent current sheet model (ECSM) is used together with a harmonic restoration method for the 12-slot/22-pole VPMSM to study the behaviour of harmonics under the modulation effect. The quantitative contribution of gearing effect to the total torque is identified. The influence of the slot opening on the magnetic gearing effect in VPMSMs is also quantified. Based on the analysis, the magnetic gearing effect in VPMSMs is further explained and the expressions of gear ratios for different topologies are provided in this chapter. Finally, a 12-slot/22-pole VPMSM prototype is manufactured and tested to validate the FEA results.

4.2 Modulated Magnetic Field and Torque Production

In this section, the PM and armature reaction air-gap magnetic fields of VPMSMs will be derived in a general way using a simple magnetomotive force (MMF)-permeance model. Their interaction and torque production mechanism will be provided.

To obtain an analytical model for the air-gap flux density, the discussion in this section is based on the following assumptions:

1) The permeance of the steel lamination is infinite and saturation is not considered. The aim of this section is focused on the modulating effect of the stator slots and FMPs, viz., the modulated harmonic orders and speed of rotation but not on the actual amplitudes of the field harmonics. Hence, the tangential component of the air-gap magnetic field is also neglected. However, in the next section, the amplitudes of both the radial and tangential field harmonics will be considered in a FEA-based equivalent current sheet model and the torque components will be further investigated.

2) The relative permeability of permanent magnets is equal to that of the air.

3) The leakage flux and end effect are ignored for simplicity.

4.2.1 PM Air-Gap Flux Density

For a VPMSM with surface mounted PMs, the MMF generated by the PMs are shown in Fig. 4.1, and its Fourier series $F_r(\theta,t)$ is provided by (4.2).

$$F_r(\theta,t) = \sum_{i=1,3,5...}^{\infty} F_{ri} \cos p_r i(\Omega_r t - \theta) \tag{4.2}$$

where Ω_r is the rotor mechanical rotating velocity, i is a positive odd integer, F_{ri} is the amplitude of the ith order harmonic and θ is the air-gap circumferential position.

From the perspective of stator geometry, there are two kinds of VPMSMs, VPMSMs with stator FMPs and VPMSMs without stator FMPs. For VPMSMs without stator FMPs, the stator tooth plays the role of FMPs. Without loss of generality, Fig. 4.2 shows a VPMSM stator with both tooth and FMPs. The influence of stator tooth and FMPs can be accounted for by introducing a permeance function shown in Fig. 4.2, in which θ_f is half-arc of a flux modulation slot and θ_s is half-arc of the stator teeth.

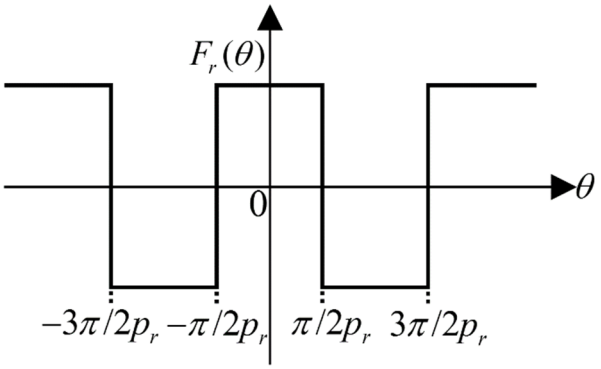

Fig. 4.1. MMF distribution generated by the PMs in FSCW machines.

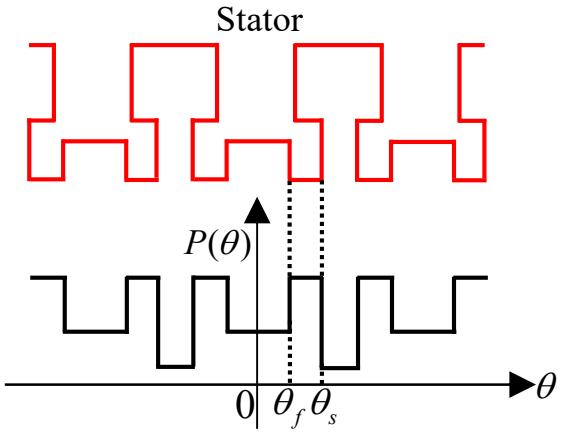

Fig. 4.2. Air-gap permeance function accounting for slotting effect.

For an N_s-slot/N_f-FMP stator, the air-gap permeance function contains the components introduced by both the N_s-slot and N_f-pole FMPs:

$$P(\theta)\begin{cases}\sum_{j=0,1,3,5\ldots}^{\infty} P_{sj}\cos(jN_s\theta) & \text{stator slots components}\\ \sum_{z=1,2,3\ldots}^{\infty} P_{fz}\cos(zN_f\theta) & \text{FMPs components}\end{cases} \tag{4.3}$$

where j is either 0 or a positive odd integer, z is a positive integer, N_s is the number of stator teeth, N_f is the number of FMPs, P_{sj} and P_{fz} are the amplitudes of the jth and zth permeance harmonics introduced by the stator slots and FMPs, respectively. For VPMSMs with FMPs evenly distributed along a mechanical period, the first item in (4.3) can be ignored. For VPMSMs without FMPs, the second item in (4.3) can be ignored.

Thus, the modulated PM air-gap flux density in the radial direction can be expressed as:

$$B_r = F_r P$$

$$B_r \begin{cases} \frac{1}{2} \sum_{j=0,1,3,5\ldots}^{\infty} \sum_{i=1,3,5\ldots}^{\infty} F_{ri} P_{sj} \cos[ip_r \Omega_r t - (p_r i \pm jN_s)\theta] \\ \frac{1}{2} \sum_{z=1,2,3\ldots}^{\infty} \sum_{i=1,3,5\ldots}^{\infty} F_{ri} P_{fz} \cos[ip_r \Omega_r t - (p_r i \pm zN_f)\theta] \end{cases} \tag{4.4}$$

From (4.4), the attributes of the modulated PM air-gap harmonics are provided inTable 4.1. It shows that after the modulation effect of the N_s-pole stator slots, apart from the original harmonics of order ip_r with the speed of rotation of Ω_r, there also exist modulated harmonics with the order of $|ip_r \pm jN_s|$ rotating at the speed of $ip_r\Omega_r/(ip_r \pm jN_s)$. In the meantime, the modulation effect of the N_f-pole FMPs produces the modulated harmonics with the order of $|ip_r \pm zN_f|$ rotating at the speed of $ip_r\Omega_r/(ip_r \pm zN_f)$. The positive and negative speeds of rotations correspond to the harmonics rotating in the same or opposite direction with the rotor. The electrical frequencies of the air-gap harmonics are also provided in Table 4.1. It shows that the air-gap flux density harmonics generated by the ip_rth PM MMF have the electrical frequency of $ip_r\Omega_r$. The air-gap flux density harmonics generated by the fundamental PM MMF have the electrical frequency of $p_r\Omega_r$ regardless of the harmonic order.

Table 4.1 Attributes of Modulated PM Field Harmonics

Harmonic order	Speed of rotation	Electrical frequency	Harmonic order	Speed of rotation	Electrical frequency
$\lvert ip_r \pm jN_s \rvert$	$\frac{ip_r\Omega_r}{ip_r \pm jN_s}$	$ip_r\Omega_r$	$\lvert ip_r \pm zN_f \rvert$	$\frac{ip_r\Omega_r}{ip_r \pm zN_f}$	$ip_r\Omega_r$

4.2.2 Armature Reaction Air-Gap Flux Density

For a VPMSM, the armature reaction MMF can be expressed as:

$$F_s(\theta,t) = \sum_{k}^{\infty} F_{sk} \cos(\omega_s - k\theta) + \sum_{m}^{\infty} F_{sm} \cos(-\omega_s - m\theta) \tag{4.5}$$

where ω_s is its electrical rotating velocity, $\omega_s=p_r\Omega_r$, m and k are positive integers depending on the distribution of stator windings, F_{sk} and F_{sm} are the amplitudes of the kth and the mth order harmonics.

Similarly, the modulated armature reaction air-gap flux density in the radial direction can be deduced

by multiplying $F_s(\theta,t)$ and $P(\theta)$ from (4.5) and (4.3):

$$B_s = F_s P$$

$$B_s \begin{cases} \frac{1}{2}\sum_{j=0,1,3...}^{\infty}\sum_{k}^{\infty} F_{sk}P_{sj}\cos[\omega_s t-(k\pm jN_s)\theta] \\ \frac{1}{2}\sum_{z=1,2,3...}^{\infty}\sum_{k}^{\infty} F_{sk}P_{fz}\cos[\omega_s t-(k\pm zN_f)\theta] \\ \frac{1}{2}\sum_{j=0,1,3...}^{\infty}\sum_{m}^{\infty} F_{sm}P_{sj}\cos[-\omega_s t-(m\pm jN_s)\theta] \\ \frac{1}{2}\sum_{z=1,2,3...}^{\infty}\sum_{m}^{\infty} F_{sm}P_{fz}\cos[-\omega_s t-(m\pm zN_f)\theta] \end{cases} \tag{4.6}$$

From (4.6)-(4.7), the attributes of the modulated armature reaction air-gap field harmonics are provided in Table 4.2. It can be seen that apart from the original kth (or mth) armature reaction magnetic field harmonic with the speed of rotation of $p_r\Omega_r/k$ (or $-p_r\Omega_r/m$), the modulation effect of the N_s-pole stator slots produces the modulated harmonics with the order of $|k(\text{or } m)\pm jN_s|$ rotating at the speed of $p_r\Omega_r/(k\pm jN_s)$ (or $-p_r\Omega_r/(m\pm jN_s)$), whereas the modulation effect of the N_f-pole FMPs produces the modulated harmonics with the order of $|k(\text{or } m)\pm zN_f|$ rotating at the speed of $p_r\Omega_r/(k\pm zN_f)$ (or $-p_r\Omega_r/(m\pm zN_f)$). The electrical frequencies of the air-gap harmonics are also provided in Table 4.2. It shows that all the air-gap flux density harmonics have the electrical frequency of $p_r\Omega_r$, which is the same with the air-gap flux density harmonics generated by the fundamental PM MMF.

Table 4.2 Attributes of Armature Reaction Field Harmonics

Harmonic order	Speed of rotation	Electrical frequency	Harmonic order	Electrical frequency	Speed of rotation
$\lvert k\pm jN_s\rvert$	$\frac{p_r\Omega_r}{k\pm jN_s}$	$p_r\Omega_r$	$\lvert m\pm jN_s\rvert$	$p_r\Omega_r$	$\frac{-p_r\Omega_r}{m\pm jN_s}$
$\lvert k\pm zN_f\rvert$	$\frac{p_r\Omega_r}{k\pm zN_f}$	$p_r\Omega_r$	$\lvert m\pm zN_f\rvert$	$p_r\Omega_r$	$\frac{-p_r\Omega_r}{m\pm zN_f}$

4.2.3 Interaction of Air-Gap Magnetic Field Harmonics

According to the classical electromagnetic theory, to produce a steady torque, the armature reaction

magnetic field and the PM magnetic field must have the same number of pole pairs and speed of rotation.

Thus, in a VPMSM, the following equations must be satisfied to produce steady torque:

$$\begin{cases} \left|ip_r \pm \left[(2n+1)N_s\right](\text{or } nN_f)\right| = \left|k \pm jN_s\right| \text{or} \left|m \pm jN_s\right| \text{or} \left|k \pm zN_f\right| \text{or} \left|m \pm zN_f\right| \\ \dfrac{ip_r\Omega_r}{ip_r \pm \left[(2n+1)N_s\right](\text{or } nN_f)} = \dfrac{p_r\Omega_r}{k \pm jN_s} \text{or} \dfrac{-p_r\Omega_r}{m \pm jN_s} \text{or} \dfrac{p_r\Omega_r}{k \pm zN_f} \text{or} \dfrac{-p_r\Omega_r}{m \pm zN_f} \end{cases} \tag{4.7}$$

This means

$$\begin{cases} i = 1 \\ \left|p_r \pm \left[(2n+1)N_s\right](\text{or } nN_f)\right| = \left|k \pm jN_s(\text{or } zN_f)\right| \text{or} \left|m \pm jN_s(\text{or } zN_f)\right| \end{cases} \tag{4.8}$$

where n is either 0 or a positive integer. Based on (4.8), useful torque can be generated under two circumstances shown by Fig. 4.3.

It is noteworthy that in both circumstances, the machine is divided into three parts: the stator where the armature reaction magnetomotive force (MMF) is generated; the rotor PM where the PM MMF is generated and the air gap where the resultant flux density harmonics interact with each other. The torque production mechanism in VPMSMs can be explained as follows:

(a) The p_rth PM fundamental and armature reaction MMF harmonics share the same order and speed of rotation. Their resultant p_rth air gap flux density harmonics can interact with each other and produce useful torque. Here both p_rth air gap flux density harmonics are generated by the PM and armature reaction MMFs and the DC component in the air-gap permeance function without modulation. In this case, the torque is produced by the principle of the conventional PMSM as shown in Fig. 4.3 (a).

(b) The p_sth armature reaction MMF harmonic has different order but same electrical frequency with the p_rth PM fundamental MMF harmonic as shown in Table 4.2. They can still interact with each other and produce steady torque under the modulation of the N_f-pole FMP or N_s-pole stator tooth as long as they satisfy (4.8). In this case, the torque is produced by magnetic gearing effect, shown in Fig. 4.3 (b).

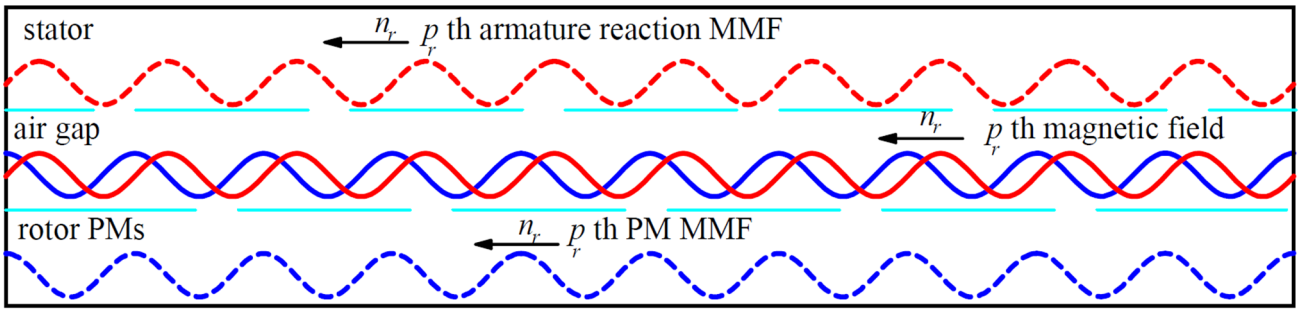

(a) Principle of conventional PMSMs.

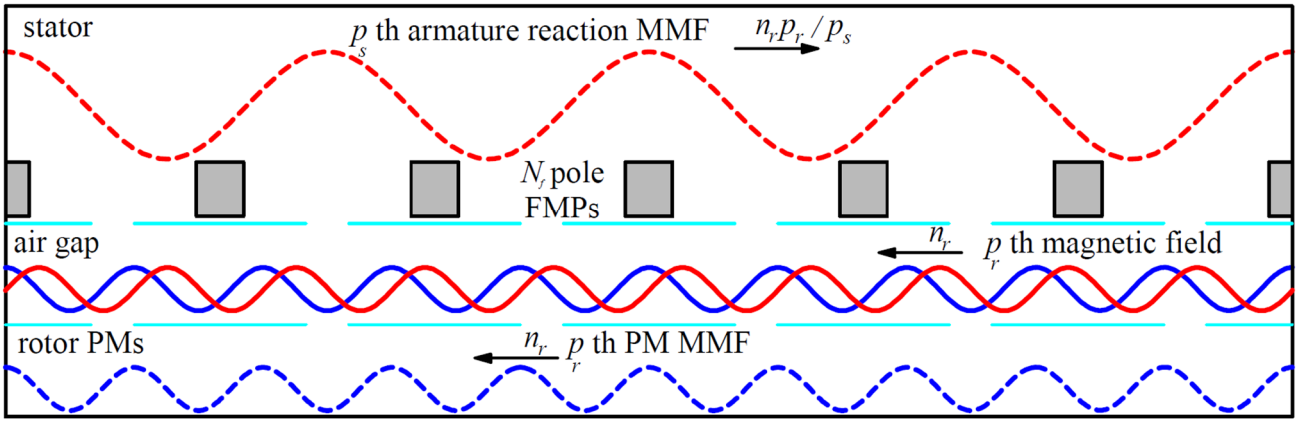

(b) Principle of magnetic gearing effect.

Fig. 4.3 Schematic of torque production mechanism.

4.2.4 Finite Element Validation

From the perspective of winding configuration, there are mainly two kinds of VPMSMs: VPMSMs with distributed windings and VPMSMs with concentrated windings. For VPMSM with concentrated windings, FMPs are needed for stator armature reaction MMF modulation, whereas for VPMSMs with distributed windings, there is no FMPs on the stator and the stator teeth play the role of FMPs. In this section, a 12-slot/22-pole surface-mounted VPMSM with distributed windings (N_s=N_f=12, p_s=1 and p_r=11) is used as an example to analyse the attributes of air-gap flux density harmonics and torque produced by each air-gap harmonic. The main design parameters of the machine are listed in Table 4.4. The cross section of the 12-slot/22-pole VPMSM is shown in Fig. 4.4. As the analysis in this section is for a VPMSM with distributed windings, a similar analysis for a 6-slot/12-FMP/20-pole VPMSM with concentrated windings is provided in Appendix B.

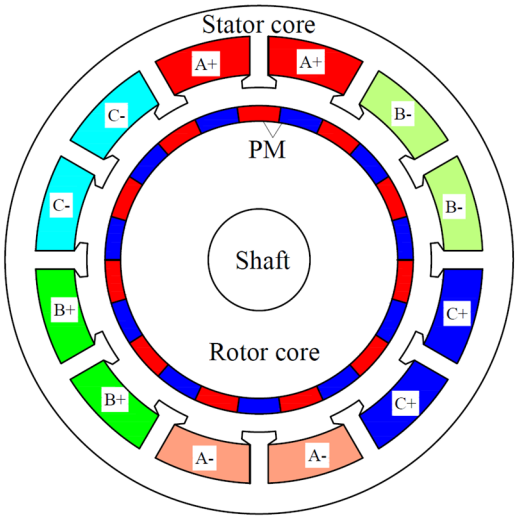

Fig. 4.4. Cross section of a 12-slot/22-pole VPMSM.

Under on-load operation condition, at a certain time, the radial component B_{gr} and the tangential component B_{gt} of air-gap flux density can be expanded by Fourier series:

$$\begin{cases} B_{gr}(t,\theta) = \sum_{k} B_{grk} \cos(k\theta - \theta_{rk}) \\ B_{gt}(t,\theta) = \sum_{k} B_{gtk} \cos(k\theta - \theta_{tk}) \end{cases} \tag{4.9}$$

where B_{grk} and B_{gtk} are the kth Fourier coefficients of B_{gr} and B_{gt}, θ_{rk} and θ_{tk} are their respective phases.

The electromagnetic torque produced by the kth radial and tangential airgap field harmonics can be derived by:

$$T_k(t) = \frac{\pi r_g^{\,2} l_{ef}}{\mu_0} B_{grk} B_{gtk} \cos(\theta_{rk}(t) - \theta_{tk}(t)) \tag{4.10}$$

where r_g is the air-gap radius, μ_0 is the vacuum permeability, l_{ef} is the effective axial length. The contribution of each air-gap harmonic to the total torque can be obtained by FEA as follows.

At a certain time over an electrical period, the FE predicted B_{gr} and B_{gt} are expanded to the Fourier series based on (4.9). Hence, the values of B_{grk}, B_{gtk}, θ_{rk} and θ_{tk} can be obtained. After this, the instantaneous electromagnetic torque produced by the kth radial and tangential airgap field harmonics is derived by (4.10). After repeating the above procedures over an electrical period, the average torque produced by the kth field harmonic within the full electric period can be obtained.

The cogging torque waveform and torque waveform when the VPMSM is fed with 5A sinusoidal phase currents and operating under I_d=0 control in an electrical period are shown in Fig. 4.5 (a). It shows that the cogging torque and torque ripple of the VPMSM are very small compared to the average torque. The waveforms and spectra of the radial and tangential air-gap fields at zero rotor position (I_a=-2I_b=-2I_c=5A; I_q=5A, I_d=0A) is provided in Fig. 4.5 (b) and (c). They show that the 1st and 11th harmonics are the main flux density harmonics in the air-gap, which is consistent with Table 4.1 and 4.2. Hence, the 1st and 11th harmonics are selected to investigate the attributes of air-gap flux density harmonics and torque produced by each air-gap harmonic. The amplitudes of their radial and tangential components over an electrical period are shown in Fig. 4.5 (d). The phase and phase difference between their radial and tangential components over an electrical period are shown in Fig. 4.5 (e)-(f). They show that the 1st and 11th harmonic have the same electrical frequency. The phase differences between the radial and tangential components of the 1st and 11th harmonic are 270 and 81 electrical degrees, respectively. The instant torque contributions of the 1st and 11th harmonic to the instant torque are calculated by (4.11) at each time instant and shown in Fig. 4.5 (g). It shows that the 1st harmonic makes no contribution to the average torque as θ_{rk}-θ_{tk} is 270 electrical degrees and the average value of cos(θ_{rk}-θ_{tk}) in (4.11) is 0 in an electrical period. Apart from the 1st and 11th air-gap flux density harmonic, the average torque produced by other air-gap harmonics within an electrical period is also calculated and the result is provided in Fig. 4.5 (h). It shows that only the 11th air-gap magnetic flux density harmonic contributes to the total torque, viz., only the fundamental harmonic contributes to the average torque. For the other harmonics, the average torque contribution is 0 because the average value of cos(θ_{rk}-θ_{tk}) in (4.11) is always 0 in an electrical period.

This result reveals that like conventional PMSMs, the VPMSM with surface mounted PMs is also a mono-harmonic machine, which means only the p_rth air-gap flux density harmonic in the air-gap contributing to the electromagnetic torque. As the conclusion is drawn from VPMSM without FMPs show in Fig. 4.4, in Appendix B, a 6-slot/12-FMP/20-pole VPMSM is also used as an example to investigate the attributes of air-gap flux density harmonics and torque produced by each air-gap harmonic, from which the same conclusion can be drawn.

Hence, (4.8) can be further written as

$$p_r = \left|k \pm jN_s(\text{or } zN_f)\right| \text{or} \left|m \pm jN_s(\text{or } zN_f)\right| \tag{4.11}$$

and the magnetic gearing effect in VPMSMs can be further described as: the armature reaction MMF

harmonic can be modulated to air-gap flux density harmonic of fundamental order by the stator slots or the FMPs, it can interact with the fundamental PM harmonic in the air-gap and produce steady torque. It should be noted that although there are multiple armature reaction MMF harmonics of different order contributing to the torque production via magnetic gearing effect, only the modulated p_rth air-gap flux density harmonic can produce useful torque in the air-gap.

From the analysis above, it can be seen that the torque production mechanism of VPMSMs with surface-mounted PM rotor is different from that of stator PM machines such as switched flux [CHE19] [JIA16] and flux reversal [LI18b] machines which have multiple working harmonics in the air gap. As a result, it brings convenience for quantification of magnetic gearing effect in VPMSM. As will be shown in Section 4.3, only the resultant p_rth armature reaction air-gap flux needs to be restored. More importantly, this also brings convenience for VPMSM design as the designer now only needs to optimize the p_rth instead of other order armature reaction and PM air-gap flux density harmonics, as will be shown in Section 4.4.

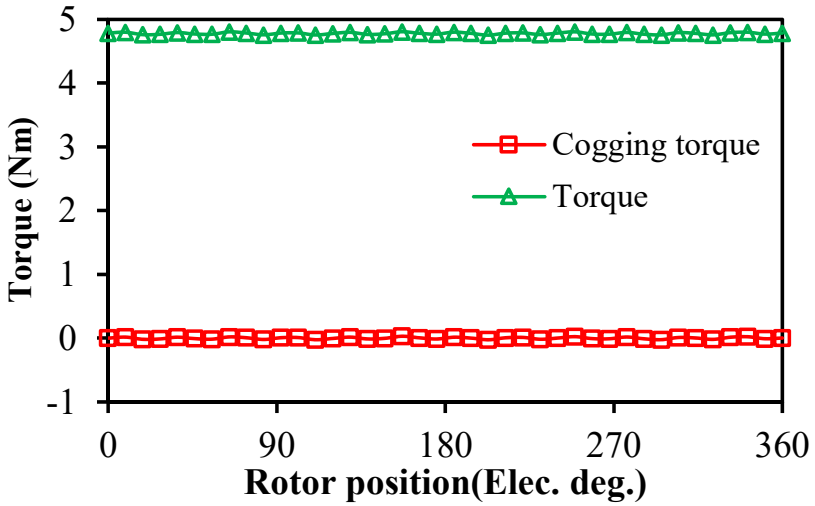

(a) Waveforms of cogging torque and torque when I_m=5A.

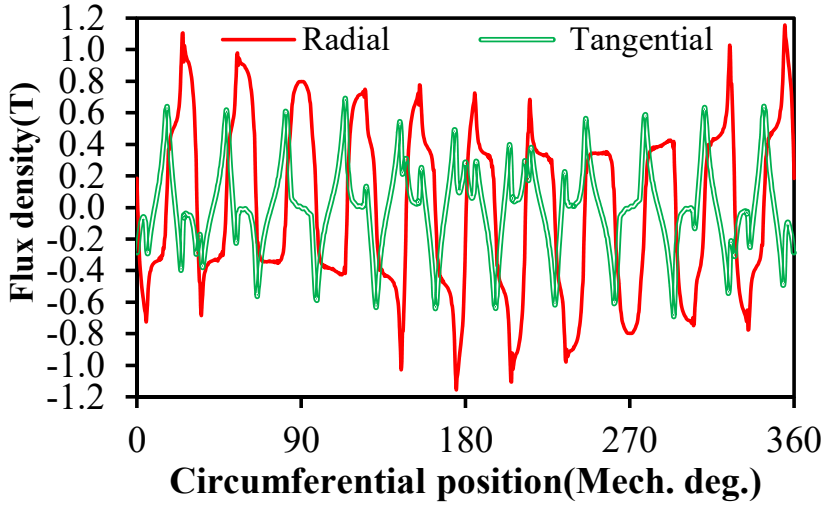

(b) Air-gap flux density waveform (I_a=-2I_b=-2I_c=5A; I_q=5A, I_d=0A).

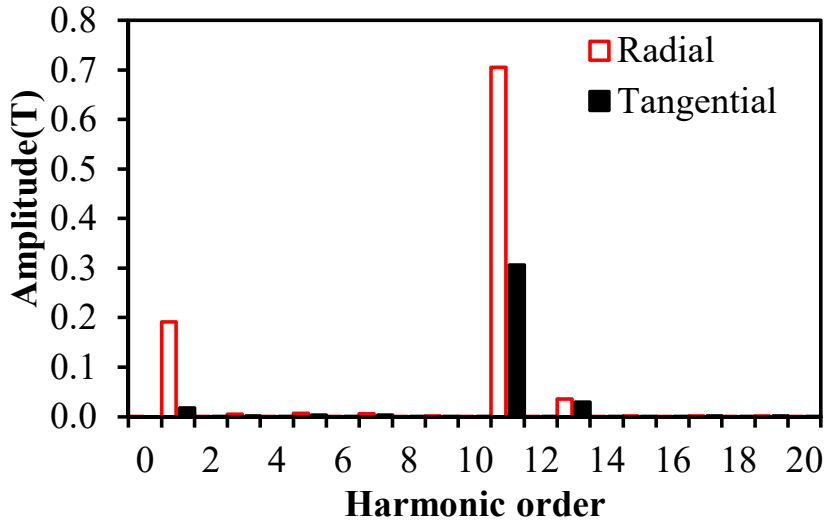

(c) Air-gap flux density spectra (I_a=-2I_b=-2I_c=5A; I_q=5A, I_d=0A).

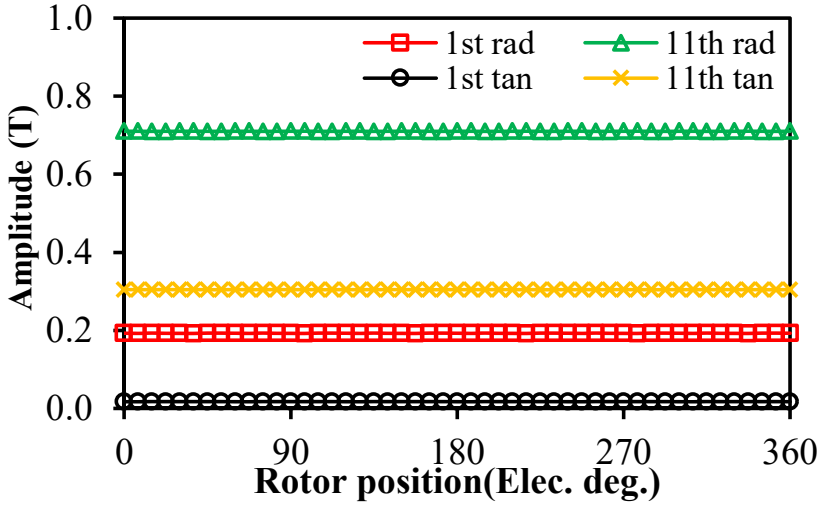

(d) Amplitude of radial and tangential air-gap magnetic flux density harmonics vs rotor position.

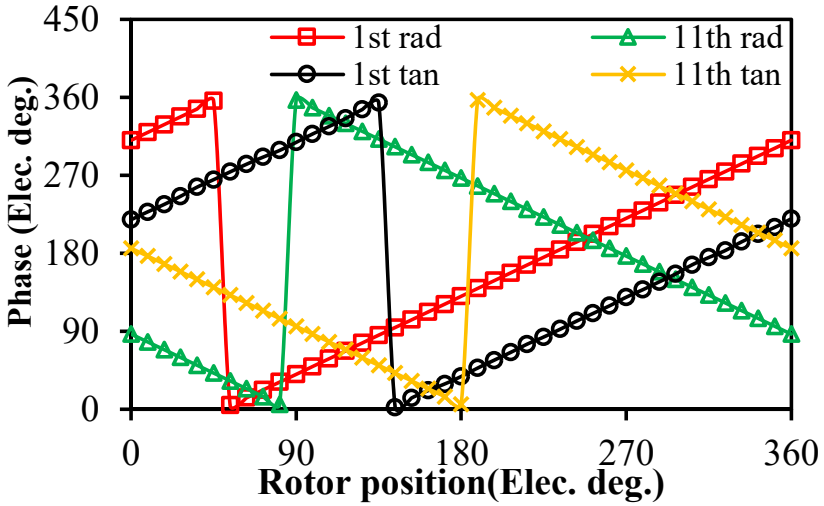

(e) Phase of radial and tangential air-gap magnetic flux density harmonics vs rotor position.

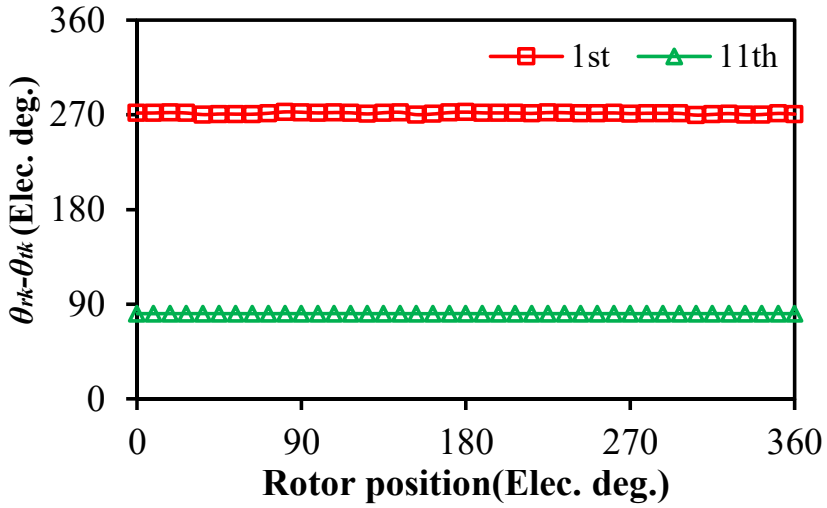

(f) Variation of (θ_{rk} -θ_{tk}) vs rotor position.

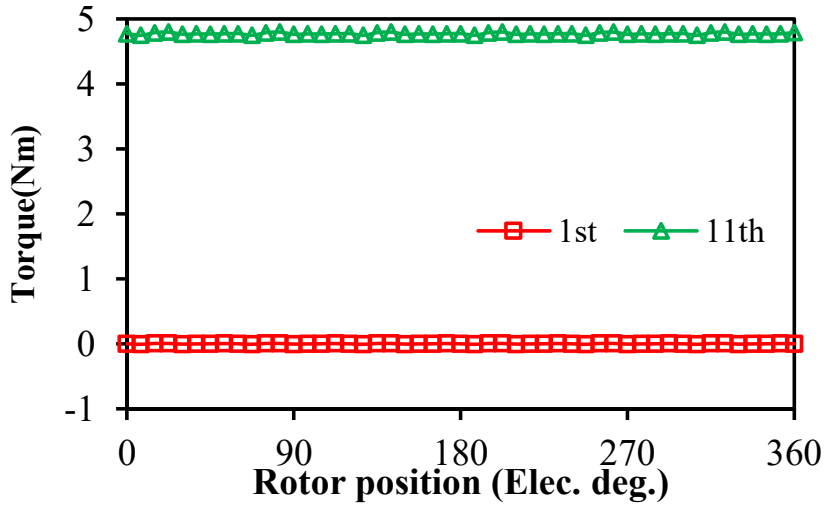

(g) Instant torque contribution of individual air-gap flux density harmonic.

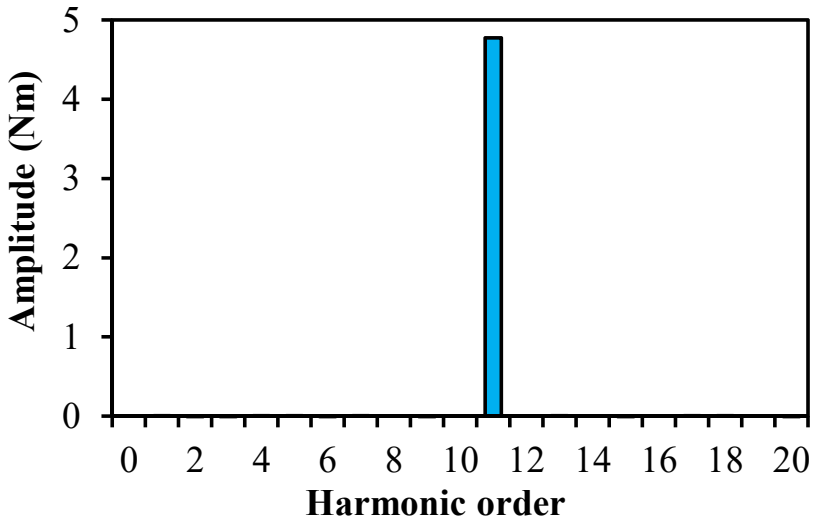

(h) Average torque contribution of each harmonic.

Fig. 4.5 FEA-predicted torque performance

4.3 Quantification of Magnetic Gearing Effect in a 12-Slot/22-Pole VPMSM

In the last section, the mechanism of magnetic gearing effect in VPMSMs is revealed. The aim of this section is to decompose the torque according to different torque production mechanisms.

4.3.1 FEA-based ECSM

Firstly, the FEA-based ECSM of the 12-slot/22-pole VPMSM is built. The schematic diagram of its FEA-based ECSM is provided in Fig. 4.6. Similar with the conventional ECSM [ISH05b], the coils are moved from the slots to the slot openings on the stator bore and wound in the same manner as in Fig. 4.4. It should be noted that in the FEA simulation, the thickness of the equivalent current sheet is designed very thin (less than 5%) compared to the air-gap length.

When the PMs are not magnetised, the coils in the VPMSM model and its FEA-based ECSM in Fig. 4.6 are injected with the same current, their respective armature reaction flux lines are provided in Fig. 4.7. It can be seen that VPMSM and its FEA-based ECSM have the same main flux path. Also, it should be noted that the replacement of the armature windings will not influence the amplitude and phase of each armature reaction MMF harmonic because the ECSM is placed at the slot opening and the MMF waveform will not change. This means that the percentage of contribution of each MMF harmonic to the torque will not be influenced by the position of the coils.

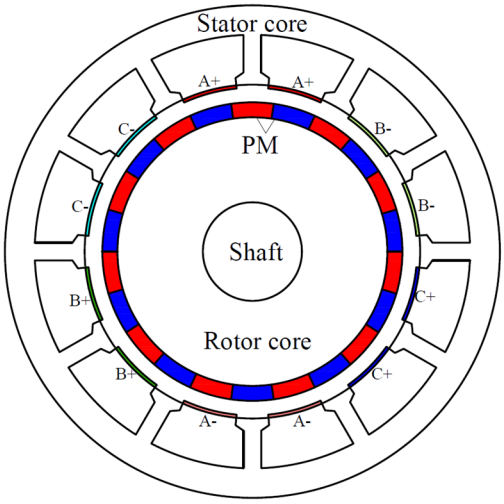

Fig. 4.6 FEA-based ECSM of the 12-slot/22-pole machine.

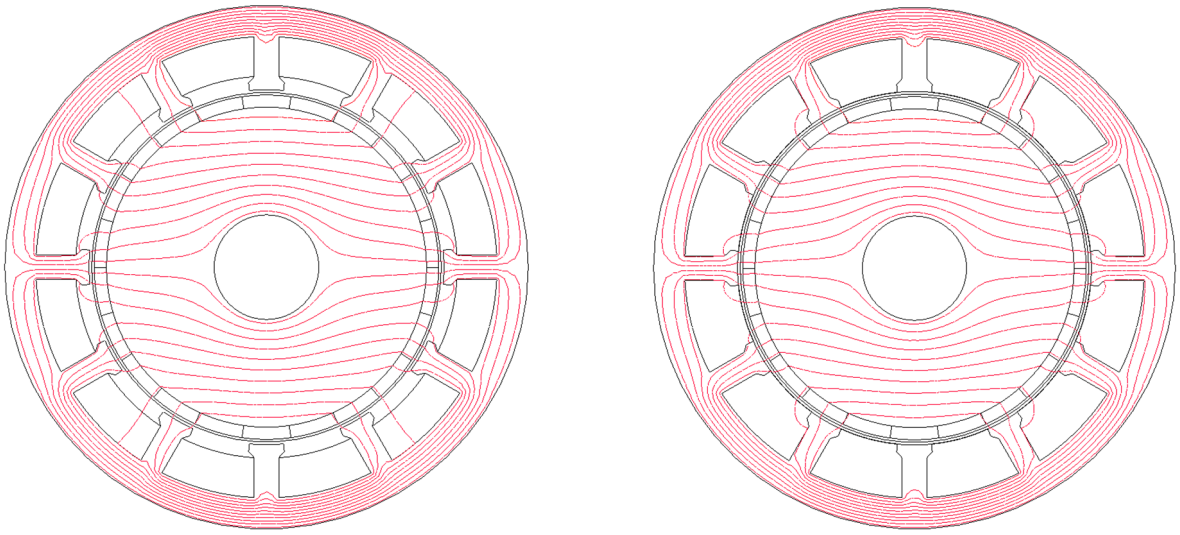

(a) VPMSM model (b) FEA-based ECSM.

Fig. 4.7 Armature reaction flux lines (I_a=5A, I_b=I_c=-2.5A).

4.3.2 Harmonic Restoration and Quantification of Torque Contribution

To quantify the respective contributions of torque produced by the principle of the conventional PMSM and magnetic gearing effect, the armature reaction harmonics should be analysed independently. From FEA-based ECSM, a model without PMs and stator slots is built to gain the information of the armature reaction harmonics before being modulated by stator slots, Fig. 4.8.

The waveform and spectrum of the armature reaction air-gap magnetic flux density harmonics before modulation are calculated from Fig. 4.8 (a) by FEA. The results are provided in Fig. 4.9. It shows that the 1st and 11th harmonics have larger amplitudes than other harmonics, and more importantly, they satisfy (4.11) and can produce torque based on magnetic gearing effect and principle of conventional PMSM, respectively. Hence, the amplitudes and phases of both harmonics are recorded in Table 4.3.

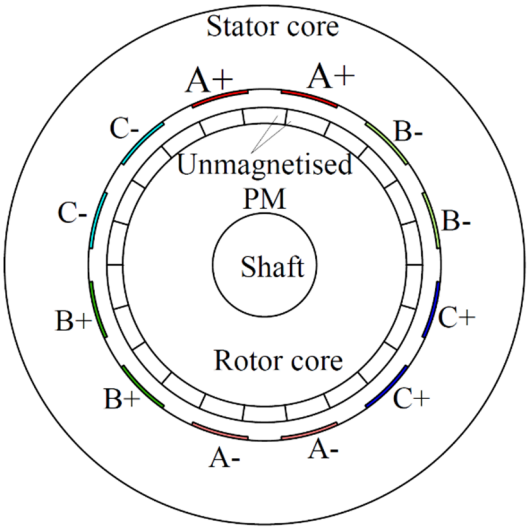

(a) A model without PMs and stator slots.

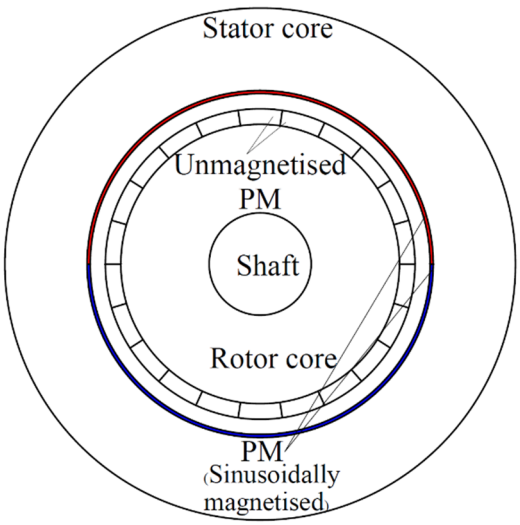

(b) Restoration of 1st harmonic.

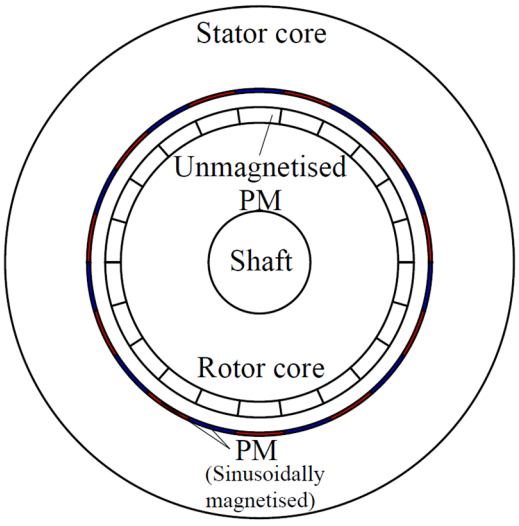

(c) Restoration of 11th harmonic.

Fig. 4.8 Restoration of fields in 12-slot/22-pole machine without modulation.

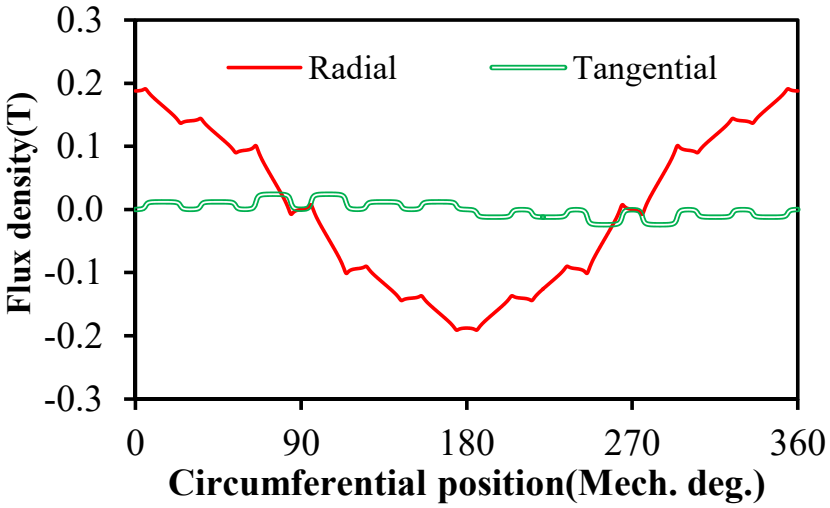

(a) Waveform.

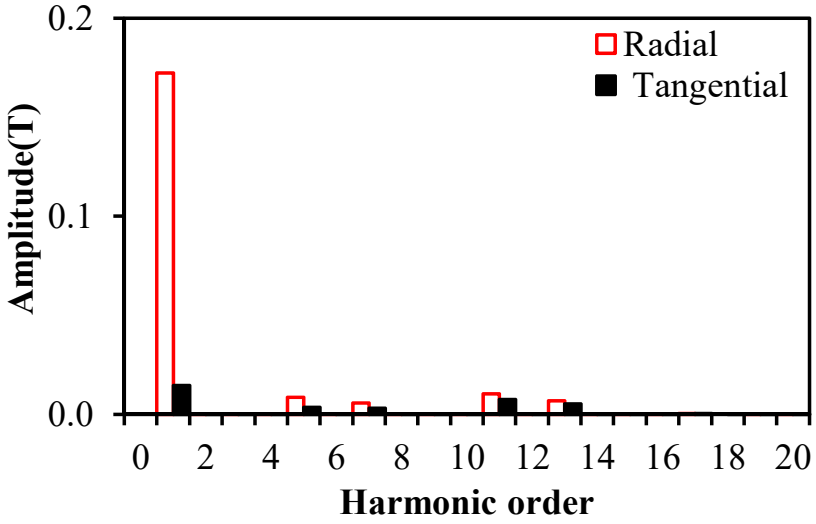

(b) Spectrum.

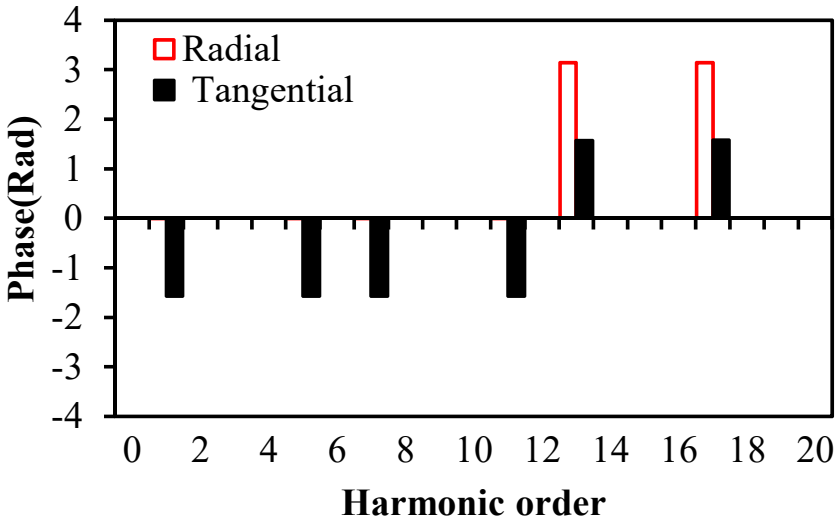

(c) Phase.

Fig. 4.9 Armature reaction flux density before modulation.

Table 4.3 Amplitude and Phases of Armature Reaction Harmonics

Harmonic order	Amplitude(T)		Phase(°)	
	Radial	Tangential	Radial	Tangential
1	0.172	0.015	0	-90
11	0.010	0.007	0	-90

To analyse the behaviour of the 1st and 11th armature reaction magnetic flux density harmonics independently, they need to be modelled individually. For the 1st armature reaction magnetic flux density harmonic, a 2-pole outer rotor which consists of sinusoidally magnetised permanent magnets are built, Fig. 4.8 (b). The thickness of the PMs is the same as that of the equivalent current sheet in Fig. 4.6. The remanence and the initial angle of the permanent magnets are adjusted so that the amplitude and phase of the 1st harmonic produced by outer PMs are the same with those by the armature reaction field before modulation. Similarly, a 22-pole outer rotor consists of sinusoidally magnetised permanent magnets are also built to simulate the 11th armature reaction field before being modulated by stator slotting, Fig. 4.8 (c).

The interactions between the PM magnetic field and the 1st and 11th armature reaction fields under the

modulation effect are shown in Fig. 4.10. A 22-pole inner rotor, which is identical to the rotor in Fig. 4.4, is used to interact with the outer PMs. Fig. 4.10 (a) shows the interaction between the 11th PM and 1st armature reaction MMF harmonics when the stator is slotted. According to Table 4.1 and 4.2, the 2-pole outer PMs rotates at 11 times mechanical speed of the 22-pole inner rotor in the opposite direction. The torque contribution of each air-gap harmonic is calculated by (4.10) at each time constant in an electrical period. The average torque contribution of each harmonic in an electrical period is illustrated in Fig. 4.11 by legend "MG". Since the 1st armature reaction and the 11th PM MMF harmonics do not share the same order, the torque component in this case is produced by the principle of the magnetic gearing effect, viz, the 1st armature reaction and 11th PM magnetic fields can produce steady torque with the modulation effect of 12th air-gap permeance.

Fig. 4.10 (b) shows the interaction between the 11th PM and 11th armature reaction MMF harmonics. Both inner and outer 22-pole PMs are rotating in the same direction at the mechanical speed n_r when the stator is slotted. The torque contribution of each air-gap harmonic is calculated by (4.10) at each time constant in an electrical period. The average torque contribution of each harmonic in an electrical period is shown in Fig. 4.11 by legend "PMSM". Since the armature reaction and PM magnetic fields share the same order in this case, the torque component is produced by the principle of the conventional electrical machine.

The accumulated result of the torque produced by the principle of conventional PMSM and magnetic gearing effect is shown in Fig. 4.11 by legend "Total". It can be seen that for the 12-slot/22-pole VPMSM, the accumulated result makes up >99% of the average torque, in which the magnetic gearing effect contributes 81.5% while the conventional PM machine principle contributes 18.4% to the average torque. According to (4.8), although there are other armature reaction MMF harmonics contributing to the average torque by magnetic gearing effect, their contribution is too trivial (less than 1%) and ignored in this analysis.

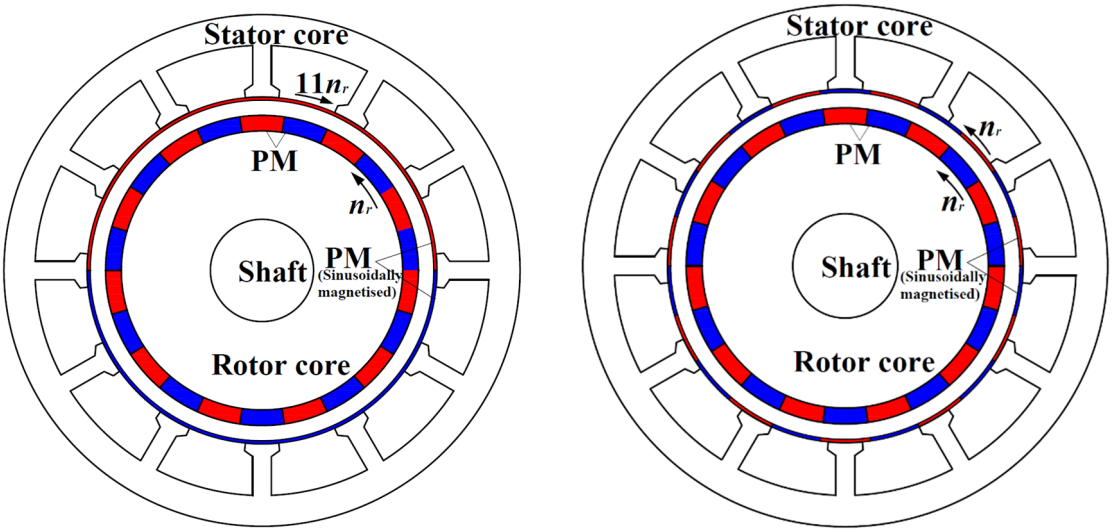

(a) 11th PM and 1st armature reaction MMF.

(b) 11th PM and 11th armature reaction MMF.

Fig. 4.10 Interaction of the field flux harmonics in 12-slot/22-pole machine.

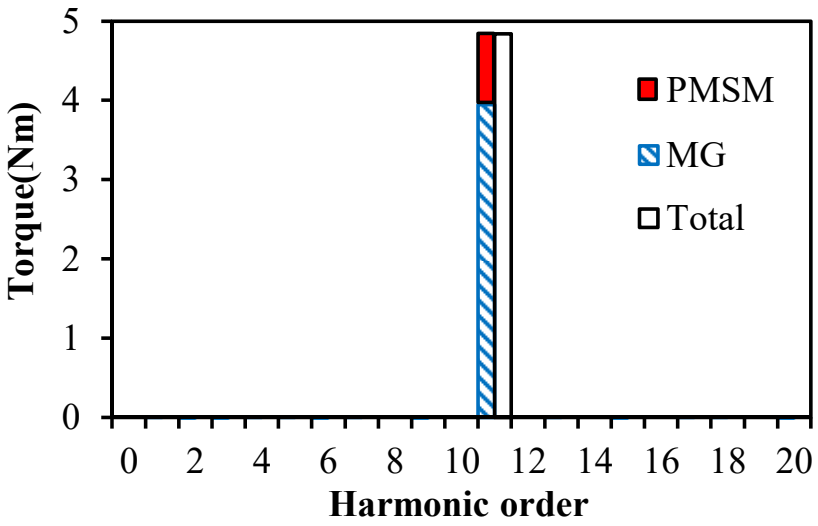

Fig. 4.11 Quantification of torque production.

4.4 Influence of Slot Opening on Magnetic Gearing Effect

Since the slotting effect is the main cause of gearing effect in VPMSMs, the influence of stator slot opening on the field harmonics and the contribution of gearing effect to the average torque are investigated in this section.

The amplitudes of the 11th PM air-gap magnetic flux density harmonics in the radial direction with respect to different slot opening angles are provided in Fig. 4.12 (a). It can be seen that for the 12-slot/22-pole VPMSM under investigation, the amplitude of 11th PM fundamental harmonic decreases with the increase of slot opening angle. This is because with the increase of the slot opening angle, the equivalent DC component of the air-gap permeance decreases, which reduces the amplitude of fundamental PM harmonic according to (4.3).

By adopting the FEA-based ECSM and the harmonic restoration method, the modulated 11th armature reaction air-gap magnetic flux density harmonic which is originated from the 1st armature reaction MMF and the unmodulated 11th armature reaction air-gap magnetic flux density harmonic which is originated from the 11th armature reaction MMF can be separated, as shown in Fig. 4.12 (b). It shows that the modulated 11th armature reaction air-gap magnetic flux density harmonic increases whereas the unmodulated 11th armature reaction air-gap magnetic flux density harmonic decreases with the increase of slot opening.

The tangential PM and armature reaction air-gap flux density harmonics follow the same trend with the radial components.

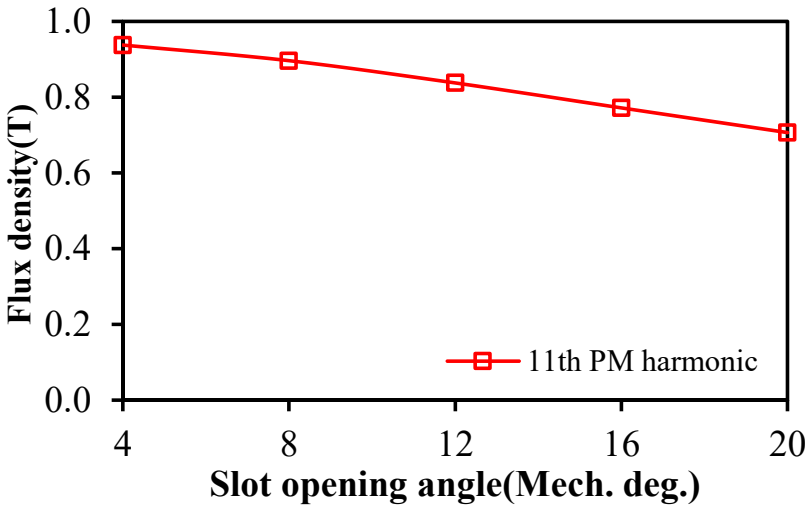

(a) 11th PM harmonic.

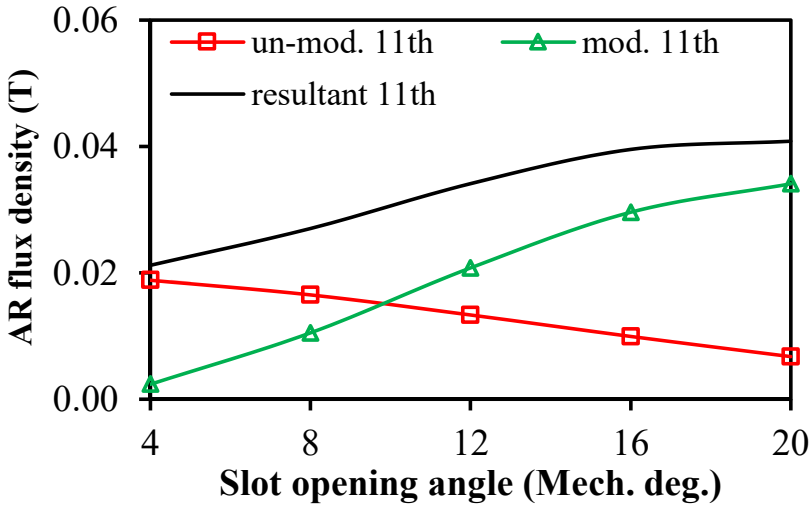

(b) Armature reaction harmonics.

Fig. 4.12 Influence of slot opening on the field harmonics.

The torque produced by the interaction of the modulated 11th armature reaction harmonic and PM harmonic is based on the principle of magnetic gearing effect, whereas the torque produced by the unmodulated 11th armature reaction harmonic and PM harmonic is based on the principle of conventional PMSM. Therefore, their respective contribution to the average electromagnetic torque can also be quantified, which is shown in Fig. 4.13. It can be seen that with the increase of slot opening, the contribution of magnetic gearing effect increases whereas that of the principle of conventional PMSM decreases. Since the magnetic gearing effect makes the main contribution to the total torque, the machine reaches its maximum total torque at a larger slot opening as a trade-off between torque produced by the magnetic gearing effect and the principle of conventional PMSM.

In Chapter 2, the ratio ρ is used to evaluate the contribution of magnetic gearing effect to torque production. In this chapter, the variation of ρ with slot opening angle for the 12-slot/22-pole VPMSM is also calculated and shown in Fig. 4.13. It shows that in VPMSMs, the magnetic gearing effect becomes stronger with the increase of the slot opening.

Since the VPMSMs with FMPs have different stator geometry with VPMSMs without FMPs, in Appendix B, the FEA-based ECSM and harmonic restoration method are also used for the 6-slot/12-FMP/20-pole VPMSM to investigate the influence of geometrical features on the torque contribution, from which the crucial geometrical parameters for torque production can be identified.

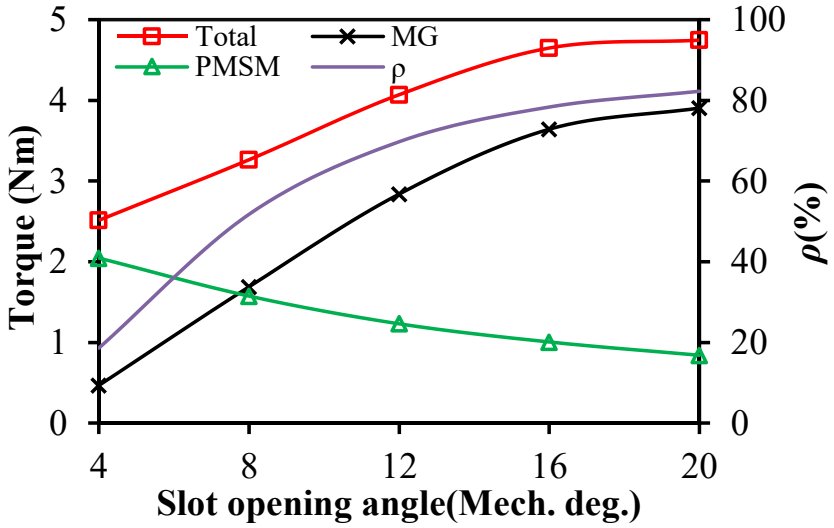

Fig. 4.13 Influence of slot opening on torque contribution.

4.5 Gear Ratio for Different VPMSM Topologies

In the 12-slot/22-pole VPMSM, the 1st armature reaction MMF harmonic rotates at 11 times the speed of the fundamental harmonic, but in the opposite direction. After the modulation effect, it can interact with the 11th PM harmonic and produce steady torque. This is like a conventional magnetic gear with a 1-pole-pair outer rotor, an 11-pole-pair inner rotor and 12 FMPs. In the conventional gear, the ratio of speeds of rotation between rotors is called the gear ratio. Hence, the gear ratio of the magnetic gearing effect in the 12-slot/22-pole VPMSM is the ratio of the speeds of the 1st armature reaction and fundamental MMF harmonics, which is

$$G_r = -\frac{1}{11} \tag{4.12}$$

Generally, in a well-designed VPMSMs without FMPs, the magnetic gearing effect is generated by the $|N_s\text{-}p_r|$th armature reaction MMF harmonic rotating at the speed of $-\omega_s/|N_s\text{-}p_r|$, the N_s-slot stator, and the fundamental PM MMF harmonic with the order of p_r and the speed of rotation of ω_s/p_r. The gear ratio of the magnetic gearing effect is:

$$G_r = -\frac{|\,p_r - N_s\,|}{p_r} \tag{4.13}$$

Similarly, in a well-designed VPMSMs with FMPs, the magnetic gearing effect is generated by the $|N_f\text{-}p_r|$th armature reaction MMF harmonic rotating at the speed of $-\omega_s/|N_f\text{-}p_r|$, the N_f FMP, and the

fundamental harmonic with the order of p_r and the speed of rotation of ω_s/p_r. And the gear ratio in VPMSMs with FMPs can be defined as:

$$G_r = -\frac{|p_r - N_f|}{p_r} \tag{4.14}$$

4.6 Experimental Validation

To validate the previous analyses, the 12-slot/22-pole VPMSM is prototyped. Fig. 4.14 shows the photos of stator and rotor. The dimensional parameters of the prototype are provided in Table 4.4

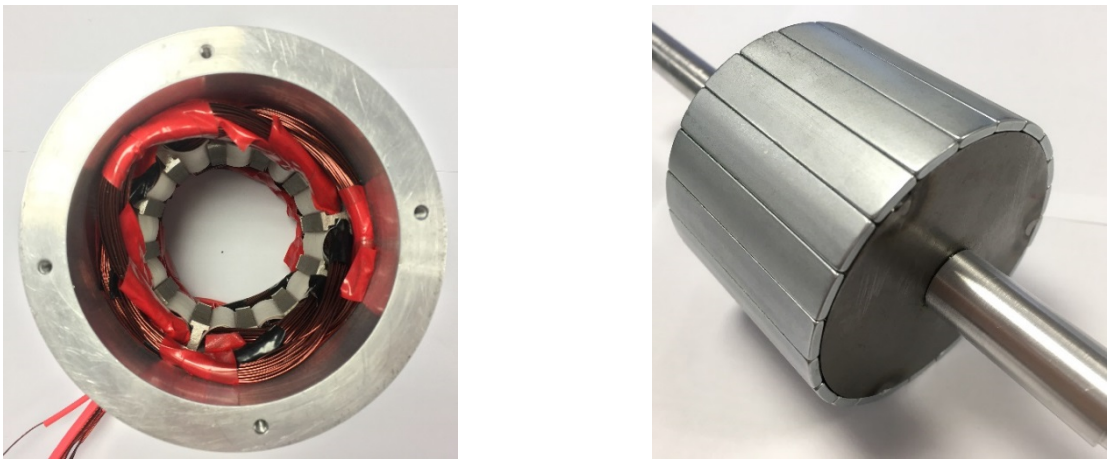

(a) Stator. (b) Rotor.

Fig. 4.14 Prototype photos of the 12-slot/22-pole VPMSM.

Firstly, the back-EMF waveform and spectrum of the VPMSM is tested and compared with the FEA results, Fig. 4.15 (a). It can be seen that there is a 5% discrepancy between the FEA and test results due to the end effect.

The magnetic gearing effect and the torque components in the foregoing sections cannot be measured directly on the prototypes, only the FEA predicted electromagnetic torque can be measured in the experiments using the same method with Chapter 1 [ZHU09c]. Average static torques within 0–180 electric degrees and the maximum static torque under different current amplitudes of the prototype machines are calculated by 2-D FEA and compared with measurements as shown in Fig. 4.15 (c). It shows that there is an 8.8% discrepancy between the FEA and measured results. This is because the end effect becomes more severe when the PM pole number increases. For VPMSMs, the influence of PM pole number on the end effect will be put in the future work.

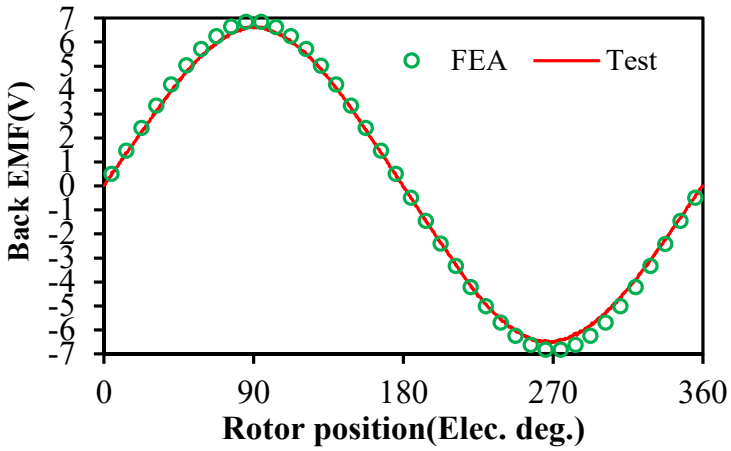

(a) Back-EMF waveform.

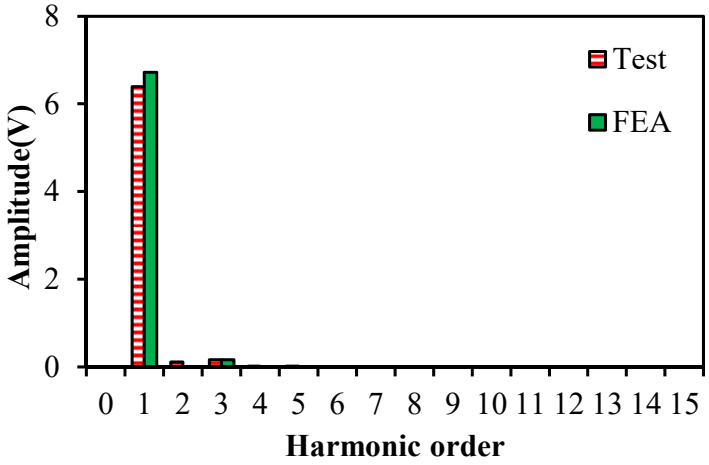

(b) Back- EMF spectra.

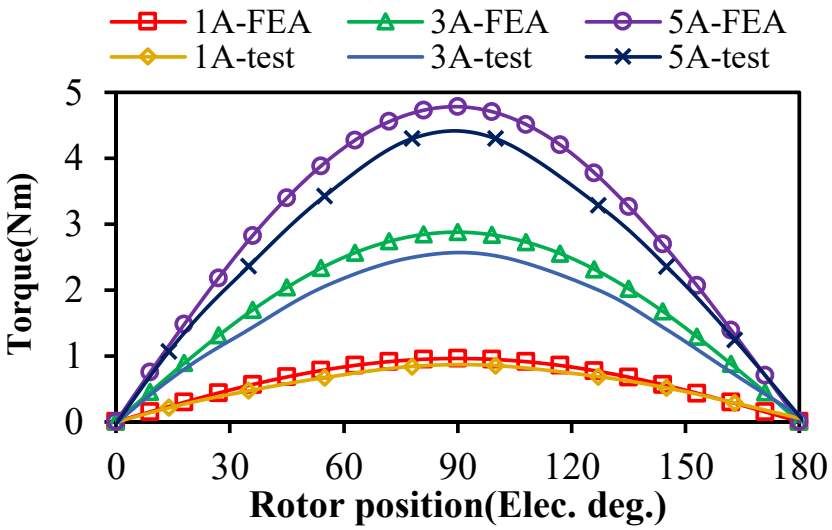

(c) Static torque waveforms.

Fig. 4.15 Comparison of measured and predicted results.

Table 4.4. Dimensional Parameters of Prototypes

Slot number	12
Pole number	22
Stator outer/inner diameter(mm)	100/68
Air-gap length(mm)	1
Turns per phase	100
PM height(mm)	2.3
PM pole arc	180° Elec.
Slot opening angle	19° Mech.
PM remanence	1.2

4.7 Summary

In this chapter, the torque production mechanism and interaction between air-gap field harmonics of VPMSMs are illustrated and validated by FEA. It reveals that the VPMSM with surface mounted PMs is a mono-harmonic torque production machine under sinusoidal current injection. A FEA-based ECSM is introduced and employed on a 12-slot/22-pole VPMSM to study the behaviour of harmonics under the modulation effect. The torque contribution of each armature reaction harmonic to the total torque is quantified. The influence of slot opening on the magnetic gearing effect in VPMSMs is also investigated, revealing that the magnetic gearing effect makes the main contribution to the total torque in VPMSMs, the machine reaches its maximum total torque as a trade-off between torque produced by the magnetic gearing effect and the principle of conventional PMSM. Based on the analysis, the magnetic gearing effect in VPMSMs is explained and the expressions of gear ratios for different topologies are provided. Finally, a prototype is manufactured and tested for validation.

CHAPTER 5

Influence of Gear Ratio on the Performance of Vernier Permanent Magnet Synchronous Machines

Vernier permanent magnet synchronous machine (VPMSM) is a promising candidate for low speed direct-drive applications. At the design stage of VPMSMs, one of the key issues is the selection of the slot/pole number combination. This chapter shows that the gear ratio is useful for selecting an appropriate slot/pole number combination in VPMSMs by acting as an index for a quick overall performance comparison. Firstly, the magnetic gearing effect and the expression of the gear ratio in the VPMSM are introduced. VPMSMs with different slot/pole number combinations are selected and globally optimised for investigation. Then, the influence of the gear ratio on flux linkage, back EMF, cogging torque, output torque, inductance, power factor and losses are investigated theoretically and validated by finite element analysis. Finally, two prototypes are manufactured and tested for validation.

5.1 Introduction

Vernier permanent magnet synchronous machine is a promising candidate for low speed direct-drive applications owing to high torque density and compact size, [JIA11] [KIM14] [LI16].

There has been extensive research on VPMSMs. In [JIA11], [LI11] and [ONE16], the air-gap field distribution in VPMSMs is calculated by analytical method. In [TOB00] and [KIM14], some design principles for maximizing the torque output are provided, while in [LI16], it is verified that torque smoothness is the inherent characteristic of VPMSMs. Apart from the aforementioned references, more research activities focus on the innovation of machine topologies as cited in Chapter 4. It is shown that the VPMSM has higher torque density than the conventional PM machines [FU10] [YAN13] and the conventional magnetically geared machines with more than one air gap [LI11]. It is well known that high torque density of a VPMSM is due to the so-called magnetic gearing effect or modulation effect [QU11] [CHE17] [ZHU18a]. The parameter used to represent the gearing effect in VPMSMs of different slot/pole combinations is defined as the gear ratio, which is a function of the slot and pole numbers.

At the design stage of VPMSM, one of the key issues is the selection of the slot/pole number

combination since it significantly affects the electromagnetic performance and the machine geometries. A quick overall performance comparison and proper selection among various VPMSM candidates is important for both academia and industry applications. However, there are few papers regarding this subject. [WU15b] investigated the influence of slot/pole number combination on the performance and optimal geometry design of VPMSMs. However, the slot/pole number combinations of the VPMSMs in the investigation vary significantly. It fails in providing a performance prediction and evaluation of VPMSMs with similar PM pole numbers under the same slot number, which is important since the performance of the VPMSMs differs a lot even if they have the same slot number and similar pole number as will be studied in this chapter. Therefore, it is worthwhile to have a foresight at their overall performance metrics at the design stage.

For VPMSMs with similar PM pole numbers, this chapter firstly establishes the relationship between the gear ratio and the overall performance metrics at the initial design stage. In Section 5.2, the torque generation principle in VPMSMs, i.e., the magnetic gearing effect, and the expression of gear ratio in VPMSMs are introduced. It is found that the gear ratio is not only a representation of the gearing effect, but once the slot and pole numbers are fixed, also an index parameter of the VPMSMs for the electromagnetic performance. In section 5.3, two groups of VPMSMs are selected and globally optimised for investigation. In sections 5.4, the influence of the gear ratio on flux linkage, back EMF, cogging torque, output torque, inductance, power factor and losses are investigated theoretically and validated by FEA, thus proving that the gear ratio can be used as an index for performance comparison and selection of the appropriate slot/pole number combination at the machine design stage. Finally, two prototypes are manufactured, tested and compared for validation.

5.2 Magnetic Gearing Effect and Gear Ratio in VPMSMs

VPMSMs are known to exhibit the following relationship:

$$p_r = N_f \pm p_s \tag{5.1}$$

where p_r is the number of PM pole-pairs in the rotor, N_f is the number of flux modulation poles (FMPs) in the stator and p_s is the armature reaction magnetic field pole pairs.

Although there are many feasible slot/pole number combinations for VPMSMs, those with

$$p_r = N_f - p_s \tag{5.2}$$

and distributed windings on the stator have been selected and will be investigated in this chapter because they have been proven to have inherent higher torque density in [TOB00]. The 12-slot/22-pole VPMSM in Chapter 4 is an example of this type. The geometry is shown in Fig. 5.2 (b), it can be seen that in this kind of VPMSM, the stator teeth play the role of flux modulation poles, and therefore, the number of stator teeth N_s=N_f.

The high torque density of a VPMSM is due to the so-called magnetic gearing effect which is the working principle of a conventional magnetic gear [ATA04]. It has been revealed in Chapter 4 that in a well-designed VPMSMs without FMPs, the p_s=|N_s-p_r|th armature reaction MMF harmonic is larger than any other armature reaction MMF harmonics. The magnetic gearing effect is generated by the |N_s-p_r|th armature reaction MMF harmonic rotating at the speed of -ω_s/|N_s-p_r|, the N_s-slot stator, and the fundamental PM MMF harmonic with the order of p_r and the speed of rotation of ω_s/p_r. The gear ratio of the magnetic gearing effect is:

$$G_r = -\frac{p_s}{p_r} = -\frac{|p_r - N_s|}{p_r} = \frac{p_r - N_s}{p_r} \tag{5.3}$$

The gear ratio has a negative value for the VPMSMs under investigation in this chapter since the armature reaction and PM magnetic fields involved in the magnetic gearing effect rotate at opposite directions. It can be seen from (5.3) that the gear ratio is not only a representation of the torque production mechanism in VPMSMs, but also a function of the slot/pole combination. Once the slot and pole numbers are fixed, the gear ratio can act as an index parameter of the VPMSMs.

5.3 Alternate Slot/Pole Number Combinations and Global Optimisation

Two groups of VPMSMs with different slot/pole number combinations subjected to (5.2) are selected to investigate the influence of gear ratio on the machines' performance. As shown in Table 5.1, the first group includes 12-slot VPMSMs with 20-pole and 22-pole rotors respectively; the second group includes 24-slot VPMSMs with 40-pole, 44-pole and 46-pole rotors. These two groups are selected due to the following reasons: (1) They have relatively larger torque density [WU15b]. (2) There will be no unbalanced magnetic pull force for all the slot/pole combinations as the greatest common divisors of slot and pole number of all the machine candidates are even. (3) There are more than two feasible slot/pole combinations in each group, which will provide adequate data for further comparisons.

The value of p_s, p_r, the mechanical speeds of rotation of the p_rth and p_sth magnetic field harmonics in the candidate machines are shown in Table 5.1. It can be seen that when the number of slots is fixed, with the increase of the rotor pole-pair number, the gear ratio increases.

Table 5.1 Gear Ratios in VPMSMs with Different Slot/Pole Combinations.

N_s	p_r		p_s		G_r
	Number	Mech. speed	Number	Mech. speed	
12	10	$\omega_s/10$	2	$-\omega_s/2$	-1/5
	11	$\omega_s/11$	1	$-\omega_s/1$	-1/11
24	20	$\omega_s/20$	4	$-\omega_s/4$	-1/5
	22	$\omega_s/22$	2	$-\omega_s/2$	-1/11
	23	$\omega_s/23$	1	$-\omega_s/1$	-1/23

To make a fair comparison, all of the selected VPMSMs have been globally optimised. The optimisation is carried out based on the Maxwell software using genetic algorithm to achieve the maximum torque under the following constrains: (1) Fixed stator outer radius r_o=50mm; (2) Fixed air-gap length l_a=1mm; (3) Fixed stack length l_{ef}=50mm; (4) Fixed shaft radius=10mm; (5) Fixed slot packing factor; (6) Fixed copper loss at 75W considering the end winding. It should be noted that copper loss is the main loss and source of heating for the machine of this size at low speed. 75W is selected within a reasonable copper loss range for the machine of this size. Therefore, all the machine candidates are optimised under the same thermal loading. The related dimensional parameters are illustrated in Fig. 5.1. During the optimisation, the stator yoke radius r_y, the stator inner radius r_i, stator tooth width w_t, slot opening angle s_o and the PM thickness l_{pm} are variables. The cross-sections of the optimised VPMSM candidates are shown in Fig. 5.2. The optimised geometric parameters are shown in Table 5.2, where N_{tpc} and N_{tpp} stands for the numbers of turns per coil and per phase, respectively. The numbers of turns per phase for all the machine candidates are adjusted to be the same (120) for a fair comparison of inductance and power factor. N_{sm} is the number of sub-motors, which is also the number of periodicities in each machine. For all the VPMSMs investigated in this chapter, single layer, full-pitch windings are used, and τ is the coil pitch. The q-axis currents at 75W copper loss for all the

machine candidates are also listed in Table 5.2. It shows that under the same slot number, the q-axis current decreases with the increase of PM pole number. This is because under the same slot number, the length of the end winding increases with the increase of the PM pole number. The total phase resistance increases and the q-axis current decreases at the same copper loss decreases.

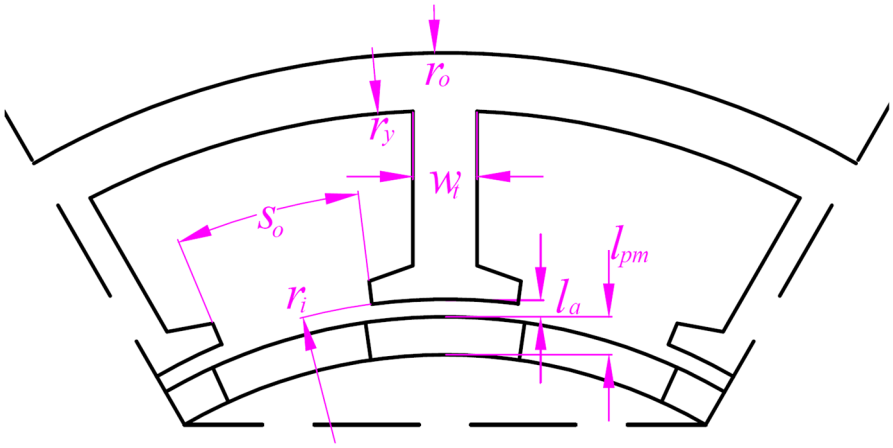

Fig. 5.1 Dimensional parameters in the optimisation.

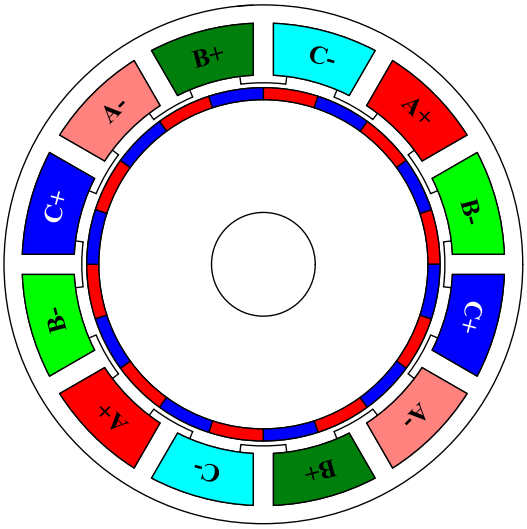

(a) 12-slot/20-pole

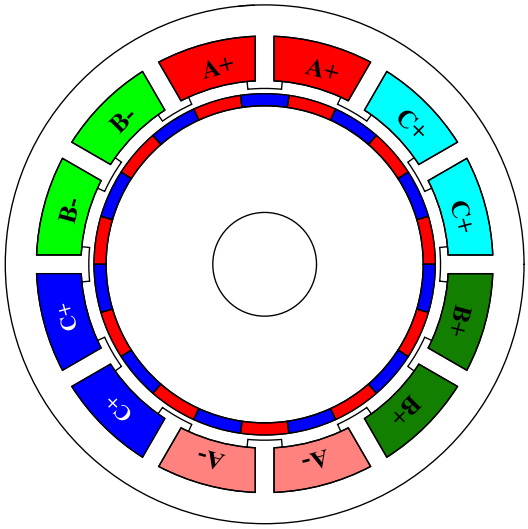

(b) 12-slot/22-pole

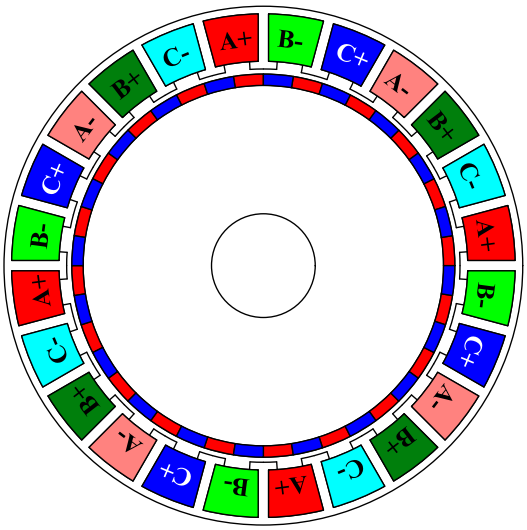

(c) 24-slot/40-pole

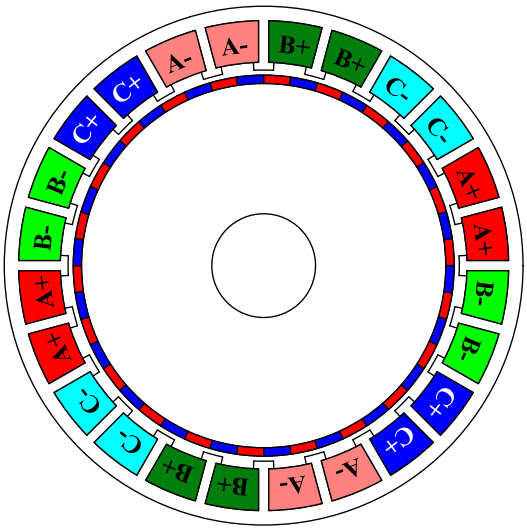

(d) 24-slot/44-pole

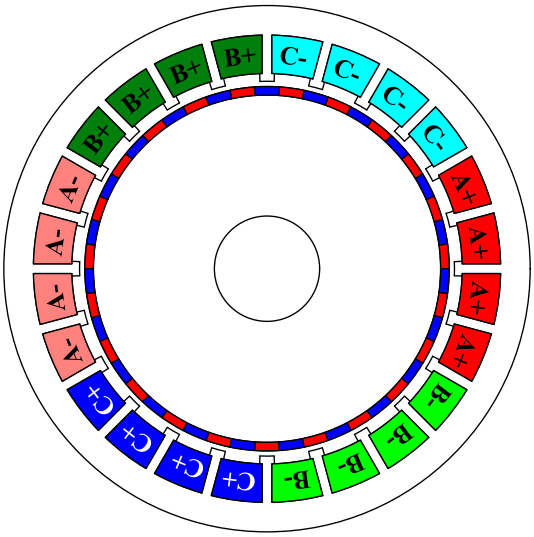

(e) 24-slot/46-pole

Fig. 5.2 Cross-sections of optimised VPMSM candidates.

Table 5.2 Specifications of Optimised VPMSMs.

N_s	$2p_r$	r_y mm	w_t mm	s_o deg.	r_i mm	l_{pm} mm	N_{sm}	τ	I_q A	N_{tpc}	N_{tpp}	r_o mm	l_a mm	l_{ef} mm
12	20	46.5	3.9	15.8	35.1	2.3	2	3	8.97	60	120	50	1	50
	22	44.0	3.6	18.9	33.9	2.3	1	6	6.69					
24	40	48.5	2.0	7.2	37.9	2.2	4	3	10.03	30				
	44	47.2	2.0	9.2	37.7	1.6	2	6	7.84					
	46	44.4	1.9	10.7	35.6	1.6	1	9	5.79					

5.4 Influence of Gear Ratio on Machine Performance

In this section, the relationship between the gear ratio and the flux linkage, back EMF, torque, overload capability, cogging torque, inductance, power factor and rotor losses in the candidate VPMSMs will be analysed. After the clarification of the relationships, the gear ratio can be used for performance comparison at the machine design stage.

5.4.1 Influence of Gear Ratio on Flux Linkage and Back EMF

To have a better understanding of the influence of slot/pole combination on the machine performance, a unified slot function is introduced in this subsection. A 6-slot/10-pole sub-motor, which is the sub-motor of 12-slot/20-pole and 24-slot/40-pole VPMSMs, is used as an example. At the position of d-axis, the waveforms of the winding function considering the slot and the fundamental component of PM flux density for the 6-slot/10-pole sub-motor are shown in 180 electrical degrees in Fig. 5.3.

It can be seen that the unified slot function is a step function whose value is 1 under the span of stator tooth arc and 0 under the span of stator slot. Because there are N_s stator teeth evenly distributed along 360° mechanical degrees, its Fourier series $F_{wA}(\theta)$ is given by (5.4).

$$F_{wA}(\theta) = \alpha + \frac{2}{\pi}\sum_{i=k}^{\infty}\frac{1}{k}\sin(k\alpha\pi)\cos(kN_s\theta) \tag{5.4}$$

where α is the DC component of the unified slot function because it only has positive values in one mechanical period, α equals the ratio of stator tooth arc to stator tooth pitch, k is a positive integer, and θ is the air-gap circumferential position in mechanical degree.

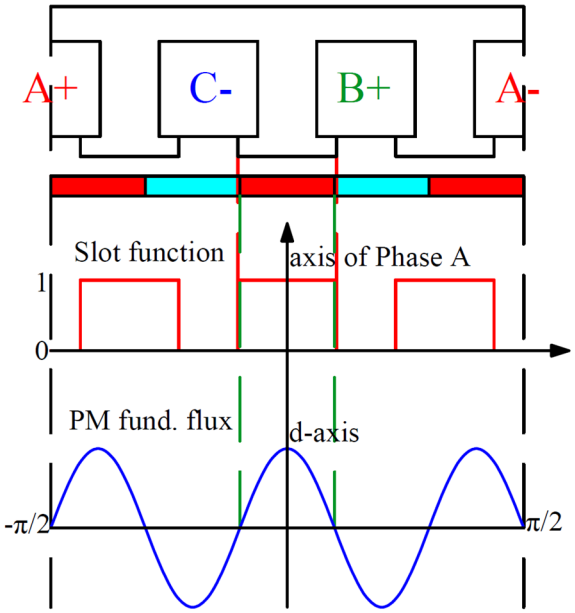

Fig. 5.3 Slot function and fundamental harmonic of a 6-slot/10-pole motor.

When the d-axis is aligned with the axis of Phase A, the waveform of the fundamental component of the air-gap PM flux density can be written as:

$$B_r(\theta) = B_{\mathrm{PM1}} \cos(p_r \theta) \tag{5.5}$$

where B_{PM1} is amplitude of the fundamental flux density.

For an N_s-slot/p_r-pole VPMSM, the phase flux linkage at d-axis ψ_{d} can be derived by:

$$\begin{aligned}
\psi_{\mathrm{d}} &= N_p r_g l_{ef} k_{d1} \int_{\frac{-\pi}{2(N_s-p_r)}}^{\frac{\pi}{2(N_s-p_r)}} F_{wA}(\theta) B_r(\theta) d\theta \\
&= N_p r_g l_{ef} B_{\mathrm{PM1}} k_{d1} \int_{\frac{-\pi}{2(N_s-p_r)}}^{\frac{\pi}{2(N_s-p_r)}} \alpha \cos(p_r \theta) \\
&\quad + \frac{1}{\pi} \sum_{i=k}^{\infty} \frac{1}{k} \sin(k\alpha\pi) \cos((kN_s + p_r)\theta) + \frac{1}{\pi} \sum_{i=k}^{\infty} \frac{1}{k} \sin(k\alpha\pi) \cos((kN_s - p_r)\theta) d\theta \\
&= N_p r_g l_{ef} B_{\mathrm{PM1}} k_{d1} \left(\frac{2\alpha}{p_r} \sin\left(\frac{\pi p_r}{2(N_s - p_r)} \right) + \sum_{i=k}^{\infty} \frac{2\sin(k\alpha\pi)}{\pi k (kN_s \pm p_r)} \sin\left(\frac{\pi(kN_s \pm p_r)}{2(N_s - p_r)} \right) \right)
\end{aligned} \tag{5.6}$$

where r_g is the radius of the air gap and k_{d1} is the coefficient caused by the distribution of coils in a

single phase.

It should be noted that in VPMSMs, the following relationship exists:

$$\begin{cases} kN_s - p_r >> N_s - p_r, k \neq 1 \\ kN_s + p_r >> N_s - p_r \end{cases} \tag{5.7}$$

Hence, (5.6) can be approximated as

$$\psi_{\mathrm{d}} \approx N_p r_g l_{ef} B_{\mathrm{PM1}} k_d \left(\frac{2\alpha}{p_r} + \frac{2\sin(\alpha\pi)}{\pi(N_s - p_r)}\right) \tag{5.8}$$

In a PM machine, the fundamental back-EMF can be expressed as:

$$\begin{aligned} E_1 &= 2\pi f \psi_d \\ &= \frac{2\pi n}{60} N_p r_g l_{ef} B_{\mathrm{PM1}} k_{d1} \left(2\alpha + \frac{2p_r \sin(\alpha\pi)}{\pi(N_s - p_r)}\right) \\ &= \frac{2\pi n}{60} N_p r_g l_{ef} B_{\mathrm{PM1}} k_{d1} \left(2\alpha - \frac{2\sin(\alpha\pi)}{\pi \mathrm{G_r}}\right) \end{aligned} \tag{5.9}$$

where f is the electrical frequency.

The variations of the fundamental harmonics of phase flux linkage with G_r for the VPMSM candidates are calculated by FEA and shown in Fig. 5.4 (a). It can be seen that for the machine candidates with the same slot number, the fundamental flux linkage increases with the increase of G_r.

When the number of slots is fixed, for well-designed VPMSMs with different number of PM poles, the geometric structure changes gradually because the PM pole number changes gradually as shown in Table 5.2. Under this circumstance, it can be seen from (5.9) that the back EMF is influenced largely by G_r because it varies significantly with the change of PM pole number as shown in Table 5.1. The variations of the back-EMF fundamental harmonics with G_r are calculated by FEA. Fig. 5.4 (b) shows that for the machine candidates with the same slot number, the back EMF increases with the increase of G_r. This is consistent with (5.9).

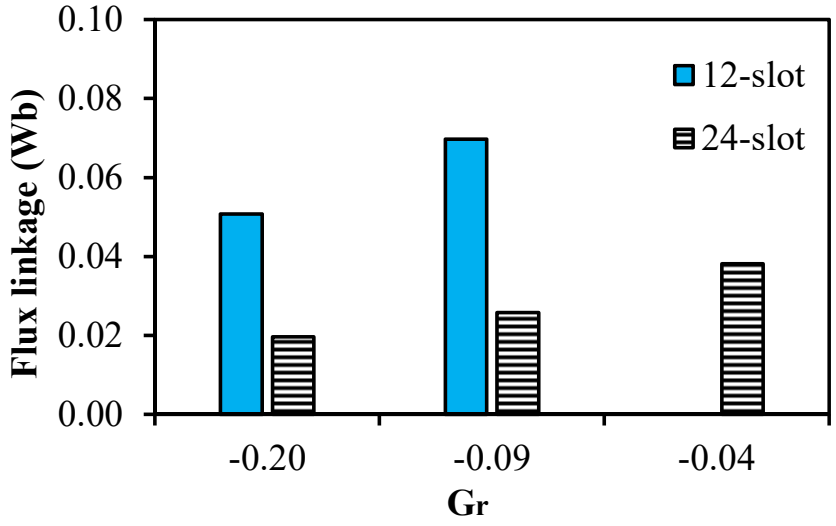

(a) Flux linkage

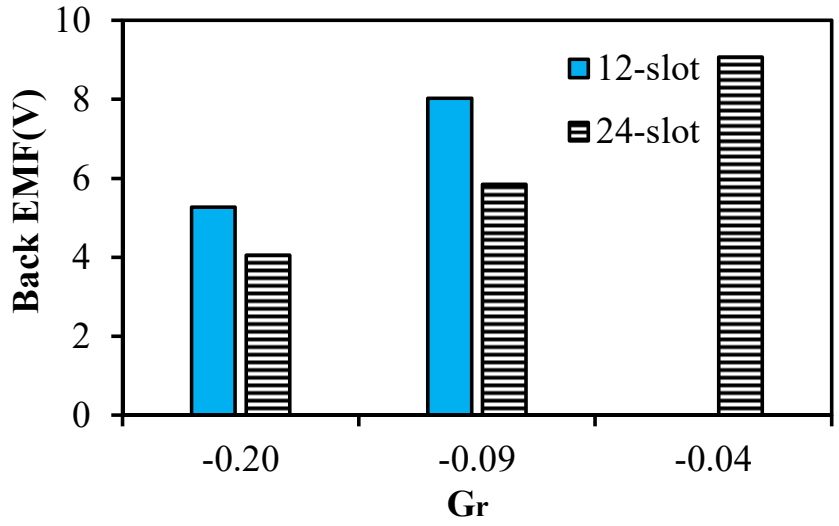

(b) Back EMF (100rpm)

Fig. 5.4 Flux linkage and back EMF vs G_r.

It can also be seen that for the VPMSMs with the same G_r, the 24-slot machines have less flux linkage and back-EMF than the 12-slot machines. The difference of flux linkage can be explained from (5.8). For the VPMSMs with the same G_r, the one with higher slot number has larger p_r and N_s-p_r, which leads to a lower flux linkage. The difference of back-EMF between machines with same G_r but different slot/pole number combinations depends on the air-gap leakage flux. For the machines with same G_r but different slot number, the PM pole number changes significantly. Under the same air-gap length, a higher PM pole number means a larger percentage of leakage flux per pole. Fig. 5.5 shows the PM flux lines of 12-slot/20-pole and 24-slot/40-pole VPMSMs in 180 mechanical degrees. It can

be seen that the 12-slot/20-pole VPMSM has a lower percentage of air-gap leakage flux per pole than the 24-slot/40-pole VPMSM. Consequently, although the electrical frequency of the 24-slot/40-pole VPMSM is twice as much as that of the 12-slot/20-pole VPMSM, the phase flux linkage of the 24-slot/40-pole VPMSM is less than half of the 12-slot/20-pole VPMSM, which leads to a smaller back-EMF in the 24-slot/40-pole VPMSM according to (5.9).

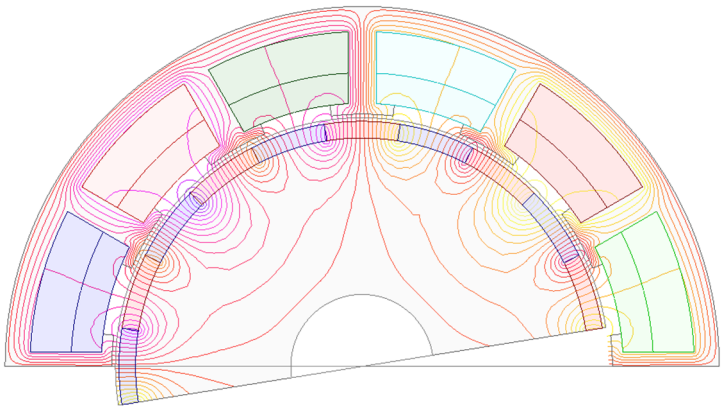

(a) 12-slot/20-pole

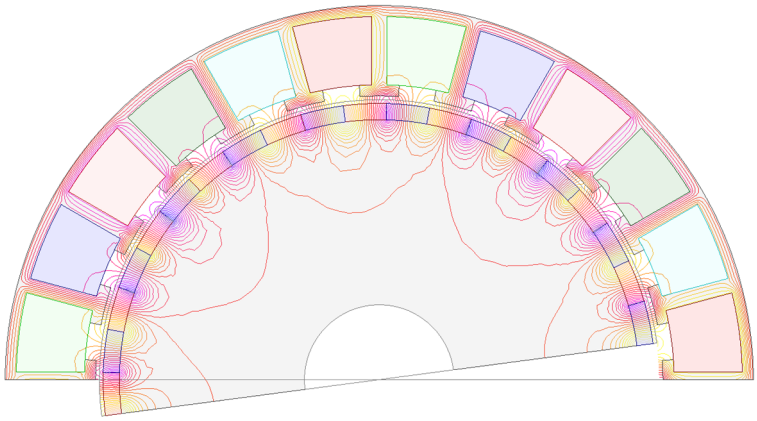

(b) 24-slot/40-pole

Fig. 5.5. No-load flux lines.

Based on the analysis above, it should also be noted that the findings regarding the back-EMF of VPMSMs with the same slot number but different G_rs in this chapter only apply for VPMSMs with surface-mounted PMs and reasonably small air-gap length. For special designs with large air-gap length, the advantage of VPMSM with larger G_r could be compromised by the large air-gap length and the findings may not be applicable.

5.4.2 Influence of Gear Ratio on Torque Capability

For an electrical machine without saliency torque, the electromagnetic torque can be determined by:

$$T_0 = \frac{mE_1 I_q}{2\Omega_r} \tag{5.10}$$

where m is the number of phases, Ω_r is the mechanical speed of the rotor (in rad/s) and I_q is the amplitude of the phase current.

The torque with respect to q-axis current of the machine candidates is shown in Fig. 5.6 (a). It can be seen that for the machine candidates with the same slot number, under the same current, the torque increases with the increase of G_r. This is because the back-EMF increases with the increase of G_r and it is proportional to the electromagnetic torque once the current is fixed. Since the magnetic gearing effect is the main torque production principle of VPMSMs, it also proves that a higher G_r means a stronger magnetic gearing effect between the armature reaction magnetic and the PM fields.

Under the same 75W copper loss, the influence of G_r on the average value of electromagnetic torque is calculated by FEA and the results are shown in Fig. 5.6 (b). It shows that under the same slot number, the advantage of the machine with a larger G_r can be compromised by a longer end winding. Fig. 5.6 (c) shows the contribution of copper loss generated by end windings to the total copper loss. It shows that under the same slot number, with the increase of G_r, the contribution of end windings to the total copper loss increases as a result of increased end winding length. For the machines with the same G_r, the one with a high slot number has a larger number of sub-motors and shorter end winding length. The contribution of the end winding to the total copper loss is therefore smaller in the one with a high slot number. Obviously, the longer the axial length, the percentage of the copper loss generated by the end windings will be lower, the larger the advantage will be.

It can also be seen that for the VPMSMs with the same G_r, the 24-slot machines have lower torque output than the 12-slot machines under the same current. This is consistent with the back EMF performance and can be explained by (5.10).

With the increase of the current, the torque waveform enters its saturation regime more quickly when the machine has a larger G_r. This means that the overload capability decreases with the increase of G_r. This can be explained from Table 5.2, the machine with a larger G_r has a longer coil pitch τ, which makes it easier for the stator yoke to be saturated at larger current excitation. This means that the torque

advantage of the machines with larger G_r will be compromised at high saturation level. Fig. 5.7 shows the flux density distribution of the 12-slot/20-pole, 12-slot/22-pole and 24-slot/40-pole VPMSMs at overload condition. It shows that the 12-slot/20-pole VPMSM has a less saturated stator yoke than the 12-slot/22-pole one due to a much shorter coil pitch.

Fig. 5.6 (a) also shows that under the same G_r, the machines with a larger number of slots have better overload capability than those with smaller number of slots. For the VPMSMs with the same G_r, the one with larger slot number has more sub-motors periodically distributed along the machine. In each sub-motor, the number of turns per coil decreases with the increase of slot number, both of them promises a shorter coil pitch, lower electrical loading and makes the machine less sensitive to saturation. This is also proved in Fig. 5.7. The 12-slot/20-pole VPMSM has a more saturated stator yoke than the 24-slot/40-pole one due to longer coil pitch and less PM poles.

In slotted PM machines, cogging torque can cause speed ripples and induces vibration at low load and speed [ZHU00]. Although there are many methods to reduce the cogging torque, such as rotor skewing, employing auxiliary slots, magnet shaping, etc., they require a more complicated structure which is difficult to manufacture and assemble. It has been proven in [LI16] that Vernier machine has sinusoidal back-EMF waveform and inherent smooth electromagnetic torque. Therefore, it is important to select a proper slot/pole combination with inherent low cogging torque at the design stage. In [ZHU00], the "goodness" of slot/pole combination, which is defined as

$$C_T = \frac{2p_r N_s}{N_c} \tag{5.11}$$

is used as an index in evaluating the cogging torque amplitude, where N_c is the least common multiple of the $2p_r$ and N_s. It has been analytically proven in [ZHU09a] that for a given slot number, the smaller the "goodness" factor is, the smaller the cogging torque will be.

The relationship between C_T and G_r for different machines are given in Fig. 5.6 (d). For the VPMSMs investigated in this chapter, C_T has a decreasing trend with the increasing of G_r. It should be noted that C_T is twice of the number of sub-motors N_{sm}. From Table 5.2, the number of periodicity in the VPMSM decreases with the increase of the number of PM poles. Hence, it can be concluded that for the VPMSMs with the same slot number, the cogging torque decreases with the increase of G_r. For the VPMSMs with the same G_r, the cogging torque decreases with the increase of slot number.

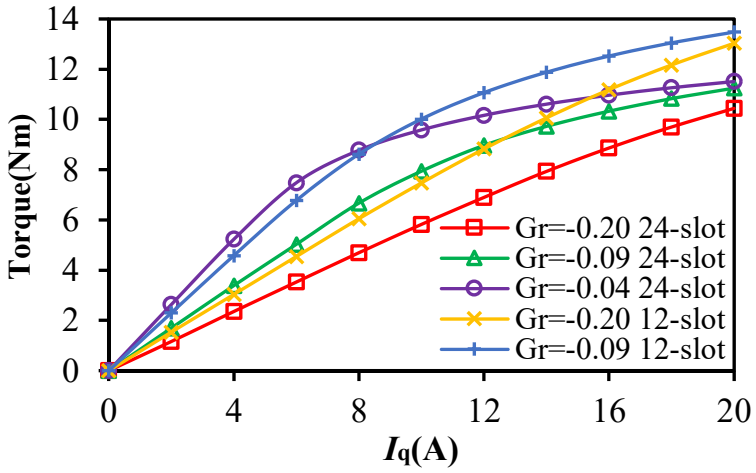

(a) Torque vs I_q

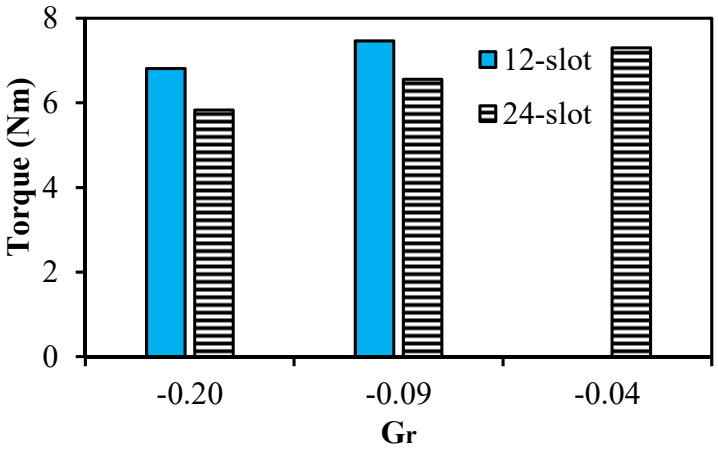

(b) Torque @ the same thermal loading

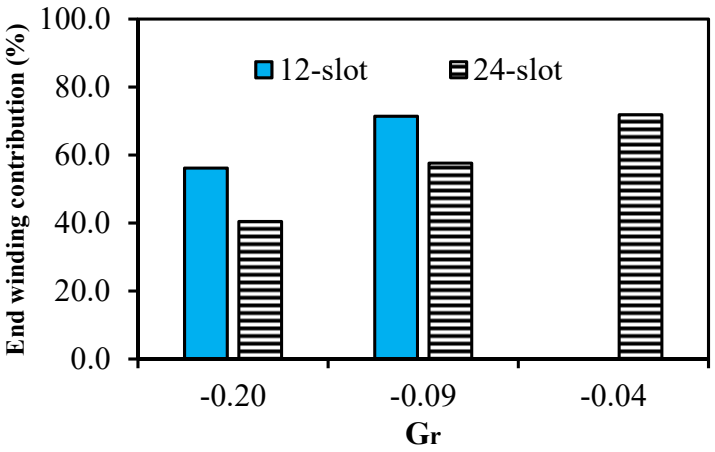

(c) Contribution of end windings to copper loss

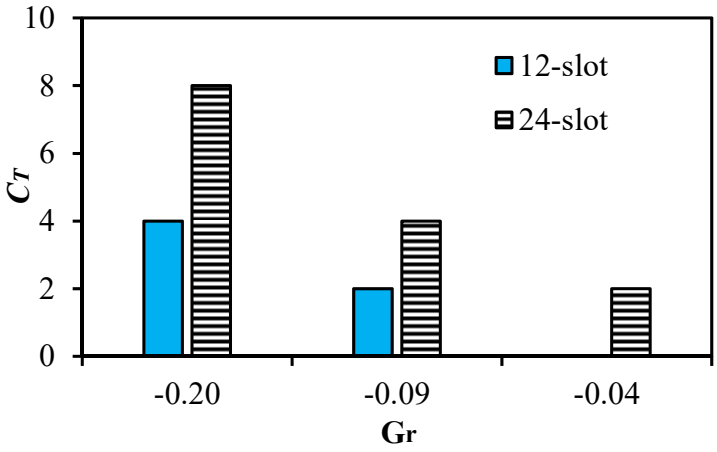

(d) "Goodness" factor vs G_r

Fig. 5.6 Torque capability vs G_r.

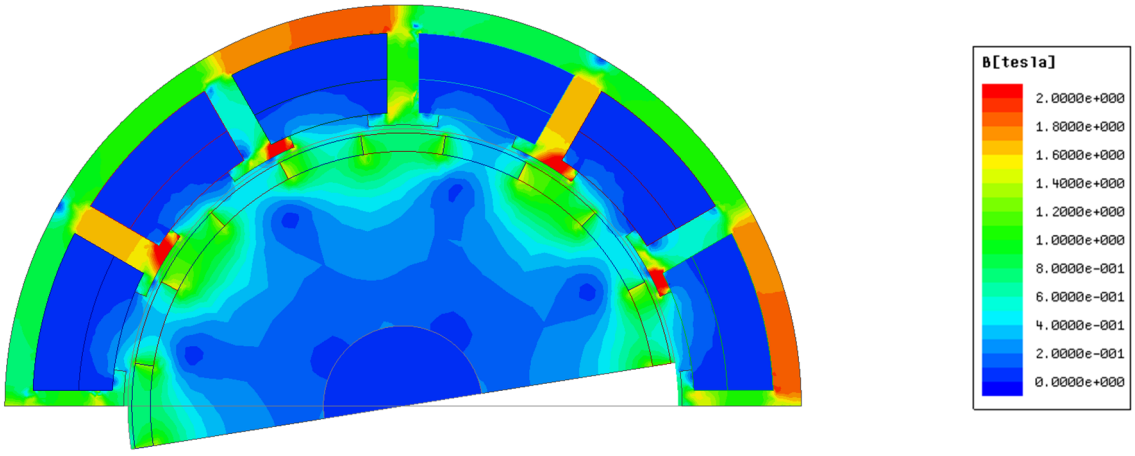

(a) 12-slot/20-pole

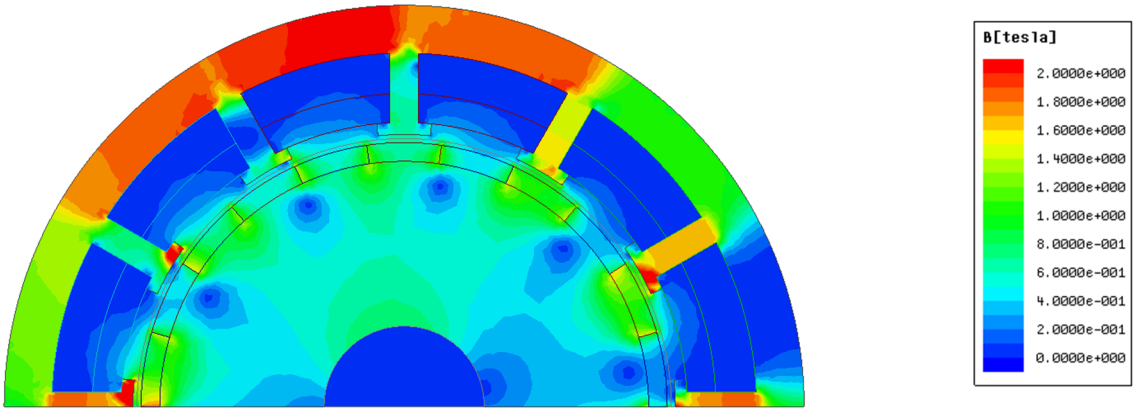

(b) 12-slot/22-pole

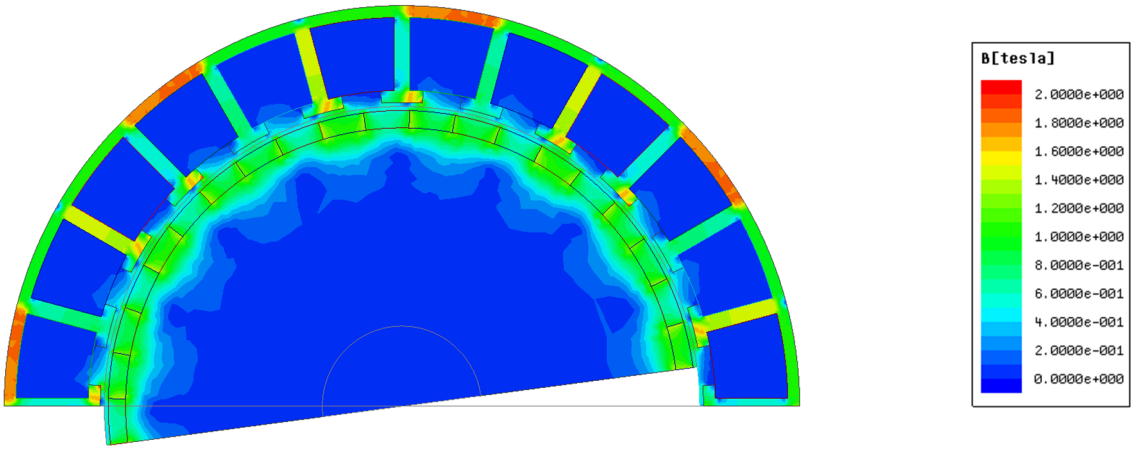

(c) 24-slot/40-pole

Fig. 5.7 Flux density distribution at overload condition (20A).

5.4.3 Influence of Gear Ratio on Inductance

One of the major problems for the VPMSM is that it has a smaller magnet flux per pole but larger d-axis inductance L_d, which makes its characteristic current [ELR05], defined as

$$I_{ch} = \frac{\psi_{PM}}{L_d} \tag{5.12}$$

much smaller than its rated current. Considering flux-weakening capability, the VPMSMs might have a smaller constant torque speed regime than PM machines of other types.

For VPMSMs investigated in this chapter, the phase self-inductance can be approximated as:

$$\begin{aligned} L_s &\approx \frac{N_p^2 r_g l_{ef} k_{d1}}{N_s - p_r} \int_{\frac{-\pi}{2(N_s-p_r)}}^{\frac{\pi}{2(N_s-p_r)}} P_0 F_{wA}(\theta) d\theta \\ &= \frac{N_p^2 r_g l_{ef} \pi \alpha P_0 k_{d1}}{(N_s - p_r)^2} \end{aligned} \tag{5.13}$$

where P_0 is the amplitude of the equivalent airgap permeance. For full pitch, distributed winding PMSMs, the d-axis inductance is approximately 1.5 times of self-inductance and the mutual inductance is approximately 0.5 times of self-inductance. It can be seen from (5.13) that the inductance is influenced largely by the difference between N_s and p_r because it varies more significantly than other parameters with the change of PM pole number. Under the same slot number, with the increase of G_r, the difference between N_s and p_r becomes smaller, and then d-axis and mutual inductances increase.

The influence of G_r on L_d for the VPMSMs is calculated by FEA and shown in Fig. 5.8. It shows that for the machines with the same slot number, L_d increases with the increase of G_r. This is consistent with the conclusion drawn from (5.13). For the VPMSM with same G_r but different slot number, the VPMSM with larger slot number has smaller L_d. This is because for the machines with same G_r, the one with higher slot number has a larger value of N_s-p_r, according to (5.13), it has smaller inductance.

The magnetic coupling between the phases should be as weak as possible so that the healthy phases can work properly when the other phases are under faulty condition. Thus, the mutual inductance between phases acts as an index for evaluating the magnetic coupling between phases. The absolute values of mutual inductance $|L_m|$ between phases are also provided in Fig. 5.8. For the VPMSMs with the same slot number, $|L_m|$ increases with the increase of G_r. For the VPMSMs with the same G_r, $|L_m|$ decreases with the increase of slot number. The reason for this relationship is the same with that for L_d.

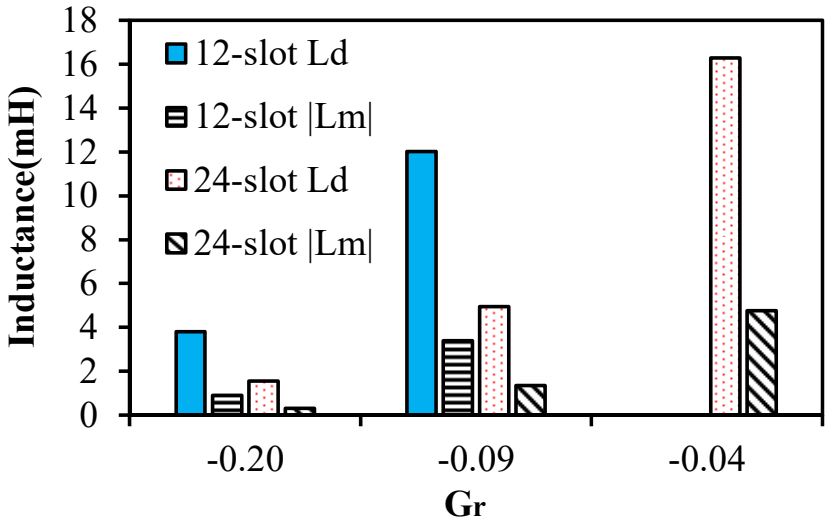

Fig. 5.8 Inductance vs G_r

5.4.4 Influence of Gear Ratio on Power Factor

It has been mentioned in various literatures that VPMSM has a low power factor which hinders its application when considering the optimum combination between the machine and the inverter. The lower power factor means an inverter of larger size and higher cost will be needed under the desired power output. When the VPMSM is under I_d=0 control and the resistance and end leakage inductance of the stator coils are ignored, the relationship between I_q, E_1, L_q ,U_1 and φ are provided in Fig. 5.9 (b). In this case, the phasors of I_q and E_1 are in the same direction, the voltage phasor produced by the stator current has 90 electrical degrees difference from E_1, and U_1 is the resultant phasor of terminal

voltage. In this case, the power factor can be expressed as:

$$\cos\varphi = \frac{E_1}{\sqrt{E_1^2 + (I_q \omega L_q)^2}} = \frac{1}{\sqrt{1 + (\frac{I_q L_q}{\psi_d})^2}} \tag{5.14}$$

It can be seen from Fig. 5.4 and 5.8 that when the slot number is fixed, with the increase of G_r, L_d increases faster than ψ_d does. In surface-mounted PM machines, the value of L_q is close to L_d. Hence, with the increase of G_r, L_q increases faster than ψ_d does, and according to (5.14), the power factor decreases. Similarly, under the same G_r, with the increase of slot number, L_q decreases more slowly than ψ_d does, and therefore, the power factor decreases. The power factors of the candidate machines are calculated in FEA and shown in Fig. 5.9. It shows that for the VPMSMs with the same slot number, the power factor decreases with the increase of G_r; for the VPMSMs with the same G_r, the power factor decreases with the increase of slot number, which are consistent with the above analyses.

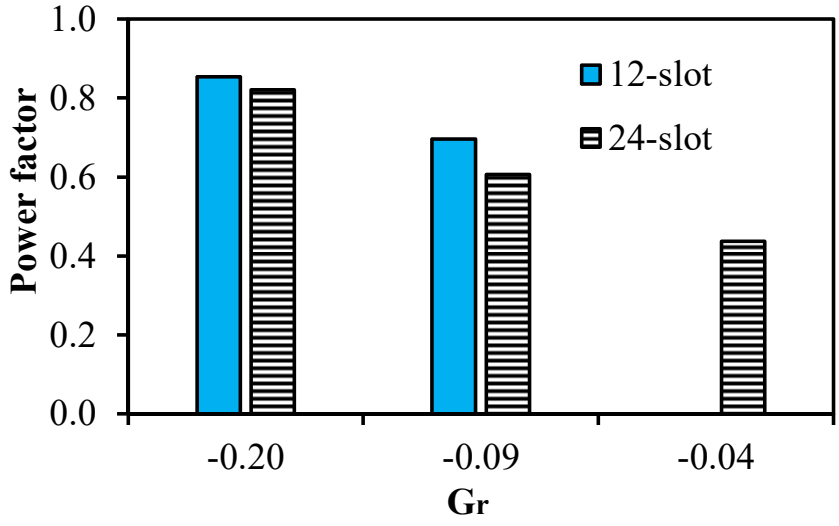

(a) Power factor vs G_r (75W copper loss)

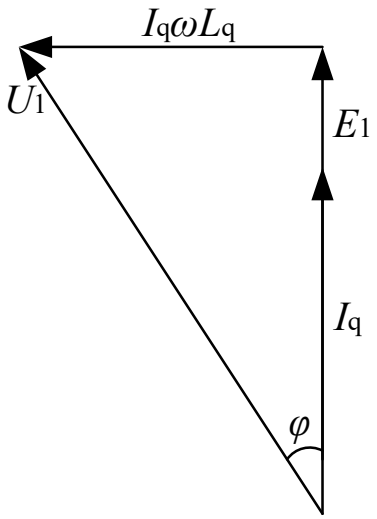

(b) Phasor diagram at I_d=0 control

Fig. 5.9 Power factor in candidate machines.

5.4.5 Influence of Gear Ratio on Losses

In PM machines, the rotor iron losses in one element can be calculated by the Bertotti losses equation, which is given by:

$$P(t) = k_f \left\{ k_h B_m^2 f + \sigma \frac{d^2}{12} \int_T \left(\frac{\mathrm{d}B}{\mathrm{d}t}(t) \right)^2 \frac{1}{T} + k_e \int_T \left(\frac{\mathrm{d}B}{\mathrm{d}t}(t) \right)^{1.5} \frac{1}{T} \right\} \tag{5.15}$$

where d is the depth of the steel lamination, k_f is the lamination factor, B is the value of flux density on the rotor core, B_m is its maximum value, σ is the conductivity of the rotor core, f is the fundamental frequency of the variation of B in the element, T is the electrical period, k_h and k_e are the hysteresis and excess loss coefficients respectively. The three items at the right side of the equation represent hysteresis losses, classical eddy current losses and excess losses respectively.

It has been discussed in Section 5.2 that for VPMSMs, the fundamental armature reaction harmonic with the pole pair number of p_s has a large amplitude and different speed of rotation with the rotor. Hence, the rotor iron loss needs to be considered for VPMSMs. The corresponding frequency induced in the rotor f_{rv} is shown as

$$f_{rv} = n_r N_s \tag{5.16}$$

The influence of G_r on the rotor and stator iron losses and PM loss are calculated by FEA under the

same working condition and the results are shown in Fig. 5.10. For the same slot number, the PM loss, rotor and stator iron losses increase with the increase of G_r. This is because with the increase of G_r, the amplitude and the wavelength of the p_sth armature reaction field increases, which results in a larger PM loss and rotor iron loss under the same f_{rv}. A larger G_r also indicates a more saturated stator (as shown in Fig. 5.7) and higher frequency on the stator, which leads to larger stator iron losses according to (5.15).

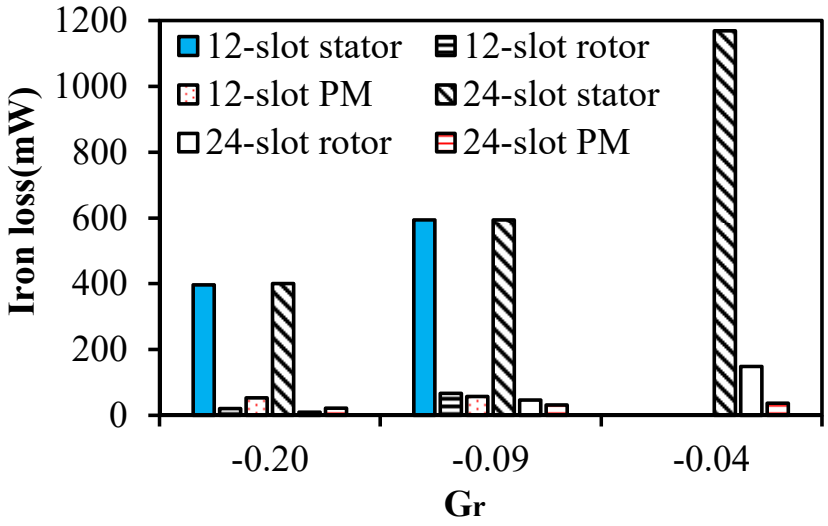

Fig. 5.10 Losses vs G_r (100rpm, 75W copper loss).

5.5 Experimental Validation

In this section, 12-slot/20-pole and 22-pole VPMSMs are manufactured and their performance are tested to validate the analyses in the above sections, Fig. 5.11. The main dimensional parameters of the prototypes are given in Table 5.3.

Firstly, the back-EMF waveforms of the machines are tested at 100rpm and compared with the FEA results, as shown in Fig. 5.12 (a) and (d). It can be seen that the FEA predicted back-EMF waveforms for both machines agree well with the test waveforms. Fig. 5.12 (b) and (c) show the comparison of back-EMF spectra between the tested and FEA results for both VPMSMs. They show that for the fundamental harmonic, there are 5% and 6% discrepancies between the FEA predicted and tested results for the 12-slot/20-pole and 12-slot/22-pole VPMSMs, respectively, which is believed to be caused by end effect.

The static torques of the prototypes are measured. The experiments are done by using the same method

with Chapter 1 [ZHU09c]. Static torques of the two prototypes within 0–180 electric degrees under different current amplitudes are calculated by 2-D FEA and compared with measurements as shown in Fig. 5.12 (c) and (f), respectively. They also show that the 12-slot/22-pole VPMSM can generate larger torque than the 12-slot/20-pole VPMSM under the same current excitation since it has a larger G_r. The discrepancies (8.8% for 12-slot/20-pole and 8.7% for 12-slot/22-pole VPMSMs) between the FEA and measured results are due to manufacturing tolerance and severe end effect brought about by large PM pole number. For VPMSMs, the influence of PM pole number on the end effect will be put in the future work.

Table 5.3 Dimensional Parameters of Prototypes

Slot number	12	12
Pole number	20	22
Stator outer diameter(mm)	100	100
Stator inner diameter(mm)	70	68
Air-gap length(mm)	1	1
Turns per phase	118	100
PM height(mm)	2.3	2.3
PM pole arc	180° Elec.	180° Elec.
Slot opening angle	16° Mech.	19° Mech.

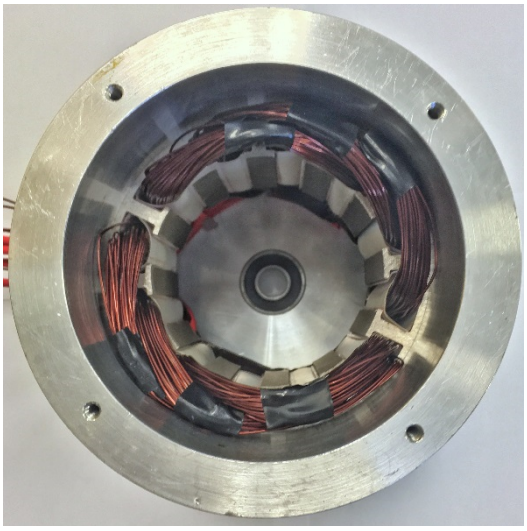

(a) 12-slot stator for 20-pole rotor

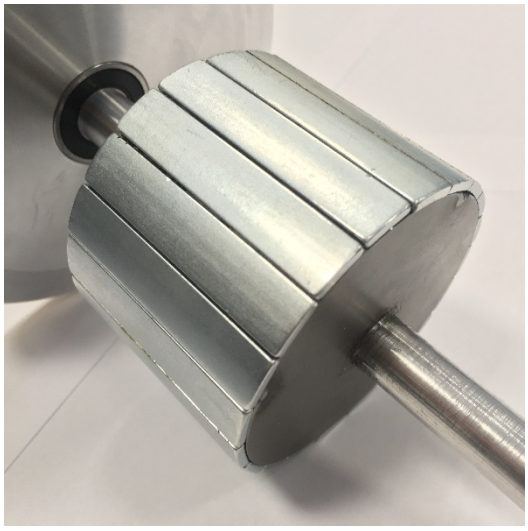

(b) 20-pole rotor

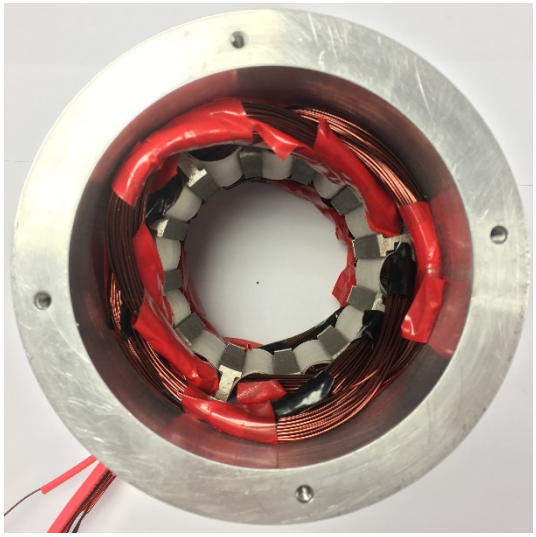

(c) 12-slot stator for 22-pole rotor

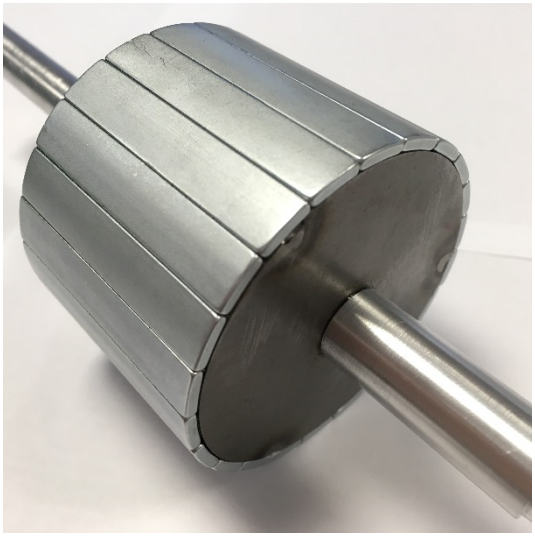

(d) 22-pole rotor

Fig. 5.11 Prototype photos and test rig.

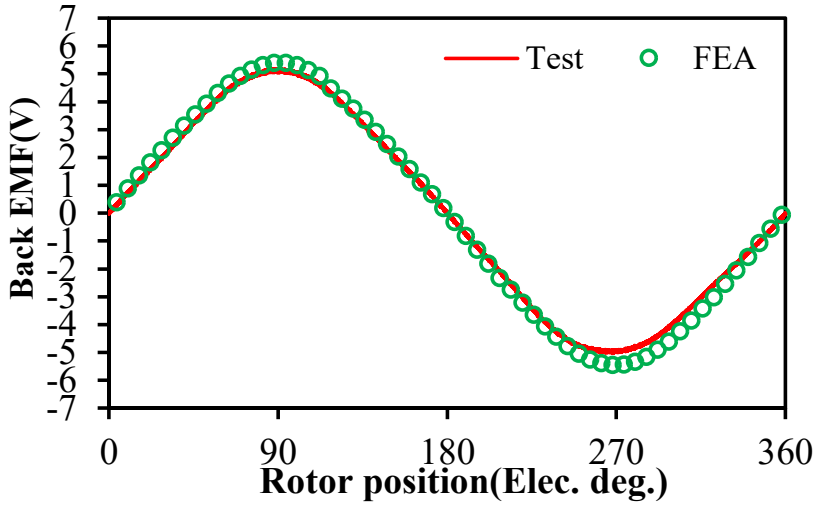

(a) Back-EMF waveform for 12-slot/20-pole machine at 100rpm

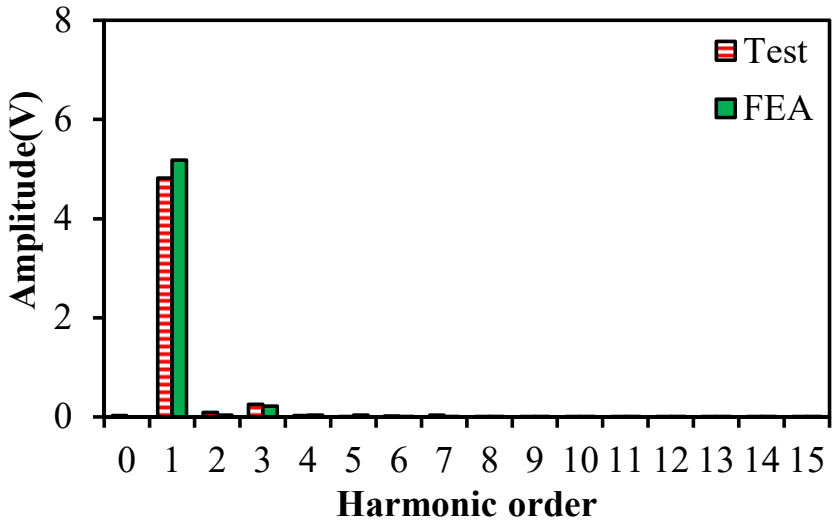

(b) Back-EMF spectrum for 12-slot/20-pole machine at 100rpm

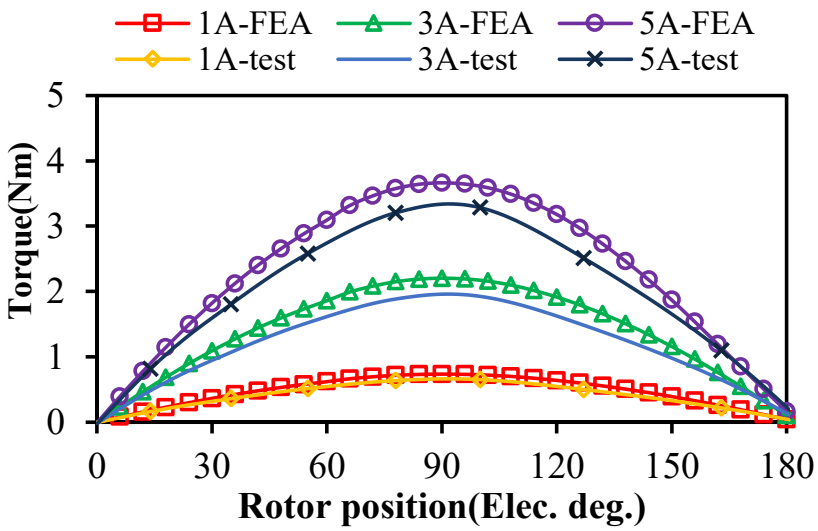

(c) Static torque waveforms for 12-slot/20-pole machine

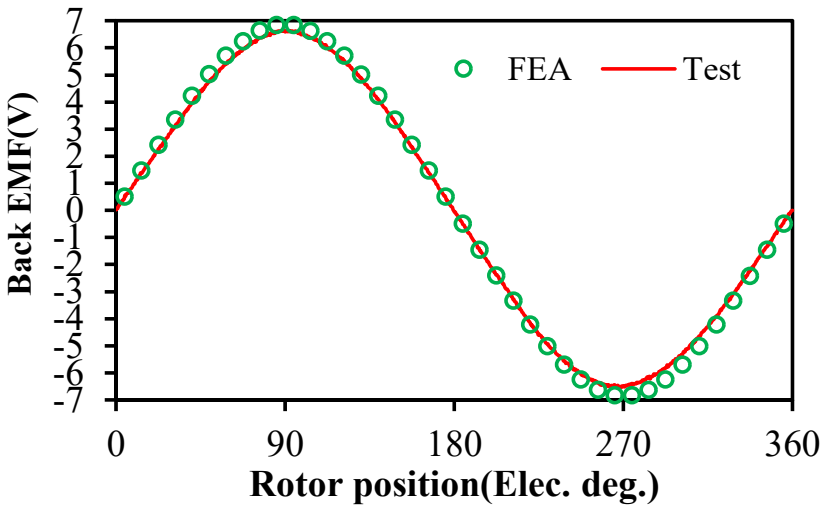

(d) Back-EMF waveform for 12-slot/22-pole machine at 100rpm

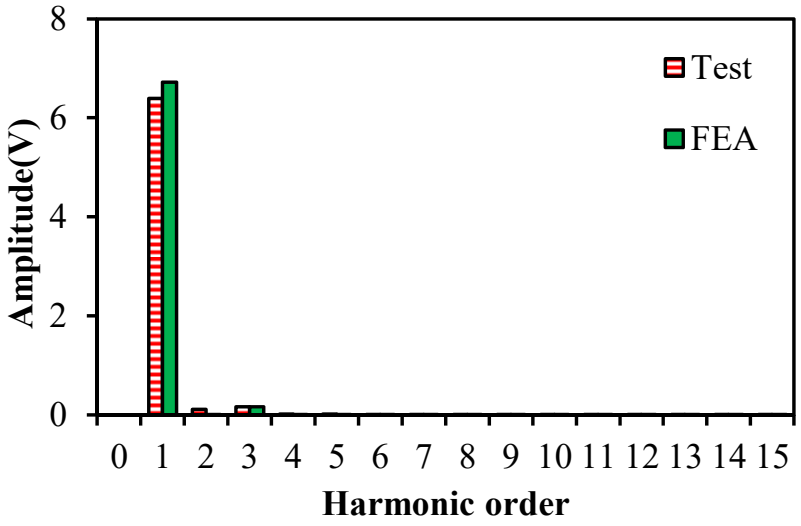

(e) Back-EMF spectrum for 12-slot/22-pole machine at 100rpm

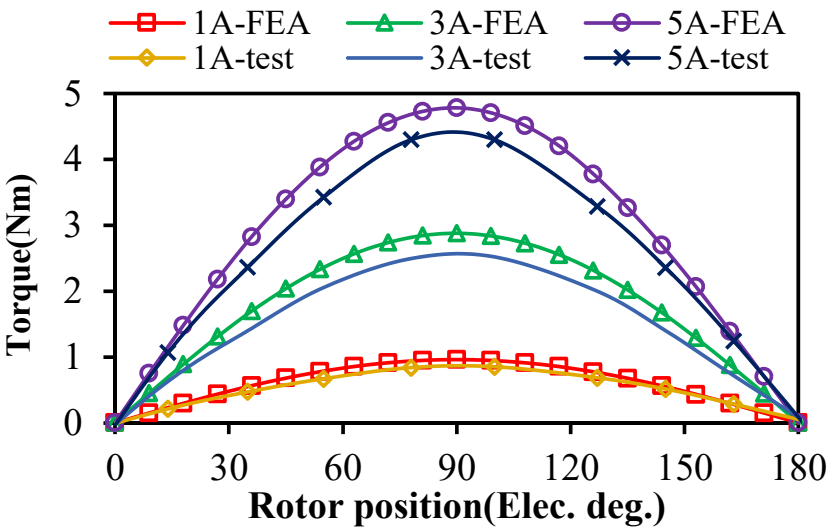

(f) Static torque waveforms for 12-slot/22-pole machine

Fig. 5.12 FEA waveforms vs test waveforms.

The d-axis and mutual inductances of the two prototypes are tested by a LCR meter by the method described in [LIU15] and the results are compared with FEA predicted results in Table 5.4. It can be seen that the FEA predicted results match well with the experimental results, and the 12-slot/22-pole machine has both larger d-axis and mutual inductances than the 12-slot/20-pole one as a consequence of larger G_r.

Table 5.4 Inductance of the Prototypes

Slot/pole combination		12-slot/20-pole	12-slot/22-pole
L_d(mH)	FEA	3.86	8.47
	Measured	3.97	8.53
$\|L_m\|$(mH)	FEA	0.92	2.39
	Measured	0.91	2.33

5.5 Summary

In this chapter, the magnetic gearing effect and the gear ratio in VPMSMs are introduced and employed to investigate its relationship between various electromagnetic performance of surface-mounted PM Vernier machines and different slot/pole number combinations. It is found that the gear ratio is not only a representation of the gearing effect, but also a good index parameter of the VPMSM once the slot/pole number combination is fixed. The influences of the gear ratio on various electromagnetic performance and geometries are investigated, thus proving that the gear ratio can be used as an index for performance comparison and selection of the appropriate slot/pole number combination at the machine design stage.

CHAPTER 6

Comparison of Torque Production of Integral Slot, Fractional Slot Concentrated Winding PM Machines and Vernier PM Machines

In this chapter, the torque production mechanism of integral slot distributed winding (ISDW), fractional slot concentrated winding (FSCW) permanent magnet synchronous machines (PMSMs) and Vernier PMSMs (VPMSMs) are firstly unified from two viewpoints: energy conversion and magnetic gearing effect. From the perspective of energy conversion, a slot opening coefficient will be proposed to show the influence of slot opening on torque production of different machine types. From the perspective of magnetic gearing effect, the influence of slot opening on the modulated, un-modulated air-gap magnetic flux density and torque contribution in different machines will be analysed. Both confirm that the VPMSM shares the same torque production mechanism with ISDW and FSCW PMSMs. Based on the analysis, the role which the slot opening plays in the torque production of different machine types and slot/pole combinations is revealed. Design guidelines for taking advantage of slot opening for different machine types are provided. Two prototypes are manufactured and tested for validation.

6.1 Introduction

Permanent magnet synchronous machines (PMSMs) have gained popularities as a result of high efficiency and high torque density. There are various kinds of PMSMs such as stator-PM machines with doubly salient structures [LIA95] [ZHU11b] [HUA18] [GAO17] [LI17], rotor-PM machines with integral slot distributed windings (ISDW) [ZHA16b] [LAS10] [BAR12], rotor PM machines with fractional slot concentrated windings (FSCW) [ELR10] [ISH05a] [ZHU11a], Vernier PMSMs (VPMSM) [KIM14] [LI16] [LI11], magnetically geared machines [ZHU18b] [CHE18] [JIA09] and so on.

Among all the aforementioned PMSMs, ISDW and FSCW PMSMs have been extensively researched and widely used as a consequence of simple structure and decent machine performance. They are considered as classical PM machines whose torque production mechanisms can be explained by classical machine theories such as the rotating field theory [HAN25] or energy conversion theory

[KRA13].

It is shown that VPMSMs have higher torque density than the conventional PM machines [FU10] [YAN13] and the conventional magnetically-geared machines with more than one airgap [LI11] [JIA09]. As stated in the previous chapters, VPMSMs have also attracted researchers' attention not only because of high torque density but also simple structure which is similar to ISDW and FSCW PMSMs: all of them have one stator wound with coils, one air gap and one rotor with PMs. Although the structure of VPMSMs is similar with ISDW and FSCW PMSMs, their torque production mechanism has not been unified. The main reason for this is that the most popular theory for explaining the torque production mechanism of VPMSM is the so-called magnetic gearing effect [TOB23] [QU11] [LIU17] or airgap flux modulation effect [CHE17]. Hence, VPMSMs are usually treated differently from conventional PMSMs regarding torque production mechanism.

In this chapter, the torque production mechanism of ISDW PMSM, FSCW PMSM and FSDW VPMSM will be firstly unified from two viewpoints: energy conversion and magnetic gearing effect. Both confirms that the VPMSM shares the same torque production mechanism with ISDW and FSCW PMSMs. The influence of slot opening on the torque is analysed from both viewpoints and the role which the slot opening plays in the torque production of different machine types will be revealed. Design guidelines for taking advantage of slot opening for different machine types and slot/pole combinations will be provided.

This chapter is organized as follows: In section 6.2, eight 12-slot PMSMs with different winding configurations and rotor PM pole numbers are selected and optimised. In section 6.3, the torque production of three kinds of machines will be analysed from energy conversion theory. Slot opening coefficient will be proposed to show the influence of slot opening on torque production among different machine candidates. In section 6.4, the torque production of the three kinds of machines will be analysed from magnetic gearing effect. The influence of slot opening on the modulated, un-modulated air-gap magnetic flux density and magnetic gearing effect in different machines will be compared. Finally, two prototypes are manufactured and tested for verification.

6.2 Machine Candidates for Comparison

To make a fair torque production mechanism comparison among different kinds of PMSMs, eight 12-slot PMSMs with different rotor pole numbers, Fig. 6.1, have been selected and optimised. 12-slot

PMSMs are selected because with this slot number, there are 2 ISDW PMSMs, 4 FSCW PMSMs and 2 FSDW VPMSMs, which provide enough machine candidates for comparison. The optimisation is carried out by the Maxwell software using genetic algorithm to achieve the maximum torque under the following constrains: (1) Fixed stator outer radius r_o; (2) Fixed air-gap length l_a; (3) Fixed stack length l_{ef}; (4) Fixed shaft radius; (5) When the end winding length is considered for different coil pitch, fixed copper loss at 75W. In the optimisation, the length of ending winding is estimated by measuring the span of a coil; (6) Fixed slot packing factor; (7) Fixed overall PM volume. The related dimensional parameters are illustrated in Fig. 6.1(a). During the optimisation, the stator yoke radius r_y, stator tooth width w_t, stator inner radius r_i, slot opening angle s_o and the PM height l_{pm} are variables. It should be noted that copper loss is the main loss and source of heating for the machine of this size at low speed, and 75W is selected within a reasonable copper loss range for the machine of this size. Therefore, all the machine candidates are optimised under the same thermal loading. The optimised geometries for all machines are shown in Fig. 6.1. The values of dimensional parameters are shown in Table 6.1,, where N_p is the number of turns per phase and τ is the coil pitch. The q-axis currents at 75W copper loss for all the machine candidates are also listed in Table 6.1.

It can be seen that the 12-slot/2-pole, 4-pole ISPMSMs and 20-pole, 22-pole VPMSMs adopt distributed windings whereas 12-slot/8-pole, 10-pole, 14-pole and 16-pole FSPMSM adopt concentrated tooth-coil windings. It is noteworthy that for any two machines investigated in this chapter, they are defined as a machine pair if their slot/pole combinations satisfy:

$$p_{rl} + p_{rh} = N_s \tag{6.1}$$

where p_{rl} and p_{rh} are the pole pair numbers of machines with lower and higher rotor PM pole pair numbers in the machine pair, respectively. Both machines in a machine pair share the same winding configuration and winding factor. The selected slot/pole number combinations in this chapter are grouped into four machine pairs as shown in Table 6.1. They are 12-slot/2-pole ISDW PM and 12-slot/22-pole FSDW VPM machine pair #1, 12-slot/4-pole ISDW PM and 12-slot/20-pole FSDW VPM machine pair #2, 12-slot/8-pole and 12-slot/16-pole FSCW PM machine pair #3 and 12-slot/10-pole and 12-slot/14-pole FSCW PM machine pair #4. VPMSMs are denoted by symbol (V) following the pole number in Table 6.1.

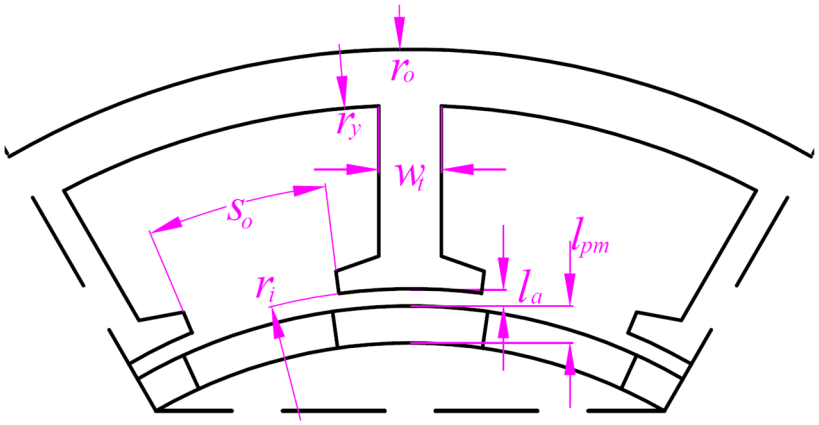

(a) Dimensional parameters

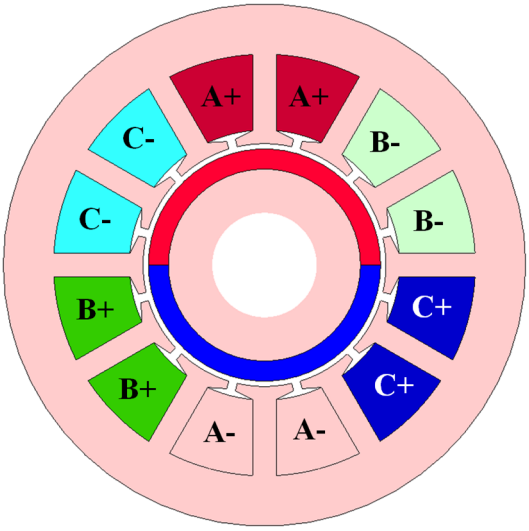

(b) 2-pole

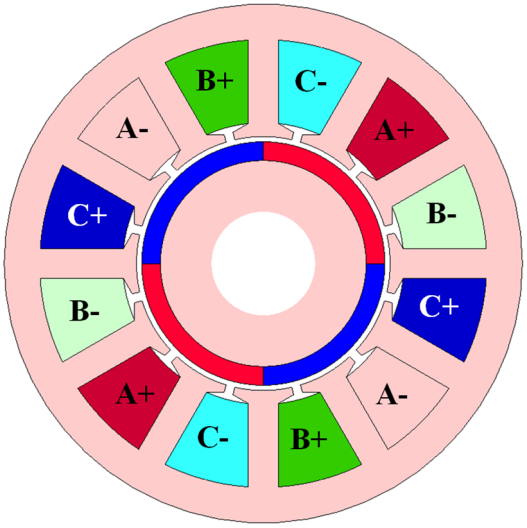

(c) 4-pole

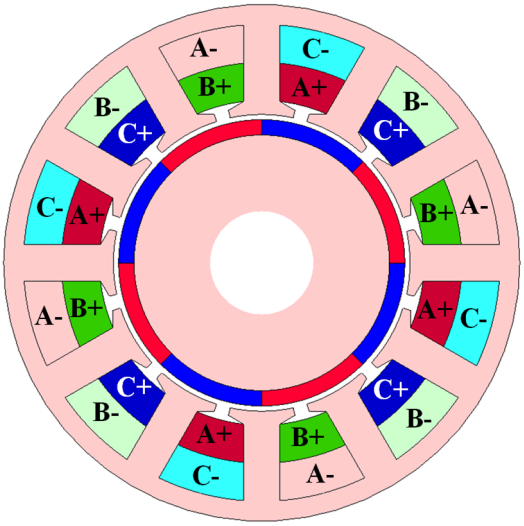

(d) 8-pole

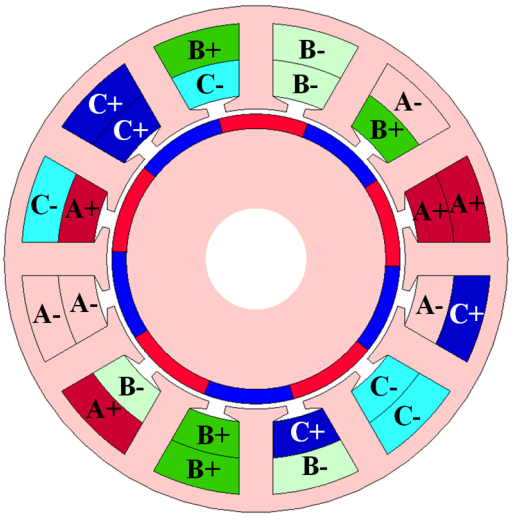

(e) 10-pole

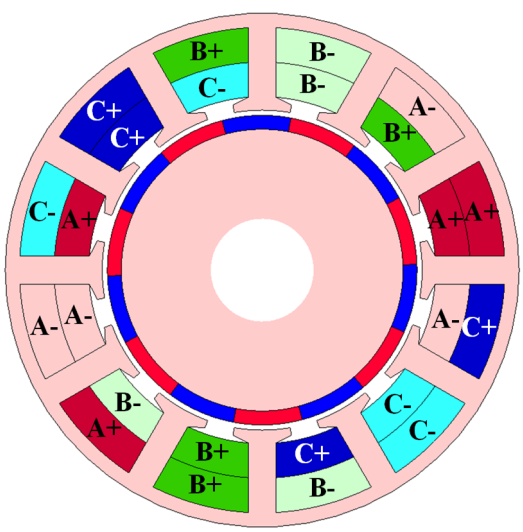

(f) 14-pole

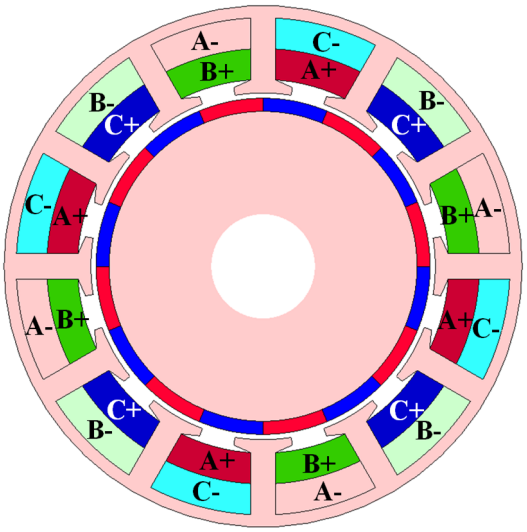

(g) 16-pole

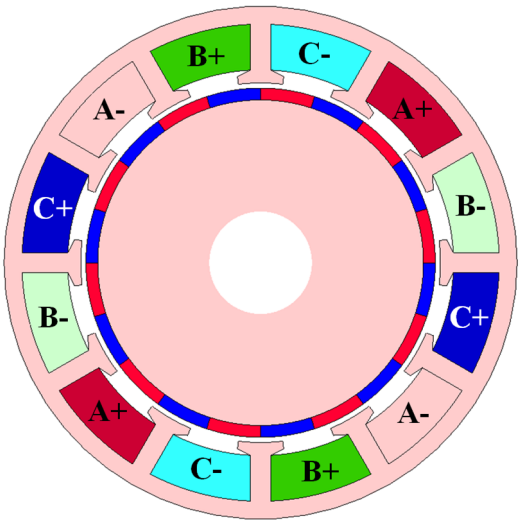

(h) 20-pole

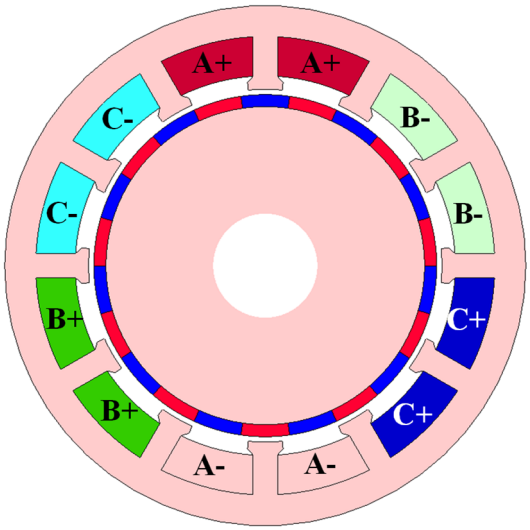

(i) 22-pole

Fig. 6.1 Optimised geometries of 12-slot machines.

Table 6.1. Dimensional Parameters of Optimised 12-Slot Machines.

N_s	12							
Machine pair	#1		#2		#3		#4	
$2p_r$	2	22(V)	4	20(V)	8	16	10	14
Winding	DW				CW			
r_o(mm)	50							
r_y(mm)	40.4	44.1	43.1	46.5	46.2	47.7	46.6	47.2
r_i(mm)	23.2	33.9	24.5	35.1	28.7	33.2	29.6	31.1
s_o(deg)	5.5	18.9	5.6	15.8	5.6	11.3	6.6	9.9
l_a(mm)	1							
l_{pm}(mm)	3.9	2.3	3.6	2.3	3.0	2.5	2.9	2.7
l_{ef}(mm)	50							
N_p	122	100	130	118	128	138	132	142
I_q (A)	7.28	8.00	8.82	9.27	11.48	11.01	11.27	10.86
τ	6		3		1		1	

The torque waveforms of the 12-slot machines with different PM pole numbers are calculated by FEA in an electrical period as shown in Fig. 6.2. The torque characteristics are provided in Table 6.2, in which T_0 is the average torque, T_{pp} is the peak-to-peak torque and T_{pp}/T_0 is the torque ripple index. It can be seen that in one machine pair, no matter the winding configuration is DW or CW, the machine with higher PM pole number has larger torque. The torque advantage is more significant in DW than in CW machine pairs. It should also be noted that within the machine pair, the one with higher torque has larger slot opening. The optimal slot opening angle increases with the increase of rotor PM pole number. The cogging torque waveforms for the machine candidates are provided in Fig. 6.2 (b). Their peak-to-peak values T_{cogpp} are shown in Table 6.2. It can be seen that the cogging torque is the main source of torque ripple in the machine candidates. The 12-slot/22-pole machine has the smallest torque

ripple index because it has the smallest cogging torque and largest average torque. The contribution of copper loss generated by end windings to the total copper loss is also shown in Table 6.2. It shows that the contribution of end wining increases with the increase of the coil pitch. In the machines with concentrated windings, the end windings contribute much smaller copper loss than those with distributed windings. In each machine pair, the contribution of end windings to the total copper loss is similar as they share the same winding configuration.

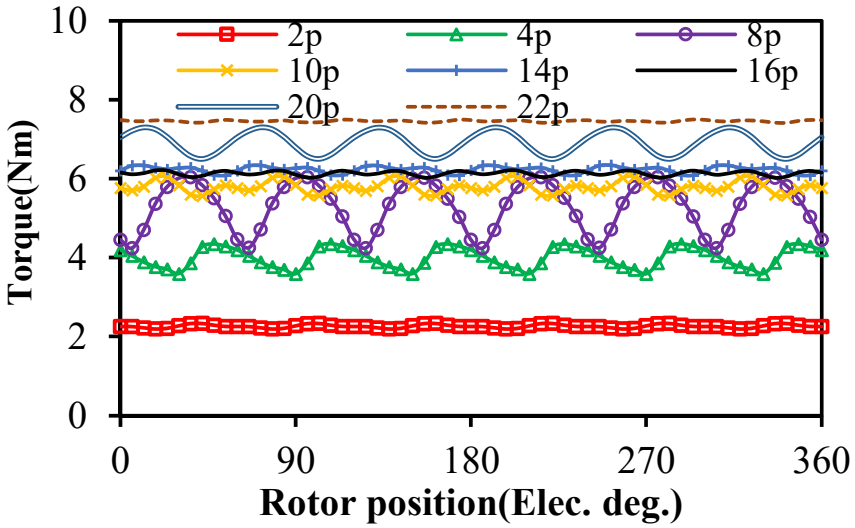

(a) Torque waveforms @75W copper loss

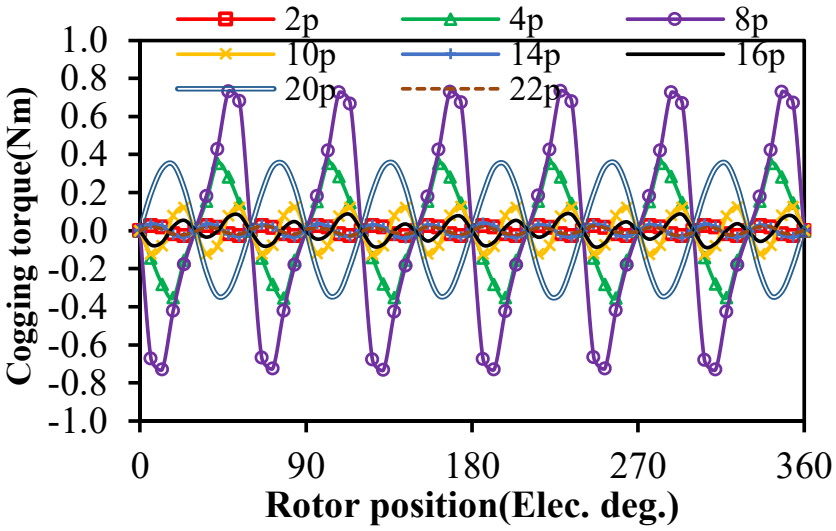

(b) Cogging torque waveforms

Fig. 6.2 Torque waveforms comparison.

Table 6.2. Torque Characteristics of 12-slot Machines.

$2p_r$	T_0(Nm)	T_{pp}(Nm)	T_{pp}/T_0(%)	T_{cogpp}(Nm)	$T_0/(\pi D^2 L/2)$ (Pa)	Contribution of end windings to copper loss (%)
2	2.3	0.1	6.2	0.1	13788	67.7
4	4.0	0.8	19.0	0.7	22160	53.3
8	5.3	1.8	34.1	1.4	21184	21.1
10	5.8	0.5	8.4	0.3	21794	21.0
14	6.2	0.3	4.1	0.1	21042	20.6
16	6.1	0.2	3.0	0.2	18125	20.6
20	6.9	0.8	11.6	0.7	18399	54.5
22	7.5	0.1	1.1	0.1	21413	69.7

6.3 Torque Production from Viewpoint of Energy Conversion

6.3.1 Introduction of Slot Opening Coefficient

From the perspective of energy conversion, the back-EMF of an electrical machine needs to be calculated first. The back EMF of an electrical machine can be written as:

$$E_1 = 2\pi f \psi_1 \tag{6.2}$$

where f is the electrical frequency and ψ_1 is the amplitude of the fundamental harmonic of phase flux linkage which can be derived by

$$\psi_1 = \frac{N_p \Phi_1 k_w}{\sigma_0} \tag{6.3}$$

where N_p is the number of turns per phase, k_w is the winding factor, σ_0 is the leakage coefficient and Φ_1 is the maximum flux which a PM pole can offer and can be derived as

$$\Phi_1 = \frac{2 B_{\mathrm{PM1}} r_g l_{ef}}{p_r} \tag{6.4}$$

where B_{PM1} is the amplitude of fundamental harmonic of PM flux density, r_g is the air gap radius.

For surface mounted PMSMs, the reluctance torque can be ignored and the electromagnetic torque can be calculated by:

$$T_0 = \frac{3E_1 I_q}{2\Omega_r} = \frac{3p_r \psi_1 I_q}{2} \tag{6.5}$$

Where I_q is the q-axis current and Ω_r is the mechanical speed(rad/s). It can be seen from (3) that ψ_1 has a decisive impact on the electromagnetic torque.

To highlight the difference of ψ_1 in the machine candidates, at no-load condition, the d-axis flux line distribution of two machine pairs: 12-slot/4-pole and 20-pole machine pair, and 12-slot/8-pole and 16-pole machine pair, are selected as examples as shown in Fig. 6.3. It shows that for the 12-slot/4-pole machine, the flux lines over less than one PM pole are linked to Phase A because there exists leakage flux caused by slot opening and air gap. For the 12-slot/20-pole machine, the flux lines from more than one PM poles can be linked to Phase A because the stator tooth arc is close to the PM pole arc. When it comes to the 12-slot/8-pole and 16-pole machine pair, it shows that a larger percentage of PM flux per pole in the 16-pole rotor is linked to Phase A than the 8-pole rotor. This is also because the 16-pole machine has a PM pole arc whose width is closer to the tooth arc.

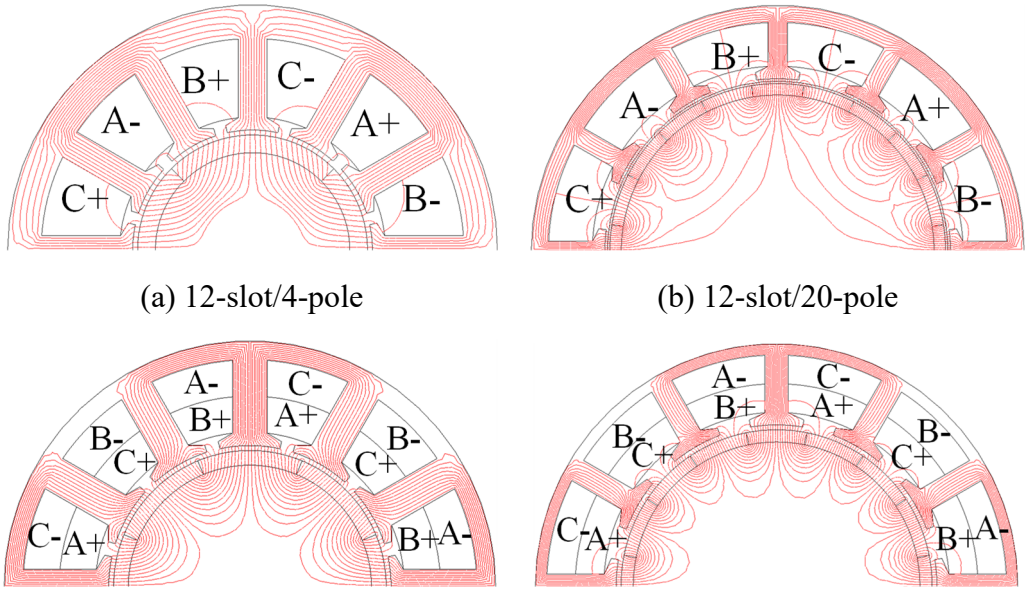

(a) 12-slot/4-pole (b) 12-slot/20-pole

(c) 12-slot/8-pole (d) 12-slot/16-pole

Fig. 6.3 Flux line distribution of machine candidates at no-load condition.

This indicates that in different PM machines, the utilisation rate of one PM, i.e. the percentages of flux linked to the stator per PM pole is different as a result of different slot/pole combination and slot openings. In conventional ways, the difference in the utilisation rate of a PM is expressed by the winding factor as shown in (6.3). The winding factors for all the machine candidates are shown in Table 6.3. It can be easily seen that the winding factor fails to be used as the PM utilisation rate indicator for comparison between the two machines (N_s-slot/$2p_{rl}$-pole and $2p_{rh}$-pole) in each machine pair as they share the same winding factor. Moreover, for VPMSMs such as the 12-slot/20-pole VPMSM, the flux lines from more than one PM poles can be linked to Phase A as shown in Fig. 6.3. This means that the utilisation rate is greater than 1. However, the maximum value of winding factor is 1. This is because that when winding factor is calculated, the influence of slot opening is not considered. However, as shown in Fig. 6.3, slot opening plays a crucial role in the PM utilisation rate which will in turn influence the torque. When the torques of different machine types in this chapter are compared, another parameter related to the slot opening is needed in addition to the winding factor.

6.3.2 Slot Opening Coefficient

To achieve this, linear models of the two machine pairs are built as shown in Fig. 6.4. A winding function considering the slot opening is used to reflect the winding distribution and the slot openings. The value of the winding function depends on the direction of current. The value of the winding function is 1 when the current is flowing from left to right side, then it is -1 when the current is flowing from right to left side. The span of this value is the same with the stator tooth arc. Over the slot opening, the value of the winding function is 0. The two machines in the same machine pair have the same winding function as a result of the same winding configuration. The waveforms of the fundamental PM flux density harmonic for the four machines are also shown in Fig. 6.4. If the leakage flux and fringing effect are not considered, the product of the winding function of each coil and PM fundamental flux density harmonic shows the portion of flux which can be linked from the PM poles to the stator side. The product of the winding function of each coil and PM fundamental flux density harmonic for the four machines in two machine pairs is shown in Fig. 6.4. It shows that in each machine pair, the machine with higher PM pole number has a larger percentage of flux per pole linked to the stator side.

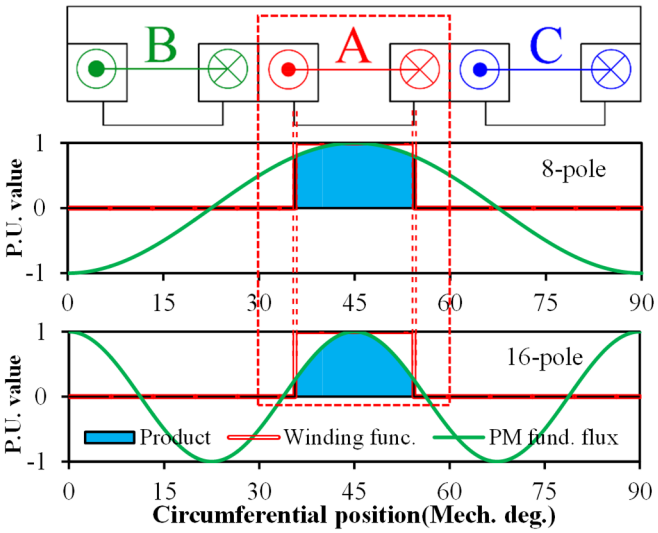

(a) 12-slot/8-pole and 16-pole

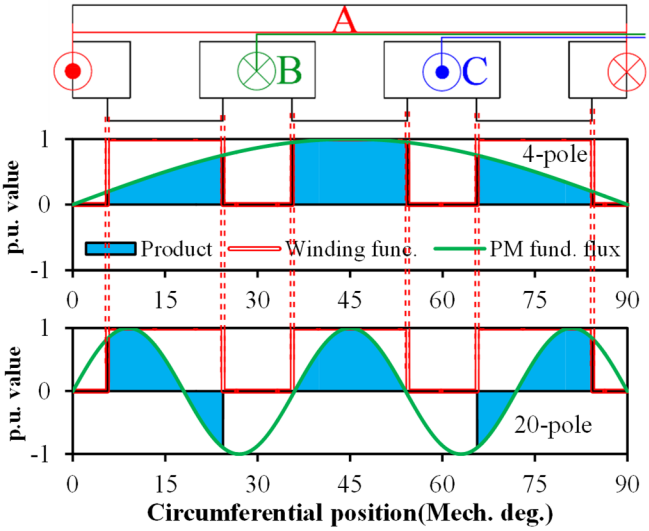

(b) 12-slot/4-pole and 20-pole

Fig. 6.4 Winding function and PM fundamental harmonic.

When the axis of a coil is aligned with d-axis as shown in Fig. 6.4, the flux linkage per turn in each coil φ_A can be derived by

$$\varphi_A = r_g l_{ef} \int_0^{\tau} F_{wA}(\theta, s_o) B_{PM} \cos(p_r(\theta - \theta_0)) d\theta \tag{6.6}$$

where F_{wA} is the winding function considering the slot opening for a coil, θ is the circumferential position and θ_0 is the initial rotor position which equals half of the coil pitch.

Hence, the flux linkage in each phase can be derived by

$$\psi_1 = N_p k_{d1} r_g l_{ef} \int_0^{\tau} F_{wA}(\theta, s_o) B_{PM1} \cos(p_r(\theta - \theta_0)) d\theta \tag{6.7}$$

where k_{d1} is the distribution factor.

Substituting (6.4) into (6.3) and then compared with (6.7), the influence of the slot opening and slot/pole combination on the back-EMF can be reflected by a new coefficient called slot opening coefficient, expressed as:

$$k_{so} = \frac{\psi_1}{N_p \Phi_1 k_w} = \frac{p_r k_{d1} \int_0^{\tau} F_{wA}(\theta, s_o) \cos(p_r(\theta - \theta_0)) d\theta}{2k_w} \tag{6.8}$$

Hence, the torque can be calculated by:

$$T_0 = \frac{3E_1 I_q}{2\Omega_r} = \frac{3p_r \Phi_1 N_p I_q}{2\sigma_0} k_{so} k_w \tag{6.9}$$

where σ_0 is the leakage coefficient.

The variation of slot opening coefficient with slot opening angle for all the machine candidates are calculated and shown in Fig. 6.5. It shows that in each machine pair, both machines have the same slot opening coefficient when slot opening angle is zero. The slot opening coefficient decreases with the increase of slot opening for the machine with lower PM pole number. The slot opening coefficient increases and then decreases with the increase of the slot opening for the machine with higher PM pole number. This indicates that in each machine pair, the machine with higher number of poles can have an optimal slot opening angle for maximum slot opening coefficient. Fig. 6.5 also highlights the maximum slot opening coefficient points with their corresponding slot opening angles. It shows that for the machines with higher number of poles in the machine pair (N_s-slot/2p_{rh}-pole machine), the optimal slot opening angle increases with the increase of PM pole number. For the machine with lower number of poles (N_s-slot/2p_{rl}-pole machine), the optimal slot opening should be 0 if the tooth-tip leakage flux is not considered.

The product of maximum slot opening coefficients and winding factor for all the machines are shown in Table 6.3. It shows that in the machine pairs, the machine with a higher PM pole number has a larger product. The maximum product for CW machines is 1 whereas for DW machines it is greater than 1. 12-slot/20-pole and 22-pole machines have maximum products as high as 2.00 and 3.73, respectively. Take 12-slot/20-pole ISDW VPMSM as an example, this means that up to 200% of the flux per pole

can be linked to the stator side to take part in the energy conversion. Assuming that all the machine candidates have the same B_{PM} and r_g, from (6.4), the product of p_r and Φ_0 will be the same for all the machine candidates. Hence, the product of slot opening coefficient and winding factor has a decisive impact on the electromagnetic torque as shown in (6.9). This is the main reason why FSDW VPMSMs can have a larger torque than other machines. Also, for the N_s-slot/$2p_{rh}$-pole machines, k_{so} can provide a reference for design of the optimal slot opening angle.

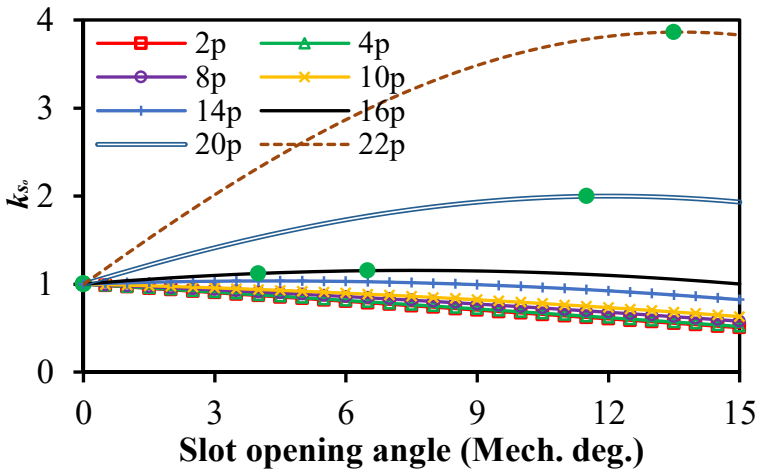

Fig. 6.5 Slot opening coefficient vs slot opening angle.

Table 6.3 Slot Opening Coefficient and Winding Factor for Different Machine Candidates.

N_s	Type	$2p_r$	k_w	k_{so}(max)	k_w*k$_{so}$(max)
12	ISDW	2	0.966	1	0.966
	FSDW	22	0.966	3.86	3.73
	ISDW	4	1	1	1
	FSDW	20	1	2	2
	FSCW	8	0.866	1	0.866
		16	0.866	1.16	1
		10	0.933	1	0.933
		14	0.933	1.03	0.966

6.4 Torque Production from Viewpoint of Magnetic Gearing Effect

6.4.1 Magnetic Gearing Effect and Torque Segregation Equation in PMSMs

It has been proven in previous chapters that for a N_s-slot/$2p_r$-pole PMSM, due to the winding distribution, the p_rth and (N_s-p_r)th armature reaction harmonics always exist in pairs. Their speeds of rotation are shown in Fig. 6.6, where n_r it the mechanical speed of the rotor. Useful torque can be generated under the following circumstances.

(a) the p_rth PM fundamental and original p_rth armature reaction MMF harmonics share the same order and speed of rotation, they can interact with each other and produce useful torque. Here "original" means that the harmonic is not modulated by the stator slots. In this case, the torque is produced by the principle of the conventional PMSM as shown in Fig. 6.6 (a).

(b) the (N_s-p_r)th armature reaction MMF harmonic has different order and speed of rotation with the p_rth PM fundamental harmonic. However, the (N_s-p_r)th harmonic can be modulated by the N_s-pole stator teeth, which results in the space harmonic with the order of p_r and the speed of Ω_r. The modulated harmonic can interact with the p_rth PM harmonic to produce a steady torque as shown in Fig. 6.6 (b). This phenomenon is called magnetic gearing effect and it has been proven in previous chapters that it can contribute to the total torque production in every machine candidate in this chapter.

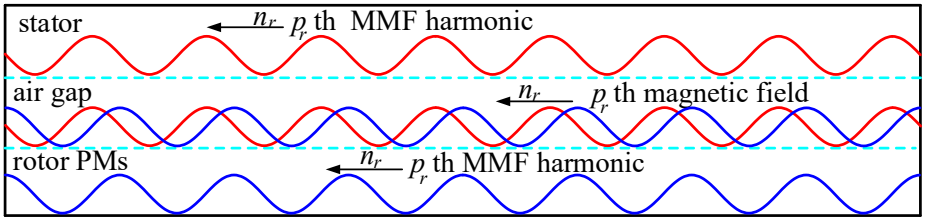

(a) Principle of conventional PMSMs

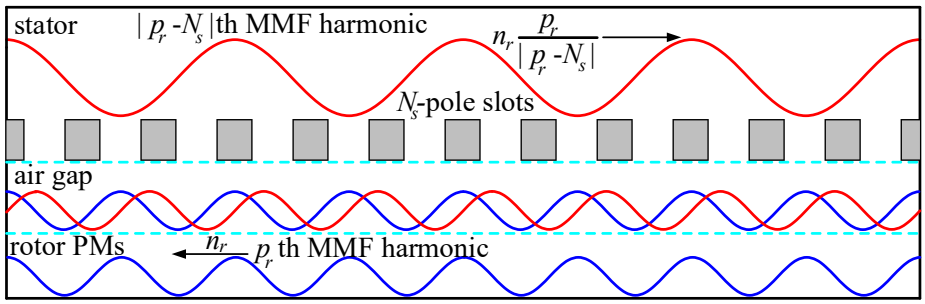

(b) Principle of magnetic gearing effect

Fig. 6.6 Schematic of torque production mechanism.

Considering the magnetic gearing effect, the torque of an electrical machine can be written as:

$$T_0 = T_U + T_M \tag{6.10}$$

where T_U and T_M are the torque produced by the principle of the conventional PMSM and magnetic gearing effect, respectively.

6.4.2 Influence of Slot Opening on Air gap Field Harmonics and Torque Production

To quantify the respective contributions of torque produced by the principle of the conventional PMSM and magnetic gearing effect, the armature reaction harmonics should be analysed independently. FEA-based ECSM and the harmonic restoration method are techniques which can restore each armature reaction harmonic individually before and after modulation effect in each machine candidates. The operation details can be found in Chapters 2 and 4, in which the contribution of magnetic gearing effect to the torque in the 12-slot/8-pole and 12-slot/22-pole machines are quantified. However, the influence of slot opening on the modulation effect is not fully addressed. Since the slot modulation effect is the main cause of magnetic gearing effect in PMSMs, the influence of stator slot opening on the air-gap magnetic field harmonics and the contribution of gearing effect to the average torque for all candidate machines are investigated in this section by following steps (12-slot/22-pole machine is used as an example):

Step 1: Build FEA-based ECSM of the selected machine, shown in Fig. 6.7 (a); calculate the air-gap PM flux density under open circuit condition, then perform spectrum analysis and record the value of fundamental harmonic;

Step 2: Demagnetise the rotor PMs and replace the slot area by silicon steel, Fig. 6.7 (b); calculate the air-gap armature reaction flux density; perform spectrum analysis on it and record the information of p_{rl}th and p_{rh}th armature reaction harmonics; restore p_{rl}th and p_{rh}th armature reaction harmonics before modulation individually by sinusoidally magnetised p_{rl} and p_{rh} pole pair stator PMs of very small thickness shown in Fig. 6.7 (c) and (d);

At this stage, for each restored armature reaction MMF harmonic of specific order, we have a specific FE model.

Step 3: For each specific FE model, set the material of slot area to be air, Fig. 6.7. (e) and (f); calculate the air-gap flux density; perform spectrum analysis and record the value of fundamental harmonic; if the order of the restored MMF harmonic equals the fundamental one, the recorded harmonic is the

unmodulated armature reaction fundamental harmonic; if not, it is the modulated one;

Step 4: In each specific FE model, restore the rotor PM magnetisation, Fig. 6.7 (g) and (h), calculate the torque produced by each armature reaction MMF and the rotor PMs; if the order of the restored MMF harmonic equals the fundamental one, the recorded torque is the torque produced by conventional torque production principle; if not, it is produced by magnetic gearing/modulation effect.

Step 5: Repeat Step 1-4 under different slot openings.

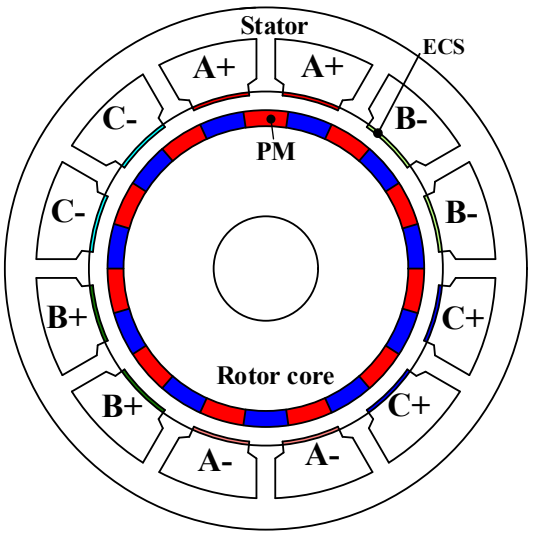

(a) FEA-base ECSM

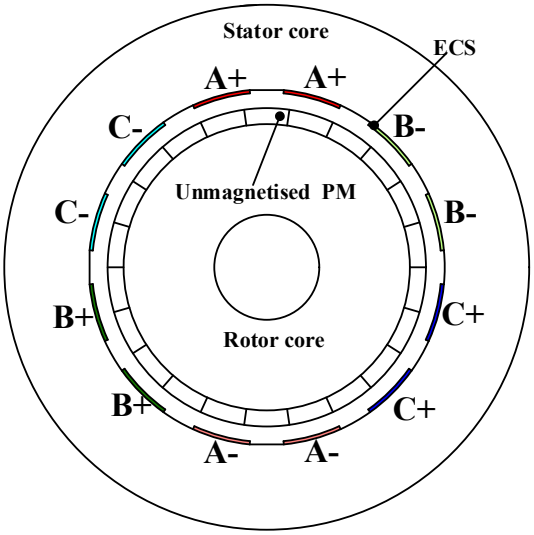

(b) Slotless FEA-based ECSM

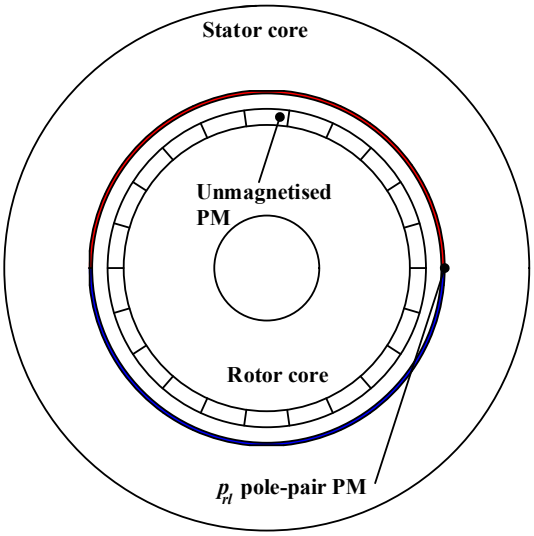

(c) Restoration of p_{rl}th harmonic before modulation

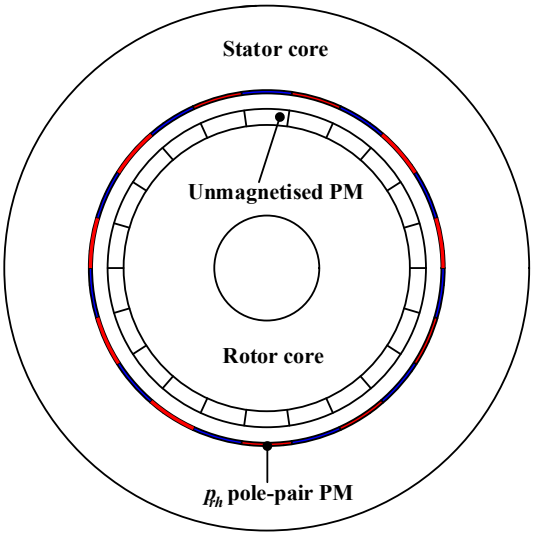

(d) Restoration of p_{rh}th harmonic before modulation

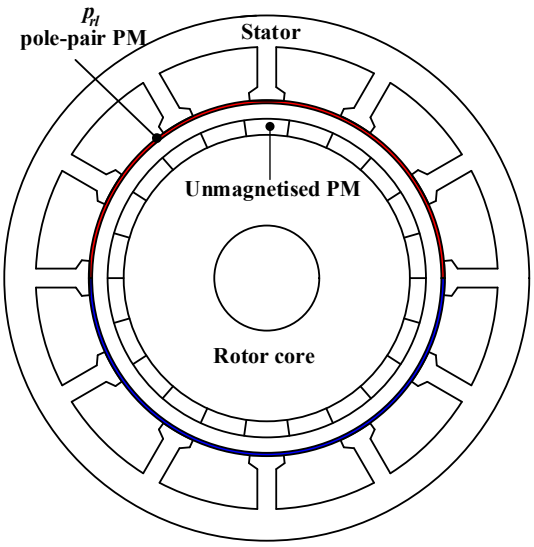

(e) Modulation effect on p_{rl}th harmonic

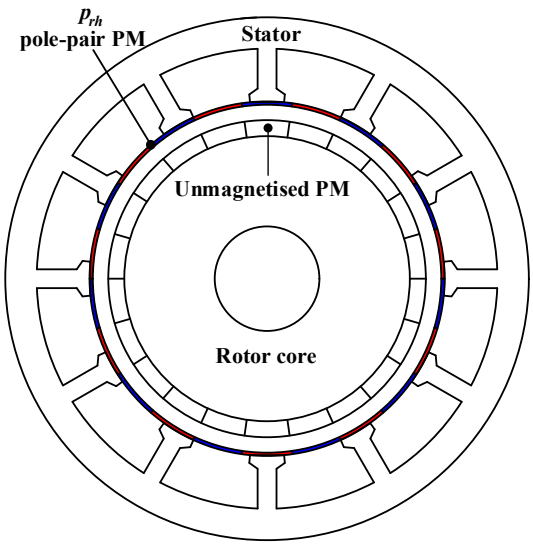

(f) Modulation effect on p_{rh}th harmonic

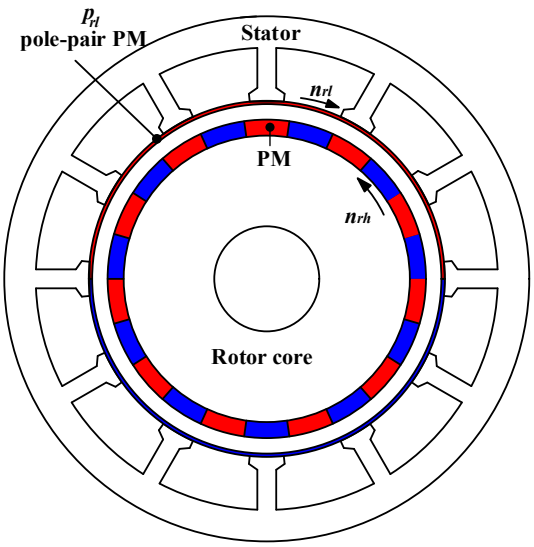

(g) Torque production of p_{rl}th MMF harmonic

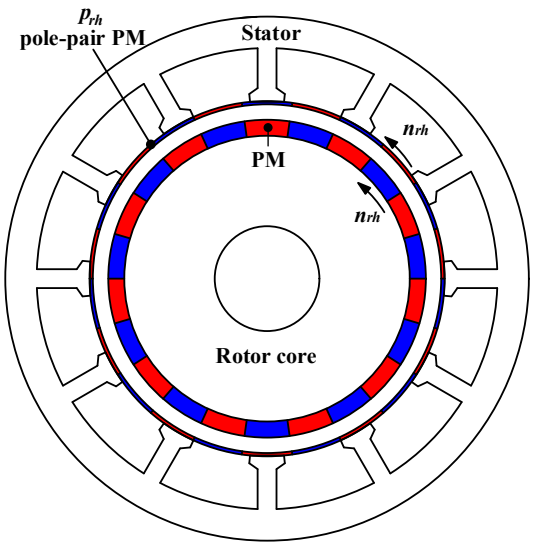

(h) Torque production of p_{rh}th MMF harmonic

Fig. 6.7 Illustration of FEA-based ECSM and harmonic restoration method.

For all investigated machines, the amplitudes of the fundamental PM air-gap magnetic flux density harmonics in the radial direction with respect to different slot opening angles are provided in Fig. 6.8 (a). It can be seen that for all the PM machines under investigation, the amplitudes of PM fundamental harmonics decrease with the increase of slot opening angle. This is because with the increase of the slot opening angle, the equivalent DC component of the air-gap permeance decreases, which reduces the amplitude of fundamental PM harmonic.

The amplitudes of the radial armature reaction air-gap magnetic flux density harmonics with respect

to different slot opening angles are provided in Fig. 6.8 (b)-(e) for the four machine pairs. The variations of the 5th and 7th armature reaction harmonics in 12-slot/10-pole and 14-pole FSCW PMSMs are taken as examples to show the modulation effect of the stator slotting on the armature reaction harmonics. Since they have the same winding configuration and harmonic contents, the influence of stator slotting on the armature reaction harmonics of both 12-slot/10-pole and 14-pole machines are shown in Fig. 6.8 (b). It should be noted that for the 12-slot/10-pole machine, only the 5th air gap armature reaction flux density harmonic, including the un-modulated part and modulated part, takes part in the torque production. For the 12-slot/14-pole machine, only the 7th air gap armature reaction flux density harmonic, including the un-modulated part and modulated part, takes part in the torque production. Fig. 6.8 (b) shows that the un-modulated 5th and 7th harmonics decrease with the increase of the slot opening as a result of decreased DC component in the permeance function. However, the modulated 7th (originally generated by the 5th MMF harmonic) and 5th (originally generated by the 7th MMF harmonic) harmonics increase with the increase of slot opening. Since the amplitude of the original 5th harmonic is larger than that of the original 7th harmonic, the reduction in the original 5th harmonic cannot be fully compensated by the modulated 5th harmonic. As a result, the resultant 5th armature reaction harmonic decreases with the increase of slot opening. However, the reduction in the original 7th harmonic is less than the increment in the modulated 7th harmonic at certain slot opening angles, and hence, the resultant 7th harmonic increases and then decreases with the increase of slot opening, reaching its peak at 8 mechanical degrees. As a result, the variations of torque with slot opening angle for both 12-slot/10-pole and 14-pole machines are consistent with those of the resultant 5th and 7th armature reaction harmonics, as shown in Fig. 6.8 (f).

The relationship between the 5th and 7th armature reaction harmonics in the 12-slot/10-pole and 14-pole machine pair also applies to the 4th and 8th harmonics in the machine pair of 12-slot/8-pole and 16-pole machines, the 2nd and 10th harmonics in the machine pair of 12-slot/4-pole and 20-pole machines and the 1st and 11th harmonics in the machine pair of 12-slot/2-pole and 22-pole machines, shown in Fig. 6.8 (c)-(e).

For all the machines in this chapter, the fundamental armature reaction harmonic is contributed by the un-modulated part and the modulated part. With the increase of slot opening, the amount of the un-modulated part decreases while that of the modulated part increases. In each machine pair, for the N_s-slot/$2p_{rl}$-pole machine, the reduction in the un-modulated p_{rl}th armature reaction harmonic cannot be compensated completely by the increment in the modulated p_{rl}th armature reaction harmonic, the resultant p_{rl}th armature reaction harmonic decreases with the increase of slot opening. That is to say,

in each machine pair, the slot opening of N_s-slot/2p_{rl}-pole machine should be as small as possible if the tooth tip leakage flux is not considered. However, for the N_s-slot/2p_{rh}-pole machine, the increment in the modulated p_{rh}th armature reaction harmonic is larger than the decrement in the un-modulated p_{rh}th armature reaction harmonic at some slot opening angles. Hence, the resultant p_{rh}th armature reaction harmonic reaches its peak at the optimal slot opening. That is to say, in each machine pair, the N_s-slot/2p_{rh}-pole machine can benefit from the magnetic gearing effect for torque production under the optimal slot opening angle.

Fig. 6.8 (b)-(e) also show that the resultant armature reaction harmonic of higher order achieves its peak at larger slot opening angle, which is consistent with the torque performance shown in Fig. 6.8 (f), in which the machines with larger PM pole number achieve their peak torque at larger slot opening angle. Hence, it can be concluded that for the N_s-slot/2p_{rh}-pole machine in every machine pair, the slot opening angle should be optimised to take advantage of the magnetic gearing effect. The larger p_{rh} is, the larger optimal slot opening angle will be. It is noteworthy that the conclusions drawn from the perspective of magnetic gearing effect are consistent with those from the slot opening coefficient in Section 6.3.

The percentage of contribution of magnetic gearing effect to the average torque is shown in Fig. 6.8 (g). It illustrates that for the 12-slot machines, the contribution of magnetic gearing effect to the average torque increases with the increase of slot opening. Moreover, at the same slot opening, magnetic gearing effect contributes more in the machine with larger PM pole number. For ISDW PMSMs, the contribution of the magnetic gearing effect to the total torque is trivial. For FSCW PMSMs, the contribution of magnetic gearing effect plays an un-ignorable part whereas for FSDW VPMSMs, the magnetic gearing effect is the major component for torque production.

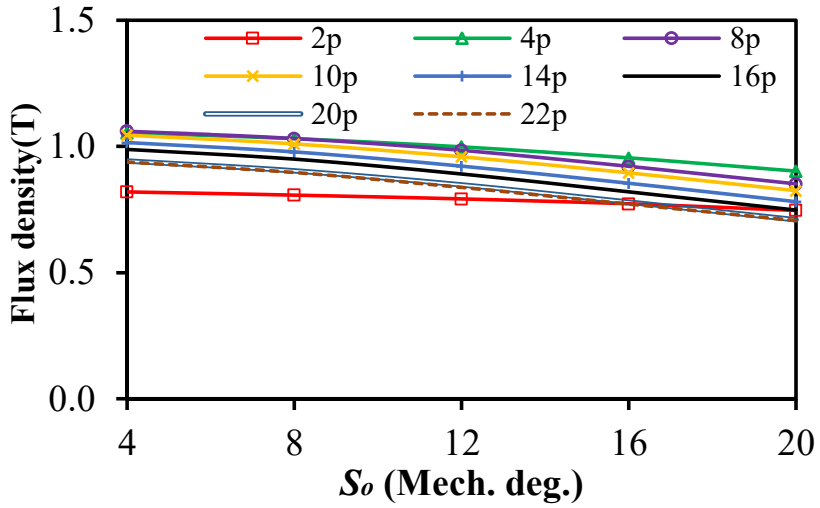

(a) PM air-gap flux density

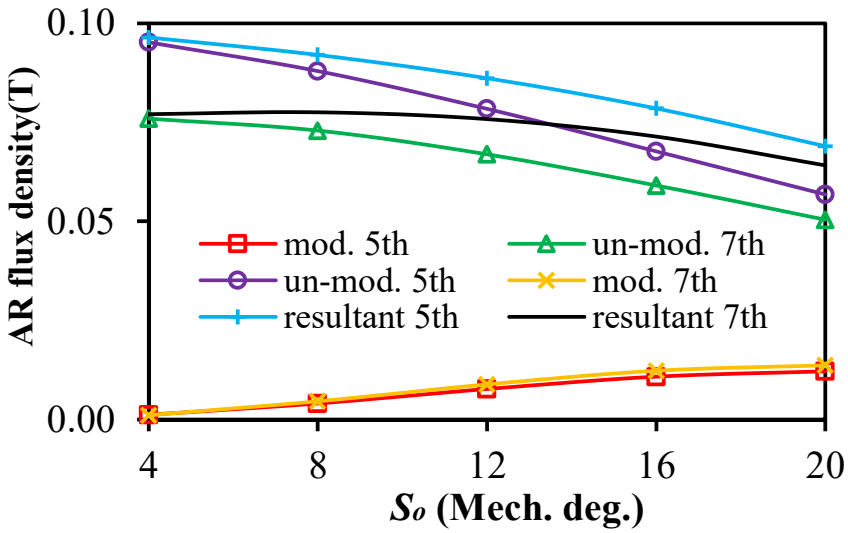

(b) 5th and 7th armature reaction air-gap flux density

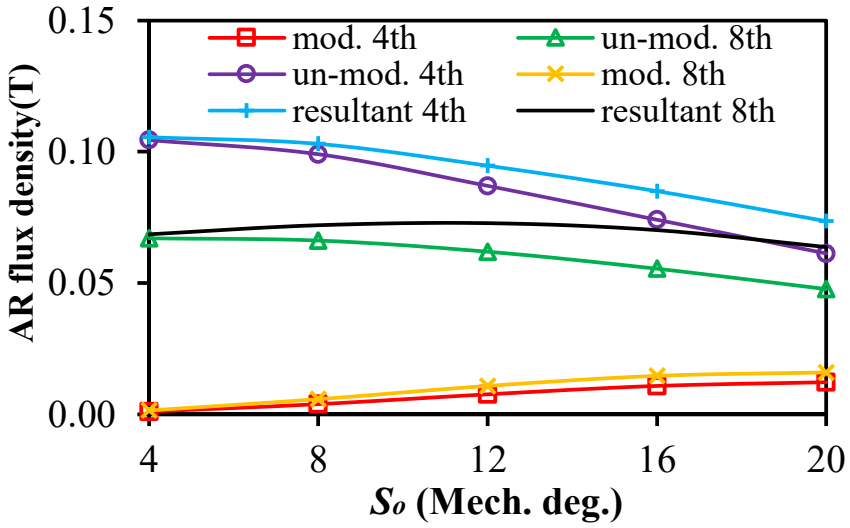

(c) 4th and 8th armature reaction air-gap flux density

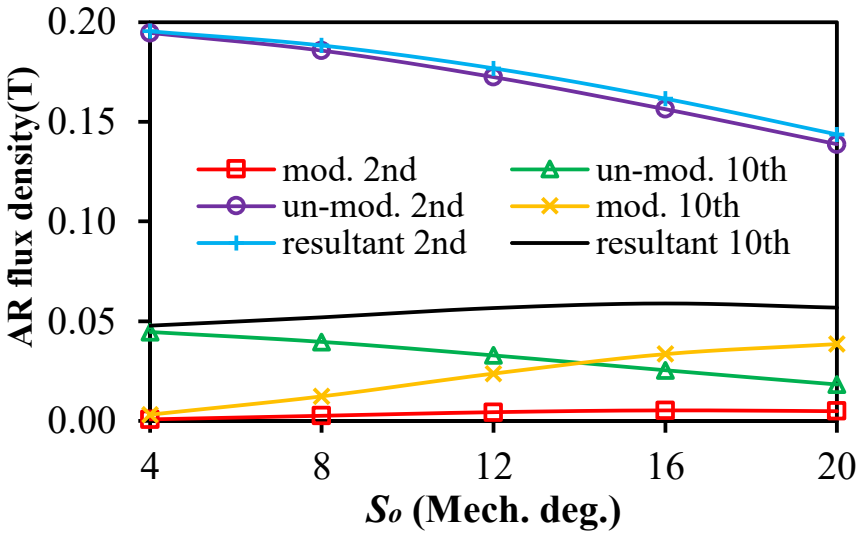

(d) 2nd and 10th armature reaction air-gap flux density

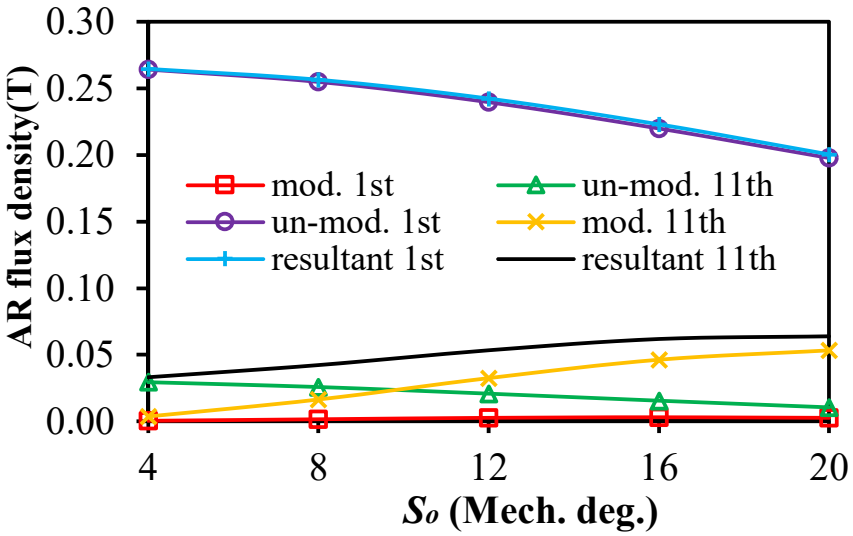

(e) 1st and 11th armature reaction air-gap flux density

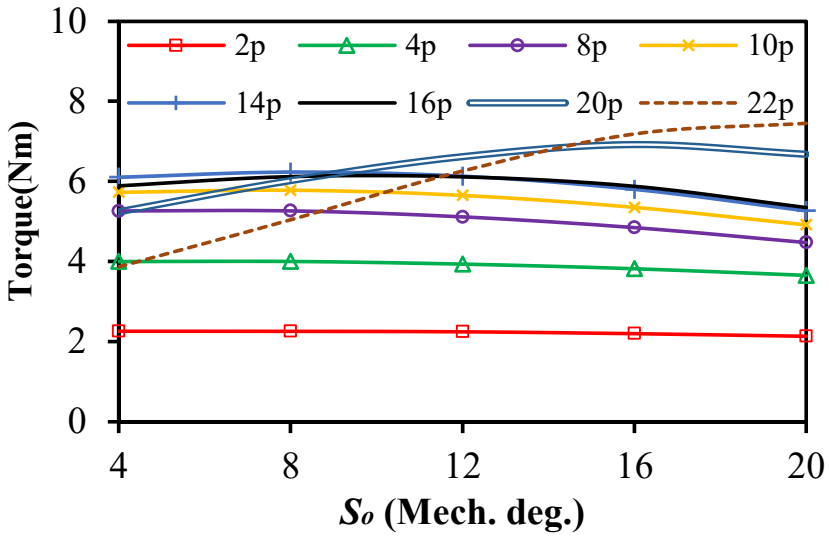

(f) Average torque

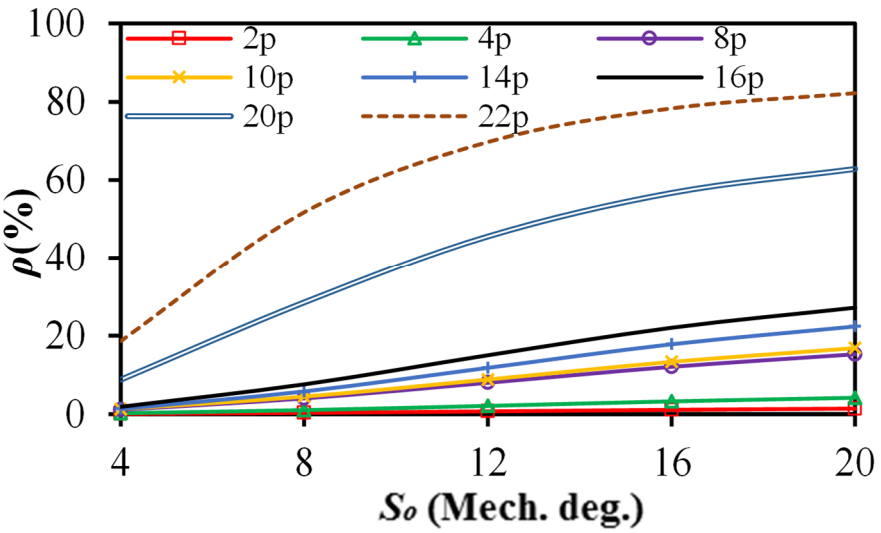

(g) Contribution of magnetic gearing effect

Fig. 6.8 Influence of slot opening on the performance of 12-slot machines.

6.5 Design Guidelines

Since the conclusions drawn from both viewpoints agree with each other, some design guidelines are provided from the analysis above.

For FSCW and DW PMSM machines, there exists an optimal slot opening to maximize k_{so} (or to achieve the best balance between the torque contribution of the conventional PMSM and the magnetic gearing effect) for those with ($2p_r$>N_s). The higher the PM pole number is, the larger the slot opening will be. For DW PMSMs, the one with ($2p_r$>N_s) is the Vernier machine. Hence, Vernier machine can be seen as a kind of conventional machine whose slot opening play a critical role in the torque production. For FSCW PMSMs, the one with ($2p_r$>N_s) can also be seen as a Vernier counterpart of the one with ($2p_r$<N_s). For those with $2p_r$<N_s. the slot opening should be as small as possible. The only balance needs to be considered is the leakage flux brought by a too small slot opening.

6.6 Experimental Validation

From the conclusion drawn in the last section, the N_s-slot/$2p_{rh}$-pole machine can benefit from the magnetic gearing effect for torque production under the optimal slot opening angle. In this section, 12-slot/14-pole FSCW and 22-pole FSDW VPMSMs are selected to be manufactured because they have the largest torque in FSCW and FSDW machine candidates in this chapter, respectively. Their

performance are tested to validate the analyses in the above sections, Fig. 6.9. The main dimensional parameters of the prototypes are given in Table IV.

Firstly, the back-EMF waveforms of the machines are tested at 100rpm and compared with the FEA results, Figs. 10 (a) and (d). It can be seen that the FEA back-EMF waveforms for both machines agree well with the test waveforms. Fig. 6.10 (b) and (e) show the comparison of back-EMF spectra between the tested and FEA results for both VPMSMs. They show that for the fundamental harmonic, there are 3% and 6% discrepancies between the FEA predicted and tested results for the 12-slot/14-pole and 12-slot/22-pole VPMSMs, respectively, which is believed to be caused by end effect.

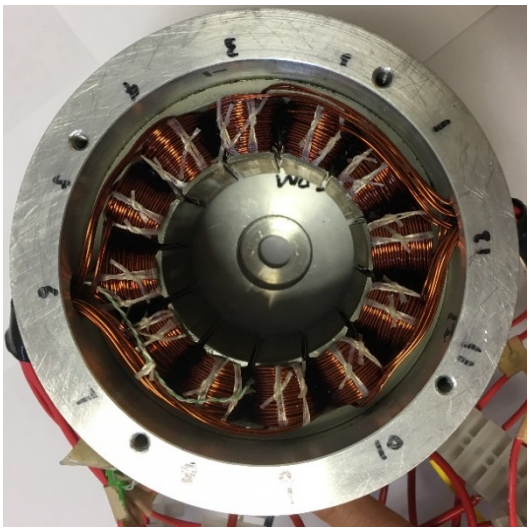

(a) 12-slot stator with CW

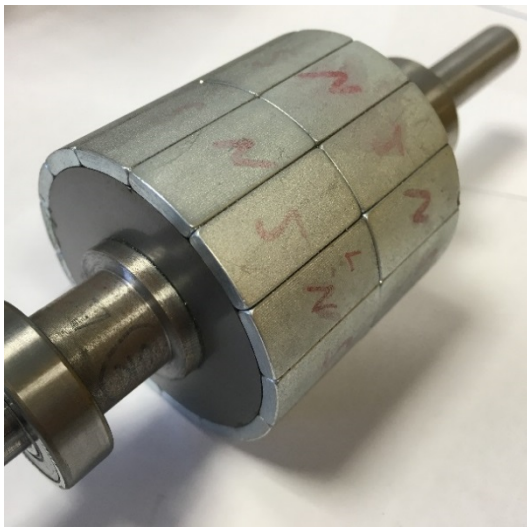

(b) 14-pole rotor

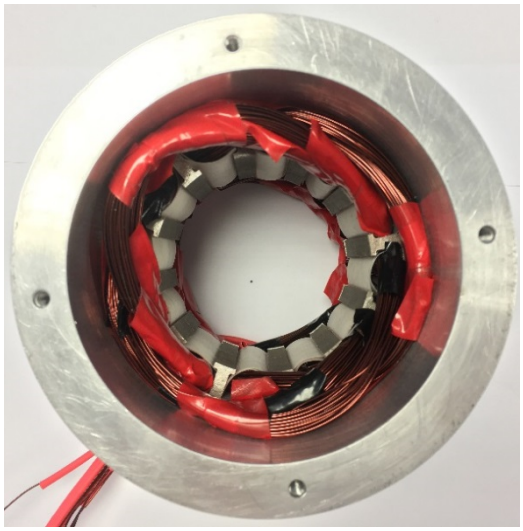

(c) 12-slot stator with DW

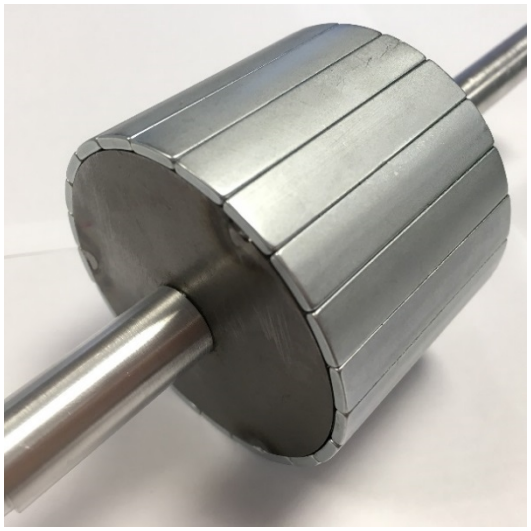

(d) 22-pole rotor

Fig. 6.9 Prototype photos and test rig.

Table 6.4 Dimensional and Material Parameters of Prototypes

Slot number	12	
Pole number	14	22
Stator outer/inner diameter(mm)	100/57	100/68
Air-gap length(mm)	1	
Turns per phase	184	100
PM height(mm)	3	2.3
PM pole arc	180° Elec.	180° Elec.
Slot opening angle	4° Mech.	19° Mech.
Remanence of PMs	1.2	
Relative permeability of PMs	1.05	

The magnetic gearing effect and the torque components in the foregoing sections cannot be measured directly on the prototypes, only the FEA predicted electromagnetic torque can be measured in the experiments. The experiment is done by the same method with Chapter 1 [ZHU09c]. Static torques of the two prototypes within 0–180 electric degrees under different current amplitudes are calculated by 2-D FEA and compared with measurements as shown in Fig. 6.10 (c) and (f), respectively. The test results confirm that the 12-slot/22-pole VPMSM can generate larger torque per ampere than the 12-slot/14-pole FSCW PMSM due to stronger magnetic gearing effect. For the 12-slot/22-pole VPMSM, the discrepancies between the FEA and measured results are due to manufacturing tolerance and severe end effect brought about by large PM pole number, as discussed in the previous chapters.

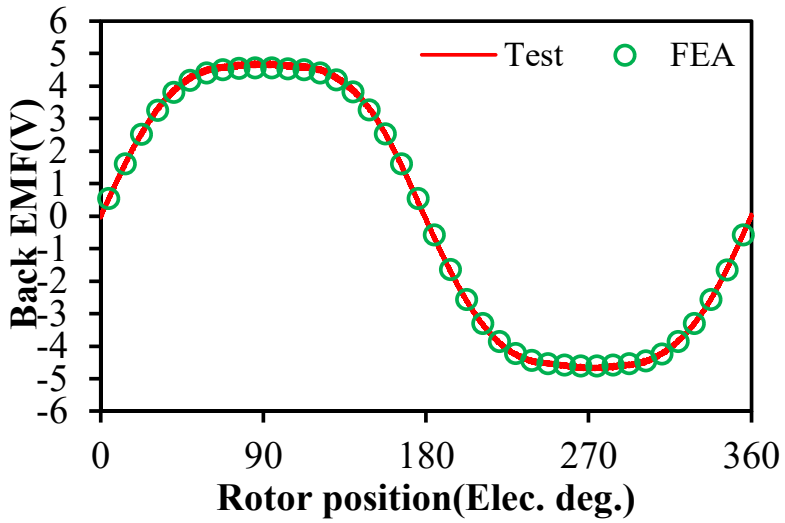

(a) Back-EMF of 12-slot/14-pole machine at 100rpm

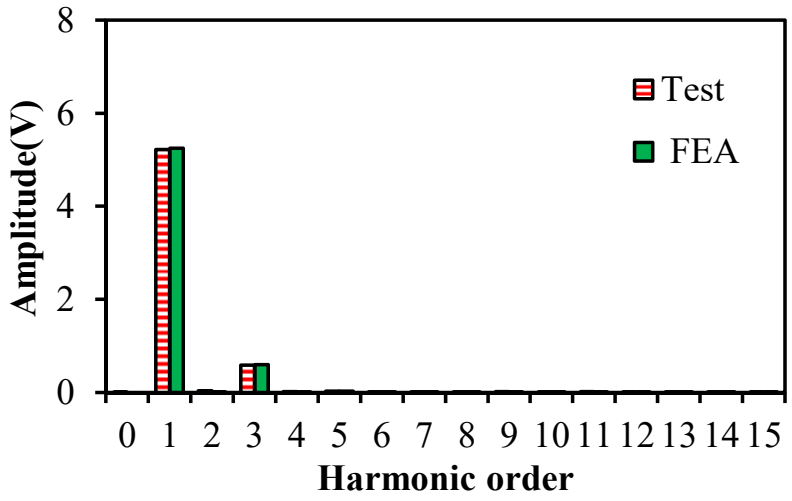

(b) Back-EMF spectrum for 12-slot/14-pole machine at 100rpm

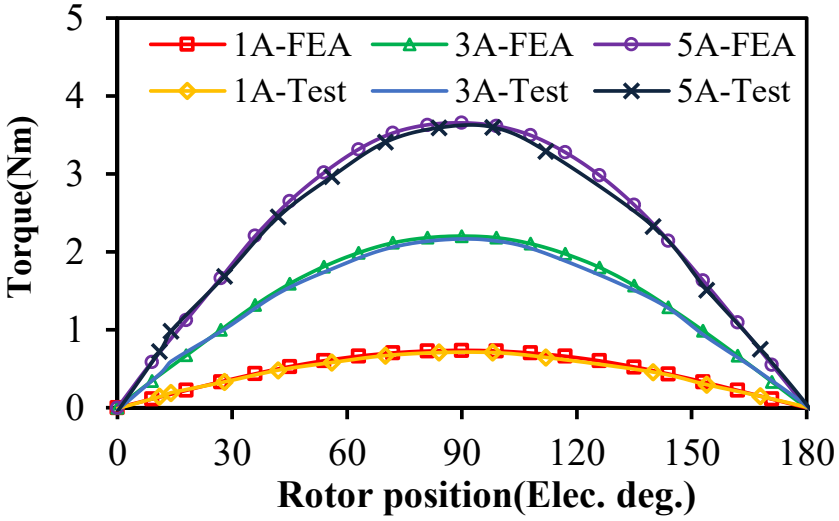

(c) Static torque of 12-slot/14-pole machine

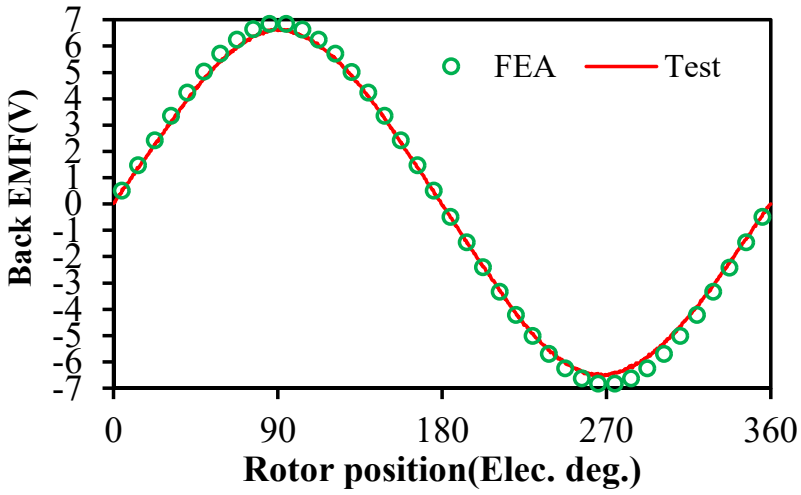

(d) Back-EMF of 12-slot/22-pole machine at 100rpm

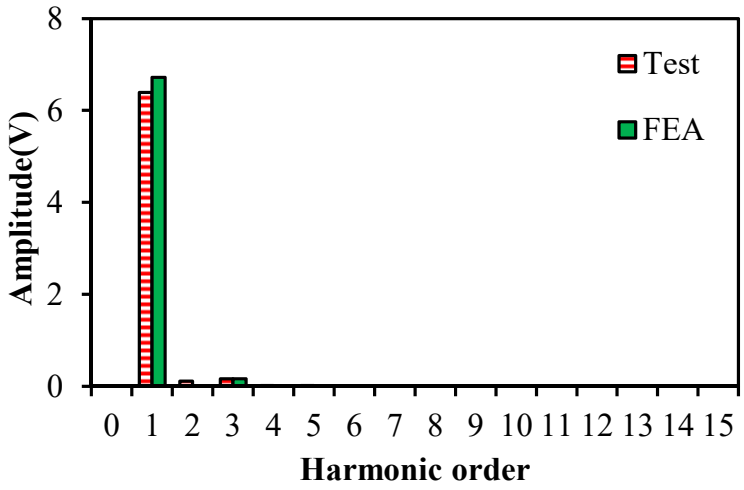

(e) Back-EMF spectrum for 12-slot/22-pole machine at 100rpm

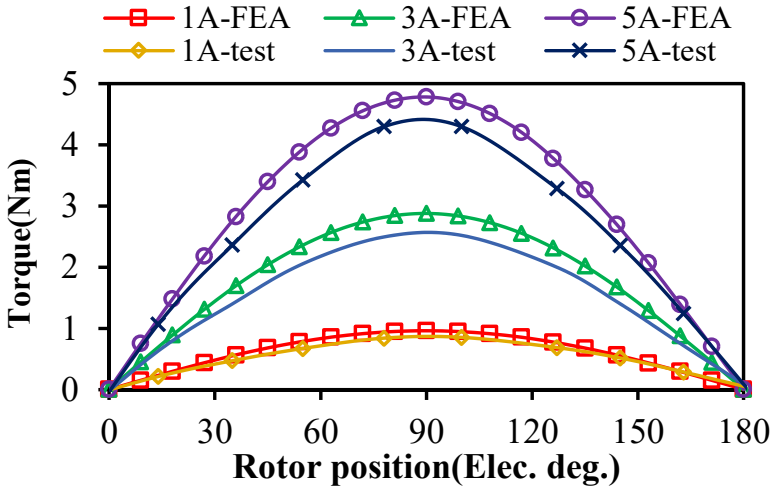

(f) Static torque of 12-slot/22-pole machine

Fig. 6.10 FEA waveforms vs test waveforms.

6.7 Summary

In this chapter, the torque production mechanism of ISDW PMSM, FSCW PMSM and FSDW VPMSM are firstly unified from two viewpoints: the energy conversion and magnetic gearing effect. Eight 12-slot PMSM with different PM pole numbers are selected and optimised for investigation. The influence of slot opening on the torque production mechanism of different machine type are analysed from both viewpoints. Both viewpoints show that the VPMSM shares the same torque production mechanism with ISDW and FSCW PMSM machines. Not only FSDW VPMSM but also N_s-slot/2p_{rh}-pole FCSW PMSMs in a machine pair can benefit from larger slot opening for larger torque output. And the larger p_{rh} is, the larger magnetic gearing effect as well as the optimal slot opening angle will be.

CHAPTER 7

High Power Factor Vernier Machines with Coil-Pitch of Two Slot Pitches

In this chapter, an 18-slot/26-pole Vernier permanent magnet synchronous machine (VPMSM) with coil-pitch of two slot pitches is proposed. The 18-slot/26-pole VPMSM is a Vernier counterpart of an 18-slot/10-pole FSCW PMSM based on the investigation in Chapter 6. It can also be derived from a 9-slot/18-FMP/26-pole VPMSM with concentrated tooth-coil windings. Compared with the 9-slot/18-flux-modulation-pole/26-pole VPMSM, the number of slots is doubled and the phase winding connection is adjusted to reduce the space harmonic content, the phase inductance, and hence, improve the power factor. All of the three machines are globally optimised and their electromagnetic performance are compared. The results show that the 18-slot/26-pole VPMSM has larger torque and torque density, smaller torque ripple, better flux weakening capability and larger high efficiency area than its 10-pole counterpart. It also increases the power factor from 0.73 to 0.95 with better torque and flux weakening capability when compared with its 26-pole counterpart. Moreover, a series of VPMSMs with high power factor are proposed from the same design principle and given design guidelines.

7.1 Introduction

Fractional slot concentrated winding (FSCW) PMSM has gained their popularities in both industry and academia due to their high torque density, high efficiency, and low torque ripple, etc. [ELR10] [CRO02] [ZHU11]. Despite these merits, the armature reaction magnetic field in FSCW PMSMs contains abundant field harmonics which lead to parasitic effects such as unbalanced magnetic force [DAJ13] [ZHU10a], torque ripple [ZAR09] and rotor iron losses [FAN12] [PYR12] [FOR12]. FSPMSMs with coil-pitch of two slot-pitches have been proposed since they exhibit low harmonic content of the armature reaction magnetic field as a consequence of a coil pitch of two, hence reducing the parasitic effects in the machines [WAN14b] [WAN14c]. A typical slot/pole combination in this kind of machine is 18-slot/10-pole [WAN14b].

The modulation/magnetic gearing effect in electrical machines of different types and the relationship

between their slot/pole number combinations have been revealed in Chapter 6. It is revealed that for an N_s-slot/2p_{rl}-pole FS PMSM, there always exists an N_s-slot/2p_{rh}-pole Vernier counterpart so that they can be seen as a machine pair. In the machine pair, the two machines have the same slot number and winding connection, the rotor pole numbers satisfy

$$p_{rl} + p_{rh} = N_s \tag{7.1}$$

where N_s is the number of slots, p_{rl} and p_{rh} are the pole pair numbers of machines with lower and higher rotor PM pole pair numbers in the machine pair. However, the FS machine pair with coil-pitch of two slot-pitches have not been analysed yet because its Vernier counterpart has not been proposed before.

Vernier permanent magnet synchronous machine (VPMSM) has become a promising candidate in direct drive application because of high torque density and low torque ripple as discussed in previous chapters [JIA11] [LI16]. However, Vernier machines suffer from lower power factors compared with the traditional PMSMs. Low power factor means power converters of larger sizes are required for the same output power, which increases the cost and hinders the application of the VPMSMs. The low power factor of VPMSM is mainly caused by the increased number of rotor PM poles which leads to a much greater inductive reactance [KIM14]. There are some papers trying to improve the power factor of VPMSMs by using Halbach PM rotor [LI14b] or dual-rotor structure [LI14a] [ZHA14]. However, special techniques or complicated structures are needed, hindering their application to common VPMSM designs. Some machine candidates with coil pitch of two slot pitches in [LI18c] are claimed to have high power factors. Although the structure is simpler, the theoretical basis for the power factor improvement is not investigated, and therefore, no guidelines are proposed on how to design a high power factor VPMSMs by a proper selection of slot/pole combination and winding arrangement.

In this chapter, an 18-slot/26-pole FS VPMSM is firstly proposed. It has the identical winding connection to the 18-slot/10-pole FSCW PMSM with coil-pitch of 2 slot-pitches [WAN14b]. It can be derived from an 18-slot/10-pole FS PMSM according to (7.1). Hence, it is a Vernier counterpart of 18-slot/10-pole FS PMSM. It can also be evolved from a 9-slot/18-flux-modulation-pole (FMP)/26-pole VPMSM with concentrated tooth-coil windings. Compared with the 9-slot/18-FMP/26-pole VPMSM, the slot number is doubled and the phase winding connection is adjusted in the proposed one to reduce the space harmonic content. Global optimisations are carried out on all three machines. The results show that the 18-slot/26-pole FS VPMSM has larger torque and torque density, smaller torque ripple, better flux weakening capability and larger high efficiency area than its 10-pole counterpart. The study also shows that such design can effectively decrease the phase inductance and improve the power

factor with better torque and flux weakening capability compared with the 9-slot/18-FMP/26-pole VPMSM. Moreover, a design guideline on slot/pole number selection and winding arrangement will be provided, a series of high power factor VPMSMs will emerge from the same theoretical basis and design principle.

7.2 Machine Structure and Working Principle

7.2.1 Geometry Evolution from 18-Slot/10-Pole FS PMSM

FS PMSMs with coil-pitch of two slot-pitches and slot/pole number satisfying $N_s=2(2p_r\pm1)$ have been proposed in literatures [WAN14b] [WAN14c] since they exhibit lower harmonic content of the armature reaction magnetic field than FSCW PMSMs. In this chapter, an 18-slot/10-pole machine is used as an example to make the investigation and comparison.

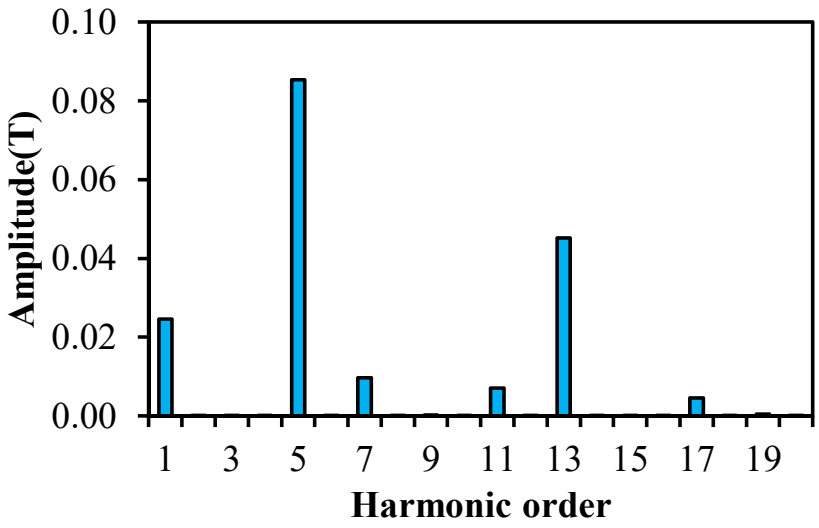

Fig. 7.1 Armature reaction field spectrum of 18-slot/10-pole machine.

The spectrum of the armature reaction magnetic field of an 18-slot/10-pole machine is shown in Fig. 7.1. It can be seen that apart from the 5th harmonic which is the fundamental harmonic of this machine, the order of the second largest harmonic is 13, which satisfies (7.1). From Chapter 6, for an N_s-slot/$2p_{rl}$-pole FS PMSM, there always exists an N_s-slot/$2p_{rh}$-pole Vernier counterpart with same slot number, winding connection but different rotor pole pair number. Two examples of machine pairs are provided in Table 7.1. It can be seen that the 12-slot/8-pole FSCW PMSM has a counterpart of 12-slot/16-pole FSCW PMSM, and the 12-slot/2-pole integral slot distributed winding (ISDW) PMSM has a counterpart of 12-slot/22-pole Vernier machine.

Table 7.1 Examples of PMSMs in Pairs

Winding type	N_s	p_{rl}	p_{rh}
FSCW	12	4	8
		8	4
ISDW	12	1	11
		11	1
FS(2 slot-pitch)	18	5	13
		13	5

Based on the analysis above, since the order of the second largest armature reaction field harmonic in the 18-slot/10-pole PMSM satisfies (7.1), it is reasonable to assume that the 18-slot/10-pole machine also has a counterpart with the same winding connection but a different rotor pole pair of 13, i.e. an 18-slot/26-pole PMSM. Different from the 10-pole machine whose torque is produced mainly from the principle of conventional PM machine, i.e., the interaction between the 5th armature reaction and PM harmonics, the torque of the 26-pole machine is mainly from magnetic gearing effect, i.e., the interaction between the 5th armature reaction field harmonic, the 13th PM field harmonic and the modulation effect of the 18-pole stator structure.

7.2.2 Geometry Evolution from 9-Slot/18-FMP/10-Pole VPMSM

7.2.2.1 Power Factor of VPMSMs

It has been mentioned in various literatures that VPMSM has a low power factor which hinders its application when considering the optimum combination between the machine and converter. The low power factor of VPMSMs can be explained by the phasor diagram shown in Fig. 7.2. When a PMSM is under I_d=0 control and the resistance of the stator windings is ignored, the phasors of q-axis current I_q and the no-load back EMF E_1 are in the same direction, the voltage phasor produced by I_q and the inductive reactance X_q has a 90-electrical-degree shift from E_1, and U_1 is the resultant phasor of terminal voltage. In this case, the power factor can be expressed as:

$$\cos\varphi = \frac{1}{\sqrt{1+\left(\frac{I_q X_q}{E_1}\right)^2}} \tag{7.2}$$

$$X_q = \omega L_q = \frac{2\pi}{60} n_r p_r L_q \tag{7.3}$$

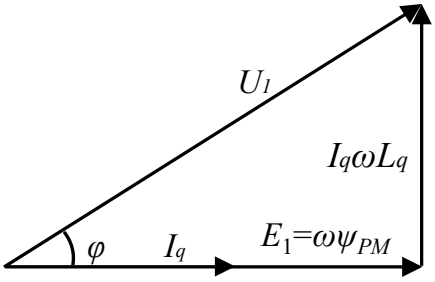

Fig. 7.2 Phasor diagram.

For a conventional PMSM, there always exists a Vernier counterpart with the same slot number, winding configuration but an increased PM pole number. When compare a conventional PMSM with its Vernier counterpart, the q-axis inductance L_q of both machines are similar since they share the same winding configuration. However, it can be seen in (7.2) that the increase in X_q is proportional to the increase of PM pole number p_r and is larger than the increase in E_1. This consequently causes a larger φ and smaller power factor for VPMSMs. Hence, it can be concluded that the low power factor is an inherent problem for VPMSMs as a result of higher PM pole number. From (7.2), since p_r cannot be changed for an existing VPMSM, one of the possible way to reduce X_q is to reduce the inductance.

7.2.2.2 Machine Topology Evolution and Principle

A 9-slot/18-FMP/26-pole VPMSM with concentrated windings is shown in Fig. 7.3 (a). This is a typical VPMSM with concentrated tooth-coil windings [OKA13] since it satisfies $p_r=N_f-p_s$, where N_f is the number of FMPs in the stator and p_s is pole pair number of the armature reaction magnetic motive force (MMF). Its armature reaction MMF waveform and spectrum are shown in Fig. 7.4 (a). It shows that there are abundant harmonics in the MMF waveform. The orders of the main harmonics are 4^{th}, 5^{th}, 13^{th} and 14^{th}. It is noteworthy that the main harmonics appear in pairs and with the order difference of 1.

To reduce the inductance of the 9-slot/18-FMP/26-pole VPMSM, the MMF harmonics need to be reduced. With this aim, an 18-slot/26-pole VPMSM with coil-pitch of two slot pitches is proposed.

The proposed machine is evolved from the original machine via the following steps: (1) Double the number of slots so that in the proposed machine the number of stator slots N_s equals to N_f in the original machine, as shown in Fig. 7.3 (b). (2) Divide the windings of phase (A, B, C) in Fig. 7.3 (b) into two groups denoted as (A1, B1, C1) and (A2, B2, C2). (3) In the proposed machine, configure (A1, B1, C1) in the same way with (A, B, C), with the coil spanning two slot pitches. (4) In the proposed machine, configure (A2, B2, C2) with a 180-mechanical-degree shift from (A1, B1, C1) (5) Invert the polarity of (A2, B2, C2).

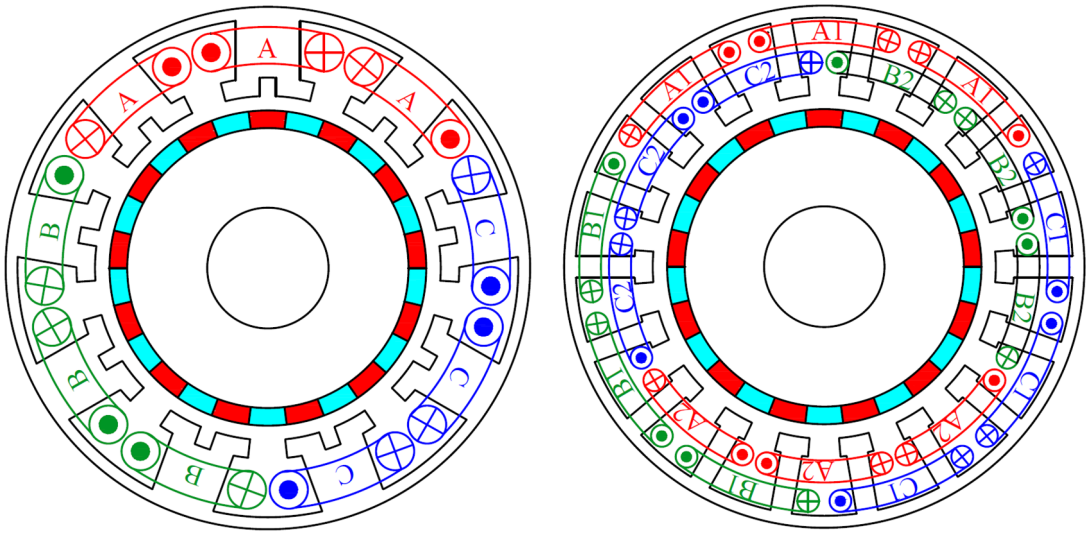

(a) 9-slot/18-FMP/26-pole (b) 18-slot/26-pole

Fig. 7.3 Machine topologies.

By doing this, the armature reaction MMF space harmonics of even orders can be effectively eliminated without affecting the harmonics of odd orders. Take the 4th and 5th harmonics for example as shown in Fig. 7.5, the 4th harmonics generated by phase A1B1CA and A2B2C2 have the same phase after a 180-mechanical-degree shift and cancel with each other after the polarity of Phase A2B2C2 is inverted. On the contrary, the 5th harmonics generated by phase A1B1CA and A2B2C2 have the opposite phase after a 180-mechanical-degree shift and after Phase A2B2C2 swaps its polarity, they are in phase. Their accumulated waveform is the same with that of the 9-slot/18-FMP/26-pole machine under the same electrical loading. This principle applies not only for the 4th and 5th harmonics but all the even and odd order harmonics in this machine. Fig. 7.4 also shows the armature reaction MMF waveforms generated by phase A1B1C1, A2B2C2 and their accumulated results. It can be clearly seen from its spectrum that all the even order harmonics have been eliminated. For machines with surface PMs, the q-axis inductance L_q can be calculated by [ELR05]:

$$L_q = \frac{\mu_0 r_g l_{ef}}{l_a} \int_0^{2\pi} F_s(\theta) N_a(\theta) d\theta \tag{7.4}$$

where μ_0 is the permeability of air, r_g is the air gap radius, l_a is the effective airgap length, l_{ef} is the effective axial length, $F_s(\theta)$ is the 3-phase resultant MMF and $N_a(\theta)$ is the winding function [NOV98]. It can be calculated from (7.4) that L_q of the 18-slot/26-pole machine is only 42% of the 9-slot/18-FMP/26-pole machine under the same geometry features and number of turns per phase. This proves that reduction of armature reaction space harmonic content can directly reduce the phase inductance, and consequently, improve the power factor.

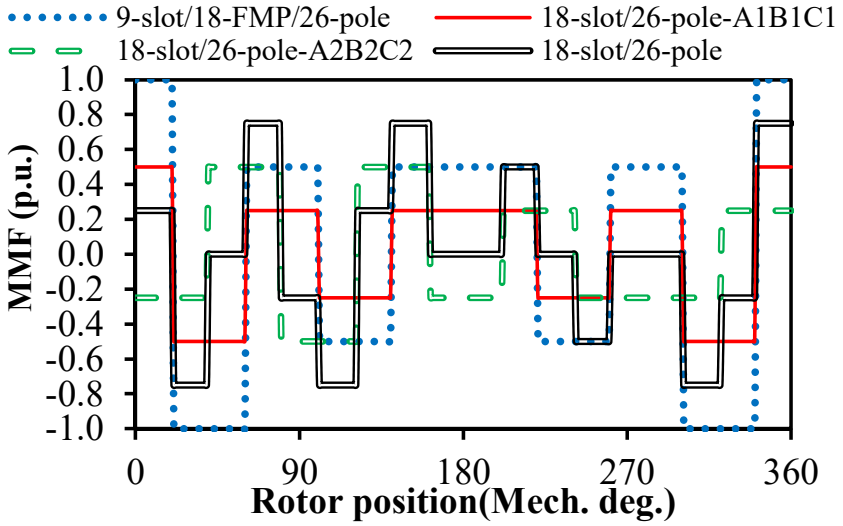

(a) Waveforms

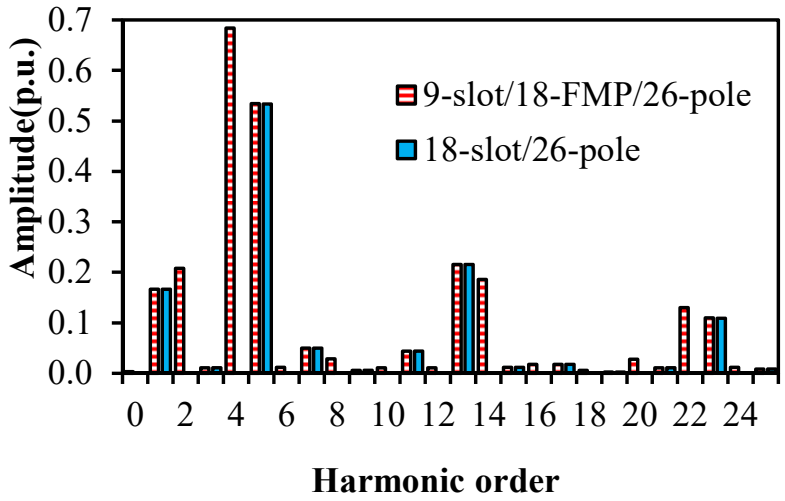

(b) Spectra

Fig. 7.4 MMF waveforms and spectra.

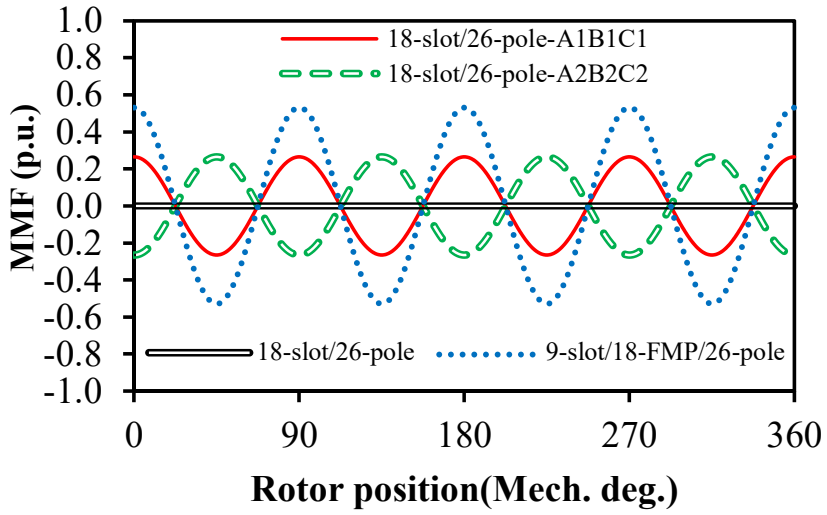

(a) 4th harmonic

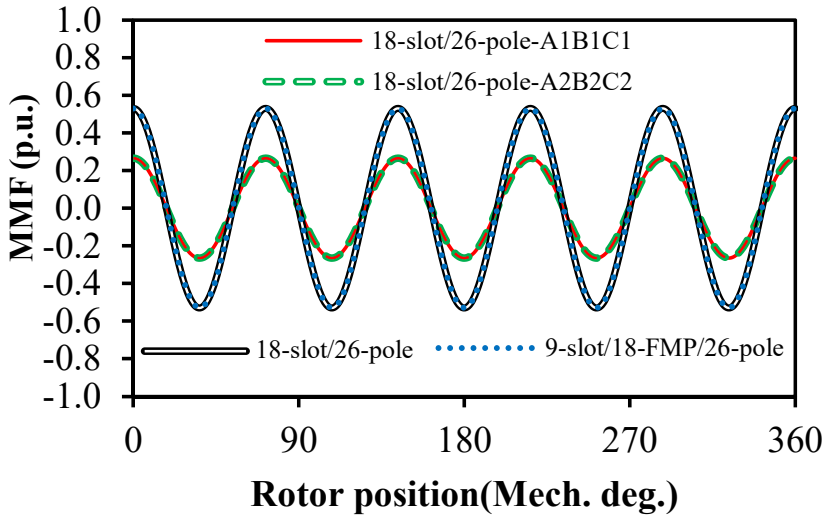

(b) 5th harmonic

Fig. 7.5 Harmonic reduction principle.

7.3 Global Optimisation

To make a fair comparison among the 18-slot/10-pole, 9-slot/18-FMP/26-pole and 18-slot/26-pole machines, all three machine candidates have been globally optimised to achieve the maximum torque under the following constrains: (1) Fixed stator outer radius r_o; (2) Fixed air-gap length l_a; (3) Fixed stack length l_{ef}; (4) Fixed shaft radius r_s; (5) Fixed copper loss at 75W considering the end windings for each machine; (6) Fixed slot packing factor; (7) Fixed overall PM volume. The related dimensional parameters are illustrated in Fig. 7.6. During the optimisation, the stator yoke radius r_y, the stator inner

radius r_i, slot opening angle a_{so}, stator teeth width w_t, PM length l_{pm} and the slot opening height h_{so} are variables for both machines. The FMP width w_f and height h_f are variables only for the 9-slot/18-FMP/26-pole VPMSM. The optimisation is carried out by genetic algorithm. The optimised results are shown in Table 7 2, where N_p stands for the number of turns per phase.

Table 7 2. Optimised Parameters

	9-slot/18-FMP/26-pole	18-slot/26-pole	18-slot/10-pole
r_o(mm)	50		
l_a(mm)	1		
r_s(mm)	5		
l_{ef}(mm)	50		
r_y(mm)	47.3	48.2	46.3
r_i(mm)	32.7	36.0	30.3
w_t(mm)	5.4	2.9	5.1
h_{so}(mm)	5.1	1.5	1.5
a_{so}(mech. deg.)	5.6	4.5	4.6
l_{pm}(mm)	3.3	3.0	3.6
N_p	102	126	120
h_f(mm)	2	-	-
w_f(mm)	10.2	-	-

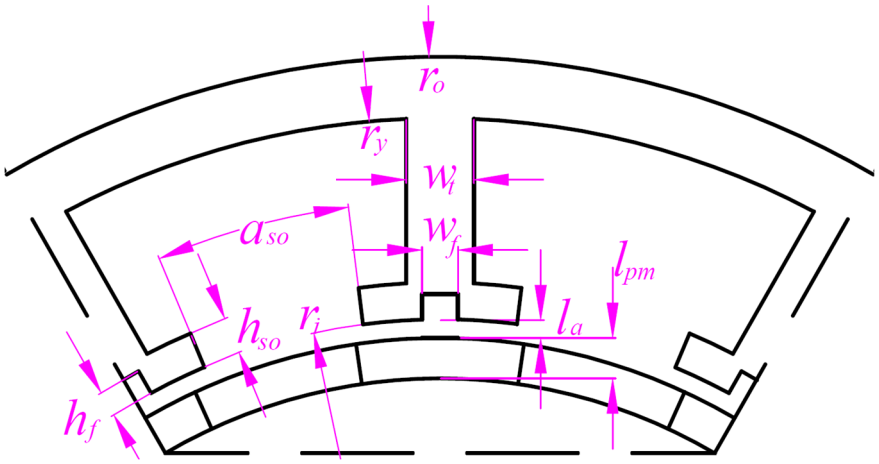

Fig. 7.6. Dimensional parameters in the optimisation.

7.4 Performance Comparison

7.4.1 No-load Flux Linkage and Back EMF

At no-load condition, the phase flux linkages and their spectra of the three machine candidates are calculated by FEM and shown in Fig. 7.7. When d-axis is aligned with the axis of phase A, the flux line distribution of three machines are shown in Fig. 7.8. It can be seen that the amplitudes of the fundamental harmonics of the 9-slot/18-FMP/26-pole and 18-slot/26-pole machine are 38% and 44% of the 18-slot/10-pole machine, respectively, mainly due to smaller PM pole arcs. However, the waveform of the 26-pole machines is more sinusoidal since they contain less high order harmonics.

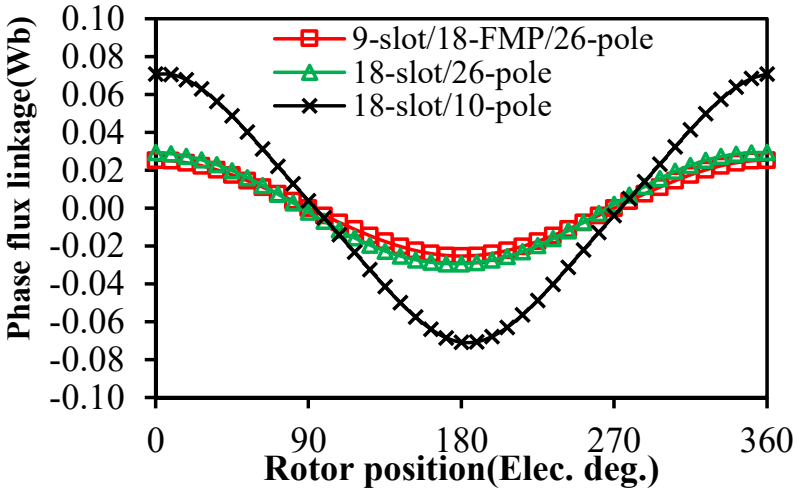

(a) Waveform

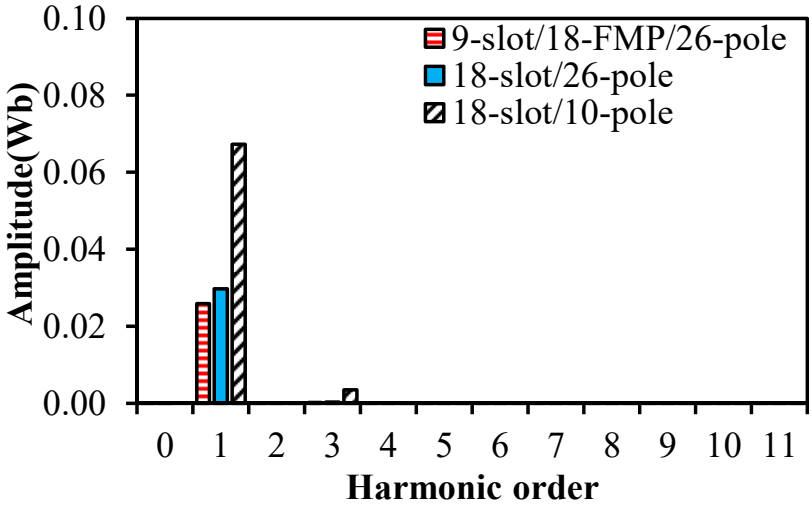

(b) Spectra

Fig. 7.7 Comparison of flux linkage.

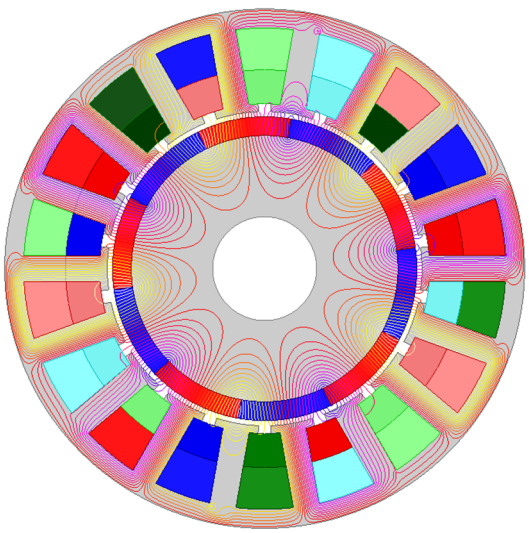

(a) 18-slot/10-pole

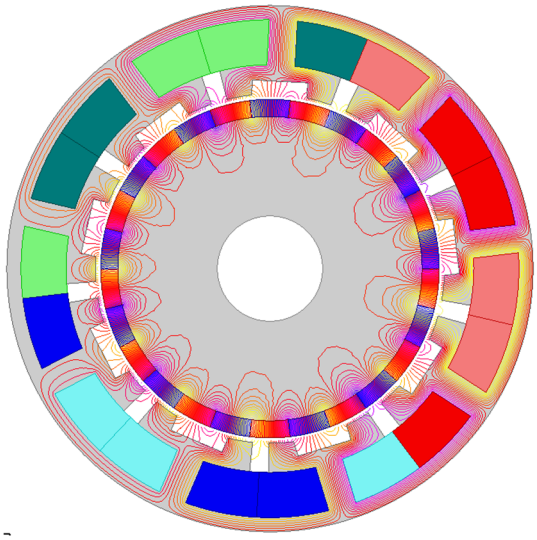

(b) 9-slot/18-FMP/26-pole

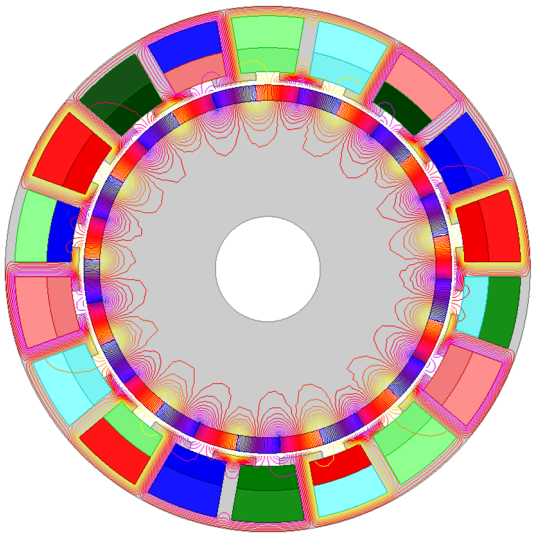

(c) 18-slot/26-pole

Fig. 7.8 No-load flux line comparison.

In a PM machine, the amplitude of the fundamental harmonic of back-EMF E_1 can be expressed as:

$$E_1 = 2\pi f \psi_d \tag{7.5}$$

where f is the electrical frequency and ψ_d is the amplitude of the fundamental harmonic of flux linkage at d-axis.

The phase back EMFs for all machines are also calculated by FEM and shown in Fig. 7.9. Although the amplitudes of fundamental phase flux linkage are smaller, the phase back EMF fundamental

harmonic of the 18-slot/26-pole machine is 14.9% larger than the 18-slot/10-pole machine as a result of higher frequency. The phase back EMF fundamental harmonic of the 18-slot/26-pole machine is 18.7% larger than that of the 9-slot/18-FMP/26-pole machine as a result of larger ψ_d.

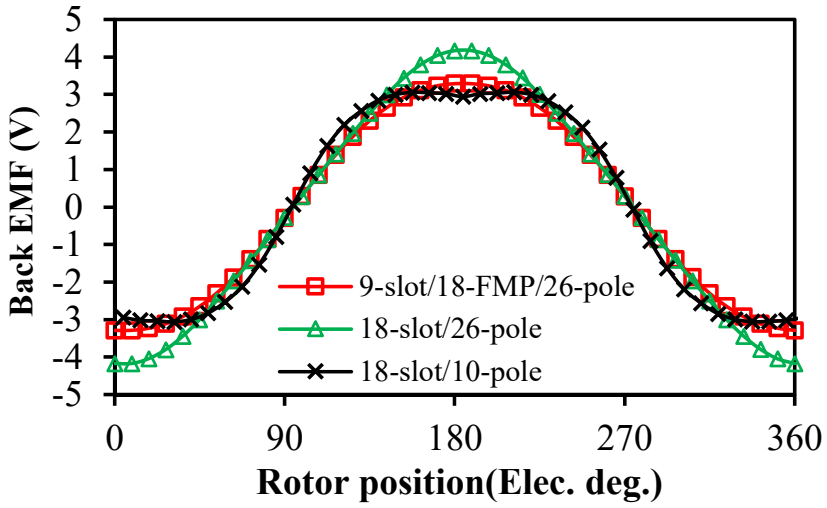

(a) Waveform.

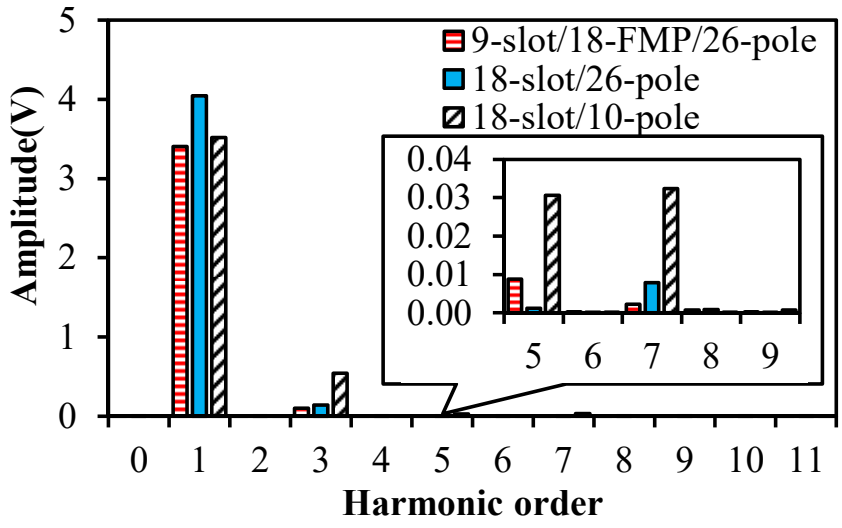

(b) Spectra.

Fig. 7.9 Comparison of phase back EMF (100rpm).

A higher fundamental harmonic indicates a higher average torque, as will be discussed in the next sub-section. Moreover, according to Fig. 7.9 (b), the higher order harmonic content in the back EMF of the 18-slot/26-pole machine is less than that in the 18-slot/10-pole and 9-slot/18-FMP/26-pole machines. It is noteworthy that more sinusoidal back EMF waveform indicates a smoother torque waveform,

which will also be discussed in the next sub-section.

7.4.2 Torque Capability

For an electrical machine with Y-connection and without saliency torque, when symmetrical 3-phase AC current is injected, the instantaneous electromagnetic torque can be approximated by [WAN14c]:

$$\begin{aligned} T_{em} &= T_0 + T_{6n} \\ &= \frac{3E_1 I_m}{2\Omega_r} + \frac{3I_m}{2\Omega_r}\sum_{n=1}^{\infty} E_{6n\pm1}\cos(6np_r\Omega_r t) \end{aligned} \tag{7.6}$$

where I_{m} is the amplitude of the fundamental harmonic of the phase current, E_n is the amplitude of the nth harmonic of the phase back EMF, Ω_r is the mechanical speed of rotation, n is a positive integer and t is the time.

In the slotted PM machines, cogging torque can cause speed ripples and induce vibration at low load and speed. Fig. 7.10 shows the FEM predicted cogging torque waveforms over a cogging torque period of 20 electrical degrees for all machines. It is shown that the 18-slot/10-pole machine has larger cogging torque than the 26-pole machines. The smallest common multiple (LCM) of the slot number and pole number of the 18-slot/10-pole and 18-slot/26-pole machine and the LCM of the FMP number and pole number of the 9-slot/18-FMP/26-pole machine are shown Table 7.3. It shows that the LCMs of the 26-pole machines are larger than those of the 18-slot/10-pole machine, which indicates smaller cogging torques.

Fig. 7.11 and Table 7.3 compare the torque waveforms when the end windings are considered and the copper loss for all machines are fixed at 75W. It shows the 18-slot/26-pole machine has almost the same torque performance with the 9-slot/18-FMP/26-pole machine, with similar average torque and torque ripple. Compared with the 18-slot/10-pole machine, the average torque of the 18-slot/26-pole machine is 9% larger as a consequence of larger fundamental harmonic in the back EMF. Furthermore, both the peak to peak torque and torque ripple index (the ratio of peak to peak torque to average torque) of the 18-slot/26-pole machine is smaller than those of the 18-slot/10-pole machine. This can be explained by the fact that the 18-slot/26-pole machine has a more sinusoidal back EMF waveform and smaller cogging torque than the 18-slot/10-pole machine.

The torque with respect to different copper loss is shown in Fig. 7.12(a), it shows that at smaller copper loss, 18-slot/26-pole and 9-slot/18-FMP/26-pole machines have similar torque output whereas the 18-slot/26-pole machine has larger torque output when the copper loss increases. This is because the 18-

slot/26-pole machine has better overload capability as a result of the reduced armature reaction MMF harmonics. Fig. 7.13 compares the flux density distributions of three machines at the same ampere-turn value under the same scale. It can be observed that both 18-slot/10-pole and 18-slot/26-pole machines are less saturated than the 9-slot/18-FMP/26-pole machine as a result of reduced armature reaction MMF harmonics. For the same reason, the 18-slot/10-pole machine has similar overload capability as shown in Fig. 7.12 (a), with smaller torque under all copper loss values.

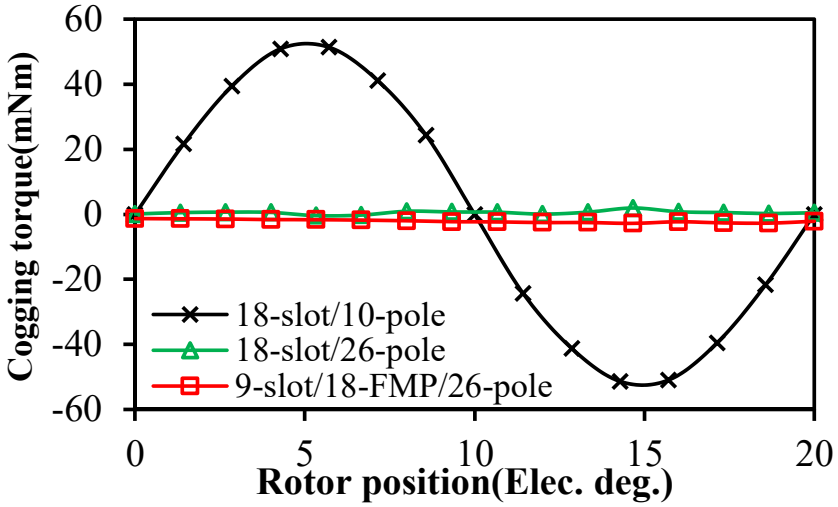

Fig. 7.10 Comparison of cogging torque.

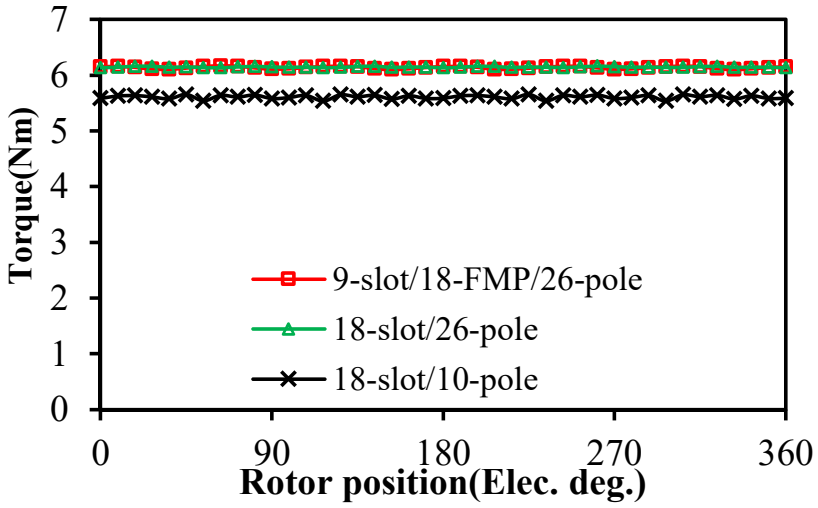

Fig. 7.11 Comparison of torque waveform at fixed copper loss of 75W.

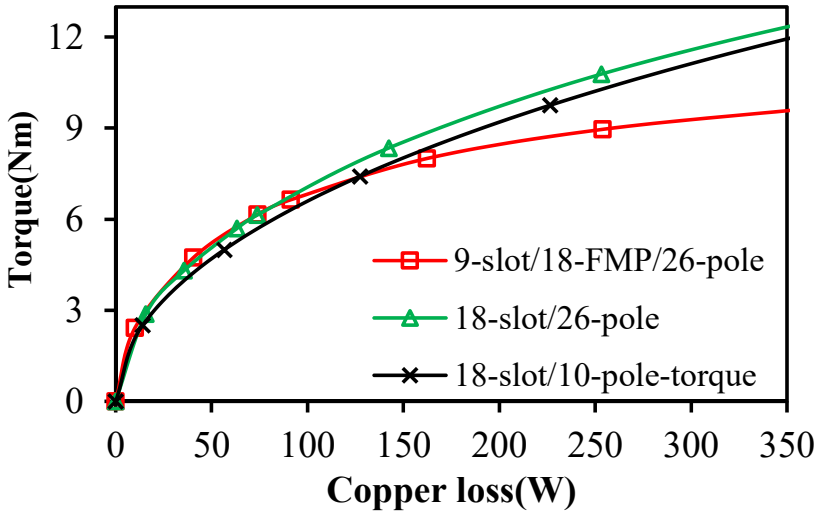

(a) Average torque vs copper loss.

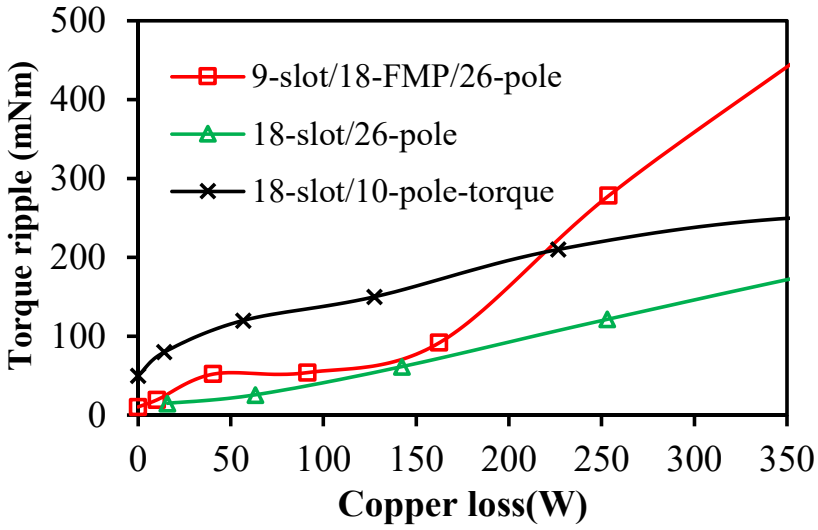

(b) Peak to peak torque vs copper loss.

Fig. 7.12 Comparison of overload capability.

The peak to peak torques with respect to different copper loss are shown in Fig. 7.12 (b). It shows that the peak to peak torques for all machines have an increasing trend with the increase of copper loss. Under smaller copper loss, the 18-slot/10-pole machine has larger torque ripple than the two 26-pole machines due to larger cogging torque. However, with the increase of copper loss, the torque ripple of the 9-slot/18-FMP/26-pole machine increases significantly and overtakes that of the 18-slot/10-pole machine due to significantly increased saturation level, as shown in Fig. 7.13. It is noteworthy that under all the copper loss values, the 18-slot/26-pole has the smallest torque ripple among the three machine candidates.

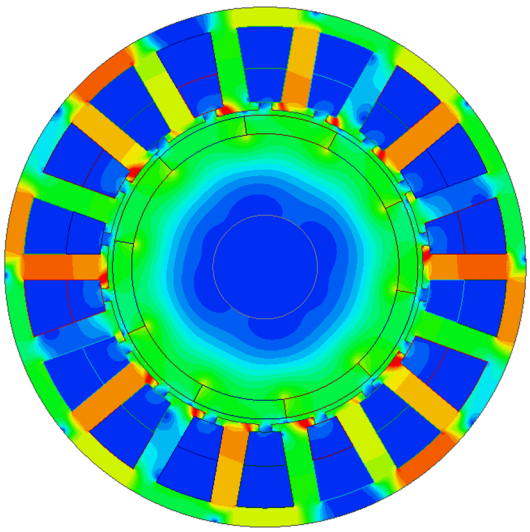

(a) 18-slot/10-pole

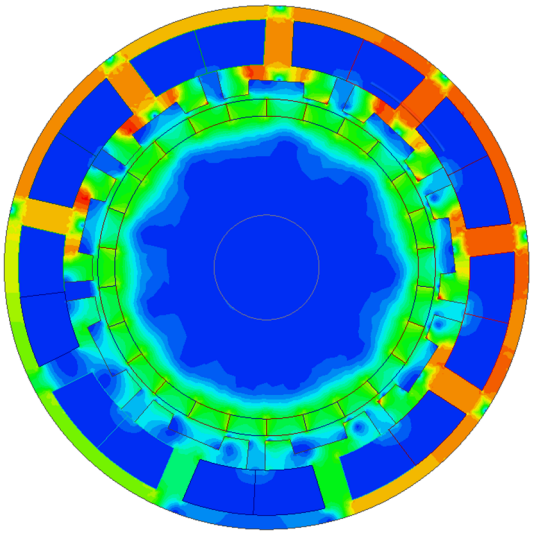

(b) 9-slot/18-FMP/26-pole

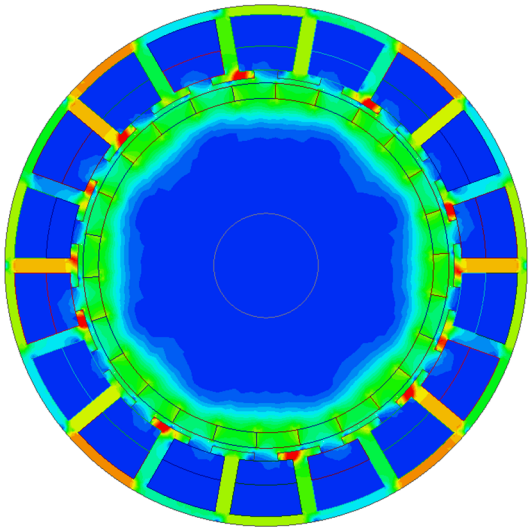

(c) 18-slot/26-pole

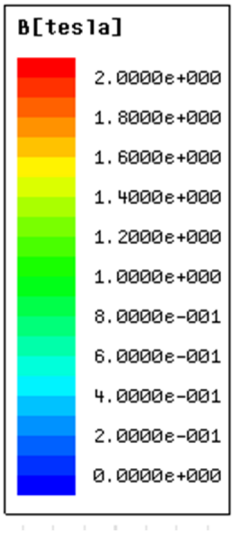

(d) Scale

Fig. 7.13 Comparison of flux density distribution at 2790 ampere turns.

Table 7.3. Performance Comparison

	9-slot/18-FMP/26-pole	18-slot/26-pole	18-slot/10-pole
Torque (Nm)	6.13	6.14	5.70
Peak to peak torque (Nm)	0.07	0.03	0.12
Torque ripple (%)	1.12	0.49	2.11
LCM [N_s(or N_f), $2p_r$]	234	234	90
L_q ($\approx L_d$)(mH)	2.72	1.24	1.23
L_q/N_p (mH)	0.026	0.011	0.010
cosφ	0.73	0.95	0.98
ψ_{PM}(mWb)	25.9	29.7	67.2
Rated current (A)	10	10	10
k_{wf}	3.15	1.25	0.55

7.4.3 Inductance and Power Factor Comparison

To make a fair comparison, both q-axis inductance and inductance per turn of all machine candidates are calculated and compared in Table 7.3. It shows that the 18-slot/26-pole and 18-slot/10-pole machines have both smaller L_q and L_q/N_p than the 9-slot/18-FMP/26-pole machine as a result of reduced armature reaction MMF harmonics. It is noteworthy that the FEA calculated L_q/N_p of the 18-slot/26-pole machine is 42% of the 9-slot/18-FMP/26-pole machine, which is consistent with the analytical results calculated by (7.4). Despite the fact that the 18-slot/26-pole machine has larger N_p, it has smaller L_q as a result of even smaller L_q/N_p. Under the same rated current of 10A, the fundamental harmonics of the induced voltage of machine candidates are shown in Fig. 7.14. It shows clearly that the power factor angle $\varphi_3 < \varphi_2 < \varphi_1$. From (7.2), it can be calculated that the 18-slot/10-pole has the largest power factor among the three machine candidates, 18-slot/26-pole machine improves the power factor of 9-slot/18-FMP/26-pole machine from 0.73 to 0.95 as shown in Table 7.3.

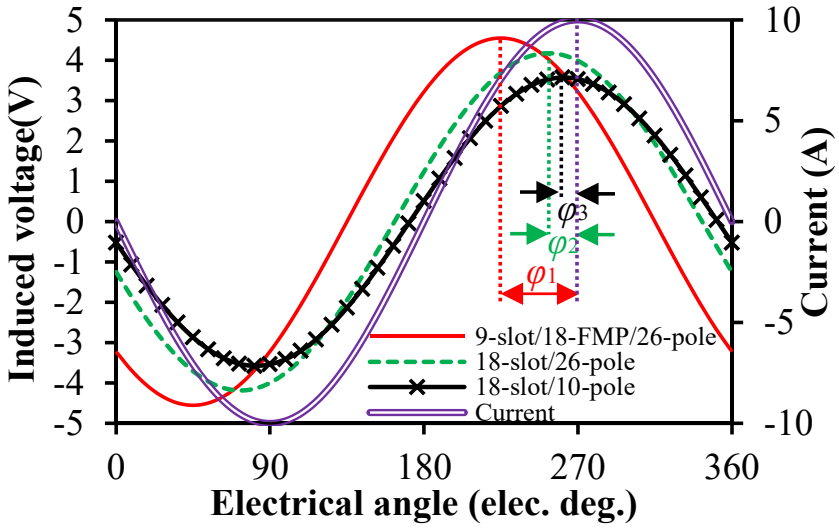

Fig. 7.14 Injecting current and induced voltage. (I_q=10A, 100rpm)

7.4.4 Flux Weakening Capability

The flux weakening capability for the PM machines can be referred to as:

$$k_{fw} = \frac{L_d I_{max}}{\psi_{PM}} \tag{7.7}$$

where L_d is the d-axis inductance, I_{max} is the maximum phase current and ψ_{PM} is the PM flux at d-axis. . It should also be noted that for a fixed motor-inverter combination, k_{fw}>1 means that the motor can achieve an infinite constant power speed ratio. The inverter capacity can be more effectively used if k_{fw} is closer to 1.

The relevant parameters for all machines are calculated by FEM and listed in Table 7.3. It shows that although the 18-slot/26-pole and 18-slot/10-pole machines have similar inductances as a consequence of identical winding distribution, close number of turns and similar airgap permeance. The d-axis flux for the 18-slot/26-pole is only 38% of the 18-slot-10-pole machine because the 26-pole one has smaller PM pole arc. Hence, under the same current, the 18-slot/26-pole machine has k_{fw} larger than 1 and the 18-slot/10-pole machine has k_{fw} smaller than 1. This means that the 18-slot/26-pole machine can achieve an infinite constant power speed ratio whereas the 18-slot/10-pole machine cannot. Compared with the 9-slot/18-FMP/26-pole machine, the 18-slot/26-pole machine has similar ψ_{PM} but only 42% L_d, consequently, k_{wf} of the 18-slot/26-pole machine is smaller than that of the 9-slot/18-FMP/26-pole machine and closer to 1. This means the inverter capacity can be more effectively used for the 18-slot/26-pole machine.

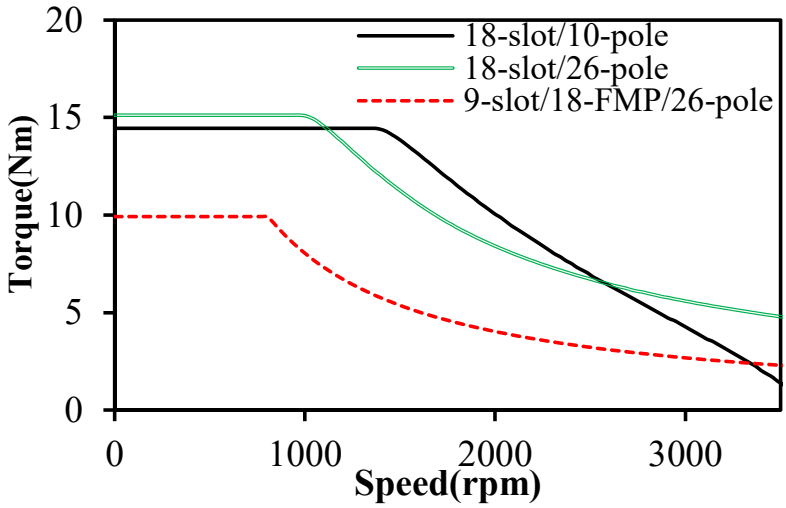

(a) Torque-speed curve

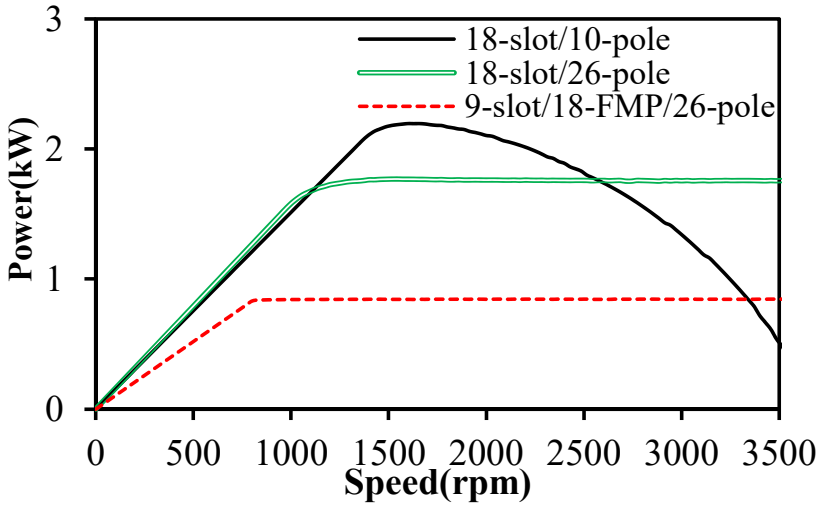

(b) Power-speed curve

Fig. 7.15 Comparison of flux weakening capability.

The flux weakening capabilities of the three machines are calculated when the maximum DC voltage and phase current I_{max} of the inverter are set to be 100V and 30A, respectively. Fig. 7.15 shows the torque-speed and power-speed curves for the machine candidates. It shows that the 18-slot/26-pole machine has 50% larger torque and 18% larger base speed than the 9-slot/18-FMP/26-pole machine as a result of better overload capability and smaller inductance, respectively. As a result, the 18-slot/26-pole machine has a larger constant power in the flux weakening region. The 18-slot/26-pole machine has larger torque but smaller base speed than the 18-slot/10-pole machine at the constant speed region as a consequence of larger back EMF. At the flux weakening region, the 18-slot/26-pole machine has

a larger maximum speed. Although the 18-slot/10-pole machine has larger power than the 18-slot/26-pole machine at some part of the flux weakening regime, the 26-pole machine has wider flux weakening operation region which can achieve infinite constant power speed ratio.

7.4.5. Losses and Efficiency

In PM machines, the rotor iron losses can be calculated by the Bertotti losses equation, which is given by (7.8)

$$P(t) = k_f \left\{ k_h B_m^2 f + \sigma \frac{d^2}{12} \int_T \left(\frac{\mathrm{d}B}{\mathrm{d}t}(t) \right)^2 \frac{1}{T} + k_e \int_T \left(\frac{\mathrm{d}B}{\mathrm{d}t}(t) \right)^{1.5} \frac{1}{T} \right\} \tag{7.8}$$

where d is the thickness of the steel lamination, k_f is the lamination factor, B is the value of flux density on the rotor core, B_m is its maximum value, σ is the conductivity of the rotor core, k_h and k_e are the hysteresis and excess loss coefficients respectively. The three parts at the right side of the equation represent hysteresis losses, classical eddy current losses and excess losses, respectively.

The iron losses of the three machines are calculated using Bertotti losses equation by FEM under the same working condition and the results are shown in Fig. 7.16. It shows that for all machines, the iron losses increase with the increase of the speed. Due to higher frequency, the 26-pole machines have larger iron losses than the 18-slot/10-pole machine over the whole speed range. Moreover, the main asynchronous harmonic for the 10-pole machine is the 13th whereas for the 26-pole machine is the 5th armature reaction harmonic. The 5th armature reaction harmonic has longer pole pitch and amplitude than the 13th harmonic, leading to higher rotor eddy current loss. The 18-slot/26-pole machine has smaller iron loss than the 9-slot/18-FMP/26-pole machine due to smaller flux density as a result of reduce armature reaction MMF harmonics.

Considering the electromagnetic power, iron losses and copper loss under different working condition and the same voltage and current ratings, the efficiency maps of all machines are calculated as shown in Fig. 7.17. It can be seen that all the machines have the similar maximum efficiency of around 94%. However, the 18-slot/26-pole machine has larger area of efficiency > 75% than the 18-slot/10-pole machine. This means that the 18-slot/26-pole machine is more capable than the 10-pole one if higher efficiency is required for most of the working conditions. Compared with the 9-slot/18-FMP/26-pole machine, the 18-slot/26-pole machine has higher efficiency at high torque and power regions thanks to the increased power factor.

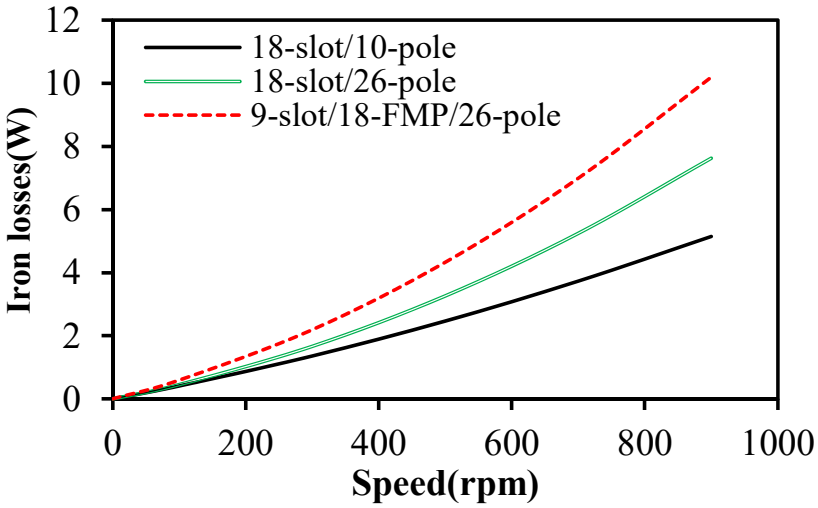

Fig. 7.16 Iron loss vs speed.

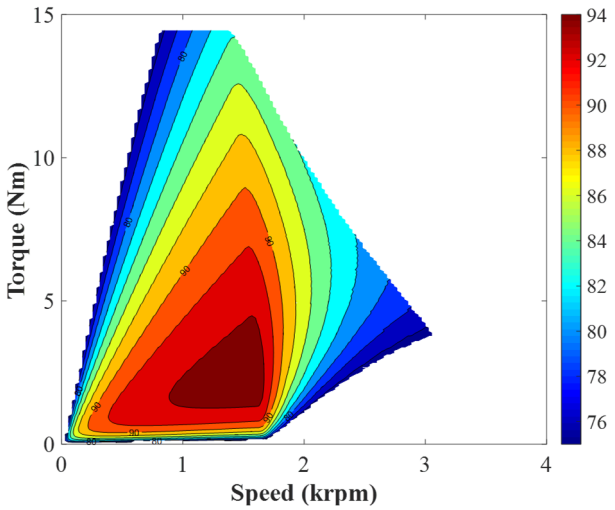

(a) 18-slot/10-pole

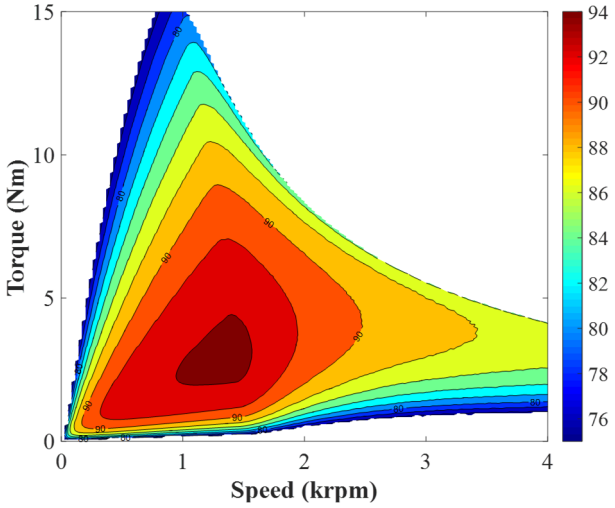

(b) 18-slot/26-pole

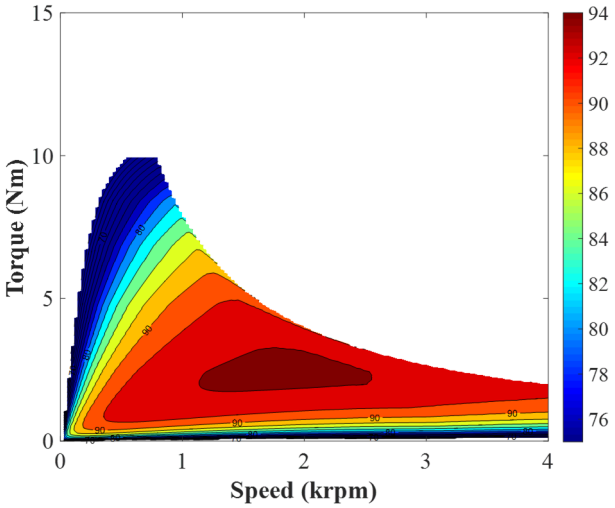

(c) 9-slot/18-FMP/26-pole

Fig. 7.17 Comparison of efficiency map.

7.5 Design Principle and Guidelines

From the geometry evolution in Section 7.2, high power factor VPMSMs with coil pitch of two slot pitches can be derived from either FSPMSM with coil pitch of two slot pitches or VPMSM with concentrated windings.

For FSPMSMs with coil pitch of two slot pitches and lower harmonic content of the armature reaction magnetic field, the feasible slot/pole combinations can be expressed as N_s=2(2p_{rl}±1) [WAN14c]. Their

VPMSM counterparts can be derived by (7.1) with the slot/pole number combinations satisfying $N_s=(4p_r\pm2)/3$ as shown in Table 7.4. It should be noted that for FSPMSMs with coil pitch of two slot pitches, there also exist machines with $N_s=2(2p_r\pm2)$. However, in these machines the MMF harmonics of certain orders cannot be eliminated, and therefore, their Vernier counterparts still have large inductance and their power factor cannot be improved.

For a N_s/2-slot/N_s-FMP/2p_{rh}-pole VPMSM with concentrated windings, if the main armature reaction MMF harmonics appear in pairs with the order difference of 1 [WAN14b], the armature reaction MMF harmonics of even (or odd) orders can be eliminated by doubling the slot numbers and configuring the windings in the way shown in Table 7.4. Since N_s is an even number, if N_s-p_{rh} is even, p_{rl} is also even and the odd harmonics can be eliminated by adopting steps (1)-(4) described in Section 7.2.2. If N_f-p_{rh} is odd, the even harmonics can be eliminated by adopting steps (1)-(5) described in 7.2.2. By doing this, the space harmonic content as well as the inductance will be reduced, and hence, the power factor will increase. Typical slot/pole combinations and their relationships are also provided in Table 7.4.

Table 7.4 Design Guidelines

Concentrated tooth coil windings N_s/2-slot/N_s-FMP/2p_{rh}-pole		⇨	High power factor VPMSM N_s-slot/2p_{rh}-pole	⇦	FS PMSM (coil pitch=2 slot pitches) N_s-slot/2p_{rl}-pole
$N_s=(4p_{rh}\pm2)/3$	N_s-p_{rh}	Steps	$N_s=(4p_{rh}\pm2)/3$	Steps	$N_s=2((2p_{rl})\pm1)$
9/18/28	Even	(1)-(4)	18/28	(7.1)	18/8
9/18/26	Odd	(1)-(5)	18/26	(7.1)	18/10

7.6 Experimental Validation

To validate the previous analyses, the 18-slot/26-pole VPMSM is prototyped. Fig. 7.18 (a) and (b) show the photos of stator and rotor. The dimensional parameters are provided in Table 7 2.

Firstly, the back-EMF is tested and compared with the FEA result, Fig. 7.19 (a). It can be seen that the FEA predicted back-EMF waveform agrees well with the test waveform. Fig. 7.19 (b) shows the comparison of back-EMF spectra between the tested and FEA results. It shows that for the fundamental harmonic, there are 8% discrepancy between the FEA predicted and tested results due to manufacturing

tolerance and end effect. The static torque waveforms within 0–180 electric degrees and under different currents are also tested and compared with the FEA results [ZHU09c] in Fig. 7.19 (c). There is a 10% discrepancy between the FEA predicted and tested torque values. This is because the end effect becomes more severe when the PM pole number increases. Although it has 9% larger torque than its 10-pole counter-part in the simulation, if the end effect for both machines is considered, the torque advantage could be compromised to some extent. The q-axis inductance is also tested by a LCR meter [LIU15] and the power factor is calculated by (6.3) and shown in Table 7.5. Although there are some discrepancies between the FEA and measured results due to the end effect and manufacturing tolerance, good agreements are obtained.

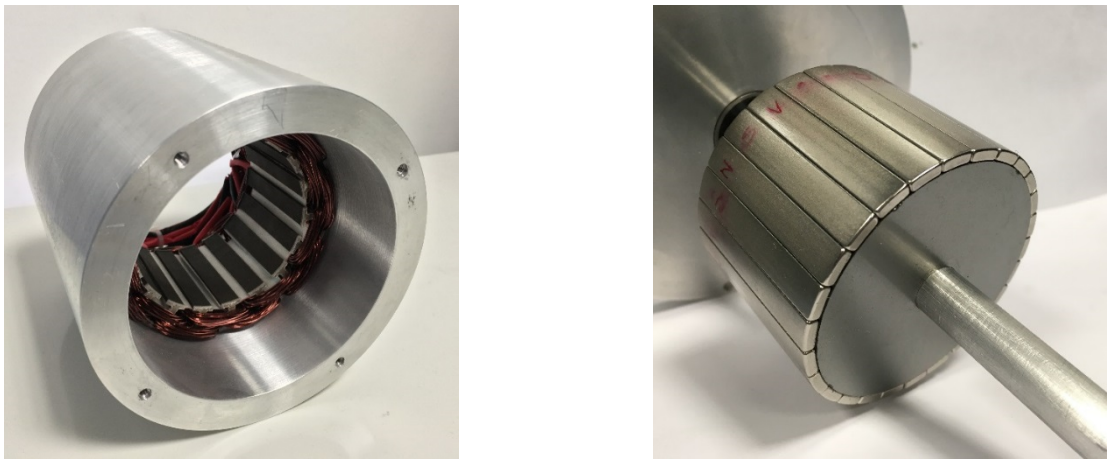

(a) Stator (b) Rotor

Fig. 7.18 Prototype and test rig photos.

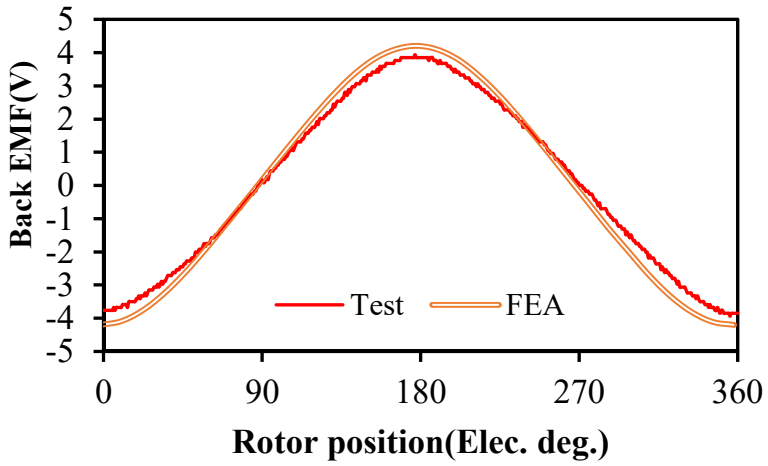

(a) Back EMF waveform (100rpm)

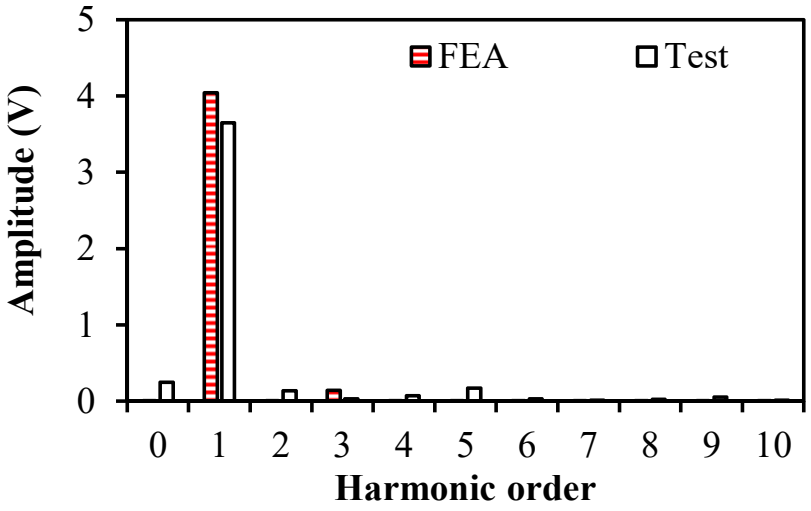

(b) Back-EMF spectrum

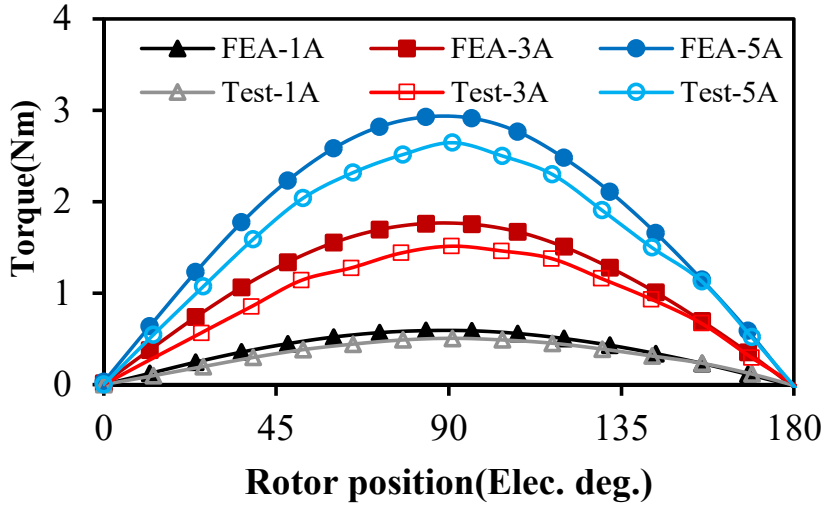

(c) Static torque

Fig. 7.19 Comparison of the measured and FEA predicted results.

Table 7.5 Inductance measurement and Power factor

	Measured	FEA predicted
L_q (mH)	1.25	1.39
cosφ	0.92	0.95

7.7 Summary

In this chapter, an 18-slot/26-pole VPMSM with coil-pitch of two slot pitches is proposed from a 18-slot/10-pole machine with coil-pitch of two slot pitches and a 9-slot/18-FMP/26-pole VPMSM with concentrated windings. Compared with its counterparts, the proposed design reduces the armature reaction space harmonic content and phase inductance without affecting the fundamental harmonic, and hence increases the power factor with better torque and flux weakening capability. The study also shows that a series of VPMSMs with coil-pitch of two slot pitches can achieve high power factor based on the same design principle and given design guidelines. Hence, the feasible slot/pole number combinations are expanded. A prototype is manufactured and tested for validation.

CHAPTER 8

General Conclusions and Future Work

8.1 General Conclusions

8.1.1 Airgap Field Modulation and Magnetic Gearing Effect in Rotor-PM Machines

For any N_s-slot/p_r-pole (or N_s-slot/N_f-FMP/p_r-pole) rotor-PM machine, the armature reaction MMF harmonics will contain a p_rth harmonic and a (N_s-p_r)th (or (N_f-p_r)th) harmonic. The p_rth armature reaction MMF harmonic can produce a p_rth flux density harmonic in the air gap and interact with the p_rth PM flux density harmonic to produce a steady torque due to the conventional rotating field theory. Due to the modulation effect of the N_s-pole stator slot (or the N_f-pole FMP), the (N_s-p_r)th (or (N_f-p_r)th) MMF harmonic can produce an additional p_rth armature reaction flux density harmonic in the air gap. It can also interact with the p_rth PM flux density harmonic and produce a steady torque. This phenomenon is termed as magnetic gearing effect and it has been proven to have contribution to the torque production of all rotor-PM machines in this thesis.

Although the magnetic gearing effect is based on the modulation effect of stator slotting on different armature reaction MMF harmonics, only the resultant p_rth flux density harmonic contributes to the torque production in the air gap.

8.1.2 Influence of Slot Opening

For a specific rotor-PM machine, the influence of slot opening on the torque production is shown in Fig. 8.1. It shows that with the increase of slot opening, the contribution of magnetic gearing effect increases whereas the contribution of conventional principle decreases.

To achieve the best balance between the torque contribution of the conventional PMSM and the magnetic gearing effect, for rotor-PM machines with $2p_r<N_s$, the contribution of magnetic gearing effect should be as small as possible. For those with $2p_r>N_s$, there exists an optimal slot opening for the best trade-off between the conventional torque production principle and magnetic gearing effect. The higher the PM pole number is, the larger the slot opening will be.

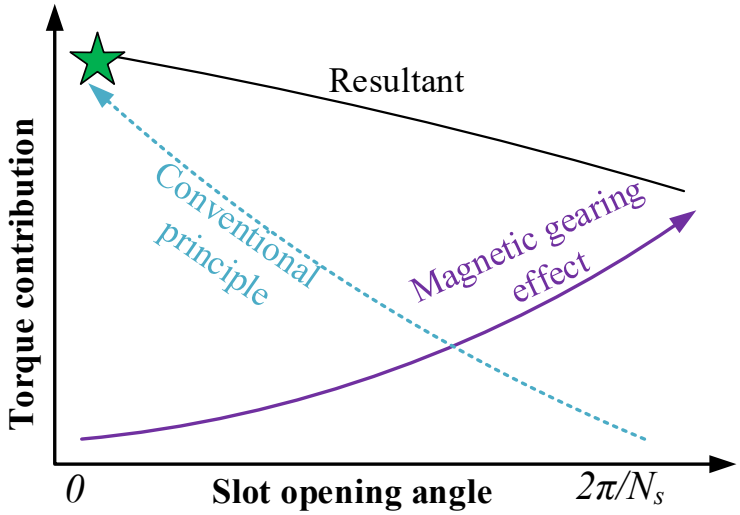

(a) N_s>$2p_r$

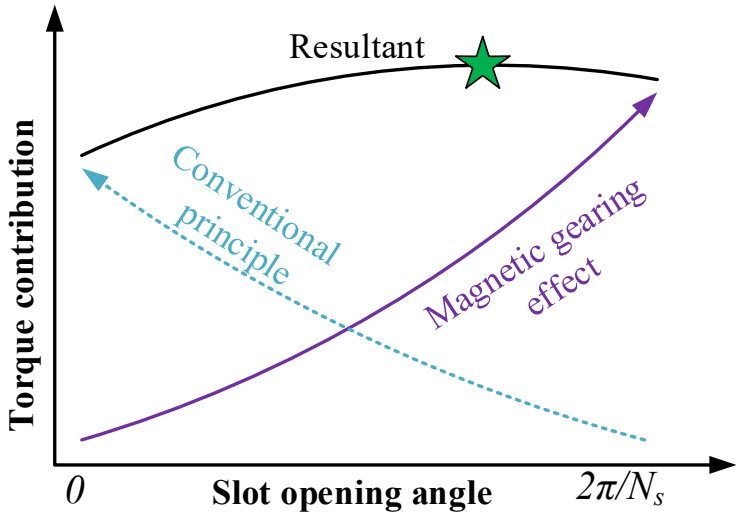

(b) N_s<$2p_r$

Fig. 8.1. Influence of slot opening.

8.1.3 Relationship between Different Rotor-PM Machines

As shown in Fig. 8.2, for N_s-slot/$2p_r$-pole rotor PM machines, when the PM pole number increases from 2, the machine type starts from the conventional ISDW PMSM. With the increase of the PM pole number, both the coil pitch and q decrease. When q decreases to 1/2, the machine type changes to FSCW PMSM and coil pitch equals one. With the further increase of the PM pole number, the machine type changes to VPMSM with distributed windings after q=1/4. After that, the coil pitch increases with the increase of PM pole number.

The contribution of magnetic gearing effect with respect to the rotor PM pole number and winding configuration is shown in Fig. 8.2. It shows that with the increase of the rotor PM pole number, the contribution of magnetic gearing effect to the total torque increases whereas the contribution of the conventional torque production principle decreases. It can be concluded that for ISDW PMSMs, the contribution of the magnetic gearing effect to the total torque is trivial. For FSCW PMSMs, the contribution of magnetic gearing effect is not ignorable whereas for FSDW VPMSMs, the magnetic gearing effect is the major component for torque production.

For DW PMSMs, the one with $2p_r>N_s$ is the VPMSM. Hence, VPMSM can be seen as a kind of conventional machine whose slot opening plays a critical role in the torque production. For FSCW PMSMs, the one with $N_s=2p_r-1$(or $N_s=2p_r-2$, $q=1/4$) can also be seen as a Vernier counterpart of the one with $N_s=2p_r+1$ (or $N_s=2p_r+2$, $q=1/2$).

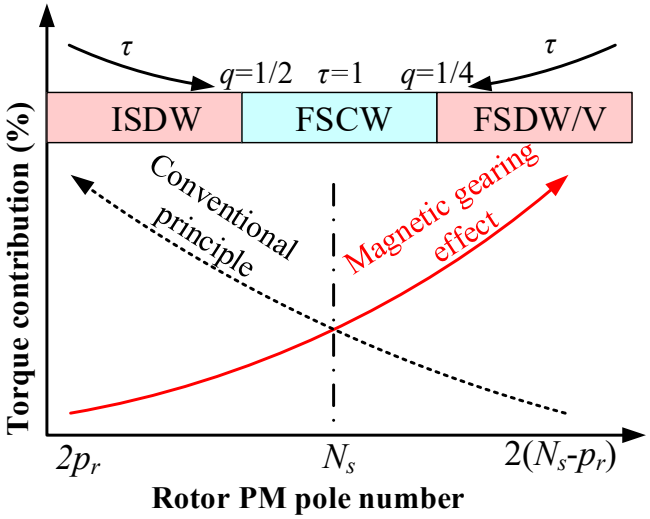

Fig. 8.2. Magnetic gearing effect in rotor-PM N_s-slot machines.

8.1.4 Influence of Gear Ratio on the Performance Metrics of FSCW and VPMSMS

The gear ratios for both FSCW and VPMSMs have been derived. The relationship between the gear ratio and different performance metrics for both kinds of machines have been investigated. For a given slot number, the following conclusions can be drawn for FSCW PMSMs of all phases: under the same slot number, (a) when the gear ratio approaches -1, the winding factor and d-axis inductance increase whereas the mutual inductance and vibration mode decrease monotonically; (b) the FSCW PM machine will have larger torque output and smaller cogging torque with the gear ratio close to -1; and (c) the rotor losses, including the PM eddy current losses and the rotor iron losses, increase with the

increase of the gear ratio.

For VPMSMs, the following conclusions can be drawn:

For the same slot number, with the increase of gear ratio,

(a) The torque increases, the cogging torque and the overload capability decrease;

(b) The d-axis, q-axis and mutual inductances increase;

(c) The power factor decreases, and

(d) The stator and rotor losses increase.

8.1.5 High Power Factor VPMSMs

A series of high power factor VPMSMs with coil-pitch of two slot pitches are evolved from the machine pair theory and harmonic reduction technique in this thesis. The slot/pole number combinations of the high power factor VPMSMs satisfy $N_s=(4p\pm2)/3$. Take 18-slot rotor PM machines as examples, Table 8.1 shows that apart from the existing slot/pole number combinations, two new VPMSM with coil pitch of two slot pitches are generated. The slot/pole number combination of rotor-PM machines has therefore, been expanded.

Table 8.1. Slot/pole number combinations of 18-slot rotor PM machines.

N_s	18											
$2p_r$	2	6	8	10	12	16	20	24	26	28	30	34
τ	9	3	2	2	1	1	1	1	2	2	3	9
Type	ISDW		FSDW		FSCW				FSDW/V		FSDW/V	

8.2 Future Work

Based on the above analyses and conclusions, some future work are summarized as follows:

(1) Investigation of magnetic gearing effect in the torque production of other FSCW PMSM topologies, such as un-equal tooth machines;

(2) Investigation of the influence of rotor topology on the magnetic gearing effect, such as interior PM and consequent pole rotors.

(3) Investigation of torque production mechanism of rotor-PM machines from the perspective of magnetic gearing effect under BLDC driving mode;

(4) Investigation of parasitic effects, such as PM eddy current losses, acoustic noise and vibration.

(5) For VPMSMs, investigation of the influence of PM pole numbers on the end effect.

REFERENCES

[ASL14] B. Aslan and E. Semail, “General analytical model of magnet average eddy-current volume losses for comparison of multiphase pm machines with concentrated winding,” *IEEE Trans. Energy Convers.*, vol. 29, no. 1, pp. 72–83, Mar. 2014.

[ATA00] K. Atallah, D. Howe, P. H. Mellor, and D. A. Stone, “Rotor loss in permanent-magnet brushless ac machines,” *IEEE Trans. Ind. Appl.*, vol. 36, no. 6, pp. 1612–1618, Nov./Dec. 2000.

[ATA03] K. Atallah, J. Wang, and D. Howe, “Torque-ripple minimization in modular permanent-magnet brushless machines,” *IEEE Trans. Ind. Appl.*, vol. 39, no. 6, pp. 1689–1695, Nov. 2003.

[ATA04] K. Atallah, S. D. Calverley, and D. Howe, “Design, analysis and realisation of a high-performance magnetic gear,” *IEE Proceedings-Electric Power Appl.*, vol. 151, no. 2, pp. 135–143, Mar. 2004.

[AZA12] Z. Azar, Z. Q. Zhu, and G. Ombach, “Investigation of torque-speed characteristics and cogging torque of fractional-slot IPM brushless AC machines having alternate slot openings,” *IEEE Trans. Ind. Appl.*, vol. 48, no. 3, pp. 903–912, May/June 2012.

[BAR11] M. Barcaro, N. Bianchi, and F. Magnussen, “Faulty operations of a pm fractional-slot machine with a dual three-phase winding,” *IEEE Trans. Ind. Electron.*, vol. 58, no. 9, pp. 3825–3832, Sept. 2011.

[BAR12] M. Barcaro, N. Bianchi, and F. Magnussen, “Permanent-magnet optimization in permanent-magnet-assisted synchronous reluctance motor for a wide constant-power speed range,” *IEEE Trans. Ind. Electron*., vol. 59, no. 6, pp. 2495–2502, Jun. 2012.

[BIA02] N. Bianchi, and S. Bolognani, “Design techniques for reducing the cogging torque in surface-mounted PM motors,” *IEEE Trans. Ind. Appl.*, vol. 38, no. 5, pp. 1259-1265, Sep./Oct. 2002.

[BIA06] N. Bianchi, S. Bolognani, M. D. Pré, and G. Grezzani, “Design considerations for fractional-slot winding configurations of synchronous machines,” *IEEE Trans. Ind. Appl.*, vol. 42, no. 4, pp. 997–1006, July/August 2006.

[BIA09] N. Bianchi and E. Fornasiero, “Index of rotor losses in three-phase fractional-slot permanent magnet machines,” *IET Electr. Power Appl.*, vol. 3, no. 5, p. 381, Aug. 2009.

[CHE17] M. Cheng, P. Han, and W. Hua, “A general airgap field modulation theory for electrical machines,” *IEEE Trans. Ind. Electron.*, vol. 64, no. 8, pp. 6063–6074, Aug. 2017.

[CHE18] M. Cheng, P. Han, G. Buja, and M. G. Jovanovic, “Emerging multi-port electrical machines and systems: past developments, current challenges and future prospects,” *IEEE Trans. Ind. Electron*., vol. 65, no. 7, pp. 5422-5435, July 2018.

[CHE19] M. Cheng, H. Wen, P. Han, and X. Zhu, “Analysis of airgap field modulation principle of simple salient poles,” *IEEE Trans. Ind. Electron.*, vol. 66, no. 4, pp. 2628–2638, April 2019.

[CHU11] S. Chung, J. Kim, B. Woo, Y. Chun, D. Hong, and J. Lee, “A novel design of modular three-phase permanent magnet Vernier machine with consequent pole rotor,” *IEEE Trans. Magn.*, vol. 47, no. 10, pp. 4215–4218, Sep. 2011.

[CHU12] S. U. Chung, J. M. Kim, D. H. Koo, B. C. Woo, D. K. Hong, and J. Y. Lee, “Fractional slot concentrated winding permanent magnet synchronous machine with consequent pole rotor for low speed direct drive,” *IEEE Trans. Magn.*, vol. 48, no. 11, pp. 2965–2968, Nov. 2012.

[CHU15] S. U. Chung, J. W. Kim, Y. Do Chun, B. C. Woo, and D. K. Hong, “Fractional slot concentrated winding PMSM with consequent pole rotor for a low-speed direct drive: Reduction of rare earth permanent magnet,” *IEEE Trans. Energy Convers.*, vol. 30, no. 1, pp. 103–109, Mar. 2015.

[GIE06] J. F. Gieras, C. Wang, and J. C. Lai, *Noise of polyphase electric motors*, Boca Raton, FL: Taylor & Francis/CRC Press, 2006.

[CRI15] J. M. Crider, and S. D. Sudhoff, “An inner rotor flux-modulated permanent magnet synchronous machine for low-speed high-torque applications,” *IEEE Trans. Energy Convers.*, vol. 30, no. 3, pp. 1247–1254, Sep. 2015.

[CRO02] J. Cros and P. Viarouge, “Synthesis of high performance PM motors with concentrated windings,” *IEEE Trans. Energy Convers*., vol. 17, no. 2, pp. 248–253, Jun. 2002.

[DAJ13] G. Dajaku and D. Gerling, “The influence of permeance effect on the magnetic radial forces of permanent magnet synchronous machines,” *IEEE Trans. Magn.*, vol. 49, no. 6, pp. 2953–2966, Jun. 2013.

[DOS07] L. Dosiek and P. Pillay, “Cogging torque reduction in permanent magnet machines,” *IEEE Ind. Appl. Conf. Annu. Meet.*, vol. 1, no. 6, pp. 1565–1571, 2007.

[DU16] Y. Du, F. Xiao, W. Hua, X. Zhu, M. Cheng, L. Quan, and K. T. Chau, “Comparison of flux-switching PM motors with different winding configurations using magnetic gearing principle,” *IEEE Trans. Magn.*, vol. 52, no. 5, May 2016.

[ELR05] A. M. El-Refaie and T. M. Jahns, “Optimal flux weakening in surface PM machines using fractional-slot concentrated windings,” *IEEE Trans. Ind. Appl.*, vol. 41, no. 3, pp. 790–800, May/ June 2005.

[ELR08] A. M. EL-Refaie, M. R. Shah, R. Qu, and J. M. Kern, “Effect of number of phases on losses in conducting sleeves of surface PM machine rotors equipped with fractional-

slot concentrated windings," *IEEE Trans. Ind. Appl.*, vol. 44, no. 5, pp. 1522–1532, Sept./Oct. 2008.

[ELR10] A. M. EL-Refaie, "Fractional-slot concentrated-windings synchronous permanent magnet machines: Opportunities and challenges," *IEEE Trans. Ind. Electron.*, vol. 57, no. 1, pp. 107–121, Jan. 2010.

[FAK15] M. Fakam, M. Hecquet, V. Lanfranchi, and A. Randria, "Design and magnetic noise reduction of the surface permanent magnet synchronous machine using complex air-gap permeance," *IEEE Trans. Magn.*, vol. 51, no. 4, pp. 1–9, Apr. 2015.

[FAN12] Z. X. Fang, Z. Q. Zhu, L. J. Wu, and Z. P. Xia, "Simple and accurate analytical estimation of slotting effect on magnet loss in fractional-slot surface-mounted PM machines," *in Proc. ICEM*, 2012, pp. 464–470.

[FOR12] E. Fornasiero, N. Bianchi, and S. Bolognani, "Slot harmonic impact on rotor losses in fractional-slot permanent-magnet machines," *IEEE Trans. Ind. Electron.*, vol. 59, no. 6, pp. 2557–2564, Jun. 2012.

[FOR13] E. Fornasiero, L. Alberti, N. Bianchi, and S. Bolognani, "Considerations on selecting fractional-slot nonoverlapped coil windings," *IEEE Trans. Ind. Appl.*, vol. 49, no. 3, pp. 1316–1324, May/Jun. 2013.

[FU10] W. N. Fu and S. L. Ho, "A quantitative comparative analysis of a novel flux-modulated permanent-magnet motor for low-speed drive," *IEEE Trans. Magn.*, vol. 46, no. 1, pp. 127–134, Jan. 2010.

[GAO17] Y. Gao, R. Qu, D. Li, and J. Li, "Design procedure of flux reversal permanent magnet machines," *IEEE Trans. Ind. Appl*., vol. 53, no. 5, pp. 4232–4241, Apr. 2017

[GER15] S. Gerber and R. Wang, "Design and evaluation of a PM Vernier machine," *2015 IEEE Energy Convers. Congr. Expo.*, Montreal, QC, Canada, pp. 5188–5194, Sept. 2015.

[GER15] S. Gerber and R. Wang, "Design and evaluation of a PM Vernier machine," *2015 IEEE Energy Convers. Congr. Expo.*, Montreal, QC, Canada, 2015, pp. 5188–5194.

[HAN25] K. L. Hansen, "The rotating magnetic field theory of A-C motors," *Journal of AIEE*, vol. 44, no. 2, pp. 170-178, Feb. 1925.

[HEN94] J. R. Hendershot, and T. J. E. Miller, *Design of brushless permanent magnet motors*, Oxford, U.K., Magna Physics & Clarendon Press, 1994.

[HSI05] M. F. Hsieh, and Y. S. Hsu, "An investigation on influence of magnet arc shaping upon back electromotive force waveforms for design of permanent magnet brushless motors," *IEEE Trans. Magn.*, vol. 41, no. 10, pp. 3949-3951, Mar. 2005.

[HUA18] W. Hua, X. Zhu, and Z. Wu, "Influence of coil pitch and stator-slot/rotor-pole combination on back-EMF harmonics in flux-reversal permanent magnet machines," *IEEE Trans. Energy Convers*., to be published, DOI: 10.1109/TEC.2018.279500.

[HUG13] A. Hughes, and B. Drury, *Electric motors and drives: fundamentals, types and applications*, Oxford, UK: Newnes, 2013.

[IFE12] C. J. Ifedi, B. C. Mecrow, J. D. Widmer, G. J. Atkinson, S. T. M. Brockway, and D. Kostic-Perovic, "A high torque density, direct drive in-wheel motor for electric vehicles," *6th IET Int. Conf. Power Electron. Mach. Drives*, Bristol, UK, pp. 1–6, Mar. 2012.

[ISH05b] D. Ishak, Z. Q. Zhu, and D. Howe, "Eddy-current loss in the rotor magnets of permanent-magnet brushless machines having a fractional number of slots per pole," *IEEE Trans. Magn.*, vol. 41, no. 9, pp. 2462–2469, Sep. 2005.

[ISH05a] D. Ishak, Z. Q. Zhu, and D. Howe, "Permanent magnet brushless machines with unequal tooth widths and similar slot and pole numbers," *IEEE Trans. Ind. Appl.*, vol. 41, no. 2, pp. 584–590, Mar./Apr. 2005.

[ISH06] D. Ishak, Z. Q. Zhu, and D. Howe, "Comparison of PM brushless motors, having either all teeth or alternate teeth wound," *IEEE Trans. Energy Convers.*, vol. 21, no. 1, pp. 95–103, Mar. 2006.

[ISH95] A. Ishizaki, T. Tanaka, K. Takasaki, and S. Nishikata, "Theory and optimum design of PM Vernier motor," *Int. Conf. Electr. Mach. Drives*, Durham, UK, pp. 208–212, Sept. 1995.

[ISL05] M. S. Islam, S. Mir., T. Sebastian, and S. Underwood, "Design consideration of sinusoidal excited permanent-magnet machines for low-torque-ripple applications," *IEEE Trans. Ind. Appl.*, vol. 41, no. 4, pp. 955-962, Jul./Aug. 2005.

[ISL09] R. Islam, I. Husain, A. Fardoun, and K. McLaughlin, "Permanent-magnet synchronous motor magnet designs with skewing for torque ripple and cogging torque reduction," *IEEE Trans. Ind. Appl.*, vol. 45, no. 1, pp. 152-160, Jan./Feb. 2009.

[JAH96] T. M. Jahns, and W. L. Soong, "Pulsating torque minimization techniques for permanent magnet AC motor drives - a review," *IEEE Trans. Ind. Electron.*, vol. 43, no. 2, pp. 321-330, Apr. 1996.

[JAN14] D. K. Jang and J. H. Chang, "Design of a Vernier machine with PM on both sides of rotor and stator," *IEEE Trans. Magn.*, vol. 50, no. 2, pp. 877–880, Feb. 2014.

[JIA09] L. Jian, K. T. Chau, and J. Z. Jiang, "A magnetic-geared outer-rotor permanent-magnet brushless machine for wind power generation," *IEEE Trans. Ind. Appl.*, vol. 45, no. 3, pp. 954–962, 2009.

[JIA11] L. Jian, G. Xu, C. C. Mi, K. T. Chau, and C. C. Chan, "Analytical method for magnetic field calculation in a low-speed permanent-magnet harmonic machine," *IEEE Trans. Energy Convers.*, vol. 26, no. 3, pp. 862–870, Sept. 2011.

[JIA15] S. Jia, R. Qu, and J. Li, “Analysis of the power factor of stator DC-excited Vernier reluctance machines,” *IEEE Trans. Magn.*, vol. 51, no. 11, Nov. 2015.

[JIA16] S. Jia, R. Qu, J. Li, and D. Li, “Principles of stator DC winding excited Vernier reluctance machines,” *IEEE Trans. Energy Convers.*, vol. 31, no. 3, pp. 935–946, Sept. 2016.

[JUS07] H. Jussila, P. Salminen, M. Niemelä, and J. Pyrhönen, “Guidelines for designing concentrated winding fractional slot permanent magnet machines,” *in Int. Conf. on Power Eng.-Energy and Electr. Drives Proc.*, pp. 191–194, Apr. 2007.

[KAT12] Y. Kataoka, M. Takayama, Y. Matsushima, and Y. Anazawa, “Comparison of three magnet array-type rotors in surface permanent magnet-type Vernier motor,” *in Proc. Int. Conf. Elect. Mach. Syst.*, pp. 1–6, Oct. 2012,

[KIM14] B. Kim and T. A. Lipo, “Operation and design principles of a PM Vernier motor,” *IEEE Trans. Ind. Appl.*, vol. 50, no. 6, pp. 3656–3663, Nov./Dec. 2014.

[KIM98] U. Kim and D. K. Lieu, “Magnetic field calculation in permanent magnet motors with rotor eccentricity: With slotting effect considered,” *IEEE Trans. Magn.*, vol. 34, no. 4, pp. 2253–2266, Jul. 1998.

[KRA13] P. Krause, O. Wasynczuk, S. Sudhoff, and S. Pekarek, "Theory of Electromechanical Energy Conversion", in *Analysis of Electric Machinery and Drive Systems*, 3rd ed, Hoboken, NJ, USA: John Wiley & Sons, Inc., 2013.

[LAS10] K. Laskaris and A. Kladas, “Internal permanent magnet motor design for electric vehicle drive,” *IEEE Trans. Ind. Electron*., vol. 57, no. 1, pp. 138–145, Jan. 2010.

[LEE63] C. H. Lee, “Vernier Motor and Its Design,” *IEEE Trans. Power Appar. Syst.*, vol. 82, no. 66, pp. 343–349, June 1963.

[LEV08] E. Levi, “Multiphase electric machines for variable-speed applications,” *IEEE Trans. Ind. Electron.*, vol. 55, no. 5, pp. 1893–1909, May 2008.

[LI10] J. Li, K. T. Chau, J. Z. Jiang, C. Liu, and W. Li, “A new efficient permanent-magnet Vernier machine for wind power generation,” *IEEE Trans. Magn.*, vol. 46, no. 6, pp. 1475–1478, June 2010.

[LI11] J. Li, K. T. Chau, and W. Li, “Harmonic analysis and comparison of permanent magnet Vernier and magnetic-geared machines,” *IEEE Trans. Magn.*, vol. 47, no. 10, pp. 3649–3652, Oct. 2011.

[LI12] [1] J. Li, J. Wang, Z. Zhao, and W. Yan, “Analytical analysis and implementation of a low-speed high-torque permanent magnet Vernier in-wheel motor for electric vehicle,” *J. Appl. Phys.*, vol. 111, no. 7, pp. 1–4, Mar. 2012.

[LI14b] D. Li, R. Qu, and Z. Zhu, “Comparison of Halbach and dual-side Vernier permanent magnet machines,” *IEEE Trans. Magn.*, vol. 50, no. 2, pp. 10–13, Feb. 2014.

[LI14a] D. Li, R. Qu, and T. A. Lipo, "High-power-factor Vernier permanent-magnet machines," *IEEE Trans. Ind. Appl.*, vol. 50, no. 6, pp. 3664–3674, Feb. 2014.

[LI15] D. Li, R. Qu, J. Li, and W. Xu, "Consequent pole, toroidal winding, outer rotor Vernier permanent magnet machines," *IEEE Trans. Ind. Appl.*, vol. 51, no. 6, pp. 4470–4480, Nov./Dec. 2015.

[LI16] D. Li, R. Qu, J. Li, L. Xiao, L. Wu, and W. Xu, "Analysis of torque capability and quality in Vernier permanent magnet machines," *IEEE Trans. Ind. Appl.*, vol. 52, no. 1, pp. 125–135, Jan./Feb. 2016.

[LI17] H. Li and Z. Q. Zhu, "Influence of magnet arrangement on performance of flux reversal permanent magnet machine," *in Int. Conf. Electr. Mach. Drives*, Miami, FL, USA, May 2017.

[LI18b] H. Y. Li, Y. Liu and Z. Q. Zhu, "Comparative study of airgap field modulation in flux reversal and Vernier permanent magnet machines," *IEEE Trans. Magn., vol. 54*, no.11, Nov. 2018, Art. ID 8105206.

[LI18c] D. Li, T. Zou, R. Qu, and D. Jiang, "Analysis of fractional-slot concentrated winding PM Vernier machines with regular open-slot stators," *IEEE Trans. Ind. Appl.*, vol. 54, no. 2, pp. 1320-1330, March/April 2018.

[LI18a] H. Y. Li, Z. Q. Zhu, and Y. Liu, "Optimal flux modulation pole number in Vernier permanent magnet synchronous machines," *IEEE Energy Convers. Congr. Expo.*, Portland, OR, USA, pp. 2343–2350, 2018.

[LIA15] Y. Liao, F. Liang, and T. A. Lipo, "A novel permanent-magnet motor with doubly salient structure," *IEEE Trans. Ind. Appl.*, vol. 31, no. 5, pp. 1069–1078, Sept./Oct. 1995.

[LIB04] F. Libert and J. Soulard, "Investigation on pole-slot combinations for permanent-magnet machines with concentrated windings," *in Int. Conf. Electr. Mach.*, pp. 5-8, 2004.

[LIU12a] G. Liu, W. Gong, Q. Chen, L. Jian, Y. Shen, and W. Zhao, "Design and analysis of new fault-tolerant permanent magnet motors for four-wheel-driving electric vehicles," *J. Appl. Phys.*, vol. 111, no. 7, pp. 167–170, 2012.

[LIU12b] C. Liu, K. T. Chau, J. Zhong, W. Li, and F. Li, "Quantitative comparison of double-stator permanent magnet Vernier machines with and without HTS bulks," *IEEE Trans. Appl. Supercond.*, vol. 22, no. 3, June 2012.

[LIU15] Y. Liu, Y. Pei, Y. Yu, Y. Shi, and F. Chai, "Increasing the saliency ratio of fractional slot concentrated winding interior permanent magnet synchronous motors," *IET Electr. Power Appl.*, vol. 9, no. 7, pp. 439–448, Jul. 2015.

[LIU17] W. Liu and T. A. Lipo, “A family of Vernier permanent magnet machines utilizing an alternating rotor leakage flux blocking design,” *2017 IEEE Energy Convers. Congr. Expo.* Cincinnati, OH, USA, 2017, pp. 2461-2468.

[MAG03] F. Magnussen and C. Sadarangani, “Winding factors and Joule losses of permanent magnet machines with concentrated windings,” *in IEEE International Electric Machines and Drives Conference*, vol. 1, pp. 333–339, Jun. 2003.

[MEN93] C. Meng, and Q. Qian, *Electromechanical Energy Conversion*, Hangzhou, Zhejiang: Zhejiang University press, 1985 (in Chinese).

[NAK06] M. Nakano, H. Kometani, and M. Kawamura, “A study on eddy-current losses in rotors of surface permanent-magnet synchronous machines,” *IEEE Trans. Ind. Appl.*, vol. 42, no. 2, pp. 429–435, Mar./April 2006.

[NI14] R. Ni, G. Wang, X. Gui, and D. Xu, “Investigation of d- and q-axis inductances influenced by slot-pole combinations based on axial flux permanent-magnet machines,” *IEEE Trans. Ind. Electron.*, vol. 61, no. 9, pp. 4539–4551, Sept. 2014.

[NIU10] S. Niu, S. L. Ho, W. N. Fu, and L. L. Wang, “Quantitative comparison of novel Vernier permanent magnet machines,” *Magn. IEEE Trans.*, vol. 46, no. 6, pp. 2032–2035, June 2010.

[NOV98] D. W. Novotny and T. A. Lipo, Vector Control and Dynamics of AC Drives. Oxford, U.K.: Clarendon, 1998.

[OKA13] K. Okada, N. Niguchi, and K. Hirata, “Analysis of a Vernier motor with concentrated windings,” *IEEE Trans. Magn.*, vol. 49, no. 5, pp. 2241–2244, May 2013.

[ONE16] Y. Oner, Z. Q. Zhu, L. Wu, X. Ge, H. Zhan, and J. Chen, “Analytical on-load sub-domain field model of permanent magnet Vernier machines,” *IEEE Trans. Ind. Electron.*, vol. 63, no. 7, pp. 4105–4117, July 2016.

[PET17] I. Petrov, M. Niemela, P. Ponomarev, and J. Pyrhonen, “Rotor surface ferrite permanent magnets in electrical machines: advantages and limitations,” *IEEE Trans. Ind. Electron.*, vol. 64, no. 7, pp. 5314–5322, July 2017.

[PON13] P. Ponomarev, P. Lindh, and J. Pyrhonen, “Effect of slot-and-pole combination on the leakage inductance and the performance of tooth-coil permanent-magnet synchronous machines,” *IEEE Trans. Ind. Electron.*, vol. 60, no. 10, pp. 4310–4317, Oct. 2013.

[PON14] P. Ponomarev, Y. Alexandrova, I. Petrov, P. Lindh, E. Lomonova, and J. Pyrhonen, “Inductance calculation of tooth-coil permanent-magnet synchronous machines,” *IEEE Trans. Ind. Electron.*, vol. 61, no. 11, pp. 5966–5973, Nov. 2014.

[PRY12] J. Pyrhönen, H. Jussila, Y. Alexandrova, P. Rafajdus, and J. Nerg, “Harmonic loss calculation in rotor surface permanent magnets—new analytic approach,” *IEEE Trans. Magn.*, vol. 48, no. 8, pp. 2358–2366, Aug. 2012.

[QU11] R. Qu, D. Li, and J. Wang, “Relationship between magnetic gears and Vernier PM machines,” in Proc. Int. *Conf. Elect. Mach. Syst.*, Beijing, China, Aug. 18–20, 2011, pp. 1–6.

[RAS00] K. F. Rasmussen, J. H. Davies, T. J. E. Miller, M. I. McGelp, and M. Olaru, “Analytical and numerical computation of air-gap magnetic fields in brushless motors with surface permanent magnets,” *IEEE Trans. Ind. Appl*., vol. 36, no. 6, pp. 1547–1554, 2000.

[SAL04] P. Salminen, M. Niemela, J. Pyrhonen, and J. Mantere, “Performance analysis of fractional slot wound PM-motors for low speed applications,” *IEEE IAS Annu. Meet., vol.2*, pp. 1032-1037, Oct. 2004.

[SHA12] S. Q. A. Shah, T. A. Lipo, and B. Kwon, “Modeling of novel permanent magnet pole shape SPM motor for reducing torque pulsation,” *IEEE Trans. Magn.*, vol. 48, no. 11, pp. 4626–4629, Nov. 2012.

[SHI16] Y. Shi, L. Jian, J. Wei, Z. Shao, W. Li, and C. C. Chan, “A new perspective on the operating principle of flux-switching permanent magnet machines,” *IEEE Trans. Ind. Electron.*, vol. 63, no. 3, pp. 1425–1437, Mar. 2016.

[SIL18] R. C. P. Silva, T. Rahman, M. H. Mohammadi, and D. A. Lowther, “Multiple operating points based optimization: application to fractional slot concentrated winding electric motors,” *IEEE Trans. Ind. Electron.*, vol. 65, no. 2, pp. 1719–1727, Feb. 2018.

[SPA14] C. M. Spargo, B. C. Mecrow, and J. D. Widmer, “A seminumerical finite-element postprocessing torque ripple analysis technique for synchronous electric machines utilizing the air-gap Maxwell stress tensor,” *IEEE Trans. Magn.*, vol. 50, no. 5, May 2014.

[SPO03] E. Spooner and L. Haydock, “Vernier hybrid machines,” *in IEE Proc. - Electr. Power Appl.*, vol. 150, no. 6, pp. 655–662, Nov. 2003.

[TAN10] J. C. Tan, *Technologies of BLDC machines*, Beijing, China: China Machine Press, 2010 (in Chinese).

[TOB00] A. Toba and T. a Lipo, “Generic torque-maximizing design methodology of surface permanent-magnet Vernier machine,” *IEEE Trans. Ind. Appl.*, vol. 36, no. 6, pp. 1539–1546, Nov./Dec. 2000.

[VAL14a] M. Valavi, S. Member, A. Nysveen, S. Member, R. Nilssen, and T. Rølvåg, “Slot harmonic effect on magnetic forces and vibration in low-speed permanent-magnet machine with concentrated windings,” *IEEE Trans. Ind. Appl.*, vol. 50, no. 5, pp. 3304–3313, Sep./Oct. 2014.

[VAL14b] M. Valavi, A. Nysveen, R. Nilssen, R. D. Lorenz, and T. Rølvåg, “Influence of pole and slot combinations on magnetic forces and vibration in low-speed PM wind generators,” *IEEE Trans. Magn.*, vol. 50, no. 5, May 2014.

[WAN05] J. Wang, Z. P. Xia, and D. Howe, “Three-phase modular permanent magnet brushless machine for torque boosting on a downsized ICE vehicle,” *IEEE Trans. Veh. Technol.*, vol. 54, no. 3, pp. 809–816, May 2005.

[WAN06] J. Wang, Z. P. Xia, S. A. Long, and D. Howe, “Radial force density and vibration characteristics of modular permanent magnet brushless AC machine,” *IEE Proc. - Electr. Power Appl.*, vol. 153, no. 6, pp. 793–801, Nov. 2006.

[WAN14b] J. Wang, V. I. Patel, and W. Wang, “Fractional-slot permanent magnet brushless machines with low space harmonic contents,” *IEEE Trans. Magn.*, vol. 50, no. 1, pp. 1–9, Jan. 2014.

[WAN14a] K. Wang, Z. Q. Zhu, and G. Ombach, “Torque enhancement of surface-mounted permanent magnet machine using third-order harmonic*,” IEEE Trans. Magn.*, vol. 50, no. 3, pp. 1-9, Mar. 2014.

[WAN14c] K. Wang, Z. Q. Zhu, and G. Ombach, “Synthesis of high performance fractional-slot permanent-magnet machines with coil-pitch of two slot-pitches,” *IEEE Trans. Energy Convers.*, vol. 29, no. 3, pp. 758–770, Sep. 2014.

[WU15b] L. Wu, R. Qu, D. Li, and Y. Gao, “Influence of pole ratio and winding pole numbers on performance and optimal design parameters of surface permanent-magnet Vernier machines,” *IEEE Trans. Ind. Appl.*, vol. 51, no. 5, pp. 3707–3715, Sep./Oct. 2015.

[WU15c] Z. Z. Wu and Z. Q. Zhu, “Analysis of air-gap field modulation and magnetic gearing effects in switched flux permanent magnet machines,” *IEEE Trans. Magn.*, vol. 51, no. 5, May 2015.

[WU15a] D. Wu and Z. Q. Zhu, “Design trade-off between cogging torque and torque ripple in fractional slot surface- mounted permanent magnet machines,” *IEEE Trans. Magn.*, vol. 15, no. 4, Nov. 2015.

[XU15] L. Xu, G. Liu, W. Zhao, J. Ji, H. Zhou, W. Zhao, and T. Jiang, “Quantitative comparison of integral and fractional slot permanent magnet Vernier motors,” *IEEE Trans. Energy Convers.*, vol. 30, no. 4, pp. 1483–1495, June 2015.

[YAN13] J. Yang, G. Liu, W. Zhao, Q. Chen, Y. Jiang, L. Sun, and X. Zhu, “Quantitative comparison for fractional-slot concentrated-winding configurations of permanent-magnet Vernier machines,” *IEEE Trans. Magn.*, vol. 49, no. 7, pp. 3826–3829, July 2013.

[ZAR06] D. Žarko, T. a Lipo, and D. Ban, “Analytical calculation of magnetic field distribution in the slotted air gap of a surface pm motor using complex relative air gap permeance,” *IEEE Trans. Magn.*, vol. 42, no. 7, pp. 1828–1837, Jul. 2006.

[ZAR08] D. Zarko, D. Ban, and T. a. Lipo, “Analytical solution for cogging torque in surface permanent-magnet motors using conformal mapping,” *IEEE Trans. Magn.*, vol. 44, no. 1, pp. 2943–2954, Jan. 2008.

[ZAR09] D. Zarko, D. Ban, and T. a. Lipo, “Analytical solution for electromagnetic torque in surface permanent-magnet motors using conformal mapping,” *IEEE Trans. Magn.*, vol. 45, no. 7, pp. 2943–2954, Jul. 2009.

[ZHA14] F. Zhao, T. A. Lipo, and B. Kwon, “A novel dual-stator axial-flux spoke-type permanent magnet Vernier machine for direct-drive applications,” *IEEE Trans. Magn.*, vol. 50, no. 11, pp. 2–5, Nov. 2014.

[ZHA16a] W. Zhao, J. Zheng, J. Wang, G. Liu, J. Zhao, and Z. Fang, “Design and analysis of a linear permanent- magnet Vernier machine with improved force density,” *IEEE Trans. Ind. Electron.*, vol. 63, no. 4, pp. 2072–2082, April 2016.

[ZHA16b] P. Zhang, D. M. Ionel, and N. A. O. Demerdash, “Saliency ratio and power factor of IPM motors with distributed windings optimally designed for high efficiency and low-cost applications,” *IEEE Trans. Ind. Appl.*, vol. 52, no. 6, pp. 4730–4739, Aug. 2016.

[ZHU00] Z. Q. Zhu and D. Howe, “Influence of design parameters on cogging torque in permanent magnet machines,” *IEEE Trans. Energy Convers.*, vol. 15, no. 4, pp. 407–412, Dec. 2000.

[ZHU09a] L. Zhu, S. Z. Jiang, Z. Q. Zhu, and C. C. Chan, “Analytical methods for minimizing cogging torque in permanent-magnet machines,” *IEEE Trans. Magn.*, vol. 45, no. 4, pp. 2023–2031, Apr. 2009.

[ZHU09b] Z. Q. Zhu, Z. P. Xia, L. J. Wu, and G. W. Jewell, “Influence of slot and pole number combination on radial force and vibration modes in fractional slot PM brushless machines having single- and double-layer windings,” *IEEE Energy Convers. Congr. Expo.*, San Jose, California, US, pp. 3443–3450, 2009.

[ZHU09c] Z. Q. Zhu, “A simple method for measuring cogging torque in permanent magnet machines,” *IEEE Power Energy Soc. Gen. Meet.*, pp. 3–6, Oct. 2009.

[ZHU10a] Z. Q. Zhu, Z. P. Xia, L. J. Wu, and G. W. Jewell, “Analytical modeling and finite-element computation of radial vibration force in fractional-slot permanent-magnet brushless machines,” *IEEE Trans. Ind. Appl.*, vol. 46, no. 5, pp. 1908–1918, Sep./Oct. 2010.

[ZHU10b] Z. Q. Zhu, L. J. Wu, and Z. P. Xia, “An accurate subdomain model for magnetic field computation in slotted surface-mounted permanent-magnet machines,” *IEEE Trans. Magn.*, vol. 46, no. 4, pp. 1100–1115, Apr. 2010.

[ZHU11a] Z. Q. Zhu, “Fractional slot permanent magnet brushless machines and drives for electric and hybrid propulsion systems,” *COMPEL - Int. J. Comput. Math. Electr. Electron. Eng.*, vol. 30, no. 1, pp. 9–31, 2011.

[ZHU11b] Z. Q. Zhu, “Switched flux permanent magnet machines - Innovation continues,” *Int. Conf. Electr. Mach. Syst.*, Beijing, China, Aug. 2011.

[ZHU13] Z. Q. Zhu, M. L. M. Jamil, and L. J. Wu, “Influence of slot and pole number combinations on unbalanced magnetic force in PM machines with diametrically asymmetric windings,” *IEEE Trans. Ind. Appl.*, vol. 49, no. 1, pp. 19–30, Jan./Feb. 2013.

[ZHU14] Z. Q. Zhu, L. J. Wu, and M. L. M. Jamil, “Influence of pole and slot number combinations on cogging Torque in permanent-magnet machines with static and rotating eccentricities,” *IEEE Trans. Ind. Appl.*, vol. 50, no. 5, pp. 3265–3277, Sept./Oct. 2014.

[ZHU18a] Z. Q. Zhu, H. Y. Li, R. Deodhar, A. Pride, and T. Sasaki, “Recent developments and comparative study of magnetically geared machines,” *CES Trans. Electr. Mach. Syst.*, vol. 2, no. 1, pp. 13–22, March 2018.

[ZHU18b] Z. Q. Zhu, “Overview of novel magnetically geared machines with partitioned stators,” *IET Electr. Power Appl.*., vol. 12, no. 5, pp. 595–604, Apr. 2018

[ZHU93] Z. Q. Zhu and D. Howe, “Instantaneous magnetic field distribution in brushless permanent magnet dc motors. Part III: Effect of stator slotting,” *IEEE Trans. Magn.*, vol. 29, no. 1, pp. 143–151, Jan. 1993.

[ZHU95] Z.Q. Zhu, D. Howe, and J. K. Mitchell, “Magnetic field analysis and inductances of brushless dc machines with surface-mounted magnets and non-overlapping stator windings,” *IEEE Trans. Magn.*, vol. 31, no. 3, pp. 2115–2118, May 1995.

[ZOU17] T. Zou, D. Li, R. Qu, D. Jiang, and J. Li, “Advanced high torque density PM Vernier machine with multiple working harmonics,” *IEEE Trans. Ind. Appl.*, vol. 53, no. 6, pp. 5295–5304, Nov./Dec. 2017.

Appendix A

Influence of Gear Ratio on the Performance of 4-Phase Fractional Slot Concentrated Winding Permanent Magnet Machines

Without loss of generality, 24-slot FSCW PM machines with 4-phase designs are also considered in this thesis. The feasible pole numbers and the corresponding gear ratios of the 24-slot 4-phase machines are provided in Table A.1. All the 4-phase machine candidates are globally optimised under the same conditions with the 3- and 6-phase machines in Chapter 3. The optimised machine parameters are provided in Table A.2

Table A.1 Gear Ratios in FSCW PM Electrical Machines.

$2p_r$	18	22	26	30
4-phase	-1.67	-1.18	-0.85	-0.60

Table A.2.Optimised Dimensional Parameters.

Phase no.	N_s	$2p_r$	r_y (mm)	w_t (mm)	s_o (Mech. deg.)	r_i (mm)	l_{pm} (mm)	N_{tpc}
4	24	18	48.0	3.8	3.3	32.5	2.6	23
		22	48.2	3.5	3.6	33.8	2.5	
		26	48.4	3.1	3.6	34.3	2.4	
		30	48.6	2.6	3.8	35.0	2.4	

* N_{tpc}-number of turns per coil

The winding factor, torque, C_T, d-axis inductance, mutual inductance, rotor PM and iron losses for the 4-phase FSCW PM machines are calculated and the results are shown in Fig. A.1. They show that G_r can still be used for performance comparison and the reference is always -1 no matter how the phase number changes: when the gear ratio approaches -1, the winding factor, torque and d-axis inductance of the 4-phase machines increase whereas the mutual inductance and C_T decrease monotonically as

shown in Fig. A.1 (a)-(c); the rotor losses, including the PM eddy current losses and the rotor iron losses, increase with the increase of the gear ratio as shown in Fig. A.1(d).

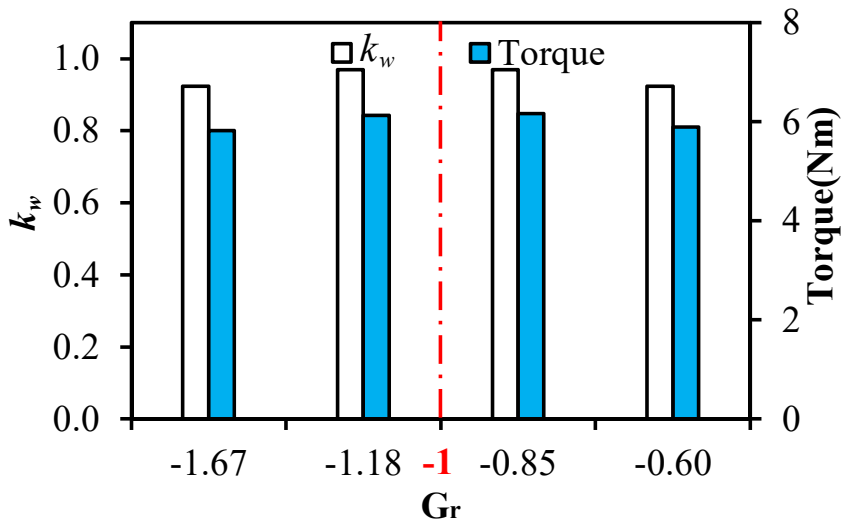

(a) Winding factor and torque (75W copper loss)

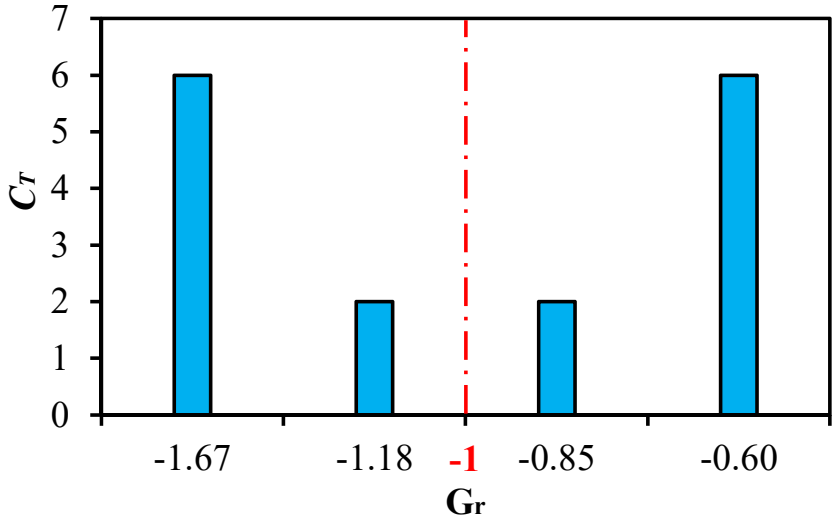

(b) C_T

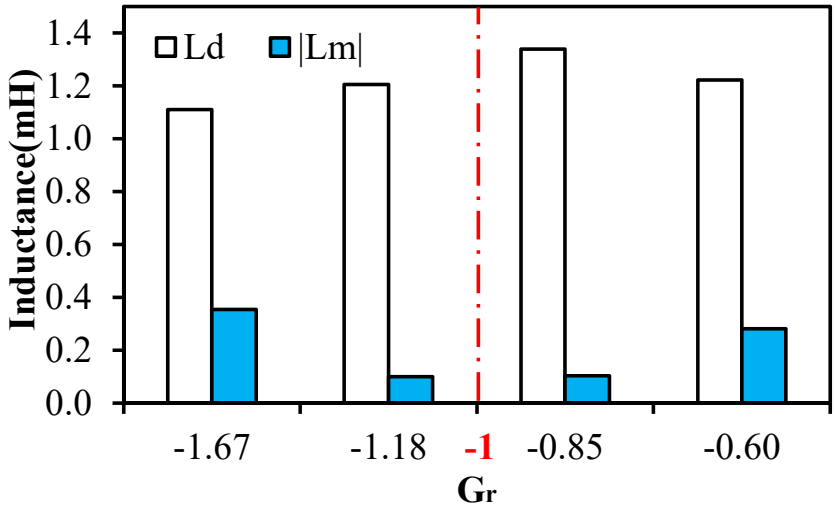

(c) Inductance

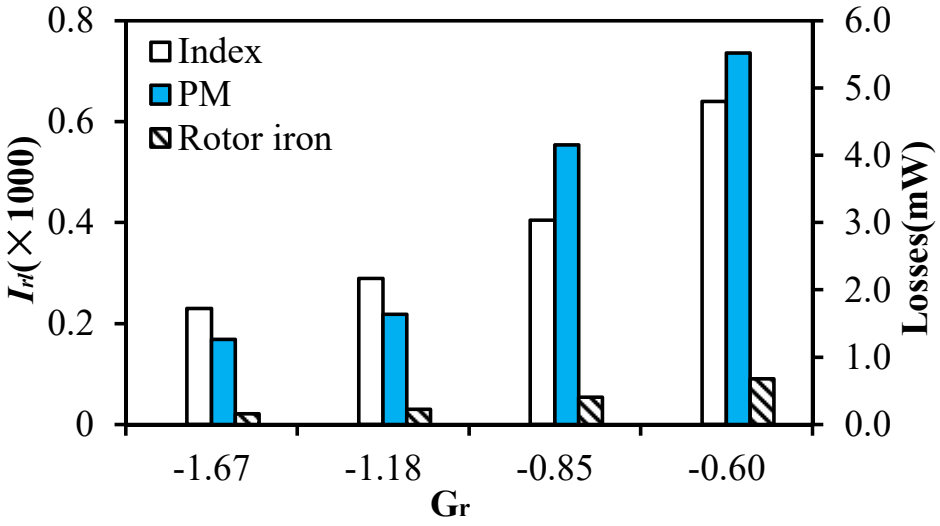

(d) Rotor losses (75W copper loss, 100rpm)

Fig. A.1. Influence of Gr on 4-phase FSCW PMSM performance.

Appendix B

Magnetic Gearing Effect in VPMSMs with Flux Modulation Poles

B.1 Quantification of Torque Contribution in a 6-Slot/12-FMP/20-Pole VPMSM

In this chapter, the FEA-based equivalent current sheet model (ECSM) is used on a 6-slot/12-FMP/20-pole VPMSM to study the harmonic behaviour under the modulation of FMPs and stator slots. Based on the analysis, the contribution of gearing effect to the total torque can be quantified.

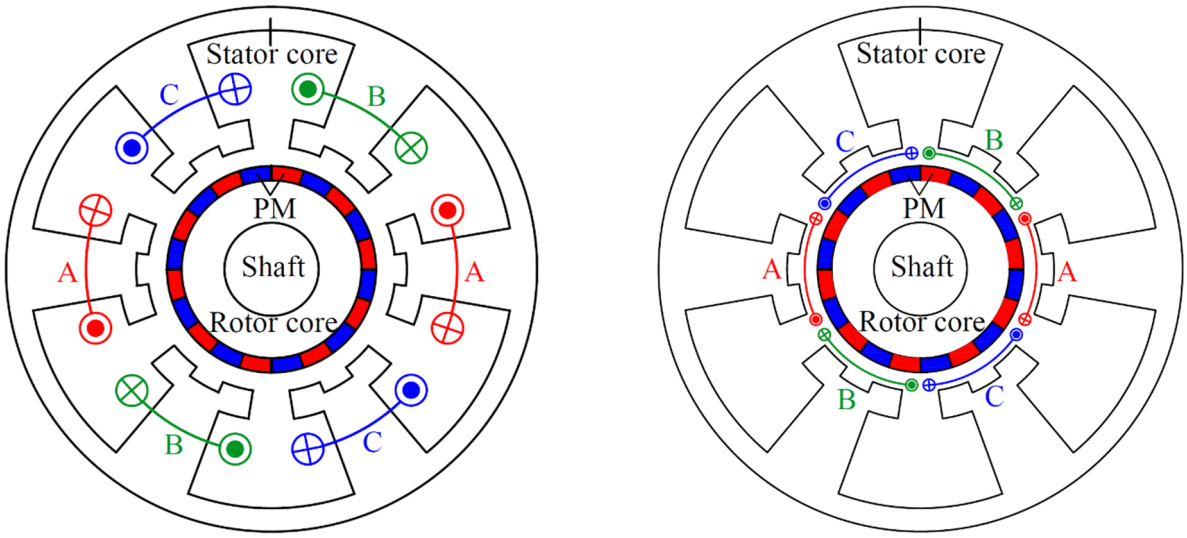

(a) Original model (b) FEA-based ECSM

Fig. B.1. 6-slot/12-FMP/20-pole Vernier machine.

Fig. B.1 shows the original FEA model of the VPMSMs. The schematic diagram of its FEA-based ECSM is provided in Fig. B.1 (b). Similar with the conventional ECSM, the coils are moved from the slots to the slot openings on the stator bore and wound in the same manner as in Fig. B.1 (a). It should be noted that in the FEA simulation, the thickness of the equivalent current sheet is designed very thin (less than 5%) compared to the air-gap length.

When the PMs are not magnetised, the coils in the VPMSM model and its FEA-based ECSM are injected with the same current, their respective armature reaction flux lines are provided in Fig. B.2. It can be seen that VPMSM and its FEA-based ECSM have the same main flux, the only difference between them is that the VPMSM has slot opening leakage flux whereas its FEA-based ECSM does

not change due to different position of coils. However, the slot opening leakage magnetic field does not interact with the PM field and makes no contribution to the output torque. Hence, this difference does not influence the calculation of torque component.

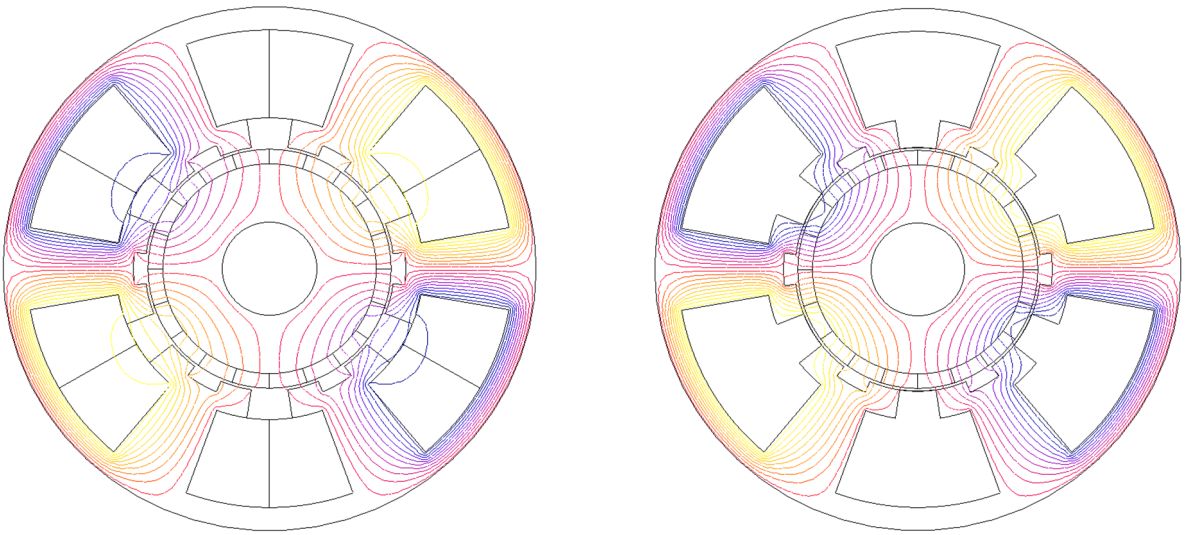

(a) VPMSM model (b) FEA-based ECSM

Fig. B.2. Armature reaction flux lines (I_a=9A, I_b=I_c=-4.5A).

The radial and tangential air-gap armature reaction field components of the VPMSM model and the FEA-based ECSM are provided under the same current injection in Fig. B.3. As aforementioned, in the VPMSM, only the fundamental harmonic contributes to the output torque. The amplitude and phase of the 10th harmonic, which is the fundamental harmonic for this VPMSM, is provided inTable B. 1. It shows that although the amplitudes of the corresponding harmonics in different models are not the same, the harmonics of the same order are in phase. To restore the fundamental harmonic in in the VPMSM model using FEA-based ECSM, the current should be adjusted by introducing a coefficient:

$$k_c = \frac{A_{\mathrm{V}}}{A_{\mathrm{E}}} \tag{B.1}$$

where A_{V} and A_{E} are the amplitudes of the fundamental harmonics in VPMSM and FEA-based equivalent current sheet model, respectively. It should be noted that by introducing k_c, the amplitude of each MMF harmonic will vary by the same proportion, which means that the percentage of contribution of each MMF harmonic to the torque will not be influenced by k_c.

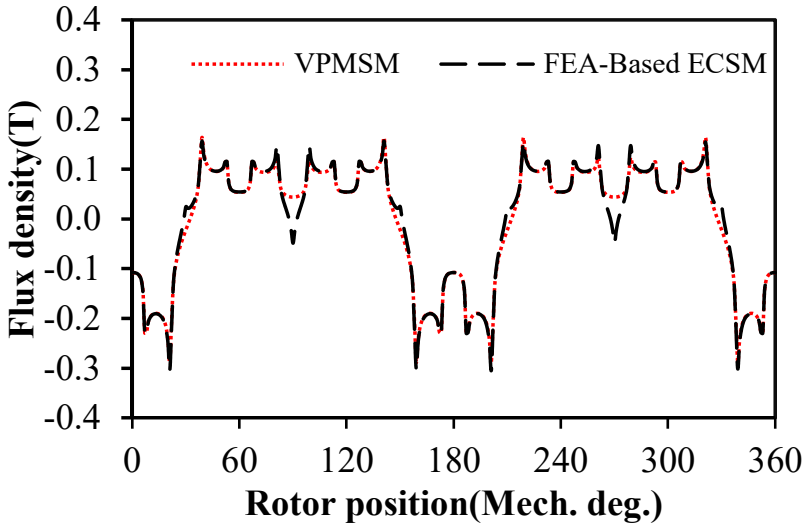

(a) Radial field

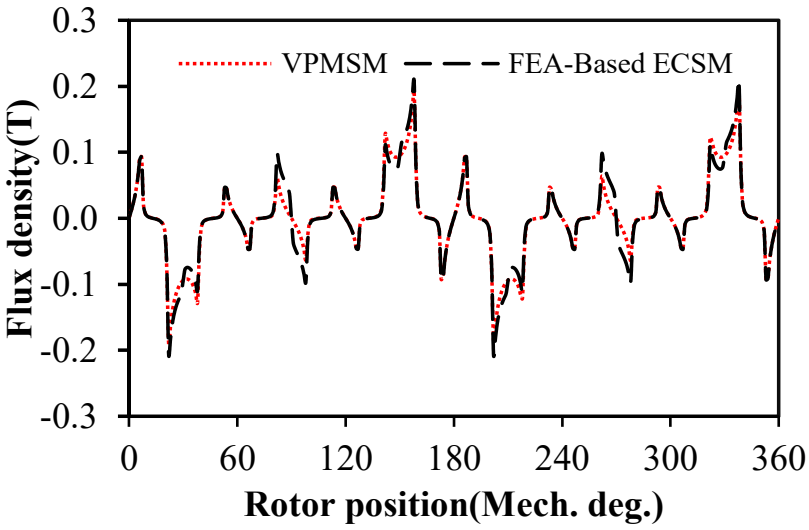

(b) Tangential field

Fig. B.3. Comparison between armature reaction air-gap fields of the two models.

Table B. 1. Amplitude and Phase of the 10th Harmonic

	VPMSM		Equivalent current sheet model	
	Normal	Tangential	Normal	Tangential
Amplitude(T)	0.046	0.041	0.055	0.049
Phase(°)	-5	-95	-5	-95

Hence, the amplitude of the 3-phase current I_E in FEA-based ECSM is set to be:

$$I_E = I_{\max} k_c \tag{B.2}$$

Based on the FEM-based ECSM, a model without PMs and stator slots is firstly built to gain the information of the armature reaction harmonics before being modulated, Fig. B.4. In this model, the amplitude of the 3-phase currents is set equal to be I_E.

The spectra of the armature reaction air-gap magnetic field are calculated by FEA and shown in Fig. B.5. It shows that the amplitudes of the 2nd, 4th and 10th harmonics are larger than the other harmonics. Furthermore, all of them can be modulated either by the FMPs or stator slots to the fundamental harmonic. The mechanism of modulation is provided in Table B.2. Hence, they are considered as of priorities and their phases are provided in Table B.3.

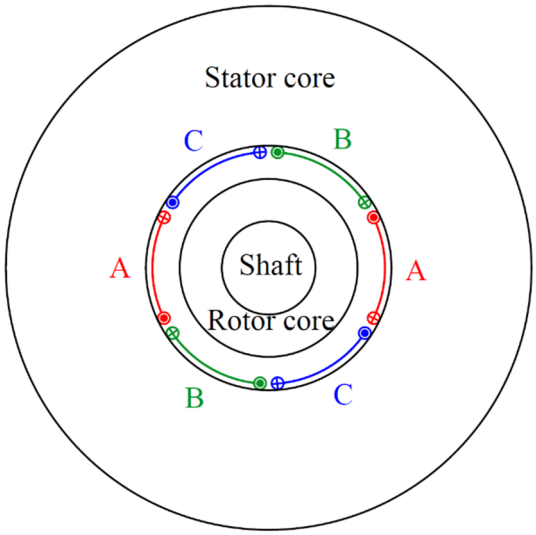

Fig. B.4. A model without PMs and stator slots.

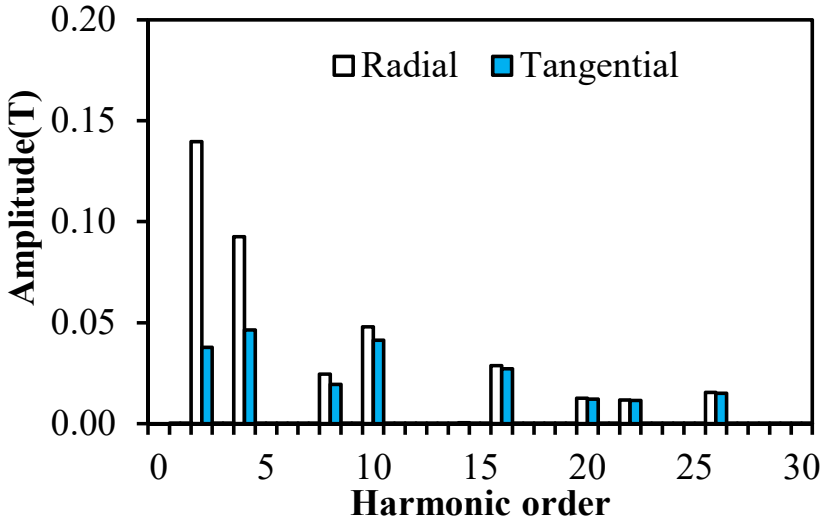

Fig. B.5. FE predicted armature reaction air-gap radial and tangential field harmonics before modulated.

Table B.2. Modulation Mechanism in Proposed VPMSM

p_s	N_s	N_f	p_r
2	-	12	10
4	6	-	10
10	-	-	10

Table B.3. Phases of Armature Reaction Air-gap Harmonics

Harmonic order	Phase(°)	
	Radial	Tangential
2	180	90
4	180	90
10	0	-90

To analyse the behaviour of the 10th armature reaction field harmonic, a 20-pole outer rotor with sinusoidal magnetisation PMs is built, which is shown in Fig. B.6 (a). The thickness of the PMs is the same with that of the equivalent current sheet. The remanence and the initial angle of the PMs are adjusted so that the amplitude and phase of the 10th harmonic produced by outer PMs are the same

with those by the armature reaction field.

A 20-pole inner rotor, which is identical to the rotor in Fig. B.1, is used to interact with the outer PM rotor. Both of them are rotating in the same direction at the mechanical speed n_r, Fig. B.6 (b). Considering the stator slotting, the torque produced by each air gap field harmonic is calculated over an electrical period and shown in Fig. B.8. It can be seen that only the 10th air-gap field harmonic contributes to the steady torque. Since the stator and rotor magnetic fields share the same pole number, this torque contribution is produced by the principle of the conventional PMSM.

The behaviour of the 2nd and 4th armature reaction field harmonic are simulated by the same method. 4-pole and 8-pole outer rotors with sinusoidal magnetisation PMs are used to simulate the behaviour of the 2nd and 4th armature reaction harmonic, respectively. The 4-pole outer rotor rotates at 5 times the speed of the 20-pole inner rotor, in the opposite direction, Fig. B.7 (a). The 8-pole outer rotor rotates at 2.5 times the speed of the 20-pole inner rotor, in the same direction, Fig. B.7 (b). Considering the modulation effect, the torque produced by each air gap field harmonic is calculated by (4.10) over an electrical period and shown in Fig. B.8. It can be seen that only the 10th air-gap field harmonic contributes to the steady torque. It is clear that the 10th harmonic in the armature reaction field is produced by the modulation effect of the FMPs and stator slots on the 2nd and 4th harmonic, respectively.

The resultant torque can be determined by adding up the torque contributions of the 2nd, 4th and 10th armature reaction field harmonics. The resultant is 1.36Nm, which matches perfectly with the average torque calculated by the original FEA model. It can also be seen from Fig. B.8 that the 2nd, 4th and 10th armature reaction harmonics before modulation contribute 36.2%, -6.8% and 70.5% to the total torque output, respectively. They make up nearly 100% of the total torque. In theory, other armature reaction harmonics of orders satisfying (4.8) can also interact with the fundamental harmonic after modulation and generate steady torque, but the amplitude is much smaller than the aforementioned three harmonics. It is clear from Fig. B.8 that for the VPMSM shown in this paper, the magnetic gearing effect contributes approximately 30% to the total torque.

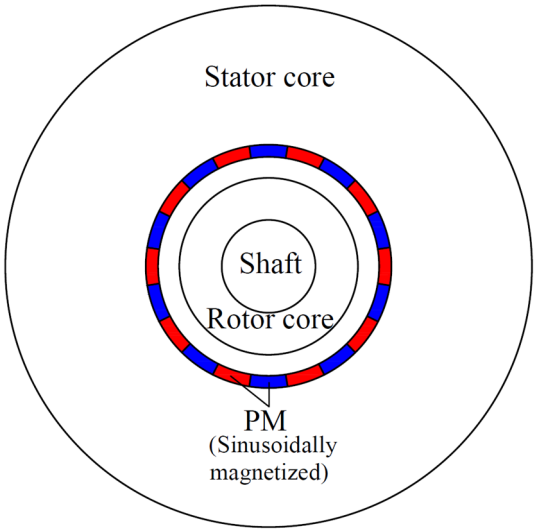

(a) 10th armature reaction harmonic

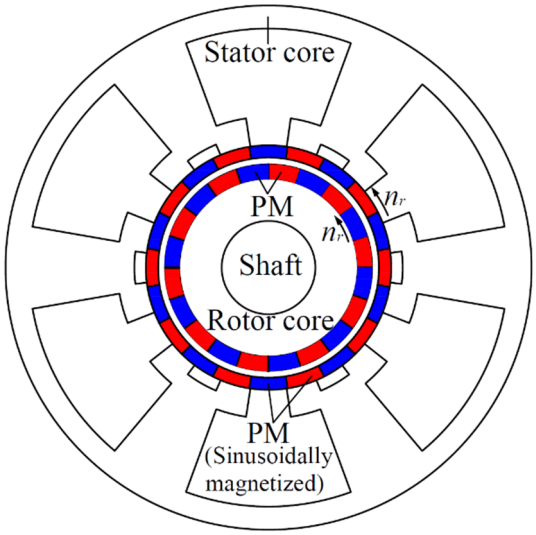

(b) Interaction of the field harmonics

Fig. B.6. Simulation of the behaviour of the 10th harmonic.

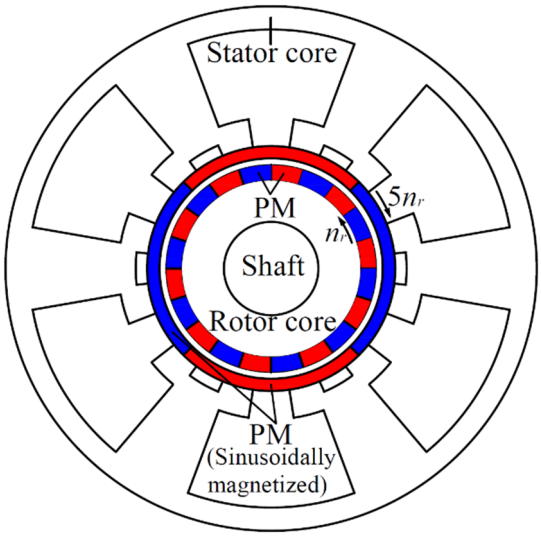

(a) 2nd armature reaction harmonic

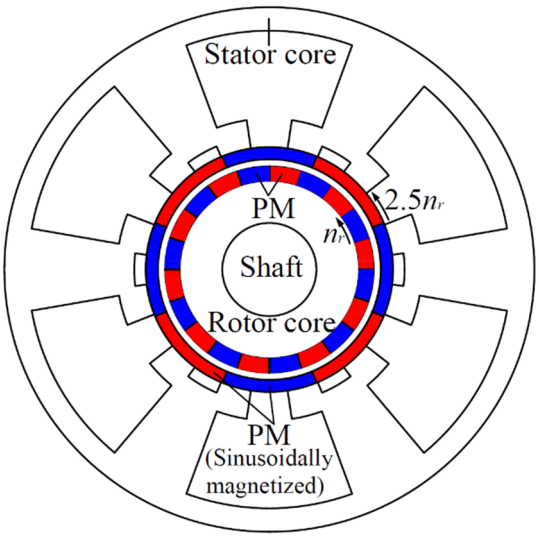

(b) 4th armature reaction harmonic

Fig. B.7. Simulation of the behaviour of the harmonics.

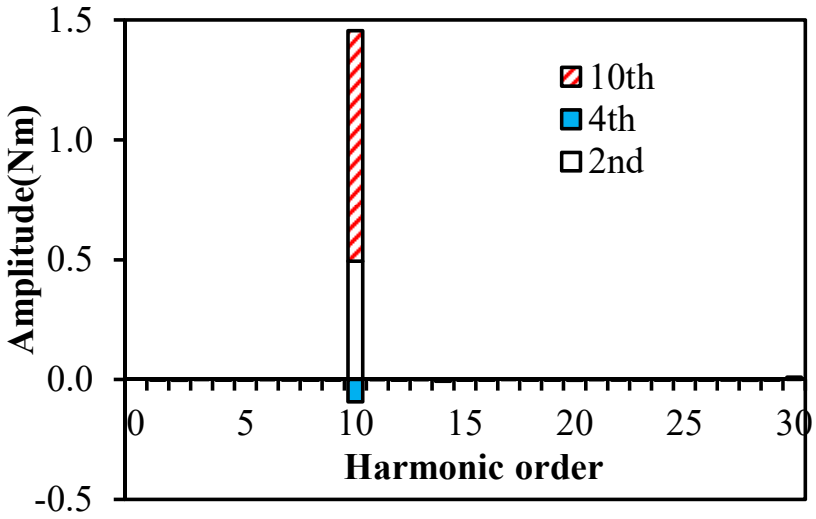

Fig. B.8. Torque contribution of the VPMSM.

B.2 Influence of Geometrical Parameters

In this section, the influence of geometrical parameters on the magnetic gearing effect in VPMSMs will be quantified based on an FEA-based ECSM. The relevant geometrical parameters are shown in Fig. B.9, where r_o and r_i are the stator outer and inner radii, r_y is the stator yoke radius, w_t is the stator tooth width, h_{so} is the stator tooth shoe height, l_a is the air-gap length, a_f and a_{so} are the mechanical slot opening angles of the stator and FMPs, respectively. h_f is the height of the stator tooth and h_{pm} is the height of the PM.

The influence of a specific geometrical parameter on the air-gap field modulation/magnetic gearing effect and the torque production will be investigated under different value of the parameter by the following steps:

Step 1: Calculate the air-gap PM flux density under open circuit condition, then perform spectrum analysis and record the value of fundamental harmonic;

Step 2: Un-magnetise the rotor PMs, perform FEA-based ECSM on the model; replace the slot area by silicon steel; calculate the air-gap armature reaction flux density; perform spectrum analysis on it and record the information of all the harmonics which may contribute torque production; restore each armature reaction MMF harmonic before modulation individually by sinusoidally magnetised PMs;

At this stage, for each restored armature reaction MMF harmonic with specific order, we have a

specific FE model like Fig. B.6 (a).

Step 3: For each specific FE model, set the material of slot area to be air; calculate the air-gap flux density; perform spectrum analysis and record the value of fundamental harmonic; if the order of the restored MMF harmonic equals the fundamental one, the recorded harmonic is the unmodulated armature reaction fundamental harmonic; if not, it is the modulated one;

Step 4: In each specific FE model, restore the rotor PM magnetisation, calculate the torque produced by each armature reaction MMF and the rotor PMs like Fig. B.6 (b); if the order of the restored MMF harmonic equals the fundamental one, the recorded torque is the torque produced by conventional torque production principle; if not, it is produced by magnetic gearing/modulation effect.

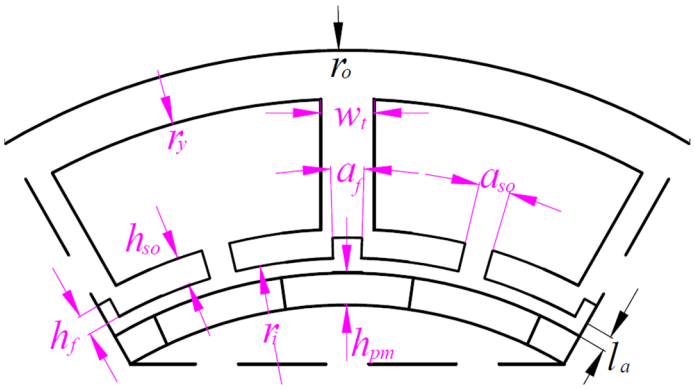

Fig. B.9. Geometrical parameters of VPMSM.

B.2.1 Influence of Slot Opening Angle

The influence of slot opening angle on the magnetic gearing effect is investigated. For simplicity, a_f and a_{so} are kept equal and vary at the same time in this investigation. Fig. B.10 (a) shows the variations of the modulated, unmodulated, total armature reaction harmonics and the PM fundamental harmonic with the increase of slot opening. It shows that with the increase of the slot opening, the modulated 10th armature reaction harmonic increases first and then decreases which means there exists an optimal slot opening angle for the best modulation/magnetic gearing effect. With the increase of the slot opening angle, the equivalent air-gap length increases which reduces the DC component in the permeance function. As a result, the unmodulated 10th armature reaction and the PM harmonic decrease as shown in Fig. B.10 (a). As a summation of the modulated and unmodulated 10th armature reaction harmonics, the total armature reaction harmonics increase first and then decrease with the increase of slot opening.

Fig. B.10 (b) shows the variations of the torque components produced by the principle of the conventional PMSM (unmodulated), the magnetic gearing effect (modulated) and the resultant torque with slot opening angle, respectively. It shows that their variations agree with the variations of the unmodulated, modulated and their resultant armature reaction harmonics, respectively. It should be noted that the maximum magnetic gearing effect does not guarantee the largest resultant torque, the machine must be carefully designed to balance the contributions of the torque components produced by the principle of the conventional PMSM and the magnetic gearing effect.

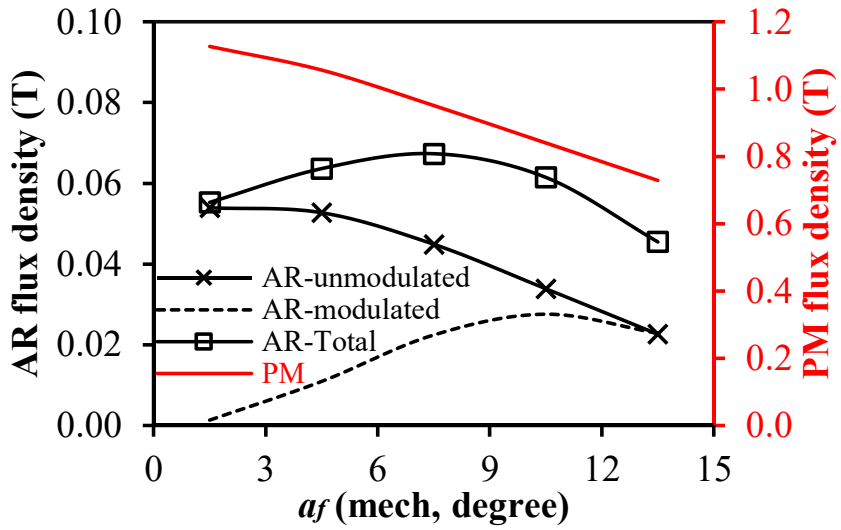

(a) On air-gap harmonics

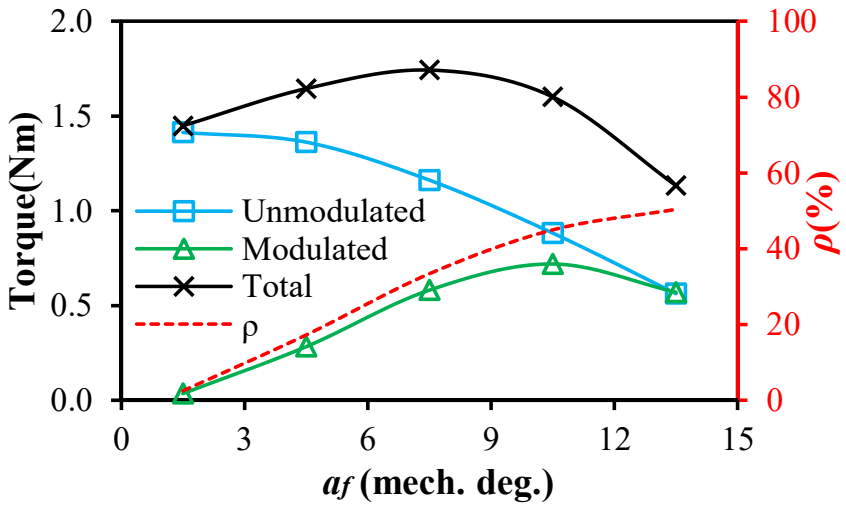

(b) On torque contribution

Fig. B.10. Influence of slot opening angle.

To evaluate the contribution of magnetic gearing effect to the average torque in VPMSMs, the ratio of the torque produced by magnetic gearing effect to the total torque is employed. The ratio ρ with respect to slot opening angle is also illustrated in Fig. B.10 (b). It shows that the percentage of torque produced by magnetic gearing effect increases with the increase of slot opening.

B.2.2 Influence of FMP Height

The influence of the FMP height h_f on the magnetic gearing effect are investigated by FEA-based ECSM. Fig. B.11 (a) shows the variations of the modulated, unmodulated, total armature reaction harmonics and the PM fundamental harmonic with h_f. It shows that with the increase of h_f, the modulated 10th armature reaction harmonic increases as a result of increased magnetic gear effect, the unmodulated 10^{th} armature reaction and PM harmonics decrease as a result of enlarged equivalent air-gap length. This means that with the increase of FMP height, the flux modulation effect increases whereas the unmodulated air-gap harmonics decrease. As a summation of the modulated and unmodulated 10^{th} armature reaction harmonics, the total armature reaction harmonic increases slightly with the increase of h_f.

Fig. B.11 (b) shows the variations of the unmodulated, modulated, resultant torques and contribution of magnetic gearing effect with h_f. Since the torque is produced from the interaction between the armature reaction and PM harmonics, the unmodulated torque decreases with the increase of h_f as a result of both decreased unmodulated armature reaction and PM harmonics. Although the modulated armature reaction harmonic increases with the increase of h_f, the modulated torque increases and then decreases slightly as a result of decreased PM harmonic. Consequently, the resultant total torque increases first and then decreases. It can be seen that not only the armature reaction harmonics but also the PM harmonics play important roles in the torque production. Hence, both a_f and h_f must be properly designed to achieve not only the best combination between the unmodulated and modulated armature reaction harmonics, but also the armature reaction and PM harmonics. The contribution of magnetic gearing effect increases with the increase of h_f.

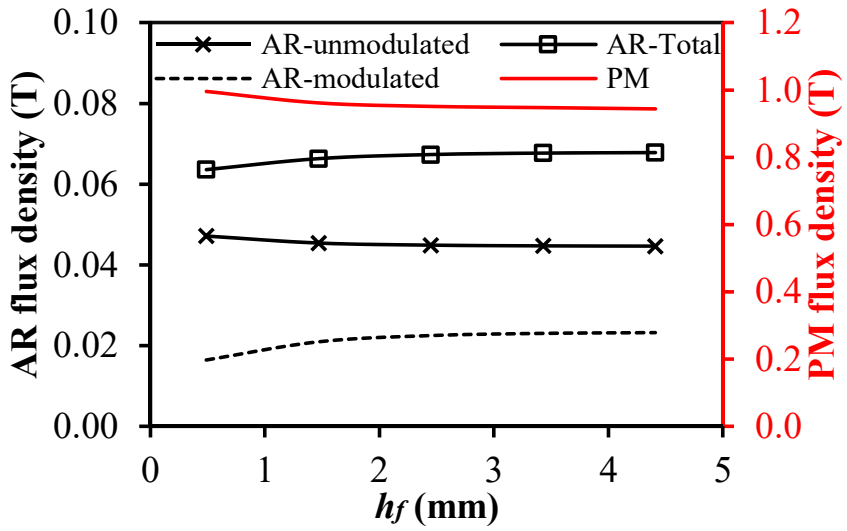

(a) On air-gap harmonics

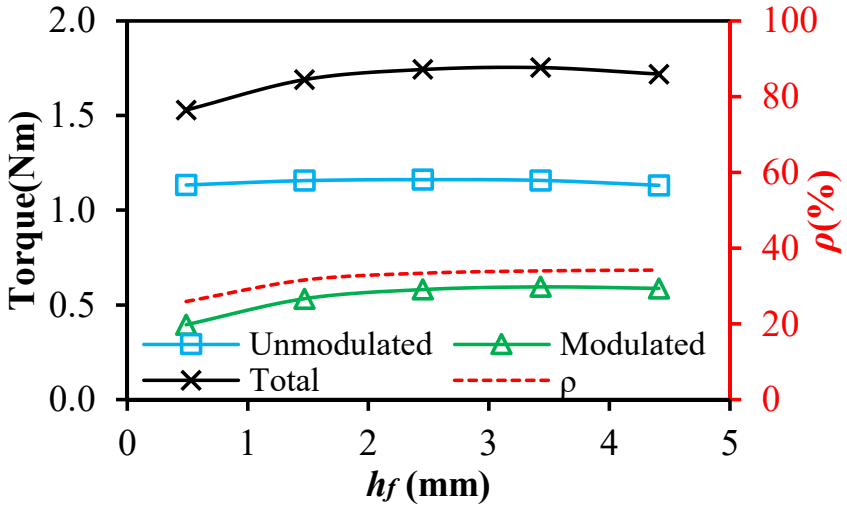

(b) On torque contribution

Fig. B.11. Influence of FMP height.

B.2.3 Influence of PM Height

The influence of PM height h_{pm} on the magnetic gearing effect is investigated by FEA-based ECSM. Fig. B.12 (a) shows the variations of the modulated, unmodulated, total armature reaction harmonics and the PM fundamental harmonic with h_{pm}. It shows that with the increase of h_{pm}, the unmodulated, modulated and resultant 10th armature reaction harmonics decrease. Since increased h_{pm} results in increased equivalent air-gap length, the results show that an enlarged equivalent air-gap length will weaken both the modulated and unmodulated armature reaction harmonics. It is also noteworthy that

the enlarged equivalent air-gap length has a larger effect in weakening the flux modulation effect since the modulated armature reaction harmonic decreases more significantly than the unmodulated one. However, the PM fundamental harmonic increases with the increase of h_{pm} due to increased PM usage. Hence, it is clear that there is an optimal PM height to balance the tradeoff between the armature reaction and PM fundamental harmonics and achieve the largest torque in VPMSMs.

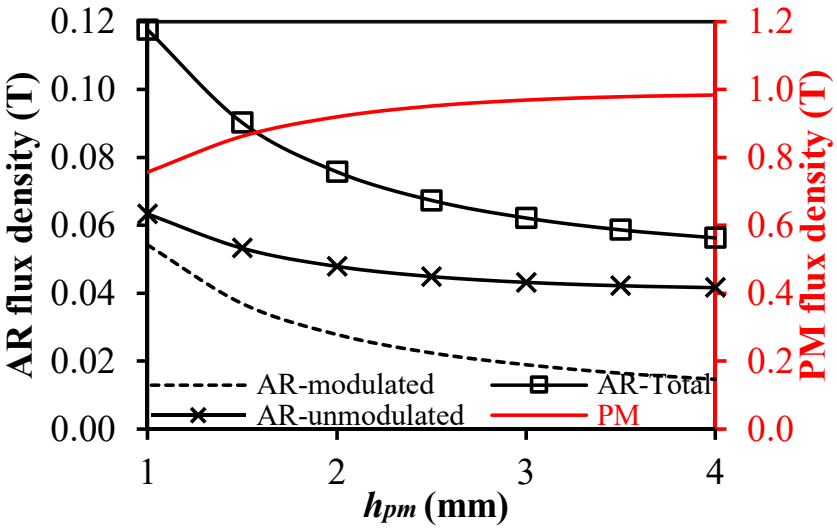

(a) On air-gap harmonics

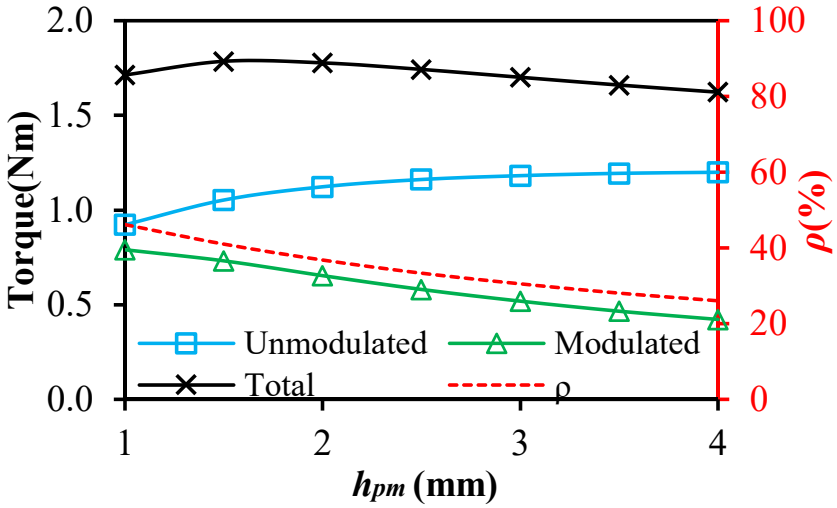

(b) On torque contribution

Fig. B.12. Influence of PM height.

Fig. B.12 (b) shows the variations of the unmodulated, modulated, resultant torques and contribution of magnetic gearing effect with h_{pm}. It shows that although the unmodulated armature reaction

harmonic decreases with the increase of h_{pm}, the decrease can be compensated by the increased PM harmonic and the resultant unmodulated torque increases with the increase of h_{pm}. Compared with the unmodulated harmonic, the decrease in the modulated harmonic is so significant that cannot be totally compensated by the increase of PM harmonic. As a result, the modulated torque and the contribution of magnetic gearing effect decrease with the increase of h_{pm}. The resultant torque reaches its maximum value at a relatively smaller h_{pm} which is a major difference between VPMSMs and conventional PM machines.

B.2.4 Influence of FMP Number

To make a fair comparison between VPMSMs with different FMP numbers, four VPMSM candidates with different slot/FMP/pole combinations have been selected according to and globally optimised in Ansys Maxwell to achieve the maximum torque under the following fixed constrains: (1) stator outer radius r_o; (2) air-gap length l_a; (3) stack length l_{ef}; (4) shaft radius r_s; (5) slot packing factor; (6) copper loss at 20W considering the end windings for each machine. It should be noted that copper loss is the main loss and source of heating for the machine of this size at low speed, and 20W is selected within a reasonable copper loss range for the machine of this size. Therefore, all the machine candidates are optimised under the same thermal loading. The length of the ending winding is estimated by measuring the span of a coil. The related dimensional parameters are illustrated in Fig. B.9. During the optimisation, the stator yoke radius r_y, the stator inner radius r_i, the stator and FMP slot opening angles a_{so} and a_f, the PM height h_{pm}, the stator and FMP slot opening heights h_f and h_{so} are variables for all machines. Genetic algorithm is used in the global optimisation. Optimised results are shown in Table B.4

From Table B.4, it can be seen that when N_f increases from 0 to 3, the 2nd armature reaction harmonic can be modulated to the 4th, 10th, 16th and 20th harmonics. The influence of the FMP number on the magnetic gearing effect is investigated by FEA-based ECSM. Fig. B.13 shows that with the increase of N_f, the unmodulated armature reaction harmonic decreases since with the increase of N_f, the order of the fundamental harmonic p_r increases as shown in Table B.4, which in turn decreases its amplitude. However, the modulated armature reaction harmonic sees an opposite trend: increases with the increase of N_f, reaching its peak when N_f=2 and remaining at the same level after that. This indicates that the flux modulation effect increases with the increase of N_f. The PM fundamental harmonic sees a decreasing trend with the increase of N_f as a result of decreased h_{pm}. Considering the influence of h_{PM} on magnetic gearing effect in the last sub-section, this indicates that for VPMSMs, the optimal

equivalent air-gap length decreases with the increase of N_f to achieve larger flux modulation/ magnetic gearing effect for optimal torque output.

Table B.4. Optimised Parameters

N_s	6			
r_o(mm)	45.0			
l_a(mm)	0.5			
r_s(mm)	5.0			
l_{ef}(mm)	25.0			
N_f	0	1	2	3
p_r	4	10	16	22
r_y(mm)	40.7	41.3	41.1	41.2
r_i(mm)	25.5	27.3	27.9	30.7
a_f(mech. deg.)	0	14.7	12.1	9.5
h_{so}(mm)	2.6	5.4	5.4	4.7
a_{so}(mech. deg.)	21.9	14.7	12.1	9.5
h_{PM}(mm)	3.0	2.2	1.4	1.3
h_f(mm)	0.0	2.1	2.6	2.2
w_t(mm)	8.7	7.4	7.9	7.5

Fig. B.13 (b) shows the variations of the unmodulated, modulated, resultant torques and contribution of magnetic gearing effect with N_f. It can be seen that with the increase of N_f, the unmodulated torque decreases as a result of decreased unmodulated armature reaction and PM harmonics whereas the modulated torque increases due to increased magnetic gearing effect. The resultant torque and the contribution of magnetic gearing effect increase with the increase of N_f , proving that the magnetic gearing effect has an overwhelmingly larger torque contribution to total torque than the principle of

conventional PMSM when N_f is larger.

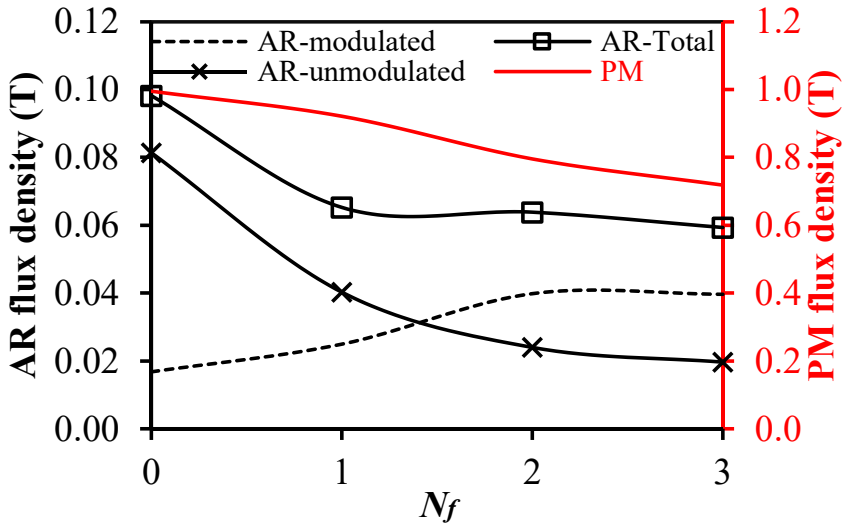

(a) On air-gap harmonics

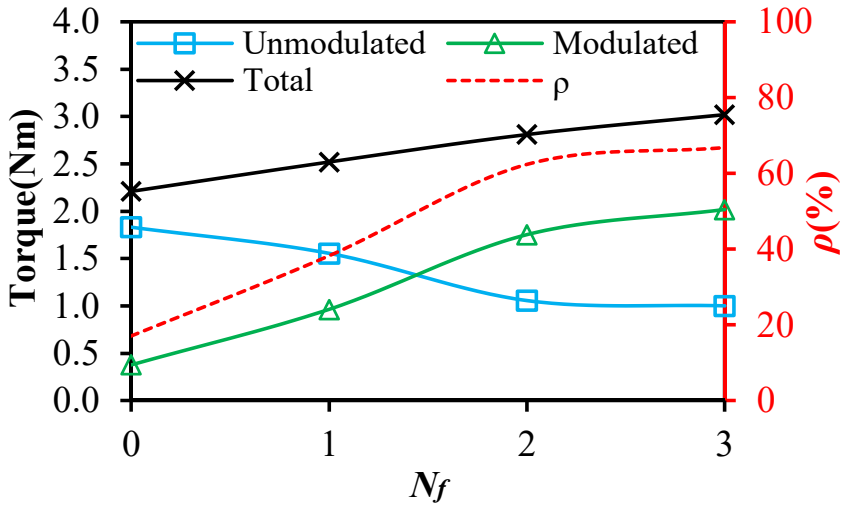

(b) On torque contribution

Fig. B.13. Influence of FMP number.

B.3 Gear Ratio for VPMSM with FMPs

In the 6-slot/12-FMP/20-pole VPMSM, the 2nd armature reaction field harmonic rotates at 5 times the speed of the fundamental harmonic, but in the opposite direction. After the modulation effect, it can interact with the 10th PM harmonic and produce steady torque. This is like a conventional magnetic gear with a 2-pole-pair outer rotor, a 10-pole-pair inner rotor and 12 FMPs. Although the 4th armature

reaction harmonic can also produce torque via magnetic gearing effect, the 2nd harmonic contributes more to the resultant torque and therefore, is named the dominating magnetic gearing effect in the VPMSM. In the conventional gear, the ratio of speeds of rotation between rotors is called the gear ratio. Hence, the gear ratio of the dominating gearing effect in the 6-slot/12-FMP/20-pole VPMSM is the ratio of the speed of the 2nd armature reaction field harmonic and fundamental harmonic, which is

$$G_r = -\frac{2}{10} = -\frac{1}{5} \tag{B.3}$$

Generally, in a well-designed VPMSMs with FMPs, the dominating magnetic gearing effect is consisted by a (N_f-p_r)th magnetic field harmonic rotating at the speed of -ω_s/(N_f-p_r), a N_f FMP, and the fundamental harmonic with the order of p_r and the speed of rotation of ω_s/p_r. Based on the analysis above, the gear ratio of the dominating gearing effect in VPMSMs with FMPs can be defined as:

$$G_r = \frac{p_r - N_f}{p_r} \tag{B.4}$$

B.4 Experimental Validation

To validate the previous analyses, the 6-slot/12-FMP/20-pole VPMSM is prototyped. Fig. B.14 shows the photos of stator and rotor. The dimensional parameters of the prototype are provided in Table B.5. Since this paper aims to reveal the torque production mechanism and influence of geometric parameters instead of optimisation, the geometry of the prototype is the same with the original FEA model in Fig. B.1 (a), which is different from the optimised one.

Firstly, the back-EMF of the VPMSM is tested and compared with the FEA result, Fig. B.15. It can be seen that the FEA back-EMF waveform agrees well with the test waveform.

The magnetic gearing effect and the torque components in the foregoing sections cannot be measured directly on the prototypes, only the FEA predicted electromagnetic torque can be measured in the experiments. The experiment is done by applying DC current to the windings (I_b=I_c=-I_a/2) and obtaining the static torque from the test rig shown in Fig. B.14 (c). Average static torques within 0–180 electric degrees and the maximum static torque under different current amplitudes of the prototype machines are calculated by 2-D FEA and compared with measurements as shown in Fig. B.16 (a) and (c), respectively. Moreover, the dynamic torque is tested on the test rig shown in Fig. B.14 (d) by

employing the dSPACE system. The prototypes are connected in tandem with the load machine and the dynamic torque is measured via the torque transducer and the results are provided in 360 mechanical degrees in Fig. B.16 (b). Although there are some discrepancies between the FEA and measured results, good agreements are obtained.

Table B.5. Dimensional Parameters of Prototype VPMSM

Parameters	Values
Slot number	6
Pole number	20
FMP number	12
Stator outer diameter	90mm
Stator inner diameter	42mm
Rotor outer diameter	41mm
Turns per phase	100
PM height	2.5mm
PM pole arc	180°
Axial length	25mm

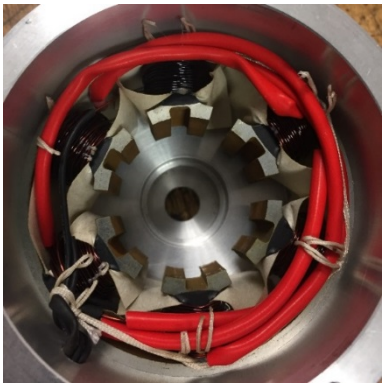

(a) Stator

(b) Rotor

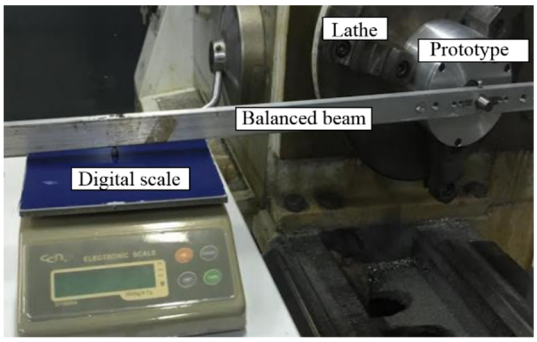

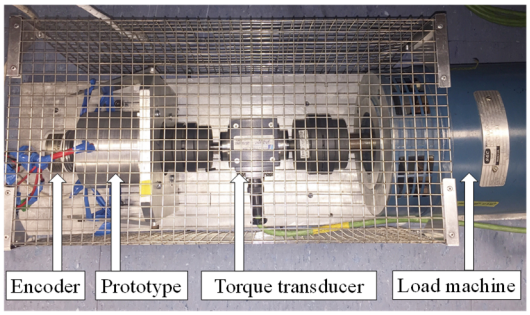

(c) Static torque test rig (d) Dynamic torque test rig

Fig. B.14. Prototype photos of the 20-pole-12-slot VPMSM, FMP=12.

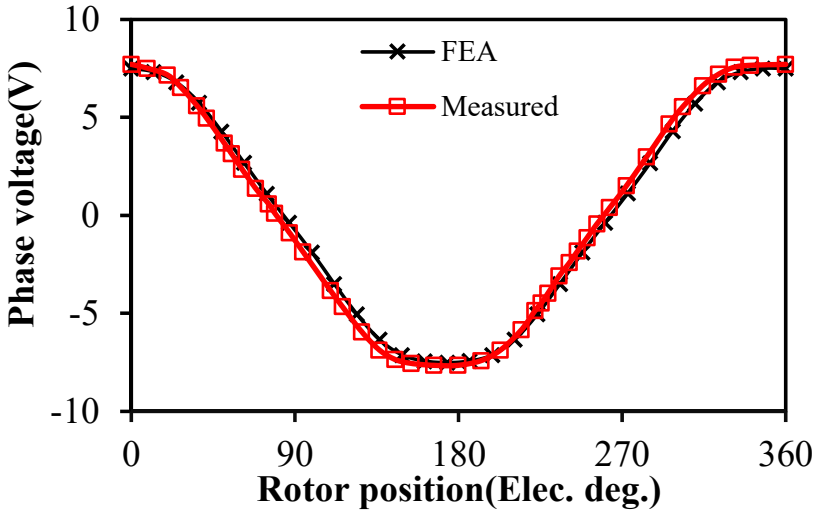

Fig. B.15. Comparison of the measured and FEA predicted back-EMF.

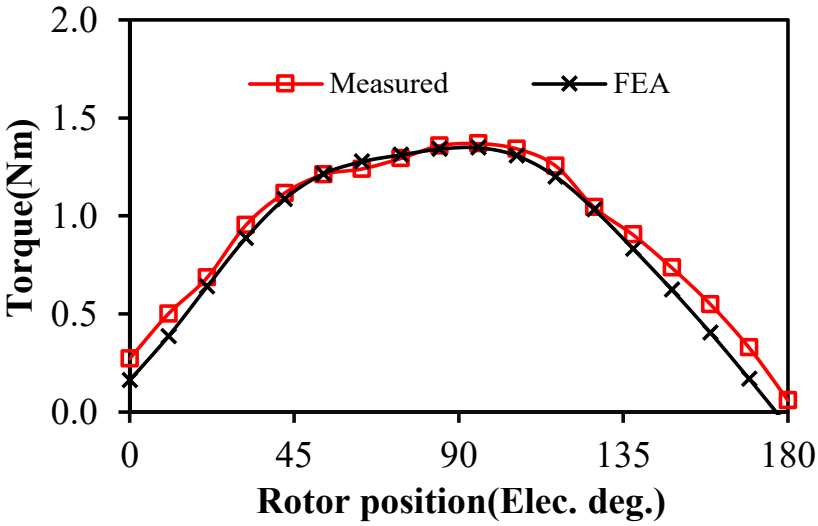

(a) Waveforms (I_a=9A, I_b=I_c=-4.5A)

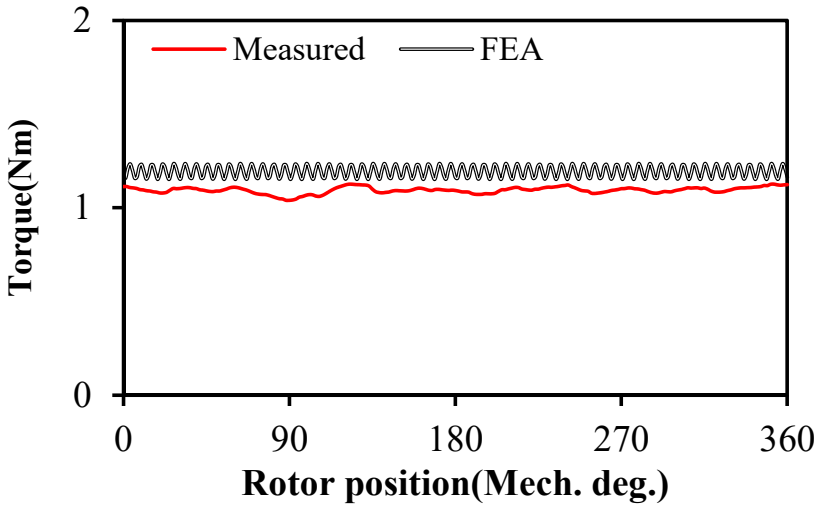

(b) Dynamic torque waveform (I_m=7.8A)

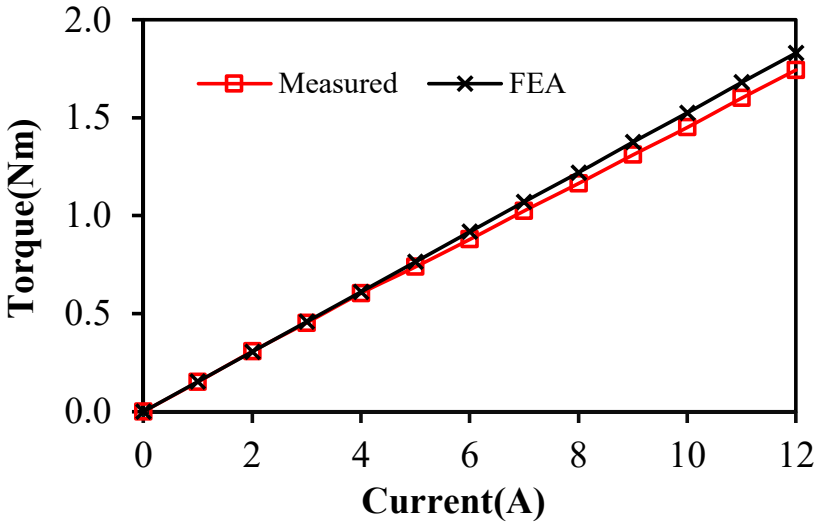

(c) Torque amplitude under different current

Fig. B.16. Comparison of measured and predicted.

B.5 Summary

In this chapter, a FEA-based ECSM is employed on a 6-slot/12-FMP/20-pole VPMSM to study the behaviour of harmonics under the modulation effect. The torque contribution of each armature reaction harmonic to the total torque is quantified. The influence of the machine geometric parameters on the magnetic gearing effect in VPMSMs with concentrated tooth-coil windings is also investigated. Based on the analysis, the magnetic gearing effect in VPMSMs is explained and the expressions of gear ratios for different topologies are provided. Finally, a prototype is manufactured.

Appendix C

CAD Drawings of Prototypes

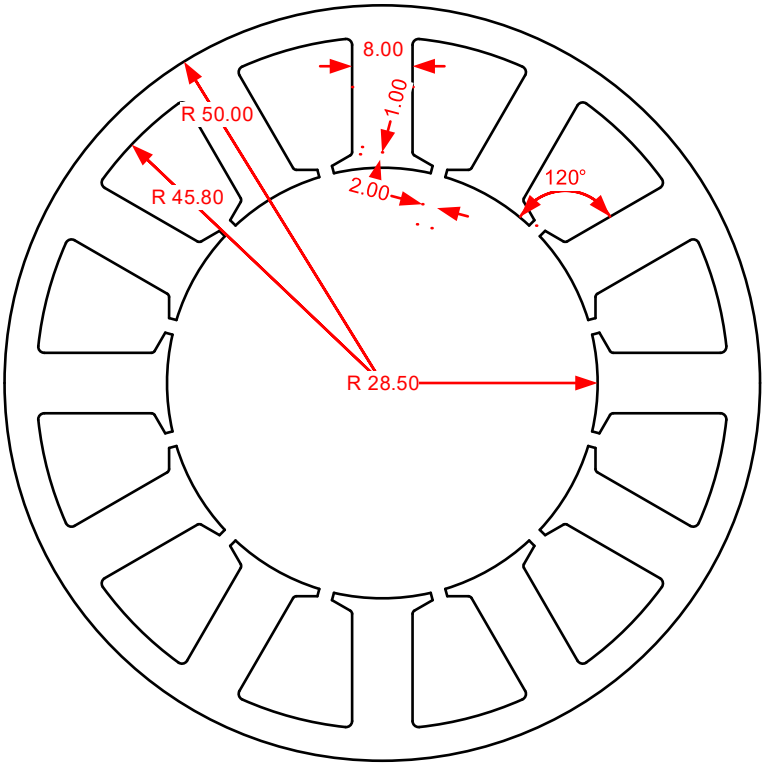

(a) Semi-closed slot

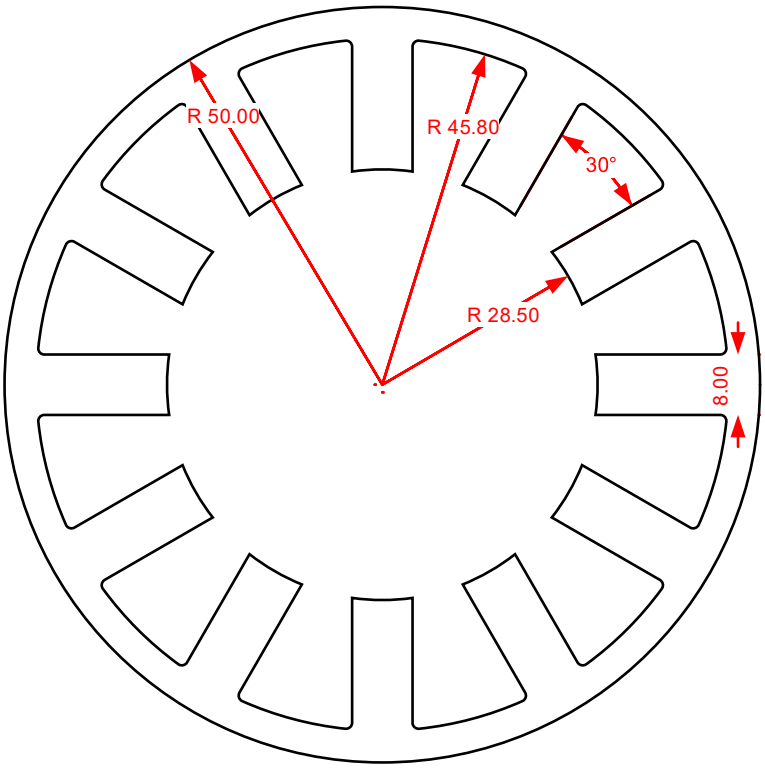

(b) Open slot

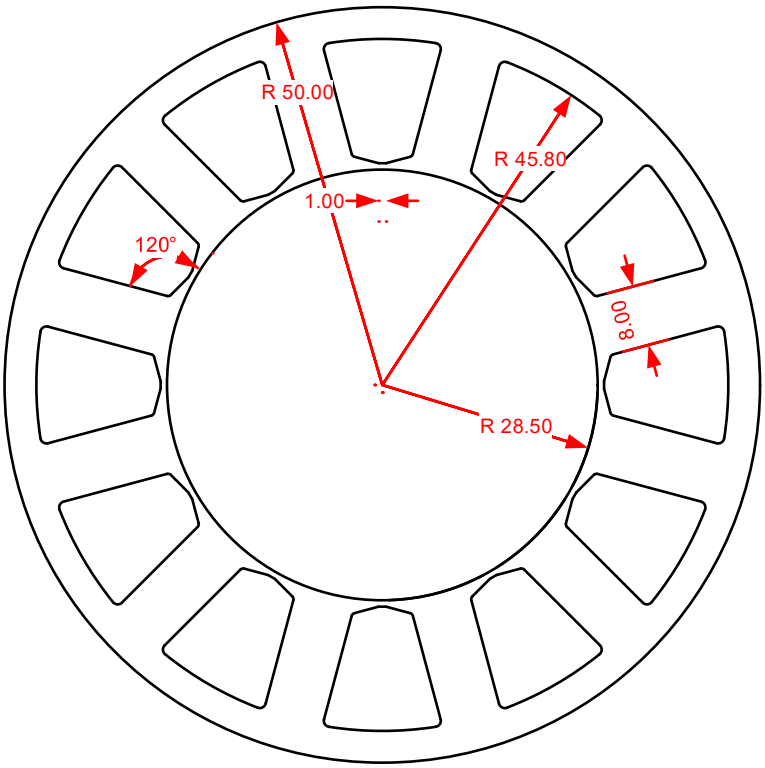

(c) Closed slot

Fig. C.1. Dimensions of 12-slot stators.

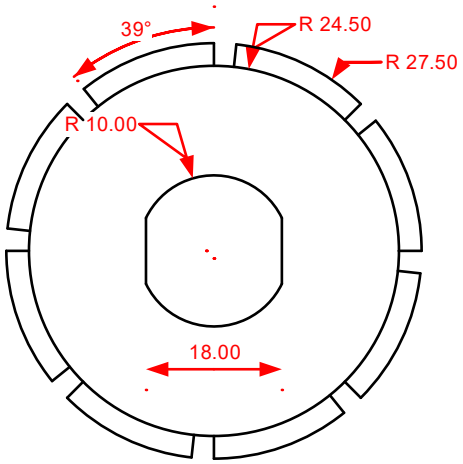

(a) 8-pole

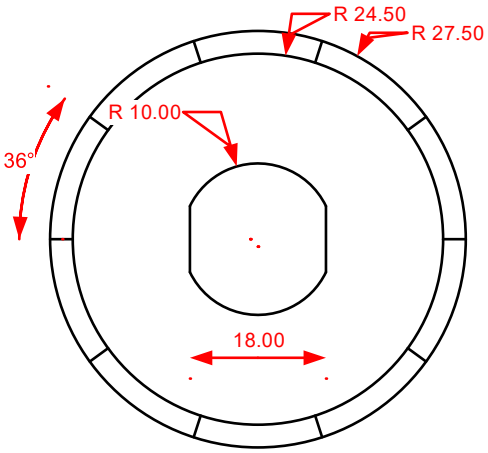

(b) 10-pole

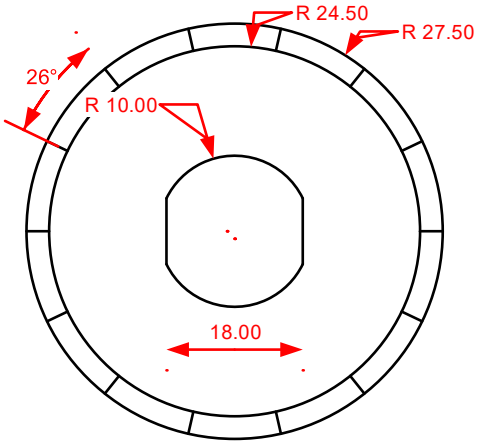

(c) 14-pole

Fig. C.2. Dimensions of rotors

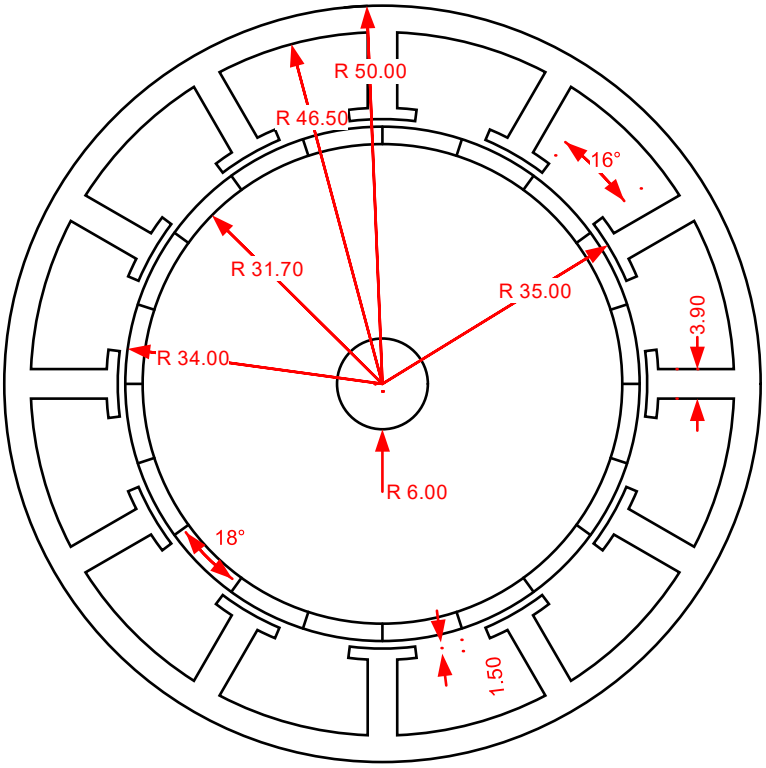

(a) 12-slot/20-pole

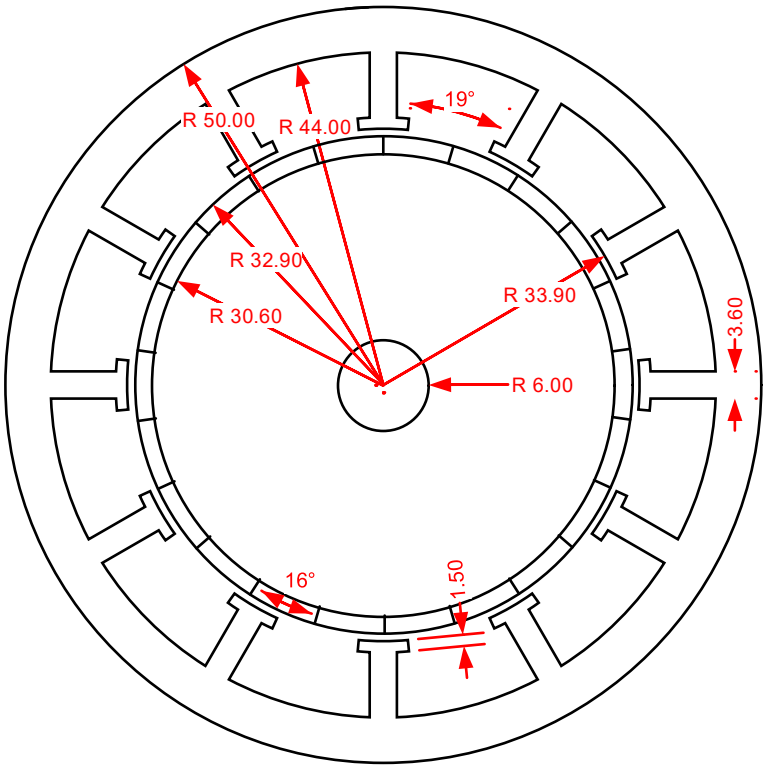

(b) 12-slot/22-pole

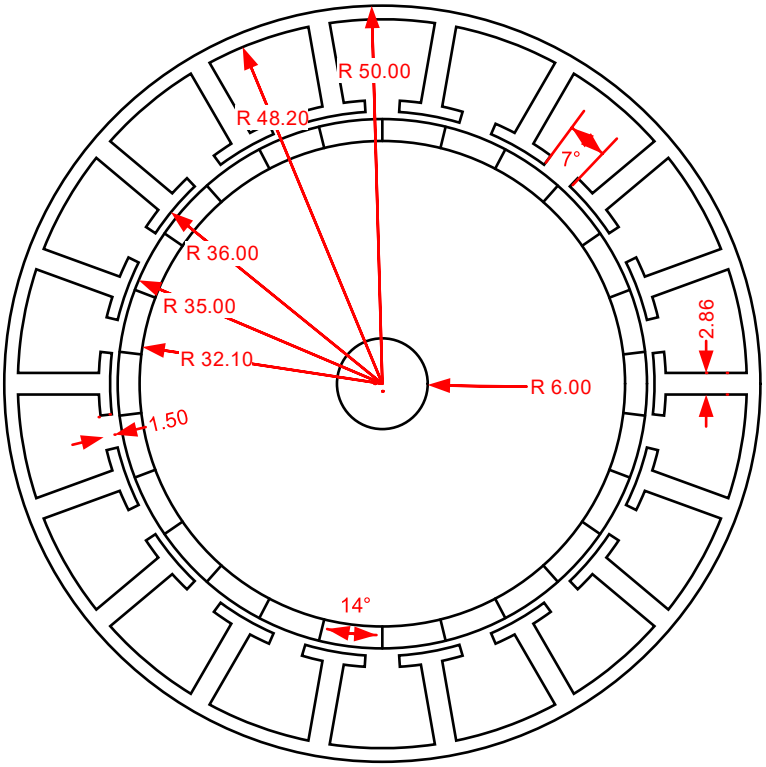

(c) 18-slot/26-pole

Fig. C.3. Dimensions of rotors

Appendix D

Publications

Journal papers

[1] Z. Q. Zhu and **Y. Liu**, "Analysis of air-gap field modulation and magnetic gearing effect in fractional slot concentrated winding permanent magnet synchronous machines," *IEEE Trans. Ind. Electron*., vol. 65, no. 5, pp. 3688–3698, May 2018. **(Chapter 2)**

[2] **Y. Liu** and Z. Q. Zhu, "Influence of gear ratio on the performance of fractional slot concentrated winding permanent magnet machines," *IEEE Trans. Ind. Electron.*, doi: 10.1109/TIE.2018.2885728. **(Chapter 3)**

[3] **Y. Liu**, H. Y. Li and Z. Q. Zhu, "A high power factor Vernier machine with coil-pitch of two slot pitches," *IEEE Trans. Magn*., vol. 54, no.11, Nov. 2018, Art. ID 8105405. **(Chapter 7)**

[4] **Y. Liu**, Z.Q. Zhu, C. Gan, S. Brockway, C. Hilton, "Comparison of optimal slot/pole number combinations in fractional slot permanent magnet synchronous machines having similar slot and pole numbers," *IET J. Eng.*, in press. **(Chapter 6)**

[5] H. Y. Li, **Y. Liu** and Z. Q. Zhu, "," *IEEE Trans. Magn.,* vol. 54, no.11, Nov. 2018, Art. ID 8105206.

[6] Z. Q. Zhu, M. F. H. Khatab, H. Y. Li and **Y. Liu**, "A novel axial flux magnetically geared machine for power split application," *IEEE Trans. Ind. Appl.*, vol. 54, no. 6, pp. 5954–5966, Nov. 2018.

[7] M. Zheng, Z. Q. Zhu, S. Cai, H. Y. Li and **Y. Liu**, "Influence of magnetic saturation and rotor eccentricity on back-EMF of novel hybrid-excited stator slot opening permanent magnet machine," *IEEE Trans. Magn.*, vol. 54, no.11, Nov. 2018, Art. ID 8105905.

[8] M. Zheng, Z. Q. Zhu, S. Cai, H. Y. Li, and **Y. Liu**, "Influence of stator and rotor pole number combinations on the electromagnetic performance of stator slot-opening PM hybrid-excited machine," *IEEE Trans. Magn.,* early access, doi: 10.1109/TMAG.2019.2903769.

[9] M. F. H. Khatab, Z. Q. Zhu, H. Y. Li, and **Y. Liu**, "Comparative study of axial flux magnetically geared machine with conventional axial flux YASA machine," *CES Trans. Elect. Mach. Syst.*, vol. 2, no. 4, pp. 392–398, Dec. 2018.

[10] M. F. H. Khatab, Z. Q. Zhu, H. Y. Li, and **Y. Liu**, "Influence of static and dynamic rotor/stator misalignments in axial flux magnetically geared machine," *IET J. Eng.*, in press.

Conference papers

[11] **Y. Liu** and Z. Q. Zhu, "Comparative study of magnetic gearing effect in integral slot, fractional slot winding and Vernier PM machines," *in 20th Int. Conf. Electr. Mach. Syst*., Sydney, Australia, 2017. **(Chapter 6)**

[12] **Y. Liu** and Z. Q. Zhu, "Electromagnetic performance comparison of 18-slot/26-pole and 18-slot/10-pole fractional slot permanent magnet surface-mounted machines," *in 20th Int. Conf. Electr. Mach. Syst.*, Sydney, Australia, 2017. **(Chapter 7)**

[13] **Y. Liu** and Z. Q. Zhu, "Magnetic gearing effect in Vernier permanent magnet synchronous machines," *in IEEE Energy Convers. Congr. Expo.*, Cincinnati, USA, 2017, pp. 5025–5032. **(Chapter 4)**

[14] **Y. Liu** and Z. Q. Zhu, "Influence of gear ratio on electromagnetic performance and geometries of Vernier permanent magnet synchronous machines," *in IEEE Energy Convers. Congr. Expo.*, Cincinnati, USA, 2017, pp. 2453-2460. **(Chapter 5)**

[16] H. Yang, Z. Q. Zhu, **Y. Liu**, H. Y. Li and J. Mipo, "Comparative study of doubly salient machines with/without stator slot permanent magnets," *in Proc. Int. Elec. Mach. Drives. Conf.*, USA, May 20-24, 2017.

[17] M. F. H. Khatab, Z. Q. Zhu, H. Y. Li, and **Y. Liu**, "Optimal design of a novel axial flux magnetically geared PM machine," *Int. Conf. Ecological Veh. Renewable Energies,* Monte Carlo, Monaco, 2017.

[18] Z. Q. Zhu, H. Yang, S. Cai, H. Y. Li, **Y. Liu**, J. Mipo, and S. Personnaz, "Hybrid excited stator slot PM machines with overlapping windings," *Int. Conf. Elect. Mach.*, Alexandroupoli, Greece, 2018, pp. 2185-2191.

[19] H. Yang, Z. Q. Zhu, S. Cai, H. Y. Li, **Y. Liu**, J. Mipo, and S. Personnaz, "Performance comparison of stator slot PM machines with non-overlapping and overlapping windings," *Int. Conf. Elect. Mach.*, Alexandroupoli, Greece, 2018, pp. 2283-2289.

[20] Yang, Z. Q. Zhu, **Y. Liu**, H. Y. Li, and J. Mipo, "Comparative study of doubly salient machines with/without stator slot permanent magnets," in *IEEE Int. Elect. Mach. Drives. Conf.*, Miami, FL, 2017.